DMPCO 2023

2nd International Conference

DESIGN AND MANAGEMENT OF PORT, COASTAL AND OFFSHORE WORKS

Organised by:

Laboratory of Maritime Engineering and Maritime Works

Laboratory of Harbour Works

Laboratory of Floating Structures and Mooring Systems

Hydraulic Engineering Laboratory

PROCEEDINGS VOLUME I

MAY 24-27, 2023

Aristotle University's Research Dissemination Center

Thessaloniki, Greece

DMPCO 2023

2nd International Conference

DESIGN AND MANAGEMENT OF PORT, COASTAL AND OFFSHORE WORKS

MAY 24-27, 2023

Aristotle University's Research Dissemination Center

Thessaloniki, Greece

Proceedings of the 2nd International Conference
Design and Management of Port, Coastal and Offshore Works

ISSN: 2945-1299
ISBN: 978-960-99922-6-8

VOLUME I

ISBN: 978-960-99922-7-5

Published by: Laboratory of Maritime Engineering and Maritime Works,
Civil Engineering Department, AUTh

Edited by: T. Karambas, E. Loukogeorgaki, C. Makris

Year of Publication: 2023

Organised by:

Laboratory of Maritime Engineering and Maritime Works

Laboratory of Harbour Works

Laboratory of Floating Structures and Mooring Systems

Hydraulic Engineering Laboratory

COMMITTEES

ORGANIZING COMMITTEE

CHAIRS

Theofanis Karambas, Professor, Director Lab. of Maritime Engineering & Maritime Works, AUTh
Eva Loukogeorgaki, Associate Professor, AUTh

MEMBERS

Spyros Christopoulos, Dr. Coastal Engineer, HYDROMARE
Christos Makris, Research Associate, AUTh
Afrodite Papageorgiou, Civil Engineer, AUTh

SCIENTIFIC COMMITTEE

Androulidakis Y., Research Assoc., AUTh, University Fellow Scholar, Un. of the Aegean
Athanasoulis G., Professor Em., NTUA
Chalmoukis I., Postdoctoral Assoc., University of Patras
Chatjigeorgiou I., Professor, NTUA
Chatzimpiros K., Professor Em., AUTh
Chlomoudis K., Professor, University of Piraeus
Chondros M., Assist. Professor, NTUA
Christopoulos S., Dr. Coastal Engineer, HYDROMARE
Dimakopoulos A., Dr. Civil Engineer, Associate Director, Jacobs, UK
Dimas A., Professor, University of Patras
Fourniotis N., Assist. Professor, University of Peloponnese
Galani K., Dr. Coastal Engineer, Patras Port Authority
Grigoriadis D., Assoc. Professor, University of Cyprus, Cyprus
Grigoropoulos G., Professor, NTUA
Karambas Th., Professor, AUTh
Karmpadakis I., Assoc. Professor, Imperial College, UK
Katsardi V., Assist. Professor, UTH
Klonaris G., Dr. Civil Engineer, Research Assoc., NTUA
Kokkosis Ch., Professor, UTH
Kolokythas G., Dr. Coastal Engineer, AKTAIA
Konispoliatis D., Assist. Professor, NTUA
Koutitas Ch., Professor Em., AUTH
Koutrouveli Th., Dr. Coastal Engineer, IMDC, Belgium
Krestenitis Y., Professor Em., AUTh
Kupraios N., Dr. Civil Engineer
Leftheriotis G., Postdoctoral Assoc., University of Patras
Loizidou M., Professor, NTUA
Loizidou X., Dr. Coastal Engineer, ISOTECH, Cyprus
Loukogeorgaki E., Assoc. Professor, AUTh
Makris Ch., Dr. Civil Engineer, Research Assoc., AUTh
Mavrakos S., Professor Em., NTUA
Melissas D., Professor, NTUA
Memos K., Professor Em., NTUA
Metallinos A., Dr. Civil Engineer, Research Assoc., NTUA
Michailidis C., Assist. Professor, IHU
Mpardakis B., Dr. Civil Engineer, President of HCCE
Pallis Ath., Professor, University of the Aegean
Panagiotopoulos I., Assist. Professor, UOA
Papadopoulou M., Professor, NTUA
Papatheodorou G., Professor, University of Patras
Poulos S., Professor, UOA
Prinos P., Professor, AUTh
Samaras Ach., Assist. Professor, DUTh
Savvidis Y., Professor, IHU
Soukisian T., Dr. Naval Architecture and Marine Engineer, HCMR
Stamou A., Professor, NTUA
Sylaios G., Professor, UTH
Toumazis A., Dr. Civil Engineer, University of Cyprus
Tsanis I., Professor, University of Crete
Tsoukala V., Professor, NTUA
Vasilakis E., Assist. Professor, UOA
Zacharias I., Professor, University of Patras

EXTERNAL ADVISORY COMMITTEE

Arena F., Professor, University Mediterranea of Reggio Calabria, Italy
Benoit M., IRPHE, France
Carevic D., Professor, University of Zagreb, Croatia
Penchev V., Professor, BDCA, Bulgaria
Sánchez-Arcilla A., Professor, UPC, Spain
Taveira Pinto F., Professor, University of Porto, Portugal
Vicinanza D., Professor, University Vanvitelli, Italy

DMPCO 2023

2nd International Conference

DESIGN AND MANAGEMENT OF PORT, COASTAL AND OFFSHORE WORKS

CONTENTS VOLUME I

OFFSHORE RENEWABLE ENERGY

MARINE SPATIAL PLANNING & ENVIRONMENT

DMPCO 2023

PREFACE

Ports, coastal and offshore structures play a strategic role for the socio-economic development of citizens in Europe and worldwide, facilitating the sustainable and secure implementation of various human activities, such as transportation, fishing, leisure and aquaculture, the protection of coastal areas and the exploitation of energy sources in the marine environment. Contemporary societal needs, including mitigation of climate change impacts, protection against coastal flooding and extreme events, clean, affordable and secure energy, security of supplies and decarbonisation of marine facilities, have redefined, nowadays, the significance of all coastal and offshore infrastructures, and have introduced new technological challenges in the whole life-cycle of those structures. Still, a great potential for innovation and growth has been emerged taking advantage of the numerous opportunities that seas and oceans provide.

The **2nd International Conference on Design and Management of Port, Coastal and Offshore Works** (DMPCO 2023) aims to stimulate comprehensive discussions and scientific interactions among the participants about the new trends and the state-of-the-art developments in the design and management of ports, coastal and offshore structures. As a sequence of DMPCO 2019, the Conference provides a forum for presenting new ideas and enhancing scientific and applied knowledge for engineers and scientists working in the relevant fields.

DMPCO 2023 has successfully attracted the interest of 221 authors from Greece, Cyprus, United Kingdom, Belgium, Netherlands, Italy, Romania, Georgia and China. The final technical program included 89 presentations allocated into 14 sessions, as well as 5 keynotes, where worldwide recognized speakers presented cutting-edge topics. This year, the "Coastal Modelling" session was organized in the honour of Professor Emeritus Christofer Koutitas and the "Offshore Renewable Energy I" session was dedicated to the memory of Professor Emeritus Demos Angelides. The two volumes of the DMPCO 2023 proceedings include 85 papers, which are grouped in ten main thematic areas of the Conference corresponding to: Coastal Modelling, Coastal Hydrodynamics, Extreme Waves – Wave Hydrodynamics, Offshore Renewable Energy, Marine Spatial Planning & Environment, Coastal Erosion & Management, Integrated Coastal Zone Management, Ports & Ports Engineering, Coastal Structures and Geotechnical & Geo-environmental Engineering.

We would like to thank all authors and keynote speakers for their contributions, as well as all the members of the Organizing, Scientific and External Advisory Committees for their valuable help and support. All these efforts resulted to a successful Conference with active participation and stimulating discussions in the field of port, coastal and offshore structures. This success gives us the energy and the motivation to continue our strong and systematic efforts towards the organization of productive DMPCO Conferences in the future.

We are looking forward to seeing you in Patras, Greece in 2025.

Professor Theofanis Karambas
Associate Professor Eva Loukogeorgaki
Chairs of the Organizing Committee

DMPCO 2023

CONFERENCE PROCEEDINGS VOLUME I

Modelling earthquake-generated tsunamis: Considerations on the effects of fault models on tsunami generation and propagation

A.G. Samaras[1*], I. Triantafyllou[2,3], A. Agalos[4], G. Papadopoulos[4,5], T.V. Karambas[6]

[1]Department of Civil Engineering, Democritus University of Thrace, University Campus - Kimmeria, 67100 Xanthi, Greece
[2]Faculty of Geology and Geoenvironment, National and Kapodistrian University of Athens, University Campus, 15771 Athens, Greece
[3]Center for Security Studies, Ministry of Citizen Protection, 10177 Athens, Greece
[4]International Society for the Prevention and Mitigation of Natural Hazards, 10681 Athens, Greece
[5]Hellenic Mediterranean University, 71410 Heraklion, Crete, Greece
[6]Department of Civil Engineering, Aristotle University of Thessaloniki, University Campus, 54124 Thessaloniki, Greece
[*]Corresponding author: achsamar@civil.duth.gr

Abstract

This work investigates the effect that earthquake fault model types and properties have on the numerical modelling of tsunami generation and propagation. This is done using a 2DH post-Boussinesq model, properly adapted to represent tsunami waves generated by dynamic bed deformations due to dip-slip faulting. Model runs are performed for fault models of varying intrinsic properties (i.e. dip/rake angles and fault depth) and fault models of different type for the same earthquake (i.e. homogeneous vs heterogeneous), with respective bed deformation fields being produced by an independent in-house computational module. Model results are presented in the form of snapshots of wave profiles and free surface elevation fields/maps. Analysis of wave generation and propagation provides useful insights regarding the modelling of earthquake-generated tsunamis.

Keywords Tsunamis, Post-Boussinesq model, Earthquake fault models.

1 INTRODUCTION

Undersea earthquakes are the most common cause of tsunamis. The abrupt earthquake-induced seafloor deformations are transferred to the sea surface, generating waves that propagate across the open sea and towards coastal areas. Accurate representation of how tsunamis generate and propagate is crucial for tsunami risk assessment, preparedness and mitigation. Numerical models are essential to the above; however, their efficacy in real-life applications is bound by the accurate representation of the source of seafloor deformation, i.e. the earthquake fault models (Satake et al. 2013, Yamazaki et al. 2018). Considering that recent relevant research shifts towards probabilistic applications that explore the variety and complexity of tsunami sources and their generation mechanisms (De Risi and Goda 2016, Li et al. 2016), this work investigates the effect that earthquake fault model types and properties have on the numerical modelling of tsunami generation and propagation. Section 2 presents a brief description of the 2DH post-Boussinesq model used in this work; Section 3 presents the characteristics of model applications and their results; Section 4 presents a brief discussion on the results and the conclusions drawn from this work.

2 THE 2DH POST-BOUSSINESQ MODEL

2.1 Governing Equations

The present work is based on the 2DH post-Boussinesq model of Karambas and Memos (2009) for weakly nonlinear fully dispersive water waves. The model has been applied since in several research and engineering applications (Karambas and Samaras 2014, Samaras et al., 2015, Samaras and Karambas 2021a,b). Its capability in representing tsunami generation and propagation has been

validated through comparison with 1D and 2D analytical solutions (Hammack 1973, Dutykh and Dias 2007). The model's momentum and continuity equations are written as follows:

$$\frac{\partial U}{\partial t}+U\frac{\partial U}{\partial x}+V\frac{\partial U}{\partial y}+g\frac{\partial \zeta}{\partial x}=-\int_{\infty}^{\infty}\int_{-\infty}^{\infty}\left(\frac{\partial \zeta}{\partial x}(x-\xi_1,x-\xi_2,t)-\frac{\partial \zeta}{\partial x}\right)K(\xi_1,\xi_2)\,d\xi_1 d\xi_2 \tag{1}$$

$$\frac{\partial V}{\partial t}+U\frac{\partial V}{\partial x}+V\frac{\partial V}{\partial y}+g\frac{\partial \zeta}{\partial y}=-\int_{-\infty}^{\infty}\int_{-\infty}^{\infty}\left(\frac{\partial \zeta}{\partial y}(x-\xi_1,x-\xi_2,t)-\frac{\partial \zeta}{\partial y}\right)K(\xi_1,\xi_2)\,d\xi_1 d\xi_2 \tag{2}$$

$$\frac{\partial \zeta}{\partial t}+\frac{\partial\left[(d+\zeta)U\right]}{\partial x}+\frac{\partial\left[(d+\zeta)V\right]}{\partial y}=0 \tag{3}$$

where U, V are the depth-averaged velocity components along the x- and y- directions, respectively, ζ is the free surface elevation, d is the water depth and the kernel $K(x,y)$ is given by Eq. 4, in which $r^2=x^2+y^2$. Further details on the model can be found in Samaras and Karambas (2021a).

$$K(x,y)=\frac{g}{2\pi d^2}\left[\frac{1}{r/d}-\sum_{n=1}^{\infty}\frac{(-1)^{n-1}}{\sqrt{n^2+(r/d)^2/4}}\right] \tag{4}$$

2.2 Bed Deformations and Model Adaptation

In the case of a finite rectangular fault of width W and length L, positioned at a depth d_f below the bed surface, exponential bed deformation is expressed as

$$\zeta_b(x,y,t)=O(x,y)\left(1-e^{-\kappa t}\right) \tag{5}$$

where $O(x,y)$ is the vertical displacement field according to Okada (1992) and κ is a coefficient for the description of the exponential motion. It is noted that the formula proposed by Okada (1992) represents a homogeneous fault model; for heterogeneous fault models the composite deformation field is derived by first applying the formula to each of the sub-faults and then merging all sub-faults' contributions. In the present work, bed deformation fields are produced by an independent in-house computational module developed by the authors. Finally, the post-Boussinesq model is adapted to represent the active generation of tsunami waves, through additional terms (including ζ_b) in the momentum (Eqs. 1-2) and continuity (Eq. 3) equations.

3 MODEL APPLICATIONS AND RESULTS

3.1 Fault models of varying properties

In order to investigate the effect of earthquake fault model properties on tsunami generation and propagation, the 2DH post-Boussinesq model was applied using the bottom deformation fields produced by a set of eight homogeneous fault models (d = 3km for all runs). All models' properties are presented in Table 1; FM1 refers to the basis model, i.e. the fault model presented and tested in Mitsotakis (2009).

Table 1 Fault model properties for the homogeneous fault models runs: FM1 – basis model; FM2, FM3 – varying dip angles; FM4, FM5, FM6 – varying fault depths; FM7, FM8 – varying rake angles.

	FM1	FM2	FM3	FM4	FM5	FM6	FM7	FM8
Dip angle δ [deg]	7	15	22	7	7	7	7	7
Rake angle φ [deg]	67	67	67	67	67	67	30	15
Strike angle [deg]	90	90	90	90	90	90	90	90
Slip amount $\|D\|$ [m]	2	2	2	2	2	2	2	2
Fault length L [km]	40	40	40	40	40	40	40	40
Fault width W [km]	20	20	20	20	20	20	20	20

Fault depth d_f [km]	10	10	10	5	15	20	10	10
Young modulus E [GPa]	9.5	9.5	9.5	9.5	9.5	9.5	9.5	9.5
Poisson ration v	0.27	0.27	0.27	0.27	0.27	0.27	0.27	0.27

Figure 1 presents the bottom deformation fields and the respective deformation profiles along the x-axis for the eight fault models presented in Table 1. Figure 2 presents the respective wave profiles along the x-axis at t = 100s after earthquake, grouped by varying parameter (dip angle, fault depth, rake angle), as well as the free surface elevation fields for FM2, FM4 and FM7.

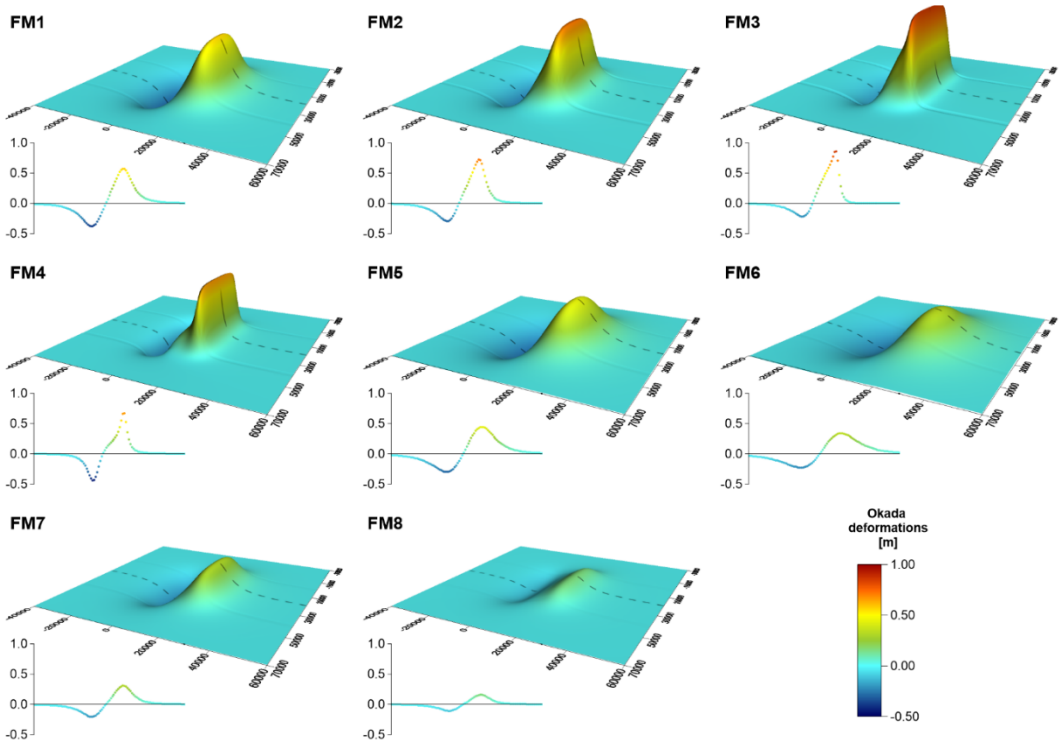

Figure 1 Bottom deformation fields and respective deformation profiles along the x-axis (dashed line) for the eight fault models presented in Table 1

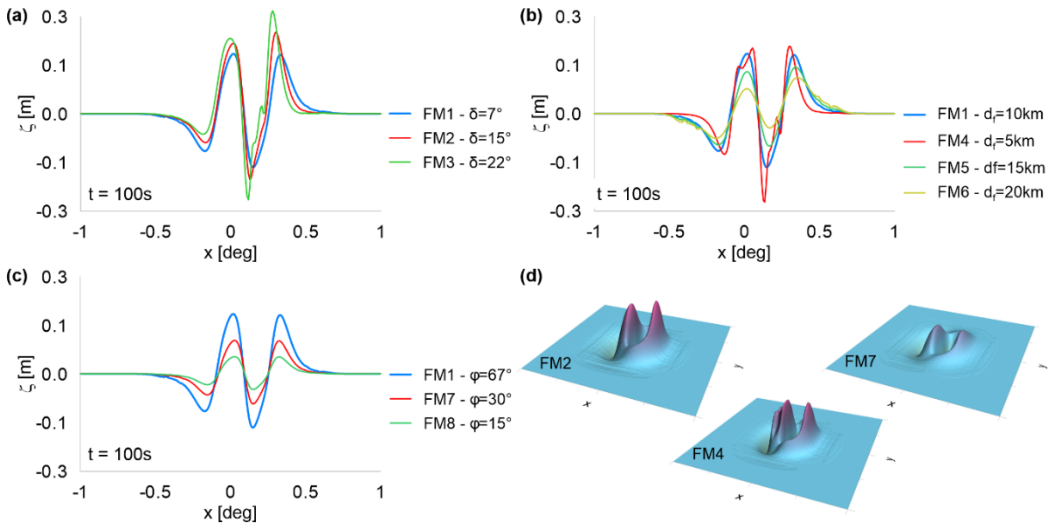

Figure 1 Wave profiles along the x-axis at t = 100s after earthquake for the eight fault models presented in Table 1 grouped by varying parameter (a - dip angle, b - fault depth, c - rake angle), and free surface elevation fields for FM2, FM4, FM7 (d)

3.2 Fault models of different types

In order to investigate the effect of earthquake fault model types on tsunami generation and propagation, the model was applied for the case study of the May 2nd, 2020 earthquake south of Crete, using the bottom deformation fields produced by a homogeneous fault model and a heterogeneous fault model, while model results were also compared to NOA Tide Gauges' mareographs at Ierapetra (Crete) and Kasos. Full analysis and results of these applications are to be found in Triantafyllou et al. (2023). Figure 3 presents the bottom deformation fields for the homogeneous and heterogeneous faults models. Figure 4 presents results of the 2DH post-Boussinesq model for the tsunami generated by the heterogeneous fault model, as snapshots of sea surface elevation at selected instances after the earthquake. Both Figures are adopted from Triantafyllou et al. (2023).

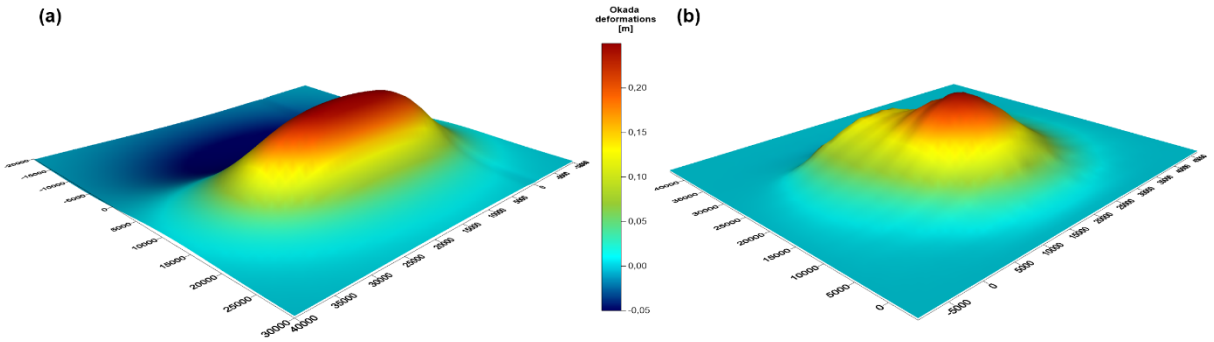

Figure 3 Bottom deformation fields for the (a) homogeneous and (b) heterogeneous fault models of the May 2nd, 2020 earthquake south of Crete (Figure adopted from Triantafyllou et al., 2023)

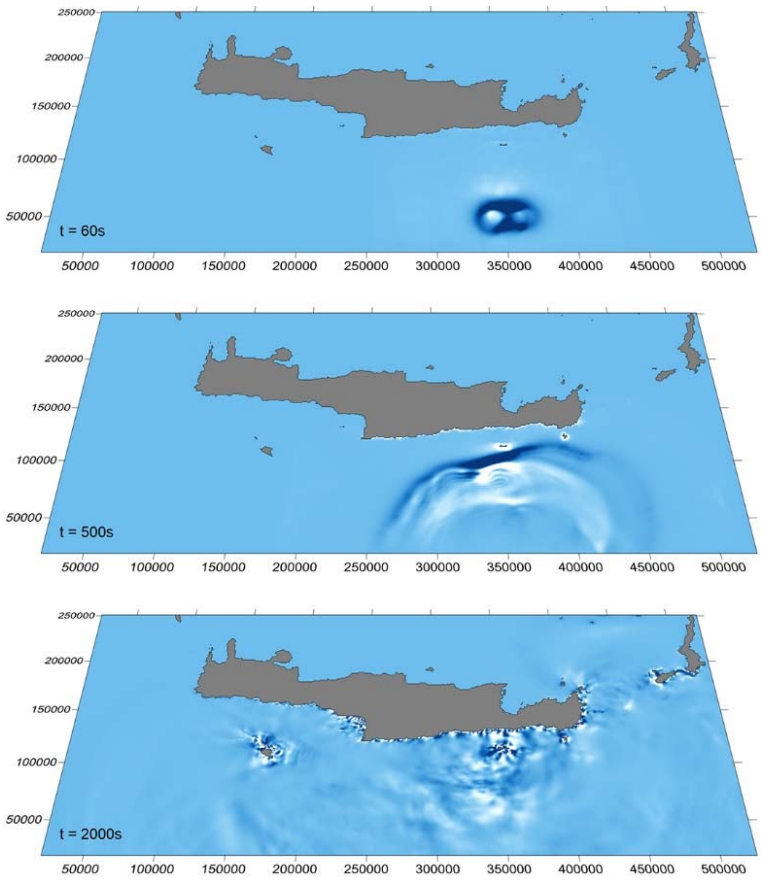

Figure 4 Results of the 2DH post-Boussinesq model for the tsunami generated by the heterogeneous fault model of the May 2nd, 2020 earthquake south of Crete (*t* = time after earthquake; Figure adopted from Triantafyllou et al., 2023)

4 DISCUSSION AND CONCLUSIONS

Figure 1 shows that fault models of different intrinsic properties, even when slip amount and fault length/width are kept constant, lead to significantly different bottom deformation fields in terms of max/min deformation, shape and size. The generated tsunami waves and their evolution are affected accordingly, with Figure 2 highlighting the effects of variations in dip angle (Figure 2a), fault depth (Figure 2b) and rake angle (Figure 2c). Regarding fault models of different types, Figure 3 highlights the difference between relying on homogeneous and on heterogeneous faults models, even when those are produced for the same earthquake, as their bottom deformation fields are critically different. It is easily deduced that the selection of fault model properties and types is not to be done without careful consideration when modelling tsunami generation and propagation, as this will essentially define tsunami hazard assessment. Especially in zones where arrival times to populated coastal areas are limited to a few minutes, like for the case of the Hellenic Subduction Zone (see Figure 4), this information will be critical for tsunami risk assessment and Civil Protection response as well.

This work delves into the intricacies of modelling earthquake-generated tsunamis from an interdisciplinary perspective, and provides useful insights for scientists involved in tsunami modelling and tsunami hazard/risk assessment.

References

De Risi R, Goda K (2016) Probabilistic Earthquake–Tsunami Multi-Hazard Analysis: Application to the Tohoku Region, Japan. Front. Built Environ. 2. doi: 10.3389/fbuil.2016.00025

Dutykh D, Dias F (2007) Water waves generated by a moving bottom. In: Kundu A (ed) Tsunami and Nonlinear Waves, Springer Berlin Heidelberg, Berlin, Heidelberg, p 65-95

Hammack JL (1973) A note on tsunamis: their generation and propagation in an ocean of uniform depth. J. Fluid Mech. 60: 769-799. doi: 10.1017/S0022112073000479

Karambas TV, Samaras AG (2014) Soft shore protection methods: The use of advanced numerical models in the evaluation of beach nourishment. Ocean Eng. 92: 129-136. doi: 10.1016/j.oceaneng.2014.09.043

Li L, Switzer AD, Chan C-H, Wang Y, Weiss R, Qiu Q (2016) How heterogeneous coseismic slip affects regional probabilistic tsunami hazard assessment: A case study in the South China Sea. J. Geophys. Res. B Solid Earth 121: 6250-6272. doi: 10.1002/2016JB013111

Mitsotakis DE (2009) Boussinesq systems in two space dimensions over a variable bottom for the generation and propagation of tsunami waves. Math. Comput. Simulat. 80: 860-873. doi: 10.1016/j.matcom.2009.08.029

Okada Y (1992) Internal deformation due to shear and tensile faults in a half-space. Bull. Seismol. Soc. Am. 82: 1018-1040. doi: 10.1785/BSSA0820021018

Samaras AG, Karambas TV, Archetti R (2015) Simulation of tsunami generation, propagation and coastal inundation in the Eastern Mediterranean. Ocean Sci, 11: 643-655. doi: 10.5194/os-11-643-2015

Samaras AG, Karambas TV Applications of a 2DH post-Boussinesq model: generation and propagation of tsunami and ship-borne waves. Paper presented at the 36th International Conference on Coastal Engineering, Baltimore, Maryland, USA.

Samaras AG, Karambas TV (2021a) Numerical simulation of ship-borne waves using a 2DH post-Boussinesq model. Applied Mathematical Modelling 89: 1547-1556. doi: 10.1016/j.apm.2020.08.034

Samaras AG, Karambas TV (2021b) Modelling the Impact of Climate Change on Coastal Flooding: Implications for Coastal Structures Design. J. Mar. Sci. Eng. 9: 1008. doi: 10.3390/jmse9091008

Satake K, Fujii Y, Harada T, Namegaya Y (2013) Time and Space Distribution of Coseismic Slip of the 2011 Tohoku Earthquake as Inferred from Tsunami Waveform Data. Bull. Seismol. Soc. Am. 103: 1473-1492. doi: 10.1785/0120120122

Triantafyllou I, Agalos A, Samaras AG, Karambas TV, Papadopoulos GA (2023) Strong earthquakes and tsunami potential in the Hellenic Subduction Zone. Journal of Geodynamics (under review).

Yamazaki Y, Cheung KF, Lay T (2018) A Self-Consistent Fault Slip Model for the 2011 Tohoku Earthquake and Tsunami. J. Geophys. Res. B Solid Earth 123: 1435-1458. doi: 10.1002/2017JB014749

Quasi-coherent spectral wave modeling

V. Baltikas[1,*], Y. Krestenitis[1]

[1]Laboratory of Maritime Engineering and Maritime Works, School of Civil Engineering, Aristotle University of Thessaloniki, GR-54124, Thessaloniki, Greece
*Corresponding author: vmpaltik@civil.auth.gr

Abstract

A numerical stochastic wave model was developed from the ground up, based on the Quasi-Coherent theoretical framework proposed by Smit and Janssen (2013). Subsequently, the resulting program coded in Fortran was implemented to reproduce and cross validate the findings of the Quasi-Coherent (QC) spectral wave modeling approach. The process included simulations of experiments conducted by Vincent and Briggs (1989). The results of the simulations agree with the expected results of the QC theory, which can account for the wave field's coherence and capture wave interference more accurately, than conventional spectral wave models. In addition, some extra insight was gained, regarding aspects of the overall numerical implementation of the QC theory.

Keywords Ocean surface waves, Spectral wave model, Quasi-coherent framework

1 INTRODUCTION

Stochastic, spectral, or phase-averaged are the most used terms that describe a family of wave models, that simulate the generation of random sea waves, as well as the evolution of the generated wave fields in space and time, due to various processes that occur as the waves propagate in a variable medium (Booij et al. 1999, Tolman 1991, The WAMDI Group 1988). Regardless of their specific differences, these models are built around a Radiative Transfer Equation (RTE), expressed as

$$\partial_t E + c_k \nabla_k E + c_x \nabla_x E = 0 \quad (1)$$

or

$$\partial_t E + c_\sigma \nabla E_\sigma + c_\theta \nabla_\theta E + c_x \nabla_x E = 0 \quad (2)$$

Equations (1) and (2) describe the transport of wave energy or action in time and also in geographical and spectral space and. $E(\boldsymbol{k},\boldsymbol{x},t)$ or $E(\sigma,\theta,\boldsymbol{x},t)$ represents the well-known wave energy or action variance density spectrum at a point ($\boldsymbol{x}$=[x,y]) in geographical space, expressed either in terms of wavenumber ($\boldsymbol{k}$=[k_x,k_y]) spectral space or frequency – direction (σ,θ) spectral space. Respectively, $\boldsymbol{c_x}$=[c_x,c_y], $\boldsymbol{c_k}$=[c_{kx},c_{ky}] and c_σ, c_θ are the matching geographical and spectral transport velocities.

Using the RTE as the basis of spectral wave models presupposes the assumption that the wave field can be described as a quasi-homogeneous and Gaussian random process. This hypothesis may hold in open sea waters, where wave statistics undergo relatively slow variations on a spatial scale of hundreds to thousands wave lengths, but that is not the case as waves approach the nearshore. There, the more intense effects of medium variations on wave propagation (e.g., topography) and the weaker dispersive behavior of the waves in shallow waters, can cause deviations from the above. These "deviations" are in essence statistical representations of wave interference patterns (e.g., in focal zones), the spatial coherency and cross-correlations of the wave field, which are more evident in shallow waters. The RTE is not able to account for these deviations, as its derivation is based on the evolution of the auto-correlation function of the sea surface, the Fourier transform of the latter yields the variance density spectrum.

Smit and Janssen (2013) presented a generalization of the theoretical framework of spectral wave models, by replacing the evolution of the auto-correlation function of the sea surface with its correlation function, that includes the contributions of cross-correlations, and introducing the more general Coupled Mode spectrum, that can capture coherent interference effects. The specifics of the governing equation's derivation and the manner it can be cast in a form like the RTE can be found in Smit and Janssen (2013), Smit et al. (2015). The present study includes results obtained in the process of reproducing and cross

validating the findings of the Quasi-Coherent (QC) spectral wave modeling approach. It is part of a wider research, which aims to further validate the underlying theory, examine the behavior of a numerical spectral wave model, that is based on the QC theory and explore additional use cases, where this modeling framework may prove more beneficial, than classic spectral, phase-averaged wave models.

2 METHODS AND DATA

2.1 Numerical Model

2.1.1 Model equations

The QC theoretical framework was implemented in a numerical spectral wave model built from the ground up and coded into a computer program using the Fortran programming language. This was a more straightforward approach to implementing the core of the theory, instead of modifying existing open-source spectral wave models, which would require addressing issues regarding their code structure.

The core of the model is consisted by the governing equation:

$$\partial_t W + c_k \nabla_k W + c_x \nabla_x W = S_{qc} \tag{2}$$

$$c_k = -\nabla_x \sigma, c_x = \nabla_k \sigma \tag{3}$$

$$\sigma = \sqrt{gktanh(kh)} \tag{4}$$

$$S_{qc} = -i \sum_{q=-q_{max}}^{q=q_{max}} \Delta\widehat{\Omega^q}(k, x, -i\nabla_x) W\left(k - \frac{q}{2}, x, t\right) + C.C. \tag{5}$$

$$\Delta\widehat{\Omega^q}(k, x, -i\nabla_x) = \Delta\widehat{\sigma^q} - \frac{i}{2}\partial_k\left(\Delta\widehat{\sigma^q}\right)\tilde{k}\vec{\nabla}_x \tag{6}$$

$\Delta\widehat{\sigma^q}$ represents the Fourier transform $\Delta\widehat{\sigma^q} = \overline{F}_{\xi,q}\{\Delta\sigma\}$, where $\Delta\sigma$ is the difference between the local dispersion function value and its local plane approximation, following Smit et al. (2015), multiplied by a Tukey Window Function, which approaches zero as $|\xi|$ approaches its maximum selected value:

$$\Delta\sigma = TWF(\xi)\left[\sigma(k, x+\xi) - \sigma(k, x) - \xi\nabla_x\sigma|_{k,x}\right] \tag{7}$$

It should be noted again that *W(k,x,t)* is not the regular wave variance density spectrum, but the more general Coupled Mode spectrum, that is essentially a Wigner-Ville distribution. The CM spectrum may reduce to the variance density spectrum, where the wave field is quasi-homogeneous. It includes the complete second-order statistics of the wave field, accounting for its coherence and more accurate stochastic representation of wave interference. When S_{qc} is absent from Eq. (1), the governing equation reduces to the radiative transfer equation and *W* to the variance density spectrum. Moreover, *W(k,x,t)* cannot be directly related to the wave energy of a specific wave component at a given point in geographical space, since the Wigner-Ville distribution can take negative values. However, it is possible to obtain the local variance density, by using the marginal properties of the Wigner distribution:

$$E(x,t) = \int W(k,x,t)dk, E(k,t) = \int W(k,x,t)dx \tag{8}$$

2.1.2 Numerical implementation

For the simulations considered in this study, the steady state form of the governing equation is evaluated (i.e., ∂W/∂t=0), using regular, rectilinear spatial and spectral grids, defined as:

$$(x,y) = [m_x\Delta x, m_y\Delta y], 0 \leqslant m_x \leqslant M_x, 0 \leqslant m_y \leqslant M_y, m_x, m_y \in \mathbb{N} \tag{9}$$

$$(k_x, k_y) = [n_x\Delta k_x, n_y\Delta k_y], 0 \leqslant n_x \leqslant N_x, 0 \leqslant n_y \leqslant N_y, n_x, n_y \in \mathbb{N} \tag{10}$$

The discrete form of Eq. (3) is obtained by approximating the gradient differential operators with second order upwind finite differences.

$$\Delta_x{}^{+}W_{k,x} = \frac{3W_{k,x}-4W_{k,x-\Delta x}+W_{k,x-2\Delta x}}{2\Delta x},\ \Delta_x{}^{-}W_{k,x} = \frac{-3W_{k,x}+4W_{k,x-\Delta x}-W_{k,x-2\Delta x}}{2\Delta x} \quad (11)$$

$$\Delta_k{}^{+}W_{k,x} = \frac{3W_{k,x}-4W_{k-\Delta k,x}+W_{k-2\Delta k,x}}{2\Delta k},\ \Delta_k{}^{-}W_{k,x} = \frac{-3W_{k,x}+4W_{k-\Delta k,x}-W_{k-2\Delta k,x}}{2\Delta k} \quad (12)$$

Where Eq. (11), Eq. (12) reference points outside the computational, the finite difference schemes revert to first order accurate ones. The incoming spectrum is applied on the southern geographical boundary, while the lateral geographical boundaries allow only outgoing waves to exit the computational domain. The CM spectrum is considered zero outside the spectral computational grid. The evaluation of S_{qc} requires at least second-order accurate spatial discretization, as the accounted wave coherence introduces into the calculations fast spatial scales (Smit et al. 2015), therefore second and fourth order accurate finite differences were used. The Fourier transforms in Eq. (5), (6) are calculated by the means of 2d DFT. Moreover, the evaluation of Eq. (5), (6) and (7), requires the definition of an auxiliary spatial grid and its conjugate auxiliary spectral grid. Both are centered around the evaluated geographical and spectral points ***x,k*** and defined as:

$$\xi = x + \left[m_x'\Delta x', m_y'\Delta y'\right],\ -0.5M_q \leqslant m_{x'} \leqslant M_q,\ -0.5M_q \leqslant m_{y'} \leqslant M_q, m_{x'}, m_{y'} \in \mathbb{N} \quad (13)$$

$$q = k + \left[n_{q_x}\Delta q_x, n_{q_y}\Delta q_y\right],\ -0.5M_q \leqslant n_{q_x} \leqslant M_q,\ -0.5M_q \leqslant n_{q_y} \leqslant M_q, n_{q_x}, n_{q_y} \in \mathbb{N} \quad (14)$$

The length of the spatial auxiliary grid equals to ξ_c, which is the length of the assigned coherence radius of the wave field, with the assumption that $\Delta k \leq 2\pi/\xi_c$. To avoid interpolation of W in spectral space, Δq_i is chosen such that $\Delta q_x = \Delta q_y = 2\Delta k$ and $\Delta x'$ is defined as $\Delta x' = 2\pi/(M_q \Delta q)$. It is obvious that M_q is the number of the Discrete Fourier components along each direction. M_q is evaluated by Δq and the choice of an appropriate q_{max}, which can be defined as $q_{max} = a \cdot k_{mean}$, where kmean is the mean wavenumber of the wave field. In the present study a=1. The described discretization yields a linear equations system, that is iteratively solved in a semi-implicit manner, like the one employed in SWAN wave model (Booij et al. 1999). Spectral space is divided in 4 quadrants where: $Q_1 = \{k_x \geq 0, k_y \geq 0\}$, $Q_2 = \{k_x \leq 0, k_y \geq 0\}$, $Q_3 = \{k_x \geq 0, k_y \leq 0\}$ and $Q_4 = \{k_x \leq 0, k_y \leq 0\}$. In each iteration, every point **x** is visited in a marching fashion 4 times, one time per sweep of the geographical domain. Each sweep is in accordance with the propagation directions implied by the wavenumber subset of each quadrant (e.g., for quadrant 1 from the lower left corner to the upper right). Spatial information is propagated from the downwind points in a Gauss-Seidel manner. This technique breaks down the linear equations system into 4 smaller ones for every point of the spatial grid. The inclusion of the S_{qc} term makes the LHS diagonal matrix denser by adding M_q^2 diagonals. The resulting systems are solved using the ILU preconditioned BicGStab method (Van der Vorst 1992). Simulations end after n iterations when the following criterion is met for 99% of the geographical points:

$$\frac{\sum_k (W_n{}^{k,x} - W_{n-1}{}^{k,x})^2}{\sum_k (W_n{}^{k,x})^2} \leqslant \alpha^2, \alpha = 0.01 \quad (15)$$

2.2 Data

The resulting model was used for simulating Test Cases from the well-known experiments of random waves propagating over a submerged shoal presented in Vincent and Briggs (1989). These include cases M2 and N4 that correspond to simulations conducted by Smit and Janssen (2013), and additionally Test Case U4. It should be noted that wave breaking does not occur in any of the three Test Cases.

Table 1. Incident spectra for model simulations (Vincent and Briggs 1989)

Test Number	Case ID	Type	Period (Tp) [sec]	Height (Hs) [cm]	A	γ (peakedness factor)	σm (directional spreading) [deg]
1	M2	Monochromatic	1.30	2.54	---	---	---
2	U4	TMA Spectrum	1.30	2.54	0.00047	20	0
3	N4	TMA Spectrum	1.30	2.54	0.00047	20	10

The spatial and spectral resolution that was selected for the simulations was $\Delta x = 0.125$ m and $\Delta k = 0.2$ rad/m.

3 RESULTS

Three distinct simulations were carried out for each Test Case: a) first with S_{qc} activated (QC model), b) second with the reduced radiative transfer equation (RTE model) and c) third with SWAN wave model in RTE mode and without considering generation or dissipation of wave energy (e.g., whitecapping, surf breaking) nor any additional processes such as approximations of nonlinear wave-wave interactions. Results show that our implementation of the QC model is able to approximate the higher significant wave height values detected in the focal zone behind the shoal, as opposed to the RTE model and SWAN in RTE mode. The QC results are closer to the available observational data (see Figure 2, middle panels), than those of the RTE model. Our version of the QC model confirms the capability of the Quasi-Coherent theory to resolve wave interference patterns, unlike the RTE approach. This is also evident by the alternating lobes of attenuated and increased wave height. In Test Case N4 the QC and RTE models produce similar results, as the more dispersive wave field quickly decorrelates, resulting in smoother wave statistics are smoother and no persistent wave interference patterns. Still, the QC model predicts higher wave heights in the focal zone, closer to the observations. Local undershoots of unnatural negative variance density and subsequently significant wave height were detected in case M2. These were probably caused by very large gradients, due to the very narrow incident CM spectrum in combination with the selected numerical scheme. The problem was ameliorated by slightly increasing the smoothing effect of TWF (Eq. (16)) in S_{qc} (α=0.3 instead of α=0.1 as in Smit and Janssen (2013)) and using a hybrid scheme of second order accurate central and first order upwind finite differences in spectral space.

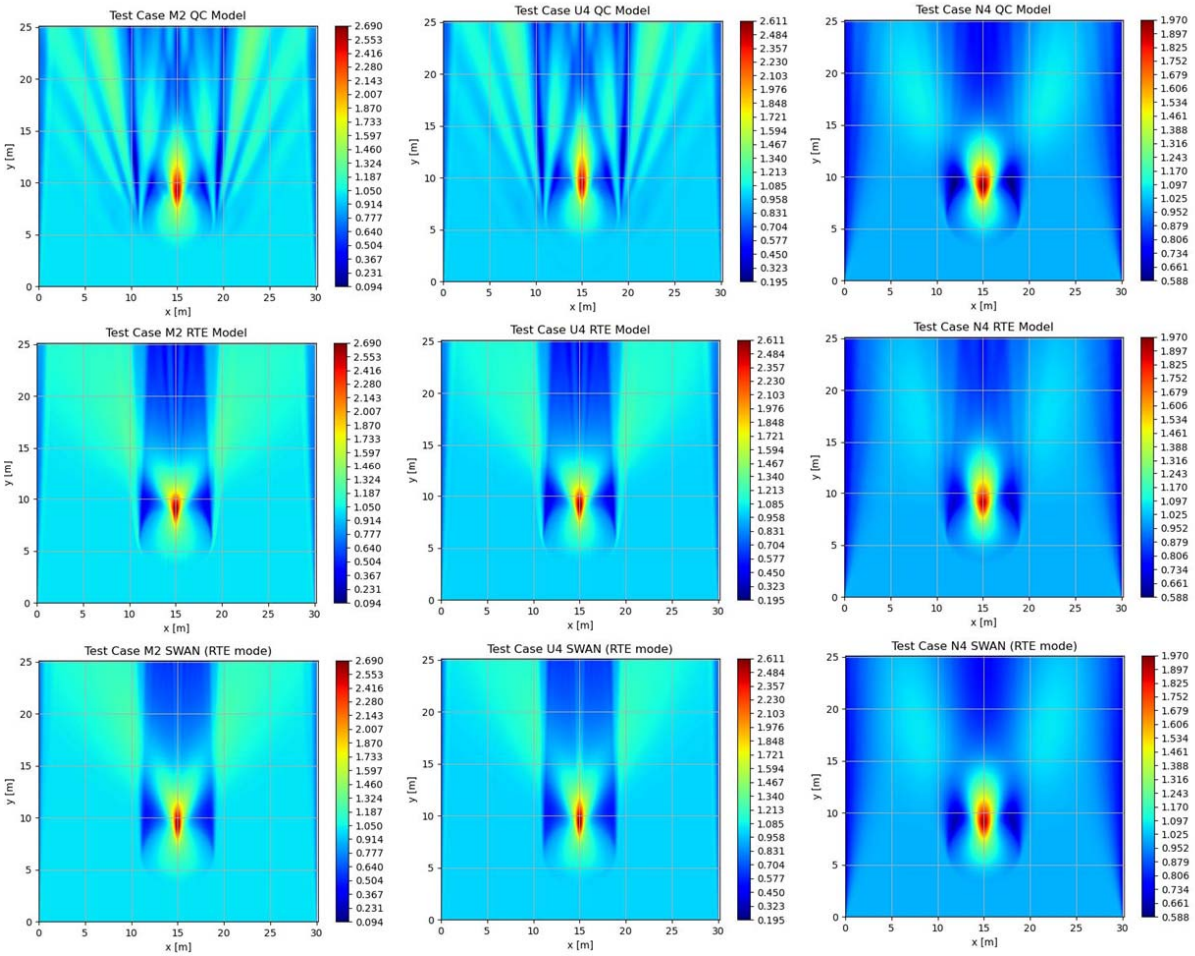

Figure 1. Plan view of simulated normalized wave heights for the experimental set-up of Vincent and Briggs (1989)

$$TWF(\xi) = \begin{cases} 0.5 + 0.5\left(\cos\left(\frac{\pi[\xi - \xi_c + \alpha\xi_c)}{a\xi_c}\right]\right), & \xi > (1-\alpha)\xi_c \\ 0.5 + 0.5\cos(\pi\left[\frac{\xi}{\alpha\xi_c} - 1\right), & \xi < \alpha\xi_c \\ 1, & (1-\alpha)\xi_c < \xi < \alpha\xi_c \end{cases} \quad (16)$$

Differences between our QC model and one of Smit and Janssen (2013) can be attributed to technical, differences between the two overall solution algorithms and computer programs. Our computer program was independently developed and that Smit and Janssen (2013) mention only very basic aspects of the QC model's numerical implementation. Such differences appear between our RTE model and SWAN, which also differ in terms of the governing equation formulation, as the former is based on Eq. (1) and the latter on Eq. (2). However, it should be noted that the results of our RTE model are closer to the results of SWAN, than the RTE results presented in the work of Smit and Janssen (2013).

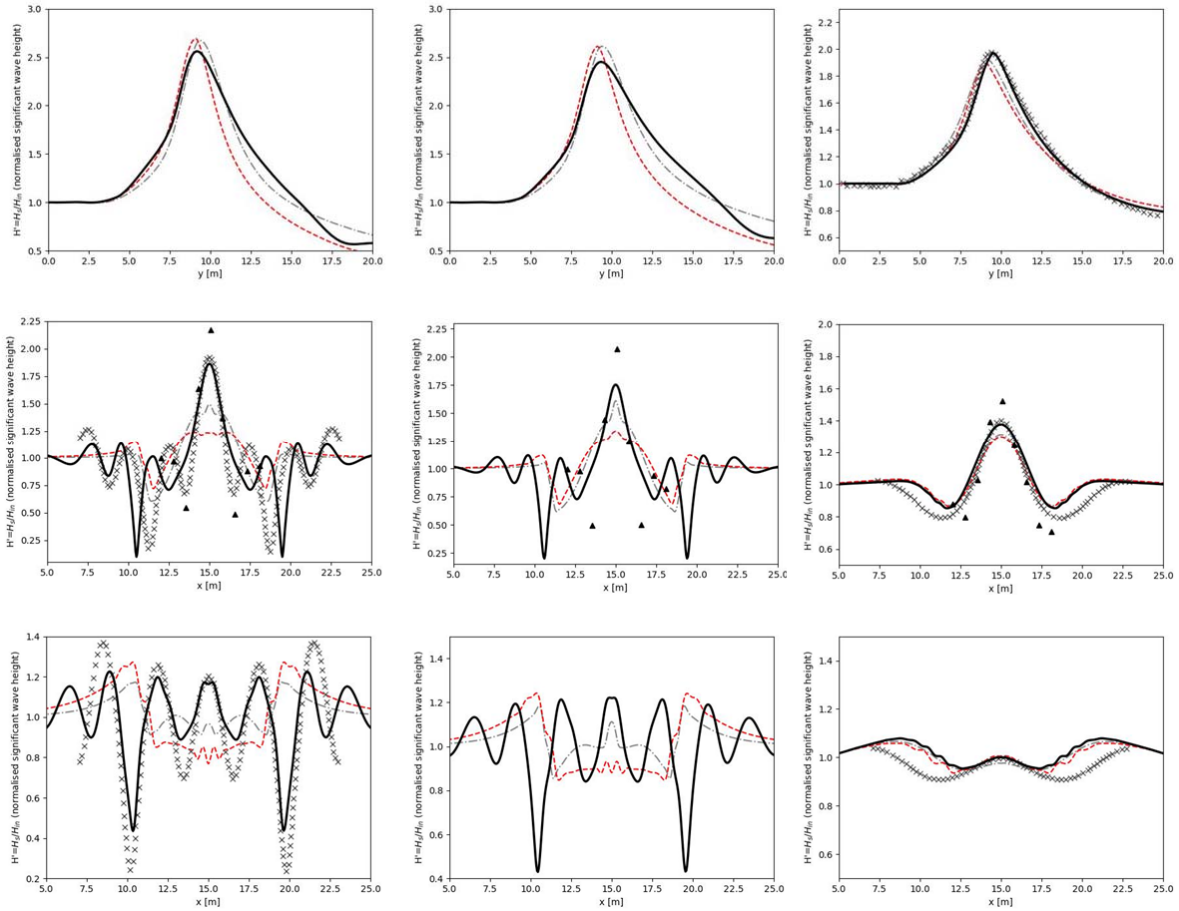

Figure 2. Normalized wave heights along transects across and behind the shoal, according to the experimental set-up of Vincent and Briggs (1989). Top panels: Transect 7-9 (along x=15 m). Middle panels: Transect 4 (along y=12.19 m). Lower panels: Transect 5 (along y=15.24 m). Each panel contains the comparison of the QC model (bold black line) with the RTE model (dashed red line) and SWAN wave model (dashed grey line) for Test Case M2 (first column), Test Case U4 (second column), Test case N4 (third column). Additional comparisons with a) observational data along Transect 4 for each case (triangular markers, available by Vincent and Briggs (1989) only along this transect for the non-breaking Test cases), b) normalized wave heights for M2 and N4 of QC model simulations shown in Smit and Janssen (2013).

4 CONCLUSIONS

The results show that our model can reproduce the findings predicted by the QC modeling framework. The QC theory and modeling framework can prove to be a valuable tool, allowing a more accurate prediction of the evolution of random wave fields near the coast, where incident waves can be weakly dispersive, as in the case of swells. Slight differences with the results of Smit and (2013) are detected, owing to the independent implementations of the QC numerical model, solution algorithm and computer

program. The selection of an appropriate TWF formulation and numerical schemes can prevent possible undershoots that lead to unnatural results, without sacrificing accuracy. Research for future improvements may include the selection of a numerical scheme that reduces the possibility of undershoots, without increasing the smoothing effect of TWF. Overall, the model implementation in the present work forms a sound basis for future research on aspects regarding the QC modelling framework and theory.

References

Booij N, Ris RC, Holthuijsen LH (1999) A third-generation wave model for coastal regions: 1. Model description and validation. J. Geoph. Res-Oceans 104:7649-7666. doi:10.1029/98JC02622

Smit PB, Janssen TT (2013) The evolution of inhomogeneous wave statistics through a variable medium. Journal of Physical Oceanography, American Meteorological Society 43:1741–1758. doi: 10.1175/JPO-D-13-046.1

Smit PB, Janssen TT, Herbers THC (2015) Stochastic modelling of inhomogeneous ocean waves. Ocean Modelling 96:26–35. https://doi.org/10.1016/j.ocemod.2015.06.009

Van Der Vorst HA (1992) BiCGSTAB: A fast and smoothly converging variant of Bi-CG for the solution of nonsymmetric linear systems. SIAM J. Sci. Stat. Comp., 13:631-644. doi:10.1137/0913035

Tolman HL (1991) A third generation model for wind waves on slowly varying, unsteady, and inhomogeneous depths and currents. J. Phys. Oceanogr. 21:782-797. doi:10.1175/1520-0485(1991)021<0782:ATGMFW>2.0.CO;2

The WAMDI Group (1988) The WAM model – a third generation ocean wave prediction model. J. Phys. Oceanogr., 18:1775–1810. doi:10.1175/1520-0485(1988)018<1775:TWMTGO>2.0.CO;2

Vincent CL, Briggs MJ (1989) Refraction-diffraction of irregular waves over a mound. Journal of Waterway, Port, Coastal and Ocean Engineering, ASCE, 115:269-284. doi:10.1061/(ASCE)0733-950X(1989)115:2(269)

CoastFLOOD: fine-resolution modelling of flood inundation due to storm surges in the coastal zone

C.V. Makris[1*], Z.C. Mallios[1], Y.S. Androulidakis[1], Y.N. Krestenitis[1]

[1]Division of Hydraulics and Environmental Engineering, School of Civil Engineering, Aristotle University of Thessaloniki, Thessaloniki, Central Macedonia, 54124, Greece
[*]Corresponding author: cmakris@civil.auth.gr

Abstract

In this paper, we present the CoastFLOOD numerical model for coastal inundation induced by sea level elevation due to storm surges enhanced by astronomical tides and mean sea level rise. CoastFLOOD is a high-resolution, O(dx)=1, raster-based, storage-cell model for mass balance floodwater flow by decoupled 2-D Manning-type equations. It may be applied on geophysical local-scale, O(x)=20km, lowland coastal areas with natural floodplains and urban settings. It can be forced by either output of regional-scale storm surge simulations or field data (i.e., satellite altimetry for sea level anomaly or *in situ* tide-gauge measurements for sea surface height). We present selected results from high resolution (2–5m) model simulations for Greek case studies at low-lying coastal sites of the Ionian Sea (east-central Mediterranean basin). New features of the model are tested concerning the detailed inclusion of terrain Manning roughness (bottom friction), incorporation of boundary conditions for coastal currents, and treatment flood front propagation over steeply varying topography. Verification of the model is performed by comparisons against satellite data of estimated flooded areas by the Normalized Difference Water Index and estimations of a "bathtub" inundation approach with hydraulic connectivity.

Keywords Coastal flooding, Littoral inundation, Storm surge, Numerical model.

1 INTRODUCTION

Storm surges threaten lowland littoral areas by increasing the risk of seawater inundation of coastal floodplains and low-lying urban environments. This threat intensifies when high seas due to storm surge (meteorological residual of sea level elevation) are combined with high astronomical tides (storm tides), leading to events of extended flood inundation over the inland part of the coastal zone. Coastal inundation is the most significant natural hazard induced by episodic maxima of Sea Surface Height (SSH) or long-term Mean Sea Level Rise (MSLR), mainly responsible for land loss, soil erosion, damages on onshore infrastructures and properties, environmental degradation of coastal aquatic ecosystems, saltwater intrusion in coastal aquifers, and occasionally human casualties, etc. For the simulation of such phenomena, a robust model, which can produce realistic inundation hazard maps is crucial in terms of coastal management and risk studies in order to enhance flood hazard mitigation and first-level response to disaster.

In this paper, we present the most recent version of a numerical modelling suite (CoastFLOOD; Makris et al., 2023a) for coastal inundation on littoral floodplains induced by storm surge and enhanced by tidal effects (and probable MSLR). The inundation model can be forced by Sea Level Anomaly (SLA) observations (*in situ* recordings from tide-gauges and satellite altimetry data) or SSH model output of storm surge simulations (Androulidakis et al., 2023). The High-Resolution Storm Surge (HiReSS; Makris et al., 2019) model has been used in operational forecast mode for short-term marine weather (sea level and currents) predictions (e.g., Makris et al., 2021), providing boundary conditions to CoastFLOOD simulations along the Greek coastal zone (Makris et al., 2022). Furthermore, it can be fed by outputs of the Mediterranean Climatic Storm Surge (MeCSS; Makris et al., 2023b) model that can implement long-term hindcasts or future projections of storm surge patterns in the Mediterranean Sea for climatic-scale studies. Herein, we attempt to verify the CoastFLOOD model's ability to simulate the coastal inundation extents due to storm tides in operational forecast mode by comparing its results against estimations of flooded areas based on either an index for "wet area" identification by satellite

ocean colour observations (Sentinel-2 images) or an enhanced "bathtub" approach for coastal flooding with hydraulic connectivity (Williams and Lück-Vogel, 2020).

2 METHODS AND DATA

2.1 Numerical Model

CoastFLOOD performs detailed modelling of the shallow and rather slow process of seawater uprush and flood routing due to episodic, mid-term, and large-scale, sea level elevation, i.e., induced by storm surges/tides. It is a fine resolution, raster-based, 2-D horizontal, mass balance flood model for coastal inland areas, following the simplified concept of a reduced complexity form of the Shallow Water Equations (SWEs) solved on an ortho-regular grid (Figure 1, representing the GIS study domain) by the storage-cell concept (Bates et al., 2010; Hunter et al., 2007). Only the large-scale low-frequency phenomena of coastal inundation due to storm surges and tides are simulated, not considering the high-frequency undulating processes of coastal flooding due to wave action. The storm-induced SLA or SSH on the coastline feeds the seawater surge on the littoral floodplain via a set of 2-D decoupled Manning-type flow equations. The simplified form of the 2-D equations for conservation of mass (continuity) and momentum describes the floodwater flow between adjacent cells, which is driven by the hydraulic head created from the inter-cell difference of water surface height in all four cardinal directions of the horizon during a typical timestep of the numerical solution. The set of equations is written as:

$$h_{i,j}^{t\prime} = h_{i,j}^{t} + dt \cdot \frac{Q_{x_{i-1/2,j}}^{t} - Q_{x_{i+1/2,j}}^{t} + Q_{y_{i,j-1/2}}^{t} - Q_{y_{i,j+1/2}}^{t}}{dx \cdot dy} \quad (1)$$

$$Q_{x_{i-1/2,j}}^{t} = \frac{h_{flow_{x_{i-1/2,j}}}^{t\,5/3}}{n} \cdot \left(\frac{h_{i-1,j}^{t} - h_{i,j}^{t}}{dx}\right)^{1/2} \cdot dy, \quad Q_{x_{i+1/2,j}}^{t} = \frac{h_{flow_{x_{i+1/2,j}}}^{t\,5/3}}{n} \cdot \left(\frac{h_{i,j}^{t} - h_{i+1,j}^{t}}{dx}\right)^{1/2} \cdot dy \quad (2)$$

$$Q_{y_{i,j-1/2}}^{t} = \frac{h_{flow_{y_{i,j-1/2}}}^{t\,5/3}}{n} \cdot \left(\frac{h_{i,j-1}^{t} - h_{i,j}^{t}}{dy}\right)^{1/2} \cdot dx, \quad Q_{y_{i,j+1/2}}^{t} = \frac{h_{flow_{y_{i,j+1/2}}}^{t\,5/3}}{n} \cdot \left(\frac{h_{i,j}^{t} - h_{i,j+1}^{t}}{dy}\right)^{1/2} \cdot dx \quad (3)$$

$$h_{flow_{x_{i-1/2,j}}} = \left(max\{H_{i-1,j}, H_{i,j}\} - max\{z_{i-1,j}, z_{i,j}\}\right) \quad (4)$$

where, i and j are the cell (i,j) centered indices in x- and y-directions of the Cartesian grid (for scalar parameters); +1/2 in indexing denotes the intercell positioning of vectorial flow parameters; t is the time and dt the timestep of temporal discretization ($t'=t+dt$ the following timestep in the solution scheme); Q_x and Q_y are the volumetric flow rates between adjacent floodplain cells in the zonal x- and meridional y-directions of the Cartesian grid, respectively; h is the local floodwater height above each grid cell's land elevation, z; dx and dy are the cell dimensions; H is the local floodwater height above MSL. The model can be applied at very high spatial resolutions (e.g., dx=1-5m) for geophysical-scale flows (e.g., O(Dx)=1-20km).

2.2 Available datasets

Bottom friction is the main parameterization feature of reduced complexity flood inundation models. As the typical model cell's dimensions and depth are assumed to be uniform for each grid element, an effective Manning's bottom roughness coefficient, n, at grid unit scale can be determined as a calibration parameter. By integrating all relevant literature, we have created a detailed collective ensemble of proposed n values discretized at 36 increments (Makris et al., 2023a). These listings are fitted to the Corine Land Cover CLC-2018 (https://land.copernicus.eu/pan-european/corine-land-cover/clc2018) codes that refer to data of natural and manmade land cover types. Terrain heterogeneities on the sub-grid level can cause discrepancies in the representation of land cover texture, thus Manning's n is commonly used as a determinative calibration parameter rather than a physical factor of actual field friction. Land elevation grids are derived by post-processing of available geospatial datasets from the Digital Elevation/Surface Model (DEM/DSM) of Hellenic Cadastre (https://www.ktimatologio.gr/en) on a GGRS87 projection. The operational forecast model validation is performed with the use of satellite observations (Sentinel-2 images) producing the Normalized Difference Water Index (NDWI; Androulidakis et al., 2023; Makris et al., 2022).

2.3 Case Studies

The CoastFLOOD model has been tested at 10 selected case study areas of the western Greek coastal zone, which are rather frequently inundated by storm surges of the Ionian Sea (e.g., due to Ianos Medicane; Androulidakis et al., 2023; Makris et al., 2022), including Manolada-Lechaina (Area 1), Vassiliki bay (Area on Lefkada Island, Preveza coast (Area 3), Igoumenitsa port (Area 4); Livadi coastal area (Area5) in Cephalonia Island; Kalamata (Area 6); Argostoli (Cephalonia Island, Area 7); Kyparissia (Area 8); Laganas (Zakynthos Island, Area 9); Patra city (Area 10).

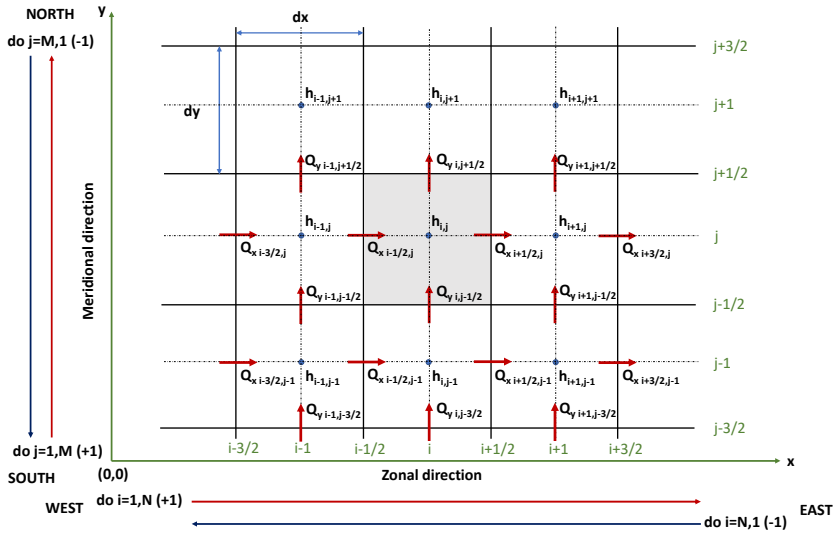

Figure 1 Prototype raster-based staggered grid of CoastFLOOD model with *dx*-*dy* cell discretization over *i*-*j* coordinate system on Cartesian *x*- and *y*-directions (zonal and meridional directions of the horizon); notation of scalar parameters (floodwater height *h*) at the grid cell center and of decoupled vectorial parameters (volumetric flow rate, Q_x and Q_y) transversal to the grid cell interface; arrows' positive direction represents flows from upstream to downstream areas

3 RESULTS

3.1 Model Validation

Two areas and events are used for qualitative verification of the coastal flooding model's performance against satellite data due to lack of *in situ* observations. Figure 2 depictions present flood maps of model simulations overlaid by satellite-tracked wet regions. The CoastFLOOD results are driven on the coastal boundary of Areas 1 and 5 by recorded SLA values on 14/12/2021 and HiReSS-modelled SSH from operational forecasts by the WaveForUs system on 17/09/2020, respectively. The maps depict the overlap of NDWI-identified wet areas by satellite images above flood inundation model output focusing on the mainly affected parts of both study areas. In general, the CoastFLOOD simulations reproduce the coastal flooding mechanism in areas that are more-or-less influenced by storm surge driving seawater onshore uprush during the timeframe of analysis. Furthermore, model results maybe overpredict the momentary depiction of flood extents as derived by the NDWI method based on the recorded images. However, there is no guarantee that the satellite data represent the actual situation of floodwater extents during the storm-induced high seas due to unavailability of data during the storm passage (e.g., no satellite track in the area or cloud contamination). Discrepancies may also stem from the fact that the NDWI depicted areas usually act as drainage bilges that are usually flooded with water originating from local intense rainfall and/or stormwater surface runoff from surrounding higher grounds. An extreme case scenario of Total Water Level, *TWL*=1m, typical for a possible cumulative sea level increase due to the combined effects of surges and waves, is also provided (yellow patches) for comparison of the flood-prone littorals against the actually impacted touristic coastal areas.

3.2 Operational Output

Figure 3 presents the simulated test case of Area 7 (left graph); CoastFLOOD model results agree well with Bathtub-HC ones for an extreme *TWL*=1m scenario as a driver of coastal inundation. As expected, the former ones are slightly underestimated compared to the latter, yet therefore, CoastFLOOD shows a more realistic perspective of littoral inundation, given the error of the DEM topography. The unmatched inland flood-prone areas identified through the Bathtub-HC approach are obviously located on inclined higher elevation ground, in areas where the bottom friction considered by CoastFLOOD plays a crucial role to the modelling of floodwater extents. The proposed model achieves similar performance in both the natural and urban settings. Figure 3 (right graph) presents operational forecasts and scenario-based model outputs for Vassiliki bay (Area 2; Lefkada Island). The natural coastal sites and the surrounding touristic residencies on its northern part seem to be more likely to be impacted by extreme seawater floods, rather than the small harbour in the north-eastern part of the bay.

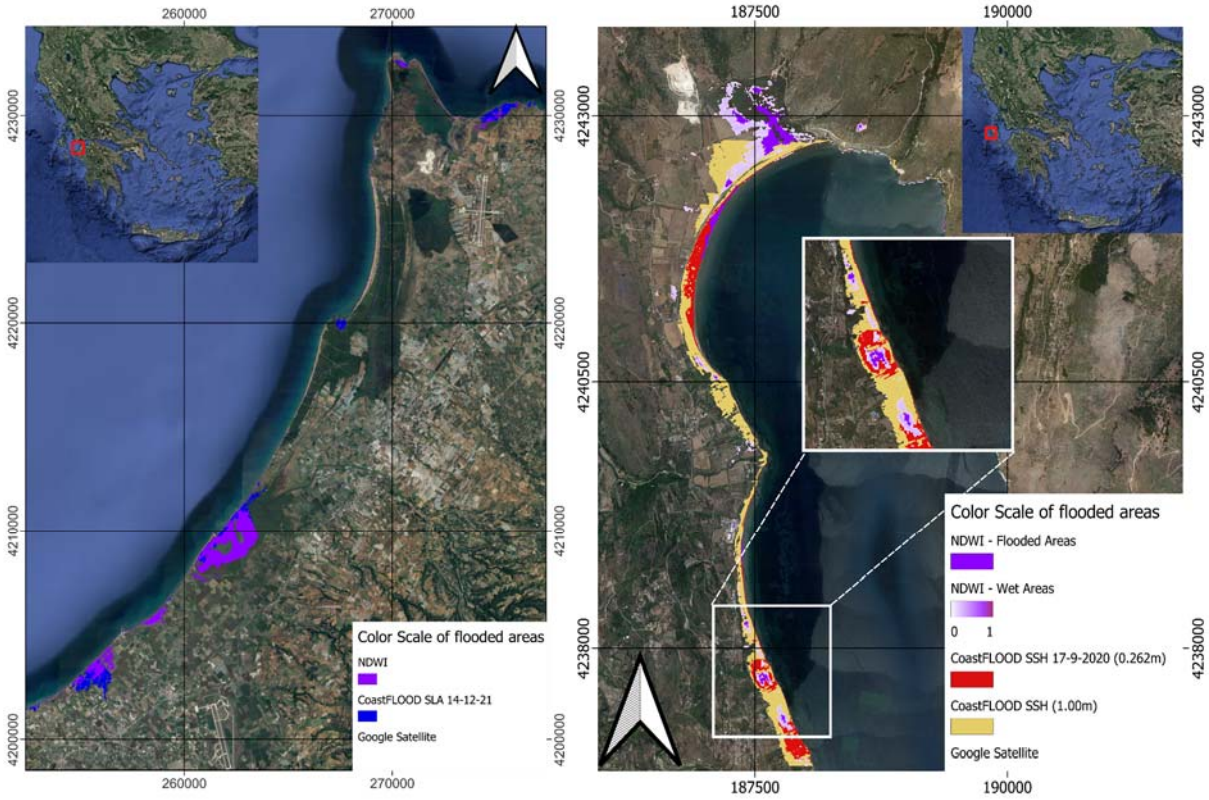

Figure 2 Left graph: Map of estimated flooded areas by NDWI satellite data (purple colour) overlaid on CoastFLOOD simulation results driven by recorded SLA on 14/12/2021 (blue colour) for Manolada-Lechaina study area; Right graph: modelled SSH (red colour) at Livadi (right) after Ianos Medicane's passage together with an extreme *TWL*=1m also provided with yellow colour; Insert map presents zoom-in depiction of impact

4 CONCLUSIONS

We presented a robust, easy-to-use, numerical tool for coastal inundation due to storm surge/tide flooding, under the reduced complexity notion, imperatively needed for operational forecasts of storm impacts on littoral areas. Comparisons against satellite datasets of NDWI are quite satisfactory; any discrepancy in the validation of modelled flood extents in the coastal zone probably also hinges on the uncertainty of field data concerning the actually occurred flood rates. The verification of the proposed model's efficiency to reproduce the highest possible flood extent in coastal plains has also tested well against an efficient Bathtub-HC estimation approach. Therefore, the CoastFLOOD model can be a useful tool for both operational forecast applications and projected climatic studies of coastal inundation under extreme scenarios (Makris et al., 2020) to help coastal zone managers, policymakers, and involved stakeholders to better estimate the characteristics of coastal (or compound) flooding under the condition of possible environmental changes.

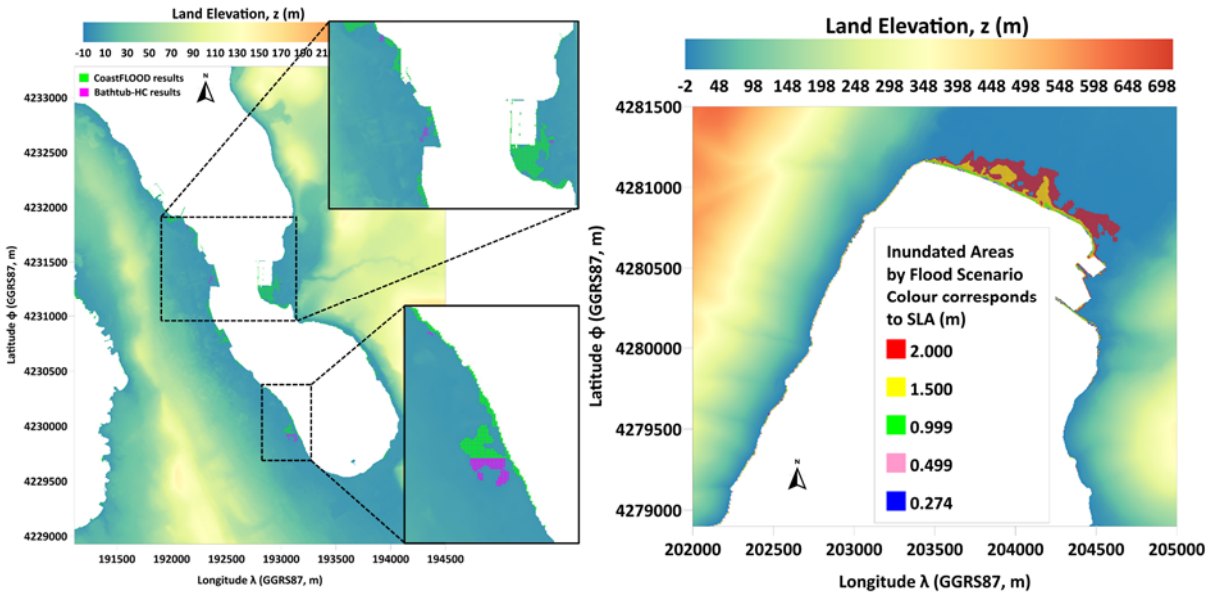

Figure 3 Left graph: Map of estimated flooded areas by Bathtub-HC approach (purple colour) and CoastFLOOD simulations (green colour), for *TWL*=1m in Argostoli coastal inlet (Area 7; Cephalonia Island) with Goodness-of-Fit=0.96; Right graph: Map of estimated flooded areas by operational CoastFLOOD simulations, driven by *in situ* recorded SLA=0.274m and 4 extreme cases of *TWL*=0.5-2.0m in Vassiliki bay (Area 2; SW Lefkada Island)

References

Androulidakis Y, Makris C, Mallios Z, Pytharoulis I, Baltikas V, Krestenitis Y (2023) Storm surges and coastal inundation during extreme events in the Mediterranean Sea: the IANOS Medicane. Nat Hazards 117:939–978. doi:10.1007/s11069-023-05890-6

Bates, P.D., Horritt, M.S. and Fewtrell, T.J., 2010. A simple inertial formulation of the shallow water equations for efficient two-dimensional flood inundation modelling. Journal of hydrology, 387(1-2), pp.33-45. doi:10.1016/j.jhydrol.2010.03.027

Hunter NM, Bates PD, Horritt MS, Wilson MD (2007) Simple spatially-distributed models for predicting flood inundation: A review. Geomorphology, 90: 208–225. doi:10.1016/j.jhydrol.2010.03.027

Makris C, Androulidakis Y, Karambas T, Papadimitriou A, Metallinos A, Kontos Y, Baltikas V, Chondros M, Krestenitis Y, Tsoukala V, Memos C (2021) Integrated modelling of sea-state forecasts for safe navigation and operational management in ports: Application in the Mediterranean Sea. Appl Math Mod 89(2): 1206-1234. doi:10.1016/j.apm.2020.08.015

Makris C, Androulidakis Y, Mallios Z, Baltikas V, Krestenitis Y (2022) Towards an Operational Forecast Model for Coastal Inundation due to Storm Surges: Application during Ianos Medicane. Paper presented at the 9th SafeThessaloniki 2022, Thessaloniki, Greece, pp. 69-72.

Makris C, Mallios Z, Androulidakis Y, Krestenitis Y (2023a) CoastFLOOD: A High-Resolution Model for the Simulation of Coastal Inundation Due to Storm Surges. Hydrol 10(5):103. doi:10.3390/hydrology10050103

Makris C, Baltikas V, Androulidakis Y., Krestenitis Y. (2020). Coastal Inundation due to Storm Surges on a Mediterranean Deltaic Area under the Effects of Climate Change. Paper presented at the 7th International Conference on Civil Protection & New Technologies, SAFE GREECE 2020, Athens.

Makris C, Androulidakis Y, Baltikas V, Kontos Y, Karambas T, Krestenitis Y (2019) HiReSS: Storm Surge Simulation Model for the Operational Forecasting of Sea Level Elevation and Currents in Marine Areas with Harbor Works. Paper presented at the 1st DMPCO, Athens, Greece, 1:11-15.

Makris C, Tolika K, Baltikas V, Velikou K, Krestenitis Y (2023b) The impact of climate change on the storm surges of the Mediterranean Sea: coastal sea level responses to deep depression atmospheric systems. Ocean Mod, 181:102149. doi:10.1016/j.ocemod.2022.102149

Williams LL, Lück-Vogel M, (2020) Comparative assessment of the GIS based bathtub model and an enhanced bathtub model for coastal inundation. J Coast Conserv, 24:1–15. doi:10.1007/s11852-020-00735-x

DMPCO 2023

e-Proceedings of the 2nd International Scientific Conference on Design and Management of Port Coastal and Offshore Works Thessaloniki, Greece, May 24-27 2023

Impact of sea level variability on coastal inundation in the Aegean, Ionian and Cretan Seas

Y.S. Androulidakis[1,2,*], C.V. Makris.[1], Z.C. Mallios[1], Y.N. Krestenitis[1]

[1]Division of Hydraulics and Environmental Engineering, School of Civil Engineering, Aristotle University of Thessaloniki, Thessaloniki, Central Macedonia, 54124, Greece
[2]Laboratory of Physical and Chemical Oceanography, Department of Marine Sciences, University of the Aegean, Mytilene, Lesvos Island, Greece
[*]Corresponding author: iandroul@civil.auth.gr

Abstract

Sea level is a key element of global scale climatic changes with potentially significant coastal impacts especially on the low-lying areas of the Mediterranean Sea, which is one of the most vulnerable regions to sea level rise worldwide. The sea level variability controls the inundation levels of the coastal zone, depending on the local topographic characteristics and the occurrence of severe meteorological events (e.g., storm surges). The scope of this study is to evaluate the interannual and spatial variability of the Sea Level Anomaly (SLA) in the Aegean, Ionian, and Cretan (AIC) Seas and evaluate its impact on the coastal inundation characteristics along the topographically complex Greek coastline. The analysis refers to a 29-years period from 1993 to 2021.

Keywords Water level, Remote sensing, Storm surge, Coastal flooding.

1 INTRODUCTION

Sea level is a key element of global scale climatic changes with potentially significant coastal impacts (Cazenave et al., 2014), especially on the low-lying areas of the Mediterranean Sea, which is one of the most vulnerable regions to Sea Level Rise (SLR) worldwide. The sea level variability controls i) the inundation levels of the coastal zone, depending on the local topographic characteristics (Ferrarin et al., 2021), ii) the shoreline retreat, coastal erosion, and land loss, and iii) the salinity levels in estuaries and freshwater aquifers. The main motivation of the current study is to assess the state and severity of coastal hazards, related to sea level increases and coastal inundation, over the Aegean, Ionian, and Cretan Seas (AIC; Figure 1a), located in the northeastern Mediterranean Sea. The investigation spans over a long recent period from 1993 to 2021 (29 years). We focus on 20 identified low-lying coastal areas (Figure 1b) that have been impacted by intense flooding events in the past and expand the analysis with the use of finer land elevation data (5 m spatial resolution model grids).

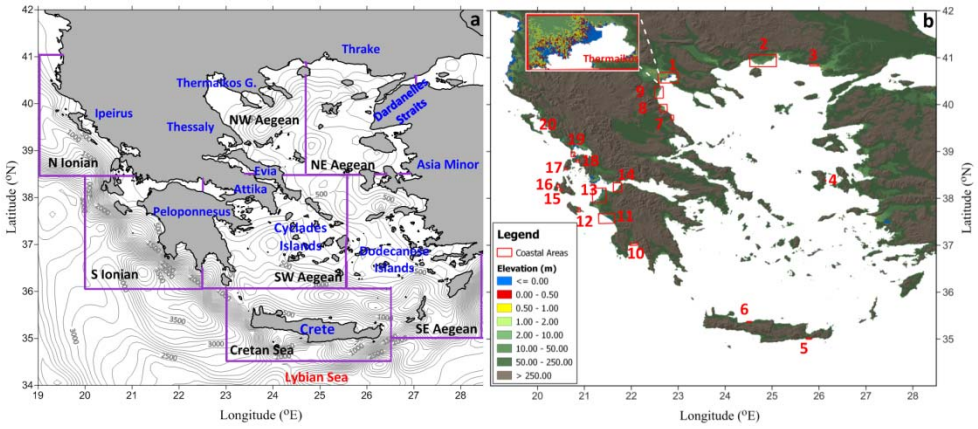

Figure 1 (a) Bathymetry of the study area divided into 7 sub-regions (b) Land elevation (m) map, derived from the 25 m Copernicus (https://land.copernicus.eu/) Digital Elevation Model (DEM) showing the study's 20 coastal areas

2 METHODS AND DATA

2.1 Sea level observations & Digital Elevation Model data

The altimeter satellite SLA data (sea surface height above mean sea level), computed with respect to a twenty-year (1993-2012) mean, has been collected from the Copernicus Marine Service (CMEMS; https://data.marine.copernicus.eu/product/SEALEVEL_EUR_PHY_L4_MY_008_068/description; accessed in January 2023; Pujol and Larnicol, 2005) to investigate the sea level variability over the 7 AIC sub-regions (Figure 1a) and provide the boundary conditions of the coastal flooding simulations at 20 study coastal areas (Figure 1b), covering the 29-year period (1/1/1993-31/12/2021). The dataset of coastal land elevation is of spatial high resolution (5 m) and was derived by the available geospatial data from the DEM of the official Greek service for comprehensive recording of real estate and property's metes-and-bounds, i.e., the Hellenic Cadastre (https://www.ktimatologio.gr/en). This high resolution dataset was used to investigate the variability of the inundation levels over the 20 coastal areas that have been impacted by recorded intense flooding events in the past (Figure 1b). The geometric accuracy of the DEM is less than 0.70 m, while its absolute accuracy is less than 1.37 m with a 95% confidence level (Chrisafinos and Kavvadas, 2016). The 20 selected case study areas (and the aquatic basins they belong to) are well-known lowland coastal areas, based on the Hellenic Cadastre's official DEM and the fact that they are prone to flooding events.

2.2 Numerical simulations of coastal inundation

We implement modeling of coastal inundation induced by slowly varying sea level on the coast due to storm surges with CoastFLOOD model (Makris et al., 2023a). CoastFLOOD is an Aristotle University of Thessaloniki (AUTh) in-house numerical model, applied in littoral inundation hydrodynamic studies focused on local scales over the selected areas of the coastal zone in Greece (Androulidakis et al., 2023). CoastFLOOD is a depth-averaged, 2-D horizontal, mass balance, flood flow model, especially indicated for coastal areas (Makris et al., 2020, 2022). It follows the concept of reduced complexity Manning-type flows for 2-D floodplains (Bates et al., 2005). Two types (realistic and idealized) of numerical simulations were developed to derive i) daily realistic estimations of coastal inundation covering the 29-year period, based on the satellite-derived SLA levels along each study area (jobs: 20 areas × 10,592 days), and ii) estimations of the extreme floods, based on four idealized extreme scenarios of SLA (0.5, 1, 1.5 and 2 m; jobs: 4 scenarios × 20 areas) along the coastline boundary of each study area.

3 RESULTS

The interannual evolution of the mean annual SLA, averaged over 7 AIC sub-regions, revealed clear positive trends during the 1993-2021 period (Figure 2a). The general trend over the entire area was 3.6 mm/year, higher than the overall Mediterranean (2.44 mm/year; Bonaduce et al., 2016). The highest Sen's slopes were derived for the Aegean Sea with strongest trends for the SW Aegean (4.1 mm/year). The northern Aegean revealed the highest 99th percentiles in 2010 (>0.25 m; Figure 1b), when the maximum SLA values of the entire study period occurred.

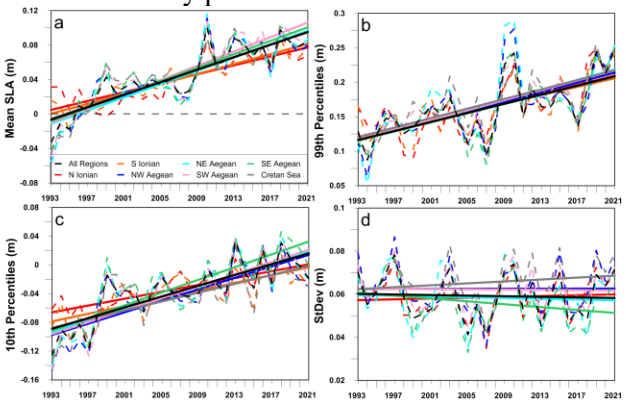

Figure 2 a) Annual variability and trends of: (a) the mean SLA; (b) the 99th percentile; (c) the 10th percentile, and (d) the standard deviation (StDev), averaged over 7 AIC regions for the period 1993–2021

To allow the comparison between different coastal areas, for which the amount of low-land cells significantly varies, and to further produce a more objective index for the estimation of coastal flooding impact for each area, the daily Flood Coverage Percentages ($FCP_{i,j}$, %) was computed as:

$$FCP_{i,j} = FA_{i,j} / FA_{ext,j} \quad (1)$$

where $FA_{i,j}$ is the flooded area for each study case j and i day based on the respective satellite-derived $SLA_{i,j}$, and $FA_{ext,j}$ is derived for each study area j based on an extreme case scenario of SLA=1 m. The FCP levels are related to two main factors (Figure 3): the sea level high peaks (e.g., 99th percentile of SLA) and the land elevation characteristics of each coastal area (e.g., distribution of low-lying areas). The FCP levels for all study areas, averaged over the 29-year period, shows strong spatial variability with very low percentages (<4%) at Alexandroupolis, Agiokampos, and 15-20% at the central and northern Ionian Sea. The very high FCPs computed for the southern Ionian areas (Areas 11 and 12) were related to both high SLA levels (>0.20 m) and the extended low-lying land (e.g., >40% of Area 11's land elevation z lays below the mean sea level: z<0 m), allowing extended flooding, especially during strong storm surge events (>16% mean FCP).

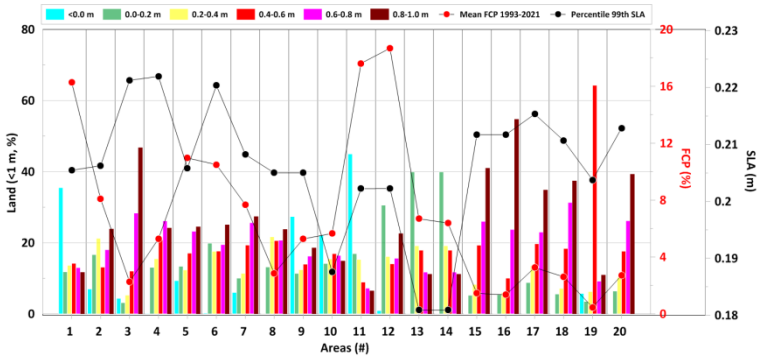

Figure 3 Frequency (%) of land elevation categories derived from all land cells (below 1 m) of each study area; the FCP averaged from daily values (zero values excluded) and the 99th Percentile of SLA are shown

The variability and trends of the annual SLA and the respective annual frequency of flooding at 20 selected low-lying areas of the AIC domain are presented in Figure 2. Strong positive trends of flooding annual frequency were computed in coastal regions of the northern Aegean (>8%/decade), associated to the increasing SLA levels and the low-land characteristics of these areas.

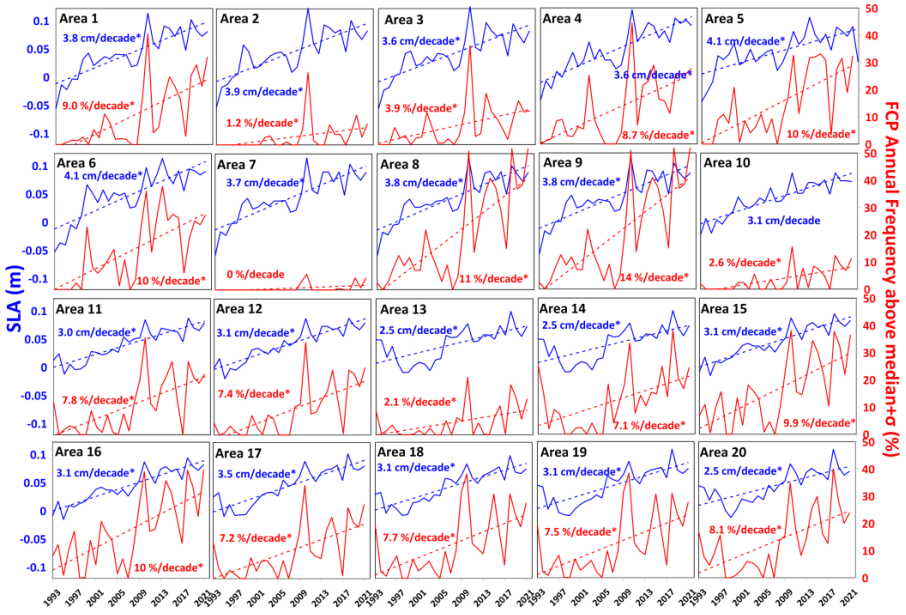

Figure 4 Annual evolution of mean SLA and annual frequency of FCP above median+σ level for 20 coastal areas during 1993-2021; the linear regressions and the respective Sen's slopes for each case are also shown

The Coastal Inundation Hazard Index (CIHI) is defined as the product of the Frequency of Occurrence (FO, %) of the days with extreme FCP_{ext} (>median+σ, %) multiplied with the temporal mean of the FCP_{ext} (derived from daily values i of the 1993-2021 period), and calculated for each study area (j) as:

$$CIHI_j = FO_j \times \overline{FCP_{ext,i,j}} \quad (2)$$

The CIHI values were normalized over their min–max range, to make individual index results for each of the 20 study areas directly comparable to each other, by following a Likert scale classification ranging from very low to very high corresponding to a 1–5 ranking system. Five areas (Areas 1, 5, 6, 11, 12) with CIHI larger than 3 were detected, characterized of high hazard to coastal inundation, as derived for the 1993-2021 period. Thermaikos Gulf (Area 1) and especially its western coastal area revealed high FO (10.4%) of extended flooding (FCP_{ext}: FCP>mean+σ), while the mean FCP_{ext} was around 19% resulting to CIHI=4. More hazardous flooding conditions (CIHI=5) were detected for the two areas in Cretan Sea (Ierapetra and Rethymno) showing FO>14% and mean FCP_{ext}>16%.

Table 1. Means and ranking (1-5) of FO, mean FCP and CIHI derived for the 20 coastal areas and the 1993-2021 period. Ranking: 1 (very low), 2 (low), 3 (medium), 4 (high), 5 (very high). CIHI values larger than 3 (high and very high) are highlighted with red color.

Area	Area	FO	MEAN FCP	CIHI (product)	CIHI (Ranked)
1	**Thermaikos**	0.104	0.188	0.019	4
2	**Nestos**	0.028	0.144	0.004	1
3	**Alexandroupoli**	0.028	0.050	0.001	1
4	**Chios**	0.130	0.103	0.013	3
5	**Ierapetra**	0.146	0.168	0.025	5
6	**Rethymno**	0.140	0.196	0.027	5
7	**Pineios**	0.006	0.092	0.001	1
8	**Agiokampos**	0.142	0.083	0.012	2
9	**Katerini**	0.197	0.074	0.015	3
10	**Kalamata**	0.035	0.065	0.002	1
11	**Katakolo**	0.106	0.264	0.028	5
12	**Laganas**	0.090	0.321	0.029	5
13	**Manolada**	0.044	0.098	0.004	1
14	**Patra**	0.068	0.097	0.007	2
15	**Argostoli**	0.160	0.029	0.005	1
16	**Livadi**	0.174	0.029	0.005	1
17	**Vassiliki**	0.100	0.075	0.008	2
18	**Palairos**	0.123	0.045	0.006	1
19	**Preveza**	0.122	0.009	0.001	1
20	**Igoumenitsa**	0.132	0.059	0.008	2

4 DISCUSSION AND CONCLUSIONS

The variability of the Sea Level Anomaly (SLA) over the Aegean, Ionian and Cretan Seas has been evaluated with the use of satellite-derived observations during a 29-year period from 1993 to 2021. The SLA observations along the coastal zone of the AIC domain were used to force numerical simulations of coastal inundation with CoastFLOOD model (Makris et al., 2023a, 3023b) at 20 selected low-lying areas to estimate their hazard levels due to episodic increases of sea level, as derived during the 29-year period. The general SLA trend over the entire AIC domain was 3.6 mm/year, which is higher than the overall Mediterranean (2.44 mm/year; Bonaduce et al., 2016) and the eastern Mediterranean (3.1 mm/year; Mohamed and Skliris, 2022) trends. The highest Sen's slopes were derived for the Aegean Sea with strongest trends for the SW Aegean (4.1 mm/year). Moreover, the Cretan Sea revealed the strongest

interannual trend of the maximum SLA values (99th percentiles; 3.5 mm/year). The highest SLA levels were detected primarily in autumn and secondarily in winter, while the lowest seasonal means occurred in spring.

The Sen's slopes of the inundation levels computed for all 20 study areas were positive (increasing trends) and statistically significant (0.07%/year for the mean levels and 0.15%/year for the maximum levels). In all cases, a clear upward shift took place after 2009, ranging around 1.39% for the mean and 2.86% for the maximum levels. The highest SLA for all areas occurred in the years of 2010, 2013, 2014, 2016, 2018, 2019, 2020, and 2021, all during the last 12-year period, confirming the strong inter-decadal increase that enhanced the flooding levels after 2009. Very strong trends of extreme flooding were computed for the Cretan Sea, where the strongest trends of maximum SLA occurred. More hazardous flooding conditions (CIHI=5) were detected for the two areas of the Cretan Sea (Ierapetra and Rethymno) compared to the other study cases, showing both high frequency (>14%) and large inundation areas (>16%). High CIHI values were computed for the coastal zone of the southern Ionian Sea (Katakolo and Laganas). To extend the findings of the study, the next step is to develop climatic projections of coastal inundation under different climate change scenarios to test if the current increasing trends in the AIC domain may be probable in the 21st century under different Representative Concentration Pathways (RCP) scenarios. Moreover, for the complete assessment of flood probability at coastal sites of the AIC domain susceptible to inundation risk, the next step is to include wave observations for the integrated estimation of the combined impact of wave action and rising water levels, especially in the wave runup zone of the low-lying inland coastal areas.

References

Androulidakis Y, Makris C, Mallios Z, Pytharoulis I, Baltikas V, Krestenitis Y (2023) Storm surges and coastal inundation during extreme events in the Mediterranean Sea: the IANOS Medicane. Nat Hazards 117:939–978. doi:10.1007/s11069-023-05890-6

Bates PD, Dawson RJ, Hall JW, et al. (2005) Simplified two-dimensional numerical modelling of coastal flooding and example applications. Coast Eng 52(9):793-810. doi:10.1016/j.coastaleng.2005.06.001

Bonaduce A, Pinardi N, Oddo P, et al. (2016) Sea-level variability in the Mediterranean Sea from altimetry and tide gauges. Clim Dyn 47(9-10):2851-66. doi:10.1007/s00382-016-3001-2

Cazenave A, Dieng HB, Meyssignac B, et al. (2014) The rate of sea-level rise. Nat Clim Chang 4(5):358-361. doi:10.1038/nclimate2159

Chrisafinos D, Kavvadas I (2016) Quality assessment of the new backgrounds LSO25. Paper presented at the 14th National Conference on Chartography of the Greek Scientific Association of Chartography "The chartography in a changing world", Thessaloniki. (in Greek)

Ferrarin C, Bajo M, Benetazzo A, Cavaleri L, et al. (2021) Local and large-scale controls of the exceptional Venice floods of 2019. Progr Oceanogr 197:102628. doi:10.1016/j.pocean.2021.102628

Makris C, Androulidakis Y, Mallios Z, Baltikas V, Krestenitis Y (2022) Towards an Operational Forecast Model for Coastal Inundation due to Storm Surges: Application during Ianos Medicane. Paper presented at the 9th International Conference on Civil Protection & New Technologies, SafeThessaloniki 2022, 29 September - 1 October, Thessaloniki, Greece, pp. 69-72.

Makris C, Baltikas V, Androulidakis Y., Krestenitis Y. (2020). Coastal Inundation due to Storm Surges on a Mediterranean Deltaic Area under the Effects of Climate Change. Paper presented at the 7th International Conference on Civil Protection & New Technologies, SAFE GREECE 2020, Athens.

Makris C, Mallios Z, Androulidakis Y, Krestenitis Y (2023) CoastFLOOD: A High-Resolution Model for the Simulation of Coastal Inundation Due to Storm Surges. Hydrol 10(5):103. doi:10.3390/hydrology10050103

Mohamed B, Skliris, N (2022) Steric and atmospheric contributions to interannual sea level variability in the eastern Mediterranean Sea over 1993–2019. Oceanologia, 64(1):50-62. doi:10.1016/j.oceano.2021.09.001

Pujol MI, Larnicol G (2005) Mediterranean Sea eddy kinetic energy variability from 11 years of altimetric data. J Mar Syst 58(3-4):121-142. doi:10.1016/j.jmarsys.2005.07.005

Analysis of extreme storm surges at the Mediterranean coastline under climate change

P. Galiatsatou[1,2*], C. Makris[3], V. Baltikas[3], Y. Krestenitis[4], P. Prinos[1]

[1]Hydraulics Laboratory, School of Civil Engineering, AUTh, Thessaloniki, 54124, Greece
[2]Thessaloniki Water Supply & Sewerage Company (EYATH S.A), Thessaloniki, 54622, Greece
[3]Maritime Engineering Laboratory, School of Civil Engineering, AUTh, Thessaloniki, 54124, Greece
[4]Professor Emeritus, School of Civil Engineering, AUTh, Thessaloniki, 54124, Greece
[*]Corresponding author: pgaliats@civil.auth.gr, pgaliatsatou@eyath.gr

Abstract

This study examines the effects of climate change on extreme storm-induced sea levels in the coastal zone of the entire Mediterranean Sea. The analysed extreme sea surface heights resulted from high-resolution simulations with a robust storm surge model (MeCSS) fed by atmospheric circulation data from the COSMO-Climate Limited-area Modelling (CCLM) Regional Climate Model (RCM) of the Med-CORDEX initiative (implemented in Goethe Universität Frankfurt, GUF), with future estimations based on Representative Concentration Pathways, RCP 4.5 and 8.5. Extreme value theory is utilised to analyse and extrapolate extreme storm surges along the Mediterranean coastline in three 35-year intervals, corresponding to the reference and two future periods. The analysis reveals local differentiations in storm surge extremes among the different areas of the Mediterranean Sea, while a projected storminess attenuation is found, especially in the second half of the 21st century for both RCPs.

Keywords Extreme value theory, Storm surge, Mediterranean Sea, Climate change.

1 INTRODUCTION

Global climate change is associated with extreme marine events of higher intensity and frequency and mean sea level rise, increasing vulnerability and exposure of coastal areas to flooding and erosion phenomena. Extreme wave and surge storm events constitute the primary sources of coastal risks, rendering a reliable estimation of their extreme levels urgent, especially for future weather conditions. Intense storm surge events threaten low-elevation coastal areas of the Mediterranean Sea with inundation risk, resulting in human casualties, severe damages to properties and infrastructure, as well as deterioration of the coastal environment. Many researchers have shown that the extreme storm surge climate varies significantly among different regions of the Mediterranean coastline, especially due to the diverse topographical characteristics of its regional seas (Šepić et al. 2012; Cid et al. 2016; Makris et al. 2016, 2018, 2023; Galiatsatou et al. 2019, 2021; Lionello et al. 2019, 2021; Calafat et al. 2022).

2 STUDY AREA AND CLIMATE CHANGE DATA

The data of storm-induced sea level (Sea Surface Height, SSH) in coastal regions of the Mediterranean Sea resulted from high-resolution simulations with Mediterranean Climate Storm Surge (MeCSS) model, a 2-DH barotropic simulator of hydrodynamic ocean circulation based on the depth-averaged shallow water equations (Androulidakis et al. 2015). Simulations covered the reference (1971-2005), the short-term (2021-2055) and the long-term (2066-2100) future climate (Makris et al. 2023). The atmospheric forcing of the model consists of wind (velocity and direction) and sea level pressure fields by a high-resolution Regional Climate Model (RCM), i.e., the COSMO-Climate Limited-area Model (CCLM) with Nucleus for European Modelling of the Ocean (NEMO) by Goethe Universität Frankfurt (GUF), implemented within MED-CORDEX initiative (https://www.medcordex.eu/; Ruti et al. 2016).

The GUF-CCLM-NEMO is an atmospheric-ocean circulation ensemble model collaboration based on a finite difference, hydrostatic, primitive equation ocean general circulation model, with free sea surface and non-linear equation of state. Historical climate data for the reference period were validated by Makris et al. (2023) against ECMWF (European Centre for Medium-Range Weather Forecasts) reanalyses, based on assimilation system fields produced under CERA-20C. Future estimations of the

GUF RCM are based on two climatic scenarios of the Representative Concentration Pathways, RCP 4.5 and RCP 8.5.

3 METHODOLOGY

Extreme value methods are powerful statistical techniques for analysing the highest values of a process and for extrapolating to levels more rare compared to any previously observed or simulated. In this work the Generalised Extreme Value (GEV) distribution is fitted to annual maximum storm surge events of all three 35-year periods (reference and two future periods) for all the littoral grid cells of the GUF-forced MeCSS model along the entire Mediterranean coastline. The cumulative distribution function of the GEV is expressed as (Coles 2001):

$$G(x;\mu,\sigma,\xi)=\begin{cases}\exp\left\{-\left[1+\xi\left(\frac{x-\mu}{\sigma}\right)\right]^{-1/\xi}\right\} & \xi\neq 0\\ \exp\left\{-\exp\left[-\left(\frac{x-\mu}{\sigma}\right)\right]\right\} & \xi=0\end{cases} \quad (1)$$

where μ is the location, σ, is the scale, and ξ is the shape parameter of the distribution, the latter also determining its limiting behaviour. Considering the small size of the 35-year annual maxima samples for the reference and future periods, the method of L-moments is used in this work to estimate the parameters of the GEV distribution function (Galiatsatou and Prinos 2016). The quantiles, X_T, corresponding to a defined return period, T, represent the T-years SSH return levels (Coles 2001):

$$X_T=\begin{cases}\mu-\frac{\sigma}{\xi}\left\{1-\left[-\ln\left(1-\frac{1}{T}\right)\right]^{-\xi}\right\} & \xi\neq 0\\ \mu-\sigma\ln\left[-\ln\left(1-\frac{1}{T}\right)\right] & \xi=0\end{cases} \quad (2)$$

Storm surge 95% confidence intervals (CI) are also calculated by means of a parametric bootstrap approach (Shao 1996). A large number of samples (500 samples) of length equal to 35 years is first generated from each fitted GEV model. GEV models are then fitted to the simulated samples using L-moments approach. Return levels are then estimated for all simulated samples using Eq. 2, to finally assess CI using the percentile method. Extrapolated storm surge return levels corresponding to return periods of 50 and 100 years are therefore extracted and intercompared among the different areas of the Mediterranean Sea. Stationarity and independence of the 35-years annual maxima for both the historical and future climate conditions are checked using the Mann-Kendall trend and the Wald-Wolfowitz tests (Galiatsatou et al. 2019).

4 RESULTS

The non-parametric Wald-Wolfowitz test, implemented to storm surge annual maxima along the Mediterranean coastline for all study periods, reveals very few samples not satisfying the null hypothesis of stationarity and independence, at a 1% significance level (i.e., less than 2% of the coastal points in all study periods). Implementation of the Mann-Kendall trend test did not identify statistically significant linear trends (1% significance level) in storm surge extremes of the Mediterranean coastline.

Figure 1 presents maps of horizontal spatial distribution of 50-years SSH return levels along the Mediterranean coastline for the reference (1971-2005) and the two future (2021-2055 and 2066-2100) periods for scenarios RCP 4.5 and 8.5. Local differentiations in storm surge extremes around the Mediterranean coastal zone are evident in all study periods, however their spatial distribution remains almost similar in the reference and the future climate. Highest storm surges are detected along parts of the northern Mediterranean coasts (Venice lagoon, Gulf of Lions, northern Adriatic and Aegean Seas, etc.) and the Gulf of Gabes in its southern part. In the reference period maximum storm surge return levels, 0.75m (upper 97.5% CI =1.05m) and 0.85m (upper 97.5% CI =1.33m) for return periods 50 and 100 years, respectively, are assessed in the Gulf of Gabes. The same area provides maximum storm surge return levels in the short-term future period for RCP 4.5 ($SSH_{50years}$ = 0.63m and $SSH_{100years}$ = 0.69m), and in the long-term future period for RCP 8.5 ($SSH_{50years}$ = 0.71m and $SSH_{100years}$ = 0.80m). The Gulf of Gabes and the northern Adriatic Sea along the coastlines of Croatia and Slovenia accommodate the largest storm surge return levels in the long-term future period for RCP 4.5 ($SSH_{50years}$ = 0.58m and $SSH_{100years}$ = 0.62m), and in the short-term future period for RCP 8.5 ($SSH_{50years}$ = 0.57m and $SSH_{100years}$ = 0.61m).

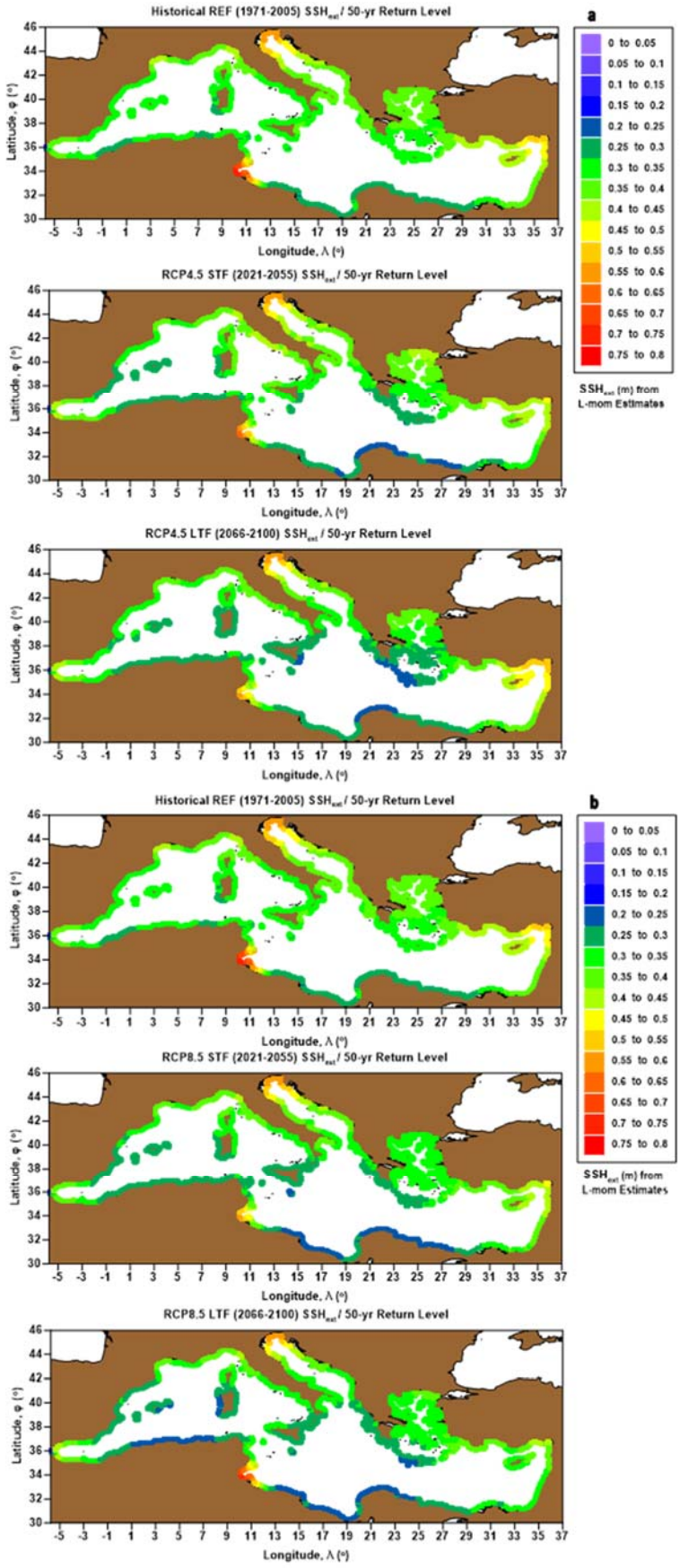

Figure 1. Map of horizontal spatial distribution of 50-year SSH (m) along the Mediterranean coastline during the Reference (1971-2005) and Future Periods (2021-2055 and 2066-2100) for scenarios: **(a)** RCP4.5, **(b)** RCP8.5

Figure 2 presents maps of horizontal spatial distribution of differences (×100%) of 50-years SSH return levels between the two future and reference periods for scenarios RCP 4.5 and 8.5. A projected storminess attenuation is evident for both RCPs and for both future periods, with more extended and pronounced effects for the long-term future period for scenario RCP 8.5. The climate change signal (difference of Future–Reference Period) reveals a decrease in 50-years storm surges up to -23% (2021-2055) or -30% (2066-2100), and -29% (2021-2055) or -28% (2066-2100), for RCP 4.5 and 8.5-driven simulations, respectively. There exist apparent differences between the climate change signals of the two scenarios (RCP4.5-8.5), not so much related to the spatial distribution of projected storm surge extremes, which presents a quite stable pattern, but more in terms of their magnitudes. Despite the general projected storminess attenuation along the Mediterranean coastline, due to a probable northward shift of the cyclogenesis centers and deep depression areas over the basin, extreme storm surges are expected to increase at specific coastal sites in south and northeastern Spain, the western and east-central coasts of the Italian Peninsula, certain gulfs and coastal inlets in south France, north-western African littorals, north Aegean coasts, Lebanon, Syria, and Israel, with more obvious increases assessed for RCP 4.5-driven simulations. Such increases range from almost 10% up to more than 30% locally for the two future periods.

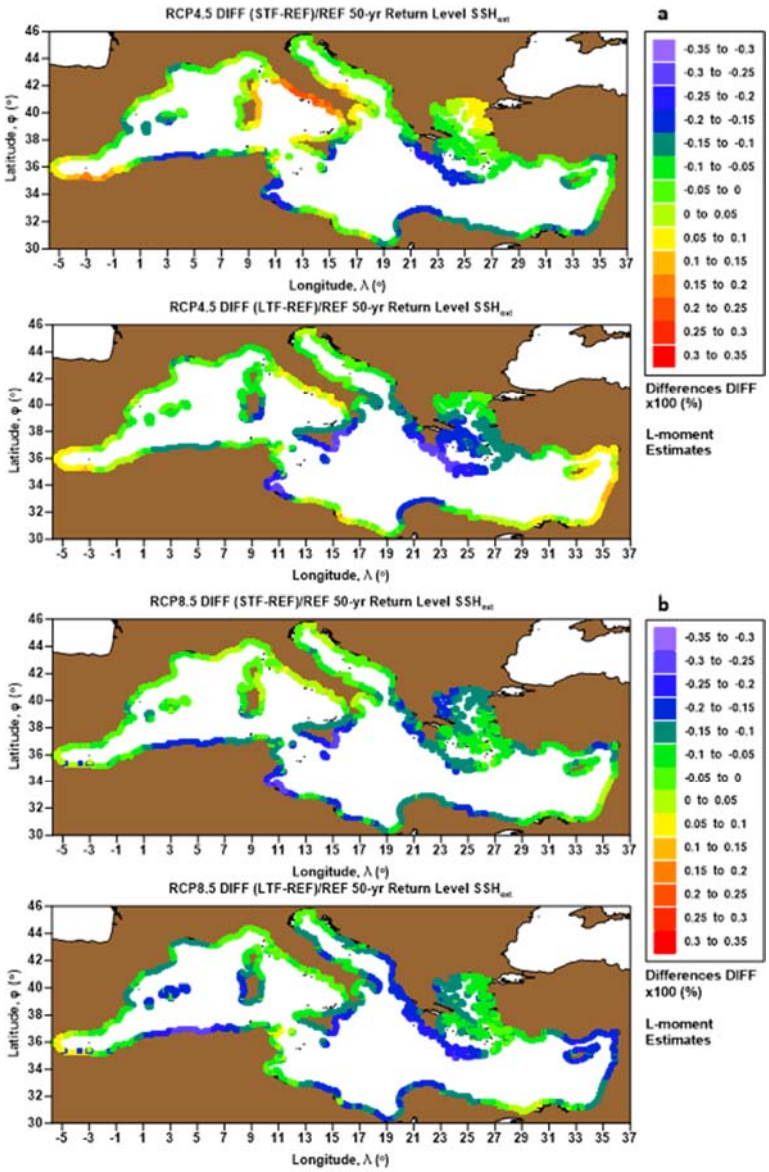

Figure 2. Map of horizontal spatial distribution of differences (×100%) of 50-year SSH (m) between the Future (2021-2055 and 2066-2100) and Reference Periods for scenarios: **(a)** RCP4.5, **(b)** RCP8.5

For RCP 8.5-driven simulations, increases in projected storm surge levels hardly reach 10% for the short-term future period and are mostly detected locally at coastal sites in Croatia, Spain, Italy, France, north-western Africa, Syria, and Lebanon, while increases in storminess and coastal surges are quite reduced in the long-term future period confined to a few coastal sites in north-western/-eastern Africa.

5 CONCLUSIONS

A projected storminess attenuation is estimated to occur in the Mediterranean basin affecting the storm surges on the coastline under the considered climate scenarios (RCP 4.5-8.5) with more extended and pronounced effects for the long-term future period for scenario RCP 8.5. The climate change signal for the long-term future period reveals a decrease in 50-years storm surges up to -30% and -28%, for RCP 4.5 and RCP 8.5-driven MECSS simulations, respectively. However, the magnitudes of storm surge extremes are estimated to increase up to 30% locally in certain regions (mainly gulfs, bights, and coastal inlets) during the 21st century. The peculiarities of topographic characteristics of the regional seas (e.g., northern Adriatic and Aegean Seas, south Libyan and eastern Levantine Seas, etc.) in the Mediterranean basin have a significant influence on the variability of storm surge extremes for all study periods.

References

Androulidakis YS, Kombiadou KD, Makris CV, Baltikas VN, Krestenitis YN (2015) Storm surges in the Mediterranean Sea: variability and trends under future climatic conditions. Dyn Atmos Oceans 71: 56–82. doi:10.1016/j.dynatmoce.2015.06.001

Calafat FM, Wahl T, Tadesse MG, Sparrow SN (2022) Trends in Europe storm surge extremes match the rate of sea-level rise. Nature 603: 841–845. doi:10.1038/s41586-022-04426-5.

Cid A, Menéndez M, Castanedo S, Abascal AJ, Méndez FJ, Medina R (2016) Long-term changes in the frequency, intensity and duration of extreme storm surge events in southern Europe. Clim Dynam 46(5): 1503–1516. doi:10.1007/s00382-015-2659-1

Coles S (2001) An introduction to statistical modeling of extreme values. Springer Verlag, London, UK.

Galiatsatou P, Prinos P (2016) Joint probability analysis of extreme wave heights and storm surges in the Aegean Sea in a changing climate. In: E3S Web of Conferences (Vol. 7, p. 02002), EDP Sciences.

Galiatsatou P, Makris C, Prinos P, Kokkinos D (2019) Nonstationary joint probability analysis of extreme marine variables to assess design water levels at the shoreline in a changing climate. Nat Hazards 98: 1051–1089. doi:10.1007/s11069-019-03645-w

Galiatsatou P, Makris C, Krestenitis Y, Prinos P (2021) Nonstationary extreme value analysis of nearshore sea-state parameters under the effects of climate change: Application to the Greek coastal zone and port structures. J Mar Sci Eng 9(8): 817. doi:10.3390/jmse9080817.

Makris CV, Tolika K, Baltikas VN, Velikou K, Krestenitis YN (2023) The impact of climate change on the storm surges of the Mediterranean Sea: coastal sea level responses to deep depression atmospheric systems. Ocean Model 181: 102–149. doi:10.1016/j.ocemod.2022.102149

Makris C et al (2018) Climate change impacts on the coastal sea level extremes of the east-central Mediterranean Sea. Paper presented at the XIV PRE Conference, Thessaloniki, Greece.

Makris C et al (2016) Climate change effects on the marine characteristics of the Aegean and the Ionian seas. Ocean Dyn 66(12): 1603–1635. doi:10.1007/s10236-016-1008-1.

Lionello P et al. (2021) Extreme floods of Venice: characteristics, dynamics, past and future evolution. Nat. Hazards Earth Syst Sci 21(8):2705–2731. doi:10.5194/nhess-21-2705-2021

Lionello P, Conte D, Reale M (2019) The effect of cyclones crossing the Mediterranean region on sea level anomalies on the Mediterranean Sea coast. Nat Hazards Earth Syst Sci 19(7): 1541–1564. doi: 10.5194/nhess-19-1541-2019

Ruti PM et al (2016) MED-CORDEX initiative for Mediterranean climate studies. Bull Am Meteorol Soc 97(7): 1187–1208. doi:10.1175/BAMS-D-14-00176.1

Šepić J, Vilibić I, Jordà G, Marcos M (2012) Mediterranean sea level forced by atmospheric pressure and wind: Variability of the present climate and future projections for several period bands. Glob Planet Change 86: 20–30. doi:10.1016/j.gloplacha.2012.01.008

Shao J (1996) Bootstrap Model Selection. J Am Stat Assoc 91(434): 655-665. doi:10.1080/01621459.1996.104769

Post-Boussinesq modelling of nonlinear irregular waves in port basins with wave-structure interaction

C.V. Makris[1], T.V. Karambas[1*], S. Christopoulos[2]

[1]Department of Civil Engineering, Aristotle University of Thessaloniki, University Campus, Thessaloniki, 54124, Greece
[2]HYDROMARE, Consulting Engineering Company, 20 L. Sofou, Thermi, Thessaloniki, 57001, Greece
[*]Corresponding author: karambas@civil.auth.gr

Abstract

In this paper we present an updated version of a horizontally two-dimensional post-Boussinesq wave model intended for irregular wave propagation in coastal areas near seaports. The model considers nonlinear wave transformation due to shoaling, refraction, diffraction, bottom friction, wave breaking, wave-structure interaction, reflection, wave-current interaction, etc. in the vicinity of nearshore structures and inside port basins. The model validation is based on comparisons against experimental data from physical simulations in laboratory-scale wave flumes. The model skill is good in reproducing both regular and irregular wave fields interacting with coastal structures.

Keywords Nonlinear wave models, Boussinesq-type model, irregular waves, coastal structures.

1 INTRODUCTION

During the last 30 years, advanced Boussinesq-type models have prevailed in the coastal modelling community for the numerical simulation of nonlinear dispersive waves' propagation in shallow and intermediate waters within port engineering projects (e.g., Karambas 1999). The most significant research efforts have focused on fundamental improvements of the dispersive properties for wave frequency and the addition of wave breaking dissipation (surface roller mechanism and eddy viscosity model approach) (e.g., Karambas and Koutitas 1992, 2002). Brocchini (2013) presents a comprehensive review on the matter and discusses the ability of Boussinesq-type models to perform robustly and also be computationally efficient based on the processing power of modern computers.

2 SCIENTIFIC BACKGROUND SCOPE OF RESEARCH

The prototype, post-Boussinesq approach, wave model with a system of 2-DH equations for fully dispersive and weakly nonlinear irregular waves over any finite water depth was presented by Karambas and Memos (2009). The model incorporated 5 terms in each momentum equation (i.e., for x- and y-direction), including the classical shallow water terms and only one frequency dispersion term, which is expressed through convolution integrals estimated by appropriate impulse functions. The numerical solution is based on an explicit Forward-Time-Central-Space (FTCS) scheme of finite differences on a staggered grid and a summative approximation of the convolution integral, restricting the system of algebraic equations compared to other Boussinesq-type model formulations; more details provided by Karambas et al. (2019).

In this paper, an updated version of the aforementioned model is presented (Karambas et al. 2019). It is implemented for wave propagation and transformation due to shoaling, refraction, diffraction, bottom friction, wave breaking, runup and overtopping, wave-structure interaction, etc., in seaport areas near coastal protection and harbour structures (Samaras and Karambas 2021). The model's performance is verified against experimental data of i) uni- and multi-directional spectral wave transformation over shoaling bed formations (Vincent and Briggs 1989), and ii) wave diffraction through a breakwater gap (Li et al., 2000; Yu et al., 2000). By expanding the previous work of Avgeris et al. (2005) for spectral wave interaction with pervious submerged breakwaters and combining the Karambas (2003) modelling approach of infiltration-exfiltration effects in the swash zone, we hereby present case studies of the post-Boussinesq model application over sub-aerial (emerged) permeable breakwaters, testing the wave transmission and overtopping, through and above porous structures, respectively.

3 NEW MODEL FEATURES

The new version of the model includes three updated features (Karambas et al. 2019; Makris et al. 2021): i) a spectral wave generator from any direction of the horizon in the computational grid, covering the needs for incident long crested waves parallel to any central or lateral open boundary *in tandem* with oblique irregular wave trains of arbitrary incident angles; ii) an enhanced methodology for peripheral sponge layers, introduced to minimize unphysical wave reflection from open boundaries or in semi-enclosed areas; and iii) an integrated extension of the Karambas and Bowers (1996) and Karambas (2003) modules, coupling the full or partial reflection from sloping (or vertical) coastal structures with a (coarse) porous flow approach for pervious bed applied to permeable breakwaters.

3.1 Multi-directional oblique wave generation and peripheral sponge layers

Irregular waves can be generated along any parallel, orthogonal, or oblique source line to the open boundaries with heterogenous incident wave characteristics along it, following e.g., the diversity of local depths and spectral wave input to the model, corresponding to surface elevation computed by established techniques (Lee and Suh 1998). This is achieved by a source term addition able to simulate both uni- and multi-directional irregular waves for several angles to each open boundary thus simulating incoming wave trains from any direction, avoiding unphysical diffraction in case of oblique incident waves. The aforementioned complex internal wave generation mechanism is based on a peripheral layer of exponential damping factor for the wave energy content (Larsen and Dancy 1983), allowing for spatial restriction of the computational field in nearshore areas adjacent to harbour structures reducing the modelling time and the respective demand for computational resources.

3.2 Flow modules for wave reflection from and porous transmission through permeable structures

The partial and/or full reflection of incident waves from coastal protection and harbour structures is simulated based on an updated version of the Karambas and Bowers (1996) modelling approach of an extra eddy viscosity dissipation term in the momentum equations. This method solves a system of complex equations of the wavenumber for pre-assigned values of the wave reflection coefficient C_R, and then assigns a fictitious friction coefficient that describes wave energy dissipation over a typical distance of double the structure's mean width in front of the solid boundary (e.g., breakwater, seawall, quay, etc.). The reflected wave amplitude is provided analytically and superimposed to the incident wave characteristics by the aforementioned methodology, based on C_R derived from well-known values in existing technical literature (CEM 2002). The relevant equations are provided by Karambas and Bowers (1996) and presented by Makris et al. (2021) for a respective hyperbolic mild-slope equation wave model.

The 'dry bed' boundary condition is used to simulate wave runup and overtopping of subaerial breakwaters following the work of Samaras and Karambas (2021). This module is coupled to a wave-induced transmission flow through subaerial (emerged) permeable breakwaters, based on a flow resistance formula of Darcy-type flows in homogenous porous media. The hydrodynamics inside the pervious structure is considered to behave like an even (water table) free-surface groundwater flow in an isotropic (shallow) phreatic aquifer. The porous flow resistance in the structure, leading to wave energy dissipation in its leeward side, is simulated by introducing an additional term in the momentum equation given by the Dupuit-Forchheimer formula along the structure's cross-section (Karambas 2003):

$$S\frac{\partial h_p u_p}{\partial t} - c_A u_p \frac{\partial h_p}{\partial t} + \frac{1}{n}\frac{\partial h_p u_p^2}{\partial x} + ng\frac{\partial \frac{1}{2}h_p^2}{\partial x} + ngh_p\left(au_p + bu_p|u_p|\right) = -\frac{qq_x}{n} + \\ +\text{Boussinesq terms} \quad (1)$$

$$\frac{\partial h_p}{\partial t} + \frac{1}{n}\frac{\partial h_p u_p}{\partial x} = -\frac{q}{n} \quad (2)$$

$$q = -\partial(up\ hp)/\partial x \quad (3)$$

where h_p is the thickness of the water layer in the porous medium; u_p is the depth-averaged filter/discharge velocity in this layer; a and b are the Forchheimer coefficients; S is the coefficient for

added mass; n is the porosity; q (m/s) is the volumetric flux rate per width between the seawater flow layer and the phreatic groundwater layer.

To avoid computationally unaffordable and exceptionally fine resolutions of the model domain (i.e., very small spatial discretization step), we propose the following approach. Instead of a (rubble-mound) breakwater, we consider an equivalent idealized vertically faced homogeneous and isotropic porous structure with a dissipative area (by a numerical friction treatment) in its upstream side. Energy loss on the upstream side of the ideal structure (i.e., rough slope of the actual breakwater) is represented by an appropriate (numerical) friction coefficient, again following the notion of wave dissipation by the reflection module of Karambas and Bowers (1996).

4 MODEL VALIDATION AND APPLICATION

The model's performance has been evaluated in the past against analytical and experimental data for 2-DH wave diffraction around semi-infinite breakwaters (Karambas et al. 2019) and 2-DV cross-sectional wave transmission or overtopping of impermeable coastal structures using the Roeber et al. (2010) datasets (presented analytically by Samaras and Karambas 2021), respectively.

Herein, the validation of the model's performance is conducted by comparisons of simulation results against experimental data (Yu et al. 2000; Li et al. 2000) for regular and irregular wave propagation through a breakwater gap (Figure 1). The incident significant wave height for the case of uni-directional irregular waves is H_s=0.05m and the spectral peak period is T_p=1.20s. Figure 1a shows the calculated diffraction coefficient for the case of gap width B=3.92m (B/L=2, where wavelength L corresponds to T_p for irregular waves). Figure 1b presents the cross-sectional distribution of the diffraction coefficient $K_D=H/H_i$ at a distance $y=3L$ from the breakwater. Comparisons of model results against experimental data are proven to be satisfactory.

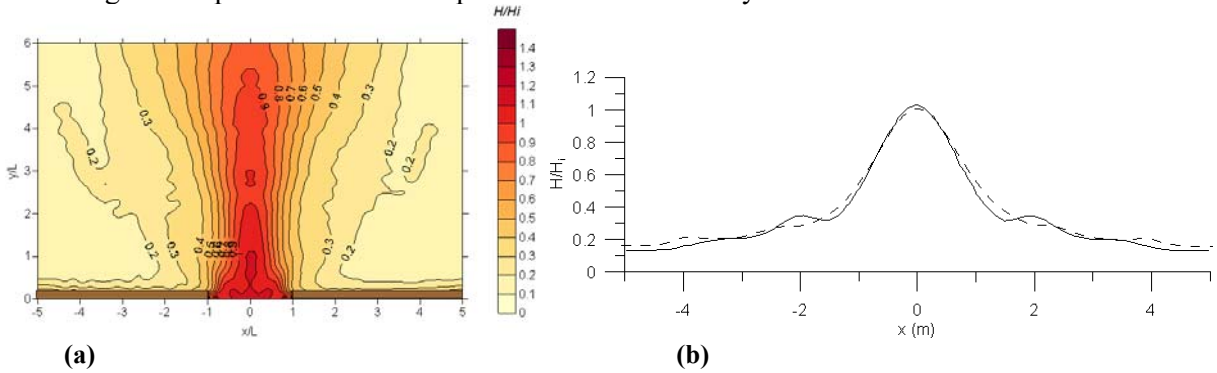

Figure 1. a) Wave propagation through breakwater gap: diffraction coefficient $K_D=H/H_i$ contours for B=3.92m; b) comparisons of wave diffraction coefficient K_D through a breakwater gap (solid line: experimental data of Yu et al. 2000 and Li et al. 2000, dashed line: post-Boussinesq type model output)

Figure 2 portrays the 2-DH distribution (by top view map) of the water's free surface for the elliptical shoal experimental setup by Vincent and Briggs (1989) incorporating a directional spectral wave generator is also numerically reproduced as a test. The directional spectral wave basin of 35 m wide by 29 m long has a constant water depth of 0.457 m. The elliptical shoal has a major axis of 3.96 m and minor axis of 3.05 m and a maximum height of 0.3048 m. The wave period T or T_p of the incident waves is equal to 1.3 sec and the representative wave height H_{in} or H_s is 2.54 cm for regular and irregular waves, respectively.

Figure 3 shows a comparison of the post-Boussinesq type model results against for narrow directional spectra against the Vincent and Briggs (1989) experimental data along transect No.4 which lies behind the shoal. The comparisons show an acceptable up to very good agreement between the model results and the experimental data, depending on the distance from the shoal's center. Figures 4 and 5 present vertical cross-section plot of typical numerical results for wave transmission over and through a steep-sloped, narrow-crested, breakwater type of structure, with and without wave overtopping, respectively.

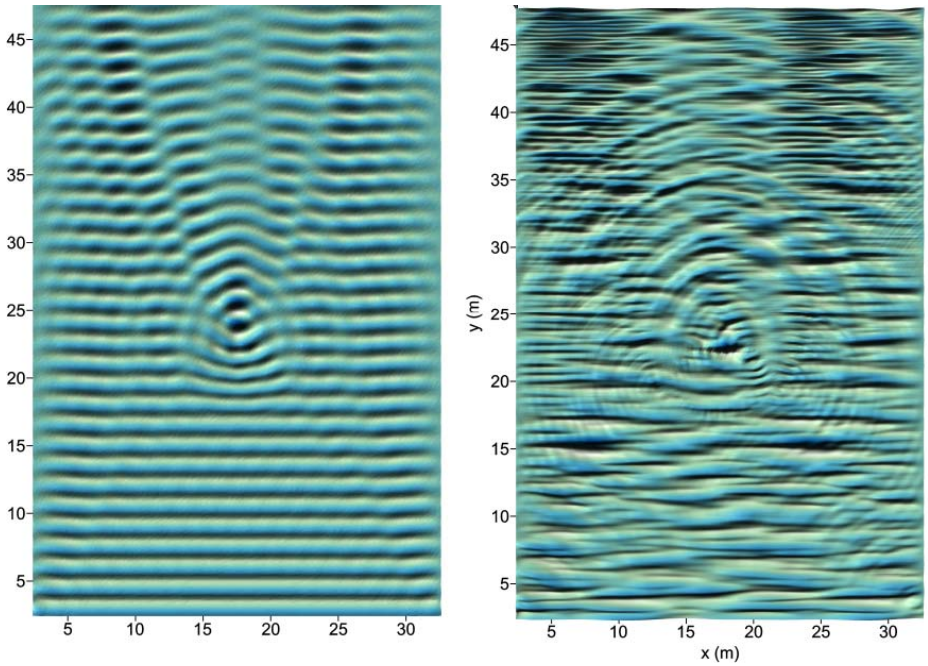

Figure 2. Monochromatic and multi-directional wave propagation over a shoal (experiments by Vincent and Briggs 1989): snapshot of the modelled free-surface elevation for (a) regular and (b) irregular wave fields

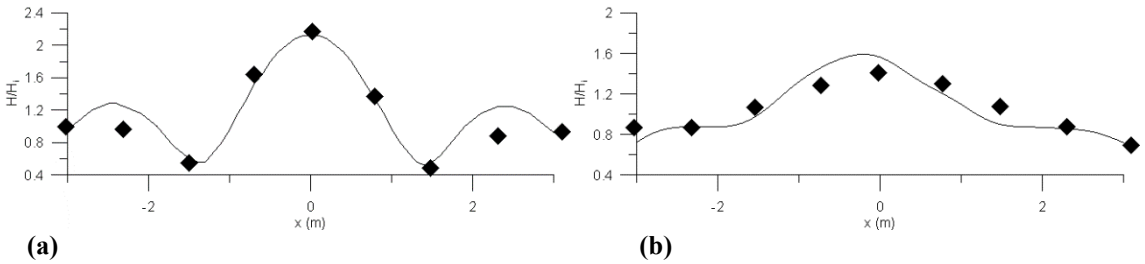

Figure 3. Comparisons of post-Boussinesq type model results against experimental data of Vincent and Briggs (1989) in terms of normalized wave height H/H_i for (a) monochromatic and (b) spectral multi-directional waves; numerical model results: solid line, experimental data: square symbols

5 CONCLUSIONS

The evaluation of a post-Boussinesq type model's performance is conducted by comparisons of simulation results with experimental data of both regular and irregular wave propagation through a breakwater gap and breaking and non-breaking waves over a shoal. Results range from plausible to very good. The proposed model can further robustly simulate the wave transmission of incident monochromatic and spectral waves over and through permeable breakwaters with and without overtopping of narrow-crested sub-aerial porous coastal protection structures.

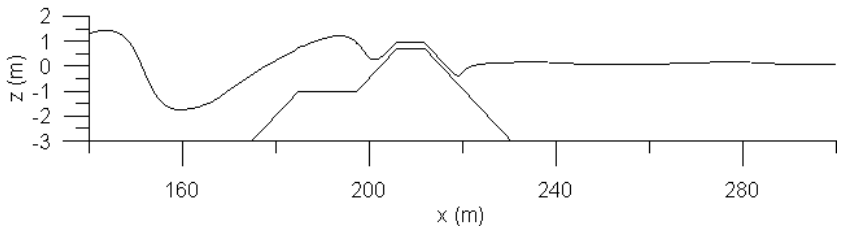

Figure 4. Modelled wave transmission over and through a breakwater with overtopping

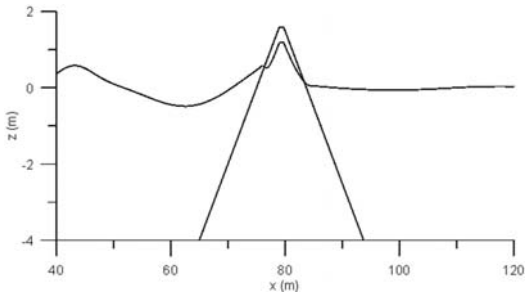

Figure 5. Modelled wave transmission over and through a breakwater without overtopping

References

Avgeris I, Karambas TV, Prinos P (2005) Boussinesq modeling of wave interaction with porous submerged breakwaters. In: Smith JM (ed) Coastal Engineering, vol 4, World Scientific, p 604-616

Brocchini M (2013) A reasoned overview on Boussinesq-type models: the interplay between physics, mathematics and numerics. Proc Roy Soc A: Math, Phys Eng Sci, 469(2160):20130496.

CEM (2002) Coastal Engineering Manual, USA Corps of Engineers, Manual, 2-1100.

Karambas Th (2003) Modelling of infiltration-exfiltration effects of cross-shore sediment transport in the swash zone. Coast Eng J, 1:63-82.

Karambas T, Memos C (2009) Boussinesq model for weakly nonlinear fully dispersive water waves. J Wtrway Port Coast Ocean Eng, 135:187–199.

Karambas TV, Bowers EC (1996) Representation of partial wave reflection and transmission for rubble mound coastal structures. WIT Trans Ecol Environ, 12:415-423.

Karambas TV, Makris CV, Baltikas VN (2019) 2-DH Post-Boussinesq Modeling of Nonlinear Wave Propagation and Transformation in Nearshore Zones and Inside Ports. Paper presented at the Coastal Structures Conference 2019, Hannover, Germany, 30/09-02/10/2019, p. 742-751

Karambas TV (1999) A unified model for periodic non linear dispersive wave in intermediate and shallow water. J Coast Res, 15(1):128-139.

Karambas TV, Koutitas C (1992) A breaking wave propagation model based on the Boussinesq equations. Coast Eng, 18(1-2):1-19.

Karambas TV, Koutitas C (2002) Surf and swash zone morphology evolution induced by nonlinear waves. J Wtrway Port Coast Ocean Eng, 128(3):102-113.

Larsen J, Dancy H (1983) Open boundaries in short wave simulations – a new approach. Coast Eng, 7:285-297.

Lee C, Suh KD (1998) Internal generation of waves for time-dependent mild-slope equations. Coast Eng, 34:35-57.

Li YS, Liu SX, Yu YX, Lai GZ (2000) Numerical modeling of multi-directional irregular waves through breakwaters. Appl Math Mod, 24(8-9):551-574.

Makris C, Androulidakis Y, Karambas T, Papadimitriou A, Metallinos A, Kontos Y, Baltikas V, Chondros M, Krestenitis Y, Tsoukala V, Memos C (2021) Integrated modelling of sea-state forecasts for safe navigation and operational management in ports: Application in the Mediterranean Sea. Appl Math Mod, 89(2): 1206-1234. doi:10.1016/j.apm.2020.08.015

Roeber V, Cheung KF, Kobayashi MH (2010) Shock-capturing Boussinesq-type model for nearshore wave processes. Coast Eng, 57:407–423.

Samaras AG, Karambas TV (2021) Modelling the Impact of Climate Change on Coastal Flooding: Implications for Coastal Structures Design. J Mar Sci Eng 9(9):1008. doi:10.3390/jmse9091008

Vincent CL, Briggs MJ (1989) Refraction-diffraction of irregular waves over a mound. J Wtrway Port Coast Ocean Eng, 115:269–284.

Yu Y-X, Liu S-X, Li YS, Wai WH (2000) Refraction and diffraction of random waves through breakwater. Ocean Eng, 27(5):489-509. doi:10.1016/S0029-8018(99)00005-0

DMPCO 2023

e-Proceedings of the 2nd International Scientific Conference on Design and Management of Port Coastal and Offshore Works Thessaloniki, Greece, May 24-27 2023

Assessing the wind wave climate at several scales in the offshore and coastal zones

K. Mosiou[1*], I. G. Mamoutos[1], V. Zervakis[1], E. Tragou[1], E. Krasakopoulou[1]

[1]Department of Marine Sciences, University of the Aegean, Mytilene, Lesvos Island, Greece
[*]Corresponding author: mard20012@marine.aegean.gr

Abstract

The results of SWAN model wave simulations performed on several model domains with varying spatial resolutions are compared with available *in-situ* data from buoys, satellites and an acoustic Doppler profiler (AWAC). Six model configurations have been used, ranging from a coarse offshore model covering the North/Central Aegean Sea at a spatial resolution of 3 km, to three coastal gulfs models, with the highest resolution (74 m) at the Gera Gulf model. The comparison demonstrates that SWAN works quite well both in the open sea and on coastal areas. In particular, the deviations between simulated (SWAN) and observed (POSEIDON system buoys' data) are very small, given the wind field (ERA5) used for the production of the former. The same applies to the domains of Lesvos and Lemnos islands, however for these simulations high-resolution wind data (compared to ERA5) were used. Regarding the three gulf models, only results for Kalloni gulf have been compared with AWAC measurements during spring-summer 2022. The results suggest that while the model reproduces to some extent the variability of H_s, there is a deviation in its range, which in our opinion should be attributed to the coarse resolution of the wind field used in comparison to the spatial resolution of the computational grid of Kalloni gulf.

Keywords Wave modelling, North Aegean Sea, Downscaling, Coastal waves.

1 INTRODUCTION

Sea state climate is an essential element of a plethora of studies, from engineering to oceanographic. As societies are moving towards more sustainable energy solutions, the estimation of wave energy available for exploitation depends, among others, on the knowledge of the wave potential at the area of interest. The future state of beach fronts regarding erosion and/or deposition of sediment, as well as the design of beach protection, require knowledge of the wave regime. Furthermore, sea state prediction is essential to any type of maritime transport, from touristic to trade and technical/operational (e.g., offshore mineral industry). Additionally, from an oceanographic scope, wave breaking contributes to air-sea interaction and fluxes. While several works have been published regarding studies of wave climate and forecasting in the Aegean Sea (Soukissian et al., 2002, 2008; Korres et al., 2011; Zacharioudaki et al., 2015; Ravdas et al., 2018), mostly dealing with deep-water waves, up until now there have been no high-resolution wave simulations focused in the coastal regions of Lesvos and Lemnos islands of the North Aegean, as well as their gulfs Gera, Kalloni and Moudros, requiring shallow-water wave propagation.

Hereby, we present the results of SWAN wave model simulations compared with three moorings of the POSEIDON system (Ntoumas et al., 2022) in the Aegean Sea, as well as Lesvos and Lemnos islands, and Gera, Kalloni and Moudros gulfs for the period of 2021-September 2022. Compared to previous studies with application to different coastal regions of the North Aegean, e.g., Anastasiou and Sylaios (2013) wave simulations of Thassos island, we have used SWAN model in non-stationary mode as a base for an operational system for the study area including wave and ocean components, which will be fully coupled at the near future.

2 MATERIALS AND METHODS

The simulations of wave conditions for the actual study comprise a) a coarse (3 km resolution) grid extending over the Greek Seas (both Aegean and Ionian) – Level 1, b) two high resolution grids of Lesvos (480 m) and Lemnos (220 m) islands – Level 2, and c) three ultra-high-resolution grids of Gera (74 m), Kalloni (120 m) and Moudros (100 m) Gulfs – Level 3 – all of which are orthogonal curvilinear. In essence the above sequence is a form of down-scaling using an offline nesting procedure in order to improve the wave dynamics simulation especially in the most challenging coastal areas in terms of

geographical extent. SWAN (version 41.31) is a third-generation phase-averaged wave model developed by Delft University of Technology (Booij et al., 1999) which is extensively used primarily for nearshore simulations. The configuration of all of our numerical simulations included a first order upwind scheme (BSBT) for the discretization in geographical space, JONSWAP boundary and initial conditions, exponential growth by wind based on a quasi-linear wind-wave theory (Janssen et al., 1989, 1991), quadruplet interactions, whitecapping, depth-induced breaking, bottom friction with coefficient by Collins (1972) and triad wave-wave interactions. This setup includes 36 number of directions and 25 number of frequencies.

The grids of Greek Seas and Lemnos have been created with GEBCO bathymetry (https://www.gebco.net/), Lesvos with GEBCO and a digitized map of the Hellenic Navy Hydrographic Service (https://www.hnhs.gr/en/) (HNHS), Kalloni with a digitized map of the HNHS, Gera bathymetry has a combination of digitized HNHS map and data collected by Manoutsoglou et al. (2018) and last, Moudros bathymetry is a digitized Navionics map (www.navionics.com). Boundary conditions for the coarse grid of the Greek Seas were selected/extracted from the Copernicus Marine Service Mediterranean Monitoring Forecasting Center (CMEMS MED-MFC) wave realanysis (https://marine.copernicus.eu/) (Ravdas et al., 2018), default initial conditions for the first run of the simulation period which are calculated from local wind velocities using the deep-water growth curve of Kahma and Calkoen (1992) and JONSWAP spectral shape, and the wind forcing from the European Centre for Medium-Range Weather Forecasts (ECMWF) ERA5 (https://climate.copernicus.eu/) (Hersbach et al., 2020).

The above run provided boundary conditions in the form of two-dimensional spectra for the downscaled simulations of Lesvos and Lemnos, which are forced by wind stress originating from a version of SKIRON data down-scaled to 4-km resolution (https://openskiron.org/en/openwrf) (Kallos et al., 1997). The resulting data were validated against *in-situ* buoy data from the POSEIDON system at Athos, Mykonos, and E1-M3A (WMO 61277) (https://poseidon.hcmr.gr/) Table 1), L3 satellite observations of ALTIKA and CFO from Copernicus Marine Service (CMEM) and Nortek's 600 kHz Acoustic Wave and Current Profiler (AWAC) recordings in Kalloni gulf. The AWAC was deployed at the 10-m deep seabed facing upwards in the vicinity of an oceanographic buoy in Kalloni gulf on 24/05/2022 and was retrieved on 8/06/2022, providing wave and current data, at hourly bursts of 1024 samples at 1 Hz sampling frequency. Lesvos and Lemnos SWAN data were interpolated temporally and spatially in order to co-locate satellite data for the validation.

Table 2. Location of POSEIDON buoys used for validation

Buoy	Longitude	Latitude
Athos	24º 43' 45,8394" E	39º 58' 30" N
Mykonos	25º 27' 34,92" E	37º 31' 9,8394" N
E1-M3A (WMO 61277)	25º 7' 50,52" E	35º 43' 34,68" N

3 RESULTS

The validation of significant wave height (H_s) and zero-crossing period (Tm_{02}) of Level 1 simulations are shown in Figure 1. The results suggest that SWAN can produce accurate results for open sea conditions, based on the statistics. In general terms, Athos and Mykonos display similar statistics for H_s (although Mykonos' buoy data availability was until the end of 2021). Regarding Level 2 and Level 3 runs, the results are shown in Figure 2. Figure 2a and Figure 2b demonstrate the comparison of Lesvos and Lemnos H_s with two of the available satellites from CMEMS, Altika and CFO respectively. Although track data are sparse in the case of Lemnos (Figure 2b), the validation shows that the wave regime can be reproduced qualitatively for these coastal scales. In the case of Moudros and Gera gulf, Figure 2c and Figure 2d represent the mean values of H_s for the duration of the simulations. The last plot of Kalloni gulf (Figure 2e) is the comparison of simulated H_s against AWAC measurements that took place during the summer of 2022. Although there is medium correlation between the simulated data and the recordings, RMSE and bias remain relatively low.

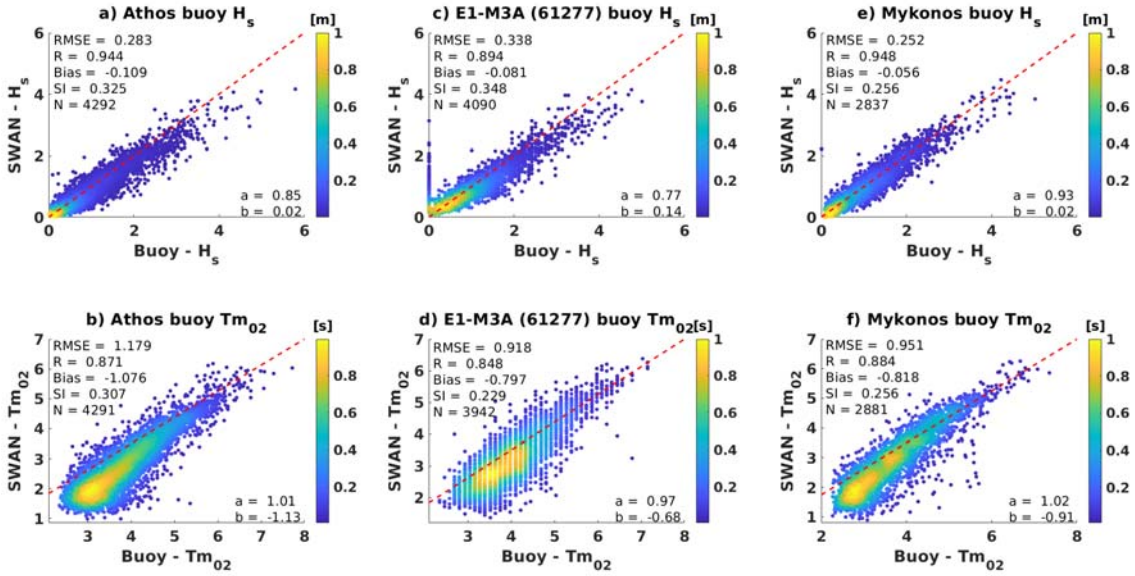

Figure 1. Scatter plots of H_s and Tm_{02} for the three POSEIDON system buoy locations: **(a)** Athos H_s, **(b)** Athos Tm_{02}, **(c)** E1-M3A (WMO 61277) H_s, **(d)** E1-M3A (WMO 61277) Tm_{02}, **(e)** Mykonos H_s and **(f)** Mykonos Tm_{02}.

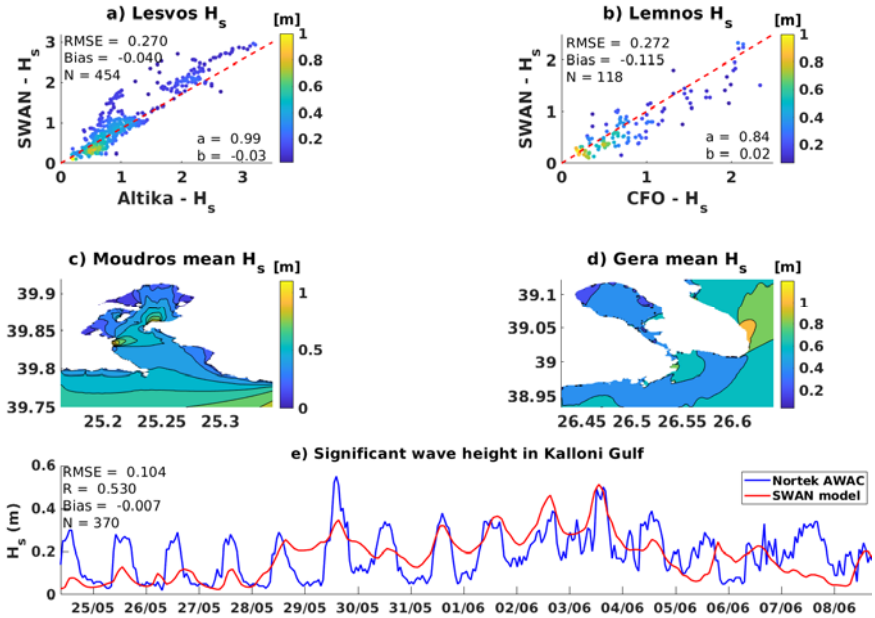

Figure 2. Validation and representation of H_s for Lesvos, Lemnos, Gera, Kalloni and Moudros: **(a)** H_s scatter plot of Lesvos SWAN against Altika satellite, **(b)** H_s scatter plot of Lemnos SWAN against CFO satellite, **(c)** Mean H_s of Moudros, **(d)** Mean H_s of Gera and **(e)** comparison between Kalloni H_s SWAN and AWAC measurements.

4 DISCUSSION

All in all, this modeling effort for the simulation of wave conditions in coastal areas of the North Aegean is a first attempt. It is demonstrated that the main open sea models like WAM (WAMDI Group, 1988) and WAVEWATCH-III (Tolman, 1997) can reproduce the wave field with high accuracy for the open sea, and this is exactly the reason behind their extensive operational use for wave forecasts (together with data assimilation). Based on the results that were shown in this document, the SWAN model can effectively simulate wave conditions in the open sea, and in finer/coastal scale. However, the accuracy of the coastal wave simulations mainly depends on the resolution (and quality) of the wind-forcing field, in addition to the quality of bathymetry and boundary/initial conditions. In the case of this study, the wind field's resolution was quite coarse for the extend of the gulf grids for the coastal runs.

Acknowledgments

This study is funded by the project "Coastal Environment Observatory and Risk Management in Island Regions AEGIS+" (MIS 5047038) implemented within the Operational Program "Competitiveness, Entrepreneurship and Innovation" (NSRF 2014-2020), co-financed by the Hellenic Government (Ministry of Development and Investments) and the European Union (European Regional Development Fund). This work was supported by computational time granted from the Greek Research and Technology Network (GRNET) in the National HPC facility, ARIS, under projects ID IMASGECOZ (pr011024). We would also like to thank Vassilis Kolovoyannis and Yannis Androulidakis for providing bathymetric data for Gera and Moudros gulf respectively.

References

Anastasiou S and Sylaios G (2013). Nearshore wave field simulation at the lee of a large island. Ocean Eng 74: 61-71

Booij N, Ris RC and Holthuijsen H (1999). A third-generation wave model for coastal regions. 1. Model description and validation. J Geophys Res 104 (C4): 7649-7666

Collins JL (1972). Prediction of shallow-water spectra. J Geophys Res 77 (15): 2693-2707

GEBCO Bathymetric Compilation Group 2020. The GEBCO_2020 Grid - a continuous terrain model of the global oceans and land. doi:10.5285/a29c5465-b138-234d-e053-6c86abc040b9

Hersbach H, Bell B, Berrisford P et al. (2020): The ERA5 global reanalysis. Q J R Meteorol Soc 146: 1999-2049

Janssen PAEM (1989). Wave induced Stress and the Drag of Air Flow over Sea Waves. Am Meteorol Soc 19: 745-754

Janssen PAEM (1991). Quasi-linear theory of wind-wave generation applied to wave forecasting. J Phys Oceanogr 21:1631-1642

Kahma KK and Calkoen CJ (1992). Reconciling Discrepancies in the Observed Growth of Wind-generated Waves. J Phys Oceanogr 22 (12): 1389-1405

Kallos G, Nickovic S, Papadopoulos A, Jovic D, Kakaliagou O, Misirlis N, Boukas L, Mimikou N, Sakellaridis G, Papageorgiou J, Anadranistakis E and Manousakis M (1997). The regional weather forecasting system SKIRON: An overview, Paper presented at the International Symposium on Regional Weather Prediction on Parallel Computer Environments, Athens, Greece, pp. 109-122.

Korres G, Papadopoulos A, Katsafados P, Ballas D, Perivoliotis L and Nittis K (2011). A 2-year intercomparison of the WAM-Cycle4 and the WAVEWATCH-III wave models implemented within the Mediterranean Sea. Med Mar Sci 12 (1): 129-152

Manoutsoglou E, Hasiotis T, Kyriakoudi D, Velegrakis A and Lowag J (2018). Puzzling micro-relief (mounds) of a soft-bottomed, semi-enclosed shallow marine environment. Geo-Mar Lett 38:359-370

Ntoumas M, Perivoliotis L, Petihakis G, Korres G, Frangoulis C, Ballas D, Pagonis P, Sotiropoulou M, Pettas M, Bourma E, Christodoulaki S, Kassis D, Zisis N, Michelinakis S, Denaxa D, Moira A, Mavroudi A, Anastasopoulou G, Papapostolou A, Oikonomou C, Stamataki N (2022): The POSEIDON Ocean Observing System: Technological Development and Challenges, J Mar Sci Eng 10 (12): 1932

Ravdas M, Zacharioudaki A and Korres G (2018): Implementation and validation of a new operational wave forecasting system of the Mediterranean Monitoring and Forecasting Center in the framework of the Copernicus Marine Environment Monitoring Service, Nat Haz Earth Sys Sci 18: 2675-2695

Soukissian TH, Prospathopoulos AM, and Diamanti C (2002). Wind and Wave Data analysis for the Aegean Sea – Preliminary Results. J Atmos Ocean Sci 8 **(**2-3):163-189

Soukissian T, Prospathopoulos A, Korres G, Papadopoulos A, Hatzinaki M and Kambouridou M (2008). A New Wind and Wave Atlas of the Hellenic Seas, Proceedings of the ASME 27th International Conference on Offshore Mechanics and Arctic Engineering, OMAE 2008, Portugal

Tolman L (1997). User manual and system documentation of WAVEWATCH-III version 1.15. NOAA/NWS/NCEP OMB Technical Note 151, pp 97

WAMDI Group (1988). The WAM Model – A Third Generation Ocean Wave Prediction Model. Am Meteorol Soc 18: 1775-1810

Zacharioudaki A, Korres G and Perivoliotis L (2015). Wave climate of the Hellenic Seas obtained from a wave hindcast for the period 1960-2001. Ocean Dyn 65: 795-816

Modeling-based results for waves propagations in the case of climate change adaptation measures assortment with specific reference to the Maritime Port of Constanta

R. Mateescu[1*], L. Rusu[2]

[1] National Institute for Marine Research and Development "Grigore Antipa", Constanta, 900581 Constanta, Romania
[2] Department of Mechanical Engineering, Faculty of Engineering, "Dunarea de Jos" University of Galati, 800008 Galati, Romania
[*]Corresponding author: razvan_doru@yahoo.com

Abstract

The occurrence and intensification in recent years of the extreme meteorological phenomena related to climate change, with strong impact on the marine ports, require a proper risks assessment in case of the ports' structures and port operations design. Considering the new expansions of the Constanta Maritime Port and its layout specificity, the risk categories specific to port infrastructure development projects were evaluated in relation to their exposure to the adverse effects of the wave propagations' climate in the port basins and its adjacent areas. In this regard, specific data of marine hydrologic regime were modeled in relation with the harbor location conditions, with medium to high sensitivity. The evaluation of the future exposure in several interest areas induced by port configuration and new occurrence of waves parameters were determine for a time horizon of 10, 50 and respectively, 100 years. In the present work, certain aspects of the numerical modeling results regarding the waves propagation in the port basins, were emphasized in order to identify specific adaptation measures, with an accent on structural and non-structural measures, but also on risk management in ensuring the sustainability of the investments for the modernization of docking conditions in specific areas of Constanta south maritime Port. Boussinesq-type wave models were considered proper for the study of the wave's propagation in the Constanta Port basins, in relation with several potential solutions against waves propagation processes in harbor waters, allowing several subsequent developments in the field of wave energy absorption systems and safe port docking conditions.

Keywords Western Black Sea maritime ports, Waves propagation, Boussinesq-type wave modelling, Docking conditions.

1 INTRODUCTION

Over the last decades the marine hydrological data collections were developed with the aim of an appropriate design of the Constanta Port. Extensions. Currently, due to the recent extension of the northern port jetty, Constanta Port offers new and different conditions for future developments.

Currently, the Port of Constanta has a total area of 3,926 hectares with an annual operating capacity of approximately 120 million tons, being served by 156 berths, 140 being operational. The total length of the quays is 29.83 km. The port is structured in two main areas: Constanta North area which includes 12 basins with 7-14m depth, 15.5 kilometers of quay and 82 operational berths. Constanta South area is partially operational and includes 14.6 kilometers of quay, 74 operational berths with different functionalities, providing complementarities and connections to the other ports. The port depths in the berths area vary between 7 and 19 m, in the anchorage area between 25m and 30m, allowing a safety anchorage for 40 - 50 large ships, in different situation of wind and currents variability.

The entrance channel of the Constanta Port has a length of 6.4 nm, a width of 0.8 nm, a depth of 21 m, on NW direction. The exact direction is 322 degrees and allows the safe navigation of ships in one direction. The internal channel has different sections and an average depth of 19 m. This channel is positioned parallel to the north breakwater which has a length of 8.34 km. The exit corridor has the general direction to SE, (142°) (figure 1).

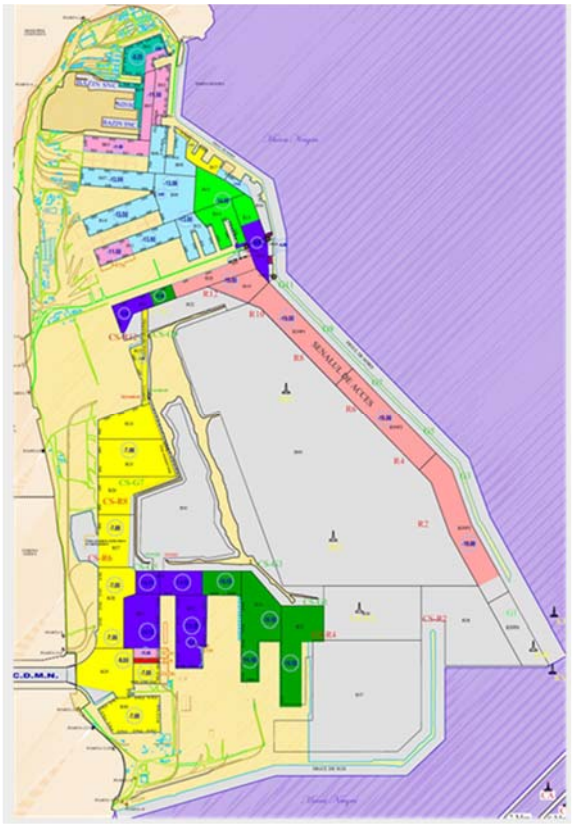

Figure 1. The internal channels (intense colored) of Constanta Port
(Source: Constanta Port Master Plan, Contract no: 4122, from 03.02.2014)

1.1 Recent developments

The specific port hydrotechnical constructions were made in the recent years in order to facilitate the navigation maneuvers in the Southern area of Constanta Port, which seems to be a limiting factor because the only suitable area for maneuvers of large ships (over 300 m long) is located at the port entrance. On the other hand, the regular mooring maneuvers are very difficult and require a towboat, thus due the naval accidents from the recent past, some navigation restrictions were extended. The port extension at different stages of the northern jetty can be visualized in images available on Google Earth.

1.2 Scope of paper

Applications of the Boussinesq type numerical models involves dispersive and nonlinear irregular waves over certain finite water depths. For Constanta Port a similar application of such model was extended in order to quantify the safe navigation requirements and to indicate possible environmental impacts (based on the specific simulations), in terms of sea level changes, waves and currents patterns inside the port area. The waves that propagate in a port basin change their direction due to the refraction, reflection and diffraction phenomena caused by the complex configuration of the basin, the quays characteristics, the breakwaters that border the entire port basin and the bathymetric characteristics of the basins, including the positioning and processes afferent to the access channels. Such case study of model application over realistic conditions of the Constanta port is presented and validated by observations.

2 MATERIAL AND METHODS

The present work was carried out using multiannual data from authorized sources, applying statistical analysis methods and specific modeling programs in accordance to the study purpose. The geometric model was built on the current configuration of Constanta Port, considering the port entrance, dams and the shape of the functional moles. The numerical modeling takes into consideration the type of hydro-technical constructions from the area, respectively vertical/sloping quays/dikes in the area of new berths design. The wave propagation modeling

considered the port bathymetry in the area of interest, updated with in-situ bathymetric measurements and by digitization of bathymetric maps.
The initialization data for hydrodynamic model integrates probability data for the synergic action of wind, waves, and currents. The combined effect of wind and waves were considered in order to set-up and calibrate the propagation models, using in-situ measurement sessions to selected model parameters, realistically combined in specific applications for numerical modeling within ports areas with hydrodynamic intensifications of wave propagation and transformation, at local scale.
The model BOUSS-2D, based on a time solution for Boussinesq equations was suitable numerical model, for simulating the wave's propagation and transformation in Constanta Port, in specific Running Steps integrated into the graphical user interface (GUI) of the SMS model. The geometric model and computational grid were applied considering the bathymetry data provided by the Port Administration and the European Emodnet Bathymetry service, the shoreline data was digitized and georeferenced according to Spot5 background satellite images. Thus, geometric model was built by coupling all the mentioned data sets, in UTM35N projection.
The boundary conditions were setup for the model grid as damping/porosity areas, in relation with properties of the port's structures, quays or vertical structures and trapezoidal-shape breakwaters of port. The model Bouss2D was set-up for a real seabed, within a model domain of 6300m x 10600m consisting of 630 × 1,060 cells with constant cell size of 10 m × 10 m, origin point (633600, 4880800) and 37-degree azimuth.

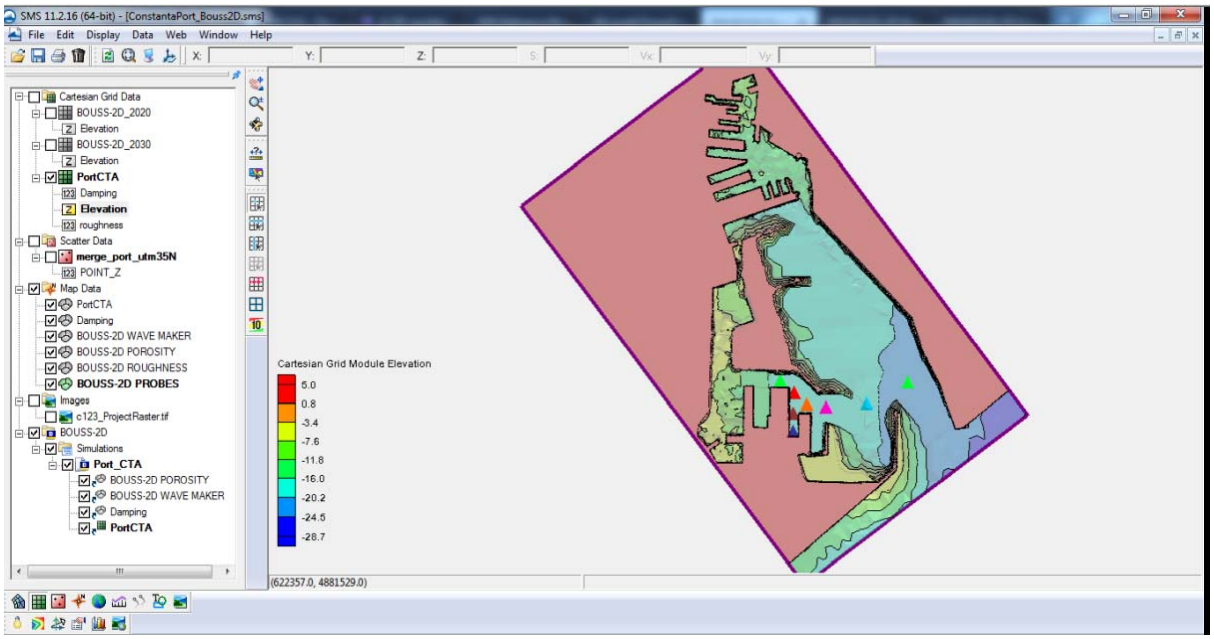

Figure 2. Positioning of test points in the access area of Constanta South Port and also in front of the maneuvering / access channel for southern berths (green triangles)

The analysis and modeling-based results of about 11-years of wave fields occurrence for the western Black Sea basin was grounded on ECMWF data (provided in front of Constanta Port: 29°E, 44°N), which became input to the BOUSS2D model application in place of the new developments of the South Constanta Port Terminal. The wave propagation model results with existing and new port extensions were linked with the Earth Observation/EO data and short range/aerial observations of the wave fields, demonstrating a good comparison of both encompassed data in the validation process of the model. As a main result, wave conditions in the new harbor facilities of Constanta South Port were assessed for suitable extension dimensioning of berths design, for the expected wave regime in the waterfront areas. The hydraulic calculation coefficients in the area of interest were selected to fulfill the long-term design criteria, respectively, for recurrence periods of 100 years (using method POT/ Pick Over Threshold).

Thus, for the calculation of waves propagations, uni and multi-directional non-stationary wave propagation regime was selected, having the JONSWAP peak enhancement parameters, for a significant

height of 5.78 meters and a peak period of 12.5 seconds, having an average direction of 155-degrees compared to the north direction, without wind forcing included in the simulations.

2 RESULTS AND DISCUSSIONS

The results obtained in BOUSS2D model application reveal the wave field propagation at 100-year recurrence intervals presents certain modification in the area of the maneuvering basin/access corridor to Danube - Black Sea Channel at termination of the Constanta South Port, as well as the wave's intensification in the proximity of vertical quays in the area Constanta-South Port, due to the existence of large areas recently dredged, has the advantage of damping waves caught in the southern basin.

Thus, the typical model results in realistic case of Constanta-South Port bathymetry and hydraulic setup (Chezy roughness coefficients for different model coverings, control time with specification of the running time and the time step, as well as the desired output data type: sea surface height, speed wave propagation) were presented in specific plotted result (fig.3) of simulated fields of gridded data (dx and dy = 10 m) for free surface elevations.

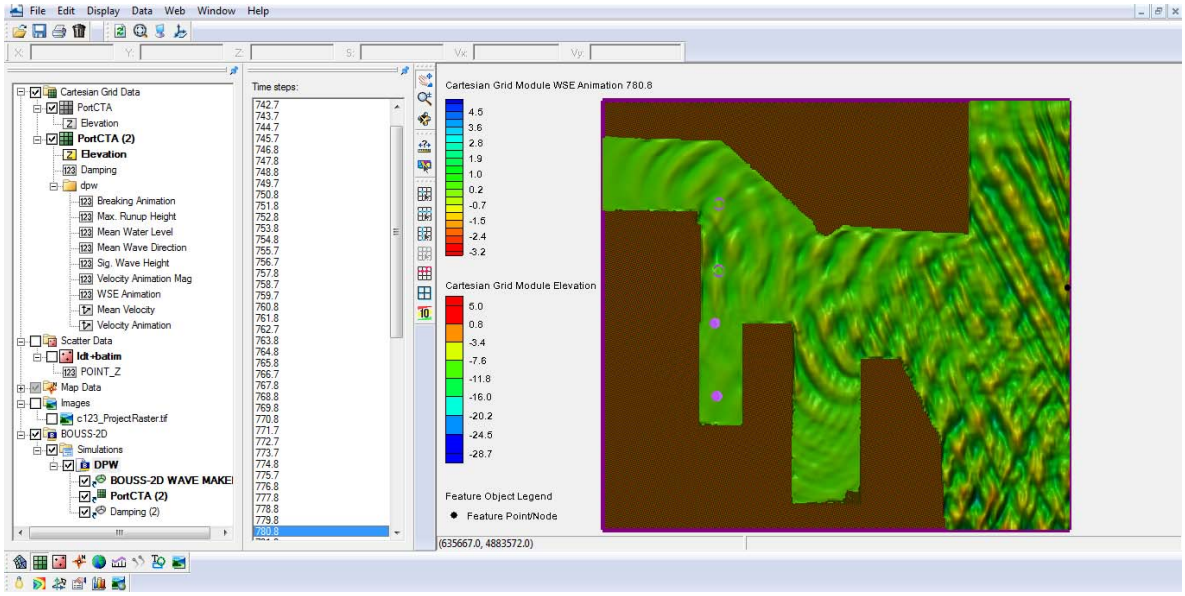

Figure 3. Waves propagation in area of the Constanta-South Port

The model results for the stations related to passage channel of Constanta South Port (fig. 4a), are moderately validated by EO data (Google Earth/time horizon: - June 2022 observation, about 0.9m propagated wave- fig.4.b)

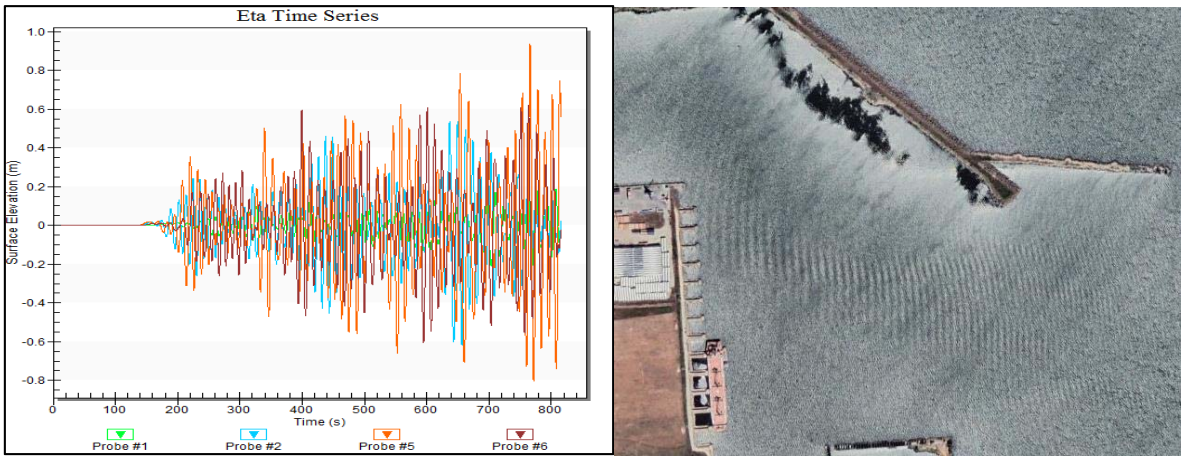

Figure 4. Free surface variation shows a maximum variation -0.8 ÷ 0.93m (respectively H_{max} = 1.73m)

4 CONCLUSIONS

In the present work a Boussinesq nonlinear dispersive wave propagation model was successfully applied for wave propagation over realistic breakwaters topographies and bathymetry setups of Constanta Port, being capable to simulate the waves' propagation in the specific case of the northern jetty extension and a direct incidence of waves from ESE-SE-S, causing a certain the wave regime intensifications inside the basin, due to the diffraction and refraction processes at the port entrance.

Regarding the evaluation of the berthing conditions, evaluations of the wind, wave and current conditions were carried out in predictable scenarios, the significant wave's height can increase by 20-40% and 60% in cases of extreme storms, due to the captive, resonant waves, as well as the sea level raise in the port in the storm situation.

The implemented model application can estimate the significant/main parameters of the waves propagated in the harbor, including significant heights and peak periods, for short return periods of 1-2 years and long calculated periods of 50-100 years. Significant parameters of waves calculated on the BOUSS2D model can range values of 0.4 - 1.73m, with variable directions described by local patterns in connection with the presence of the existing obstacles/hydrotechnical constructions in the port basin.

Despite waves and currents in-situ available data for model validation, several EO/satellite imagery and aerial/UAV observations were allowed to evaluate that the directional dispersion of the waves penetrating the basin is significantly influenced by the island existent as inner obstacle of the port. This is especially important in the cases where the induced currents meet wave from opposite directions, which can change direction up to 20° (observable from above/EO data).

For future studies the wind-induced surface currents may be responsible for changing the wave's characteristics along the transport corridors in the Constanta-South Port, in which case it is recommended to find certain solutions to further attenuate the captive waves, respectively to maintain the dissipative effect of the propagated waves and the waves developed in the current field in the opposite direction to propagation, in order to obtain safe sheltering and operating conditions in the modified context of new climate change, often with extreme atypical evolutions.

Acknowledgements

This work was carried out in the framework of the research project CLIMEWAR (CLimate change IMpact Evaluation on future WAve conditions at Regional scale for the Black and Mediterranean seas marine system), supported by a grant of the Ministry of Research, Innovation and Digitization, CNCS - UEFISCDI, project number PN-III-P4-PCE-2021-0015, within PNCDI III.

References

Bandoc G., Mateescu R., Dragomir E., Golumbeanu M., Comanescu L., Nedelea A. (2014), Systemic Approach of the Impact Induced by Climate Changes on Hydrothermic Factors at the Romanian Black Sea Coast, Journal of Environmental Protection and Ecology 15, No 2, 455–467.

Coastal Engineering Manual Part II, US Army Corps of Engineers, 2015.

Ernst & Yang SRL INROS LAKNER SE, „Master Plan Portul Constanța Versiune Finală," 2015.

Karambas, T., Memos, C., 2009. Boussinesq model for weakly nonlinear fully dispersive water waves, Journal of Waterway, Port, Coastal and Ocean Engineering, ASCE, 135, 187–199.

Niculescu D., Vlasceanu E., Ivan A., Buzbuchi și Omer I., (2017) Coastal works post-construction effectiveness validation in Eforie Bay area", Paper presenteed at International Multidisciplinary Scientific GeoConference, Albena, Bulgaria.

Rusu, E., Conley, D.C. and Coelho, E.F., (2008) A Hybrid Framework for Predicting Waves and Longshore Currents, Journal of Marine Systems, 69, 59–73.

Rusu, E Soasres G. (2011) Wave modelling at the entrance of ports, Ocean Engineering, Volume 38, Issues 17–18.

Vasceanu E., Mateescu R., Rusu, E. (2021): Waves penetratıon ınsıde the port acvatorıes associated wıth the extreme storm regime on the Romanıan coast, SGEM Proceedings

Schäffer, H.A., Madsen, P.A., Deigaard, R., 1993. A Boussinesq model for waves breaking in Engineering, 20, 185-202.

Shore Protection Manual, Volumul 1, Washington DC 20314: Department of the Army, Waterways Experiment Station, Corps of Engineers, Coastal Engineering Research Center, 1984.

DMPCO 2023

e-Proceedings of the 2nd International Scientific Conference on Design and Management of Port Coastal and Offshore Works Thessaloniki, Greece, May 24-27 2023

Interaction of gravity currents with internal waves in a linearly stratified ambient

A. Kokkinos[1*], P. Prinos[1]

[1]Hydraulics Laboratory, Department of Civil Engineering, Aristotle University of Thessaloniki, Thessaloniki, 54124, Greece

[*]Corresponding author: angeloks@civil.auth.gr

Abstract

This work presents LES results on the interaction of a partial-depth lock-release propagating gravity current (GC) with internal waves (IWs) in a linearly stratified ambient. Stratification in an ambient fluid can be found in geophysical environments such as the pycnocline in estuaries and oceans. In such environments the GC propagation generates IWs. The dynamics of the propagation depend on the Froude number and are different for subcritical GC (Fr < 1/π) and supercritical GC (Fr > 1/π). The Froude number is defined as Fr = U_f / NH where N is the buoyancy frequency of the ambient fluid, H is the tank depth and U_f is the current front velocity. The study investigates the effect of ambient stratification strength on GC motion and IW generation. Stratification is determined through the parameter S = (ρ_b – ρ_0) / (ρ_c -ρ_0) which varies from 0 up to 1 (ρ_b, ρ_0 and ρ_c are the density at the bottom of the ambient, at the top of the tank and of the heavy fluid in the lock respectively). When the GC is subcritical linear mode one IWs are generated in the ambient, propagating downstream of the current. Upstream the IWs are more complex due to their interaction with the tank wall. The supercritical GCs do not generate IWs in the ambient fluid. Both sub- and supercritical GCs have a constant-velocity phase. This phase terminates due to the interaction of GCs with the internal waves (IWs) for the former, while it is due to the decay of the head buoyancy for the latter.

Keywords Gravity currents, Stratification, Internal Waves, Large-Eddy Simulation

1 INTRODUCTION

Gravity currents (GCs) are buoyancy-driven flows in which hydrostatic pressure gradients produce a primarily horizontal motion. There are many circumstances in coastal environment where GCs propagate in a stable stratified ambient. This propagation generates internal waves (IWs) in the ambient fluid, like the offshore river plume fronts which propagate as GCs generating IWs (Nash & Moum, 2005) or the onshore GCs that can be created from tidal bores (Haney et al., 2021). GC propagation in a stratified environment depends on more parameters than that in a uniform environment. The buoyancy frequency is defined as $N = \sqrt{-(g/\rho_0)\,d\rho/dz}$ and is constant for linear stratification. The relative strength of the current and the ambient stratification is defined with the parameter $S = (\rho_b - \rho_0)/(\rho_c - \rho_0)$. GC propagation at the base of a stratified ambient is the special case of the intrusive GCs (Flynn & Sutherland, 2004) in a stratified fluid for which S varies from 0 (weak stratification) up to 1 (strong stratification). The Froude number is defined as $Fr = U_f / NH$, where NH / π is the long wave (mode one) velocity. The dynamics of propagation are different for subcritical (Fr < 1/π) and supercritical (Fr > 1/π) GCs. Maxworthy et al. (2002) found that both the sub- and supercritical GCs have a constant-velocity phase which is followed by a deceleration one. To date, the research on the dynamics of GCs in stratified environment has been focused on the constant-velocity phase (Dai et al., 2021; Maxworthy et al., 2002). This study investigates the effect of stratification strength on GC velocity for both the constant-velocity and deceleration phases. LES results of propagating GCs at the base of a linearly stratified environment are presented. The focus is on the investigation of the interaction between the GCs and the emerging IWs.

2 SETUP AND NUMERICAL MODEL

Numerical experiments are conducted in a lock-exchange configuration composed of a lock of dense fluid (ρ_c) at the left corner of a horizontal tank. The rest of the domain is covered by a linearly stratified

fluid with density ρ_b at the bottom and ρ_0 at the top. Half-depth configuration is used, while the Reynolds number is always equal to $2 \cdot 10^4$ (inviscid GCs). The size of the tank is L × H × W, where L = 24D, H = 2D, W = D, and D is the lock height. The width of the lock is L_0 = D. Numerical experiments are carried out for 0 < S < 1.

The numerical model solves the three-dimensional filtered incompressible Navier-Stokes equations (Eqs. 1a and 1b). Boussinesq GCs are considered, the density is related to concentration (C) according to $\rho / \rho_0 = 1 + \beta C$, where β is the volumetric expansion coefficient, and an extra transport equation for the concentration (Eq. 1c) is used. The unresolved scales of motion are considered using a dynamic Smagorinsky SGS model.

$$\frac{\partial u_i}{\partial x_i} = 0 \tag{1a}$$

$$\frac{\partial u_i}{\partial t} + \frac{\partial u_i u_j}{\partial x_j} = -\frac{1}{\rho_0}\frac{\partial p_*}{\partial x_i} + \frac{\partial}{\partial x_j}\left[\left(\nu + \nu_{SGS}\right)\left(\frac{\partial u_i}{\partial x_j} + \frac{\partial u_j}{\partial x_i}\right)\right] - g_j x_j \frac{\partial}{\partial x_i}\left(\frac{\rho}{\rho_0}\right) \tag{1b}$$

$$\frac{\partial C}{\partial t} + \frac{\partial u_j C}{\partial x_j} = \frac{\partial}{\partial x_j}\left[\left(\Gamma + \Gamma_{SGS}\right)\frac{\partial C}{\partial x_j}\right] \tag{1c}$$

u_i is the filtered velocity in the i direction, $p_* = p - \rho g_i x_i$ is the static pressure minus the hydrostatic part, and Γ (= ν / Sc) is the molecular diffusivity where Schmidt number (Sc) is equal to 1. A dynamic Smagorinsky SGS model is used to model the smallest less anisotropic scales of motion. These scales are considered through the SGS fluxes where SGS viscosity is $\nu_{SGS} = C_s \Delta^2 \left|S_{ij}\right|$ and SGS diffusivity is $\Gamma_{SGS} = \nu_{SGS} / Sc_t$, where Sc_t = 0.85. The smallest resolved length scale is Δ (= $V^{1/3}$), where V is the volume cell and $\left|S_{ij}\right| = \sqrt{2 S_{ij} S_{ij}}$, where S_{ij} is the deformation tensor. The simulations are performed with a FVM code using the open source OpenFOAM library. 2nd order discretization schemes are used for both the time and space. For the divergence term of the concentration equation a TVD scheme is used to keep C bounded at [0,1]. The numerical space is discretized using a uniform mesh of 0.01D, except near the bottom boundary where the mesh in the vertical direction is finer towards the wall for resolving the boundary layer ($y^+ \leq 1$) and for y > D, where the motion is weak, and the mesh is coarser starting from 0.01D up to 0.1D. The total cell number is 2400 × 129 × 100. Adjustable time-step is used to maintain the CFL number below 0.15. No slip condition is considered for the bottom wall, a periodic condition is considered in the spanwise direction to avoid the influence of the lateral walls, and slip condition is used for all the other walls.

3 RESULTS

Figure 1 shows two GCs of different S when their front displacement is at x_f / D = 7.5. The concentration field for C > S is shown where the isopleth C = S denotes the interface between the GC and the ambient fluid.

Above the current the vertical velocity (v / u_b) is also shown along with the velocity vectors. Figure 1a shows the formation of vortices in the ambient. The rotation of the vortices is anticlockwise and clockwise sequentially along the tank. This is due to the presence of IWs which, at the given moment, have overpassed the GC downstream. The circular motion of the ambient indicates that the horizontal velocity of the fluid elements is in 90° phase with the vertical one. In addition, above and downstream of the current head one vortex develops along the vertical direction. The latter two observations indicate that the developed IWs can be described as linear mode one IWs. On the contrary, Figure 1b shows that, for S = 0.2, the evolved motion in the ambient is restricted in the area above the current head with no wave propagation neither upstream nor downstream.

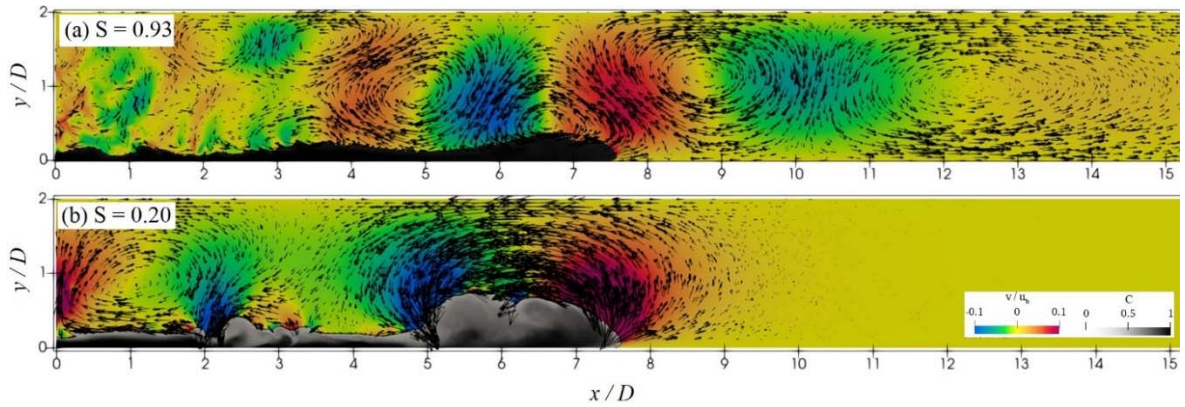

Figure 1 Vertical velocity field, velocity vectors and concentration field for C > S

Figure 2 shows v / u_b along three horizontal lines when $x_f / D = 7.5$ as in Figure 1. Figure 2a confirms the presence of IWs and shows that they have spread vertically throughout the tank. The IWs propagate with horizontal wavelength $\lambda_x \approx 4.3D$ downstream of the current ($x / D > 7.5$). Upstream, λ_x is smaller due to the interaction of the IWs with the left wall. Near the left wall λ_x increases with increasing y / D. Figure 2b shows that there are no IWs downstream of the GC. The same happens upstream where the variation of v / u_b is due to the head velocity of the current. This is the reason why this variation disappears for $y / D > 0.5$. It seems that strong stratification can support the generation of IWs in the ambient fluid contrary to weak stratification.

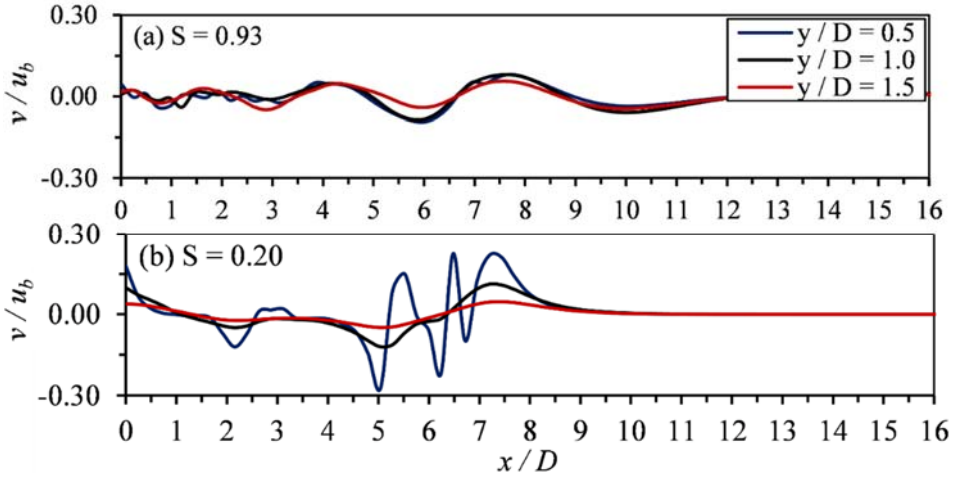

Figure 2 Variation of vertical velocity along different horizontal lines

Figure 3 shows the variation of v / u_b with y / D at five locations for $x_f / D = 7.5$ (Figure 1). For S = 0.93 the IWs downstream of the current (x / D =10 and 15) and upstream near the head ($x /D = 6$) are mode one, namely their vertical wavelength is $\lambda_y = 4D$.

Near the left wall ($x / D = 1.0$), the curve of v / u_b is more complex. For S = 0.20, v / u_b is equal to 0 downstream of the current (x / D =10 and 15). For $x / D = 6$, v / u_b is positive at the lower part of the current head and negative at the upper part due to the vortex in the ambient fluid. Near the left wall ($x / D = 1$) v / u_b is affected by another vortex which is not related with IWs generation.

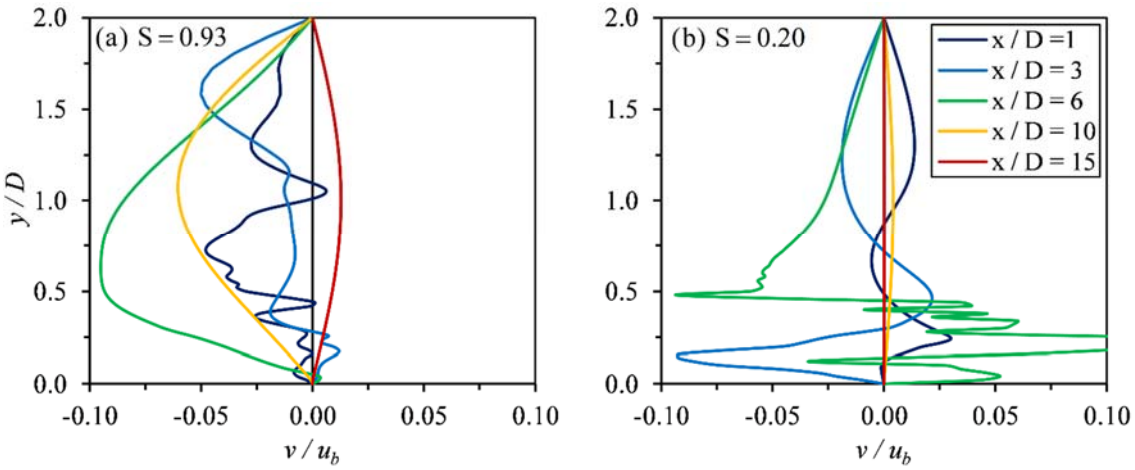

Figure 3 Variation of vertical velocity within the water depth

Figure 4 shows the variation of GC front velocity with time. From the dispersion relation of linear IWs $\omega^2 = N_0^2(k^2 / k^2 + m^2)$ where ω is the wave frequency, and assuming that the phase velocity of the IWs is equal to U_f the condition $Fr \leq 1/\pi$ for the generation of IWs is derived. The horizontal dashed lines show the value of U_f / u_b for each S and for critical GC ($Fr = 1/\pi$). A distinct velocity behavior is evident between the S = 0.93 experiment and the others. For S = 0.93 the current is subcritical and IWs are generated soon after the lock release. After the short acceleration phase there is a short period during which the current propagates with almost constant velocity. At $t / Du_b^{-1} = 11.6$ the current starts to decelerate, and its motion is affected by the interaction with the IWs thereafter. The current decelerates (or accelerates) as the anticlockwise (or the clockwise) vortices of the ambient pass above its head (periodic curve of U_f / u_b). The period during which the current has constant-velocity is the time needed for the first clockwise vortex to reach the current front.

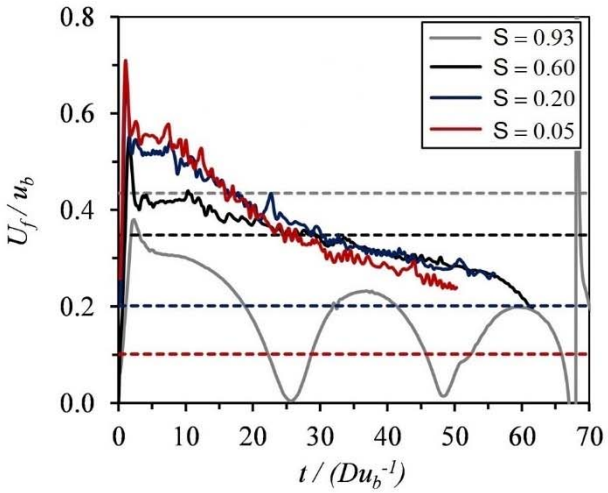

Figure 4 GC front velocity with time for various S (solid lines); the dashed lines indicate the respective critical front velocities

For weak stratification (S = 0.20 and 0.05), GCs are supercritical and there is no IWs generation in the ambient. Their motion is like the one of GCs in uniform ambient having a constant-velocity phase, after the short acceleration phase, which is followed by a deceleration one. The duration of the constant-velocity phase increases with increasing S (stronger stratification) from $t / Du_b^{-1} = 9$ up to 14 for S = 0.05 up to 0.20 respectively. The dynamics that drive the motion of the supercritical GCs are related to the way that the initial current buoyancy in the head decays as in the case of GC propagation in uniform environment.

For S = 0.60 there is a combination of the previous mechanisms. The GC is supercritical initially, propagating with no generation of IWs in the ambient. During its deceleration phase, the GC becomes subcritical and IWs are evolved. By the time the IWs outrun the current ($t / Du_b^{-1} = 30.2$), its motion is determined by the interaction with the waves as in S = 0.93.

4 CONCLUSIONS

Numerical experiments on GC propagation at the base of a linearly stratified ambient are performed for the investigation of the interaction between GCs and the generated IWs. IWs can be generated in the ambient fluid by the GC propagation depending on the strength of ambient stratification. GCs for various ambient stratification strengths are examined for a half-depth lock-exchange configuration covering both the subcritical and supercritical regimes. IWs are generated when the GC is subcritical. For the chosen setup the IWs are linear mode one with approximately equal horizontal and vertical wavelengths (~2H). Supercritical GCs do not generate IWs, and their motion is similar to the GCs propagating in uniform environment. The dynamics that drive the motion during the deceleration phase are different for the two regimes. The subcritical GCs motion is determined by the interaction with the IWs while the motion of the supercritical currents is determined by the decay of their head buoyancy.

Acknowledgements

The simulations for this work have been performed using the Aristotle University of Thessaloniki (AUTh) High Performance Computing Infrastructure and Resources.

Funding

This project is part of the first author's doctoral thesis. The implementation of the doctoral thesis is co-financed by Greece and the European Union (European Social Fund-ESF) through the Operational Programme «Human Resources Development, Education and Lifelong Learning» in the context of the Act "Enhancing Human Resources Research Potential by undertaking a Doctoral Research" Sub-action 2: IKY Scholarship Programme for PhD candidates in the Greek Universities.

References

Dai, A., Huang, Y.-L., & Hsieh, Y.-M. (2021). Gravity currents propagating at the base of a linearly stratified ambient. *Physics of Fluids*, *33*(6), 066601. https://doi.org/10.1063/5.0051567

Flynn, M. R., & Sutherland, B. R. (2004). Intrusive gravity currents and internal gravity wave generation in stratified fluid. *Journal of Fluid Mechanics*, *514*, 355–383. https://doi.org/10.1017/S0022112004000400

Haney, S. R., Simpson, A. J., McSweeney, J. M., Waterhouse, A. F., Haller, M. C., Lerczak, J. A., Barth, J. A., Lenain, L., Palóczy, A., Adams, K., & Mackinnon, J. A. (2021). Lifecycle of a Submesoscale Front Birthed from a Nearshore Internal Bore. *Journal of Physical Oceanography*, *51*(11), 3477–3493. https://doi.org/10.1175/JPO-D-21-0062.1

Maxworthy, T., Leilich, J., Simpson, J. E., & Meiburg, E. H. (2002). The propagation of a gravity current into a linearly stratified fluid. *Journal of Fluid Mechanics*, *453*, 371–394. https://doi.org/10.1017/S0022112001007054

Nash, J. D., & Moum, J. N. (2005). River plumes as a source of large-amplitude internal waves in the coastal ocean. *Nature*, *437*(7057), 400–403. https://doi.org/10.1038/nature03936

Climate change effects on the storm surges of the Mediterranean coastal zone

C. Makris[1*], K. Tolika[2], V. Baltikas[1], K. Velikou[2], Y. Krestenitis[1]

[1]Laboratory of Maritime Engineering and Maritime Works, School of Civil Engineering, Aristotle University of Thessaloniki, Thessaloniki, Central Macedonia, 54124, Greece
[2]Department of Meteorology and Climatology, School of Geology, Aristotle University of Thessaloniki, Thessaloniki, Central Macedonia, 54124, Greece
[*]Corresponding author: cmakris@civil.auth.gr

Abstract

This study aims to systematically assess the impacts of projected climate change on episodic events of sea level elevation in coastal areas of the Mediterranean Sea, induced by severe weather conditions identified as atmospheric deep depressions. We try to add new insight in the long-term, climatic timescale, identification of vulnerable parts at the Mediterranean coastal zone correlated to low atmospheric pressure patterns, indicative of the Mediterranean basin during the 21st century. An integrated quantitative assessment is proposed to achieve this goal by combining projections from available, established, climate change scenarios (based on Representative Concentration Pathways; RCP 4.5 and 8.5) with advanced numerical modelling and statistical post-processing for the definition of cyclonic weather impacts on exposed coastal zone hotspots. To this end, climate projections and outputs from several Regional Climate Models (RCMs) of the Med-CORDEX initiative at the Mediterranean basin scale are used after their evaluation. These atmospheric datasets feed a robust storm surge model (MeCSS) for the simulation of barotropic hydrodynamics (sea level elevation and currents) validated against *in situ* sea level observations by tide-gauges. Results corroborate a projected storminess attenuation for the end of the 21st century, yet local differentiations of storm surge maxima around the Mediterranean coastal zone is discussed. The analysis leads to quantification of deep depression systems' effect on the coastal sea level elevation due to storm surges towards 2100.

Keywords Storm surge, Climate change, Mediterranean Sea, Deep depression.

1 INTRODUCTION

In this paper, we attempt to systematically assess the impacts of projected climate change on episodic events of sea level elevation in coastal areas of the Mediterranean Sea, induced by severe atmospheric weather conditions identified as "deep depressions" (Lionello et al. 2019). Thus, our aim is to add new insight in the climatic-scale identification of vulnerable parts of the coastal zone correlated to peculiar atmospheric patterns indicative of the Mediterranean basin during the 21st century, assisting on the address of the European Challenges to Coastal Management from storm surges (Boyes and Elliott 2019). An integrated quantitative assessment is proposed to achieve these goals by combining projections from available established climate change scenarios (based on Representative Concentration Pathways; RCPs 4.5 and 8.5) with numerical modelling of storm surges and statistical post-processing for the identification of cyclonic weather impacts on exposed coastal zone hotspots (Makris et al. 2023).

2 METHODS AND DATA

To this end, historical data and climate projections are used for a Reference (1971–2000) and a Future (2071–2100) 30-years Period, respectively (Skoulikaris et al. 2021). The atmospheric parameters used as forcing of the hydrodynamic ocean model consist of wind (velocity and direction) and Sea Level Pressure (SLP) fields by three high-resolution Regional Climate Models (RCMs), developed and implemented by three institutions (CMCC, CNRM and GUF; Makris et al. 2023) in the framework of the Med-CORDEX initiative (Ruti et al. 2016; Reale et al., 2021). We simulated the storm-driven hydrodynamic circulation throughout the entire Mediterranean basin with special focus on the meteorologically induced sea level variations on the coastal zone (Androulidakis et al. 2023), based on a robust storm surge model (MeCSS; Androulidakis et al. 2015). The *in-situ* sea level observations use

for comparisons with MeCSS results to validate the model's performance for the Control Run during the Reference Period refer to field data from the tide gauge network of the Hellenic Navy Hydrographic Service (HNHS; http://www.hnhs.gr/portal/page/portal/HNHS) in five Greek stations, i.e., Thessaloniki, Alexandroupoli, Heraklion, Chios (Aegean Sea), and Lefkada (Ionian Sea). The available data cover the 11-years period of 1995-2005 (Makris et al. 2015; Androulidakis et al. 2023).

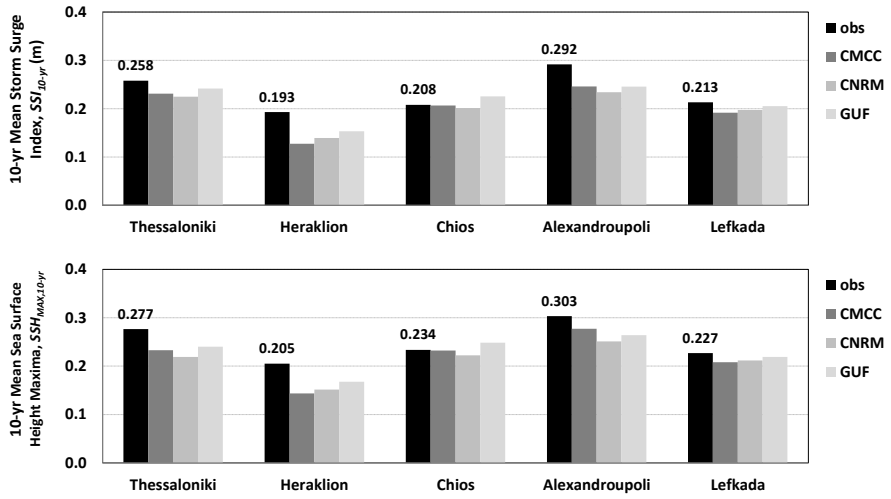

Figure 1 Comparisons of the decadal (1995-2005) average SSI (m) and SSH_{max} (m) [upper and lower graphs, respectively] in five Greek stations for field (obs) and model (mod; CMCC-, CNRM-, and GUF-MeCSS) data

Table 1 Statistical measures and skill metrics of the comparison based on decadal (1995-2005) averages of SSI (m) and SSH_{max} (m) at five Greek stations for field and model (CMCC-, CNRM-, and GUF-MeCSS) data

	RCM	Pearson Correlation	Willmott Skill Score	RMSE (m)	RMSE/SSI (%)
SSI	CMCC	0.849	0.735	0.039	17.98%
	CNRM	0.840	0.664	0.039	17.97%
	GUF	0.793	0.816	0.029	13.10%
	RCM	**Pearson Correlation**	**Willmott Skill Score**	**RMSE (m)**	**RMSE/SSH_{max} (%)**
SSH_{max}	CMCC	0.884	0.780	0.037	15.69%
	CNRM	0.828	0.582	0.043	18.70%
	GUF	0.810	0.802	0.030	12.65%

3 RESULTS

3.1 Model Validation

Thorough evaluation of the used climatic datasets against CERA-20C re-analyses (Laloyaux et al. 2019) is provided by Makris et al. (2023). Figure 1 presents the relevant comparisons of modelled and observed values for the decadal (1995–2005) average of Storm Surge Index (SSI, m) and Sea Surface Height maxima (SSH_{max}, m). All MeCSS model implementations follow the same geographical pattern as the one referring to field observations, i.e., higher storm surge levels in the northern part of the studied area and lower SSHs towards the south. Table 1 presents the aggregate estimation of MeCSS model's performance by a set of statistical measures and skill metrics. The results support the good performance of MeCSS model during the Reference Period. Even though the model underestimates SSI in all stations, the errors are generally acceptable and differences between modelled and observed SSI values are plausible. Overall, the cumulative comparisons reveal quite high Pearson correlation coefficients (>0.8), with a Root-Mean-Square-Error (RMSE) ranging from only 3 to 4.3 cm, namely a rough 12%–18% of the average SSH_{max} and <7% of the absolute observed SSH_{max}. The calculated Willmott Skill Scores also reveal a high agreement of GUF-forced MeCSS model output (>0.8) with field data in terms of the interdecadal SSH extremes.

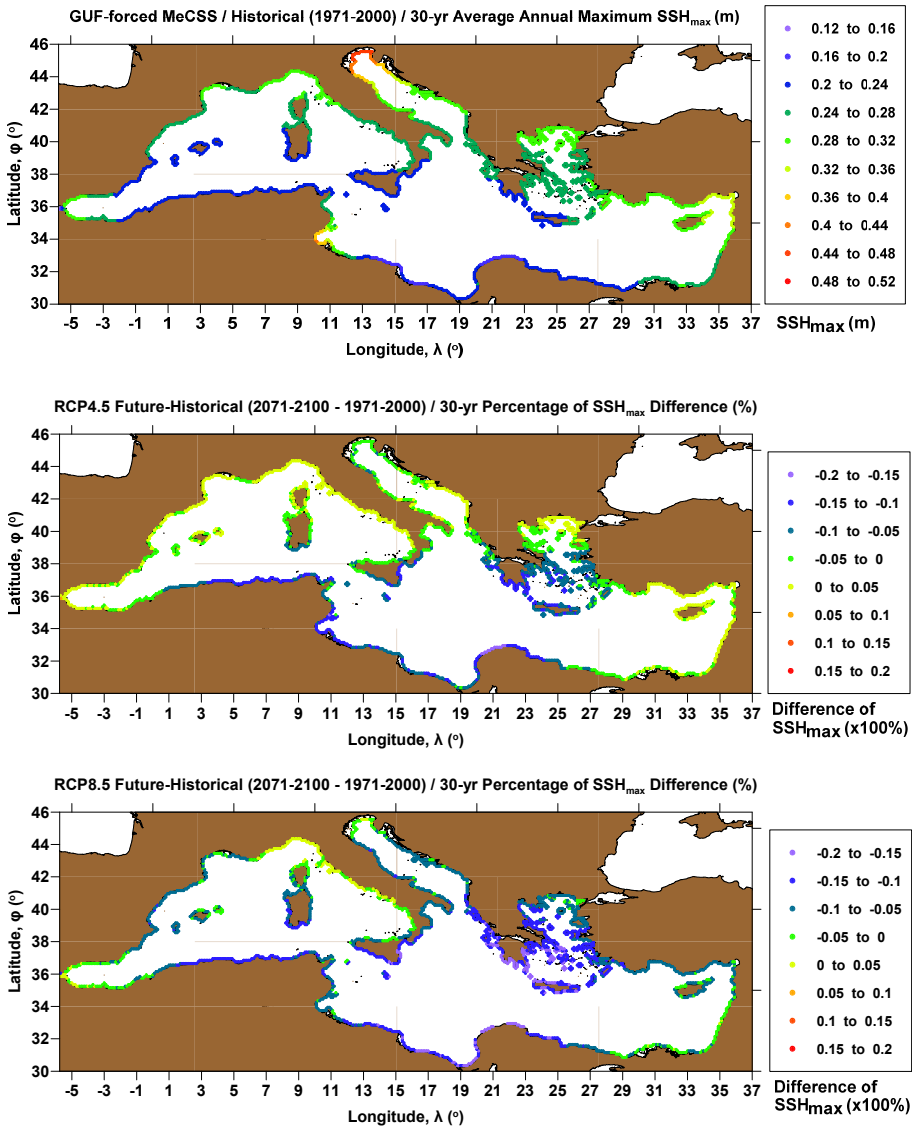

Figure 2 Map of 30-year averaged annual maxima of SSH (m) during the Reference Period (1971-2000; top graph); differences of SSH_{max} (×100%) between Future Period (2071-2100) and Reference Period for the RCP4.5 and RCP8.5 scenarios (mid and lower graphs, respectively) by the GUF-forced MeCSS model

3.2 Climate change impact on storm surges

Figure 2 presents maps of the horizontal distribution of 30-years SSH_{max} during the Reference Period and the calculated differences between it and the Future Period for both RCP4.5-8.5 scenarios for the GUF-forced MeCSS simulations. Figure 3 portrays the respective spatial distributions of the statistically significant Pearson correlation minima for SSH_{max} to identified Deep Depression centers (SLP minima) along the Mediterranean coastline. Differences of correlation between the Future-Reference Periods is also provided. Extreme storm surge magnitudes range between 0.35 and 0.50 m in the Mediterranean basin with higher values along parts of its northern coasts (Venice lagoon, Gulf of Lions, northern Adriatic and Aegean Seas, etc.) and the Gulf of Gabes in its southern part. Overall, the spatial distributions of surge maxima are estimated to remain similar to those of the past throughout the entire Mediterranean coastal zone. Differentiations between the two scenarios (RCP4.5-8.5) used are obvious, not so much related to the spatiotemporal distribution of storm surge maxima, which shows a very stable pattern, but more in terms of their magnitudes. Indicatively, a decrease of surge maxima from -30% to -2% can be observed towards the end of the 21st century, especially for RCP8.5-driven MeCSS simulations. This is a spatially averaged estimation, yet for some specific coastal sites in Croatia, Spain Italy, and France, such as Rovinj, Bakar, Toulon, Trieste, Ajaccio, Genova, Marseilles, Naples, Venice,

Cagliari, Ancona, Ibixa, and Barcelona, the storm surge maxima might increase from 1% to 22% under different RCM/RCP combinations towards the end of the 21st century. The strongest correlations of deep depression events to high sea levels are observed in several parts along the N Mediterranean (Gulfs of Valencia and Lions, Ligurian and northern Adriatic Seas). They are followed by mid-latitude areas around Corsica, Sardinia, the mid-zonal Italian Peninsula and the Adriatic, and N Aegean Sea. The influence of deep depressions on storm surges is lower for Sicily, South Italy, Peloponnese, Crete, S Aegean, and Alboran Sea. The only exceptions in the generally unaffected S Mediterranean littorals are the Gulfs of Gabes and Alexandretta. These apply to the 20th century; however, they seem to repeat for the 21st century estimations, with even more pronounced differentiations between the southern and the northern parts. A projected northward shift of the main deep depression centers over the Mediterranean towards 2100, is likely the reason for the latter.

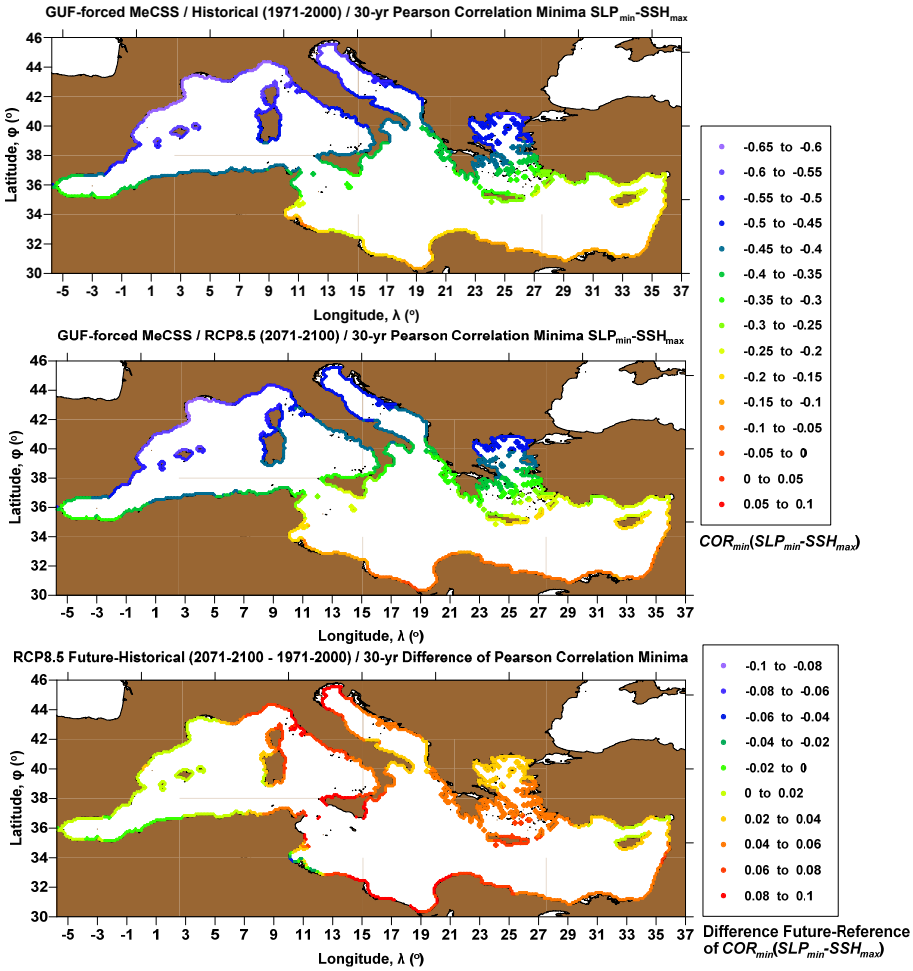

Figure 3 Spatial distribution along the Mediterranean coastline of statistically significant (p_{value}<0.01 by Mann-Kendall test) Pearson correlation minima for SSH_{max} (m) to the identified Deep Depression centers (SLP_{min}, hPa) during Reference (1971-2000; top graph) and Future (2071-2100; mid graph) Periods for RCP8.5 scenario

The climate change signal (difference of Future–Reference Period) of the deep cyclones' effect on the episodic increases of coastal sea level seems to have a very clear pattern of slight attenuation in certain regions, i.e., Sardinia, Corsica, the Ligurian and Adriatic Seas, and the entire Italian peninsula for all RCM-fed implementations towards the end of the 21st century. Conditionally, this is the case for the Gulf of Valencia, the north-western African coasts, the Alboran, Ionian, Aegean, and Libyan Sea coasts, under specific combinations of RCM/RCP forcings. On the other hand, a possible increase of the Mediterranean deep depressions' influence on the coastal storm surges might be the case for the Gulf of Lions, the Ionian, Aegean, and Levantine Sea basins, covering the north-central and north-eastern coasts of Africa.

4 CONCLUSIONS

The implemented storm surge model (Krestenitis et al. 2014; Makris et al. 2019) proved to be quite robust in reproducing the main patterns of evolution for the meteorological residual of sea level in coastal areas. Our results further corroborate a projected storminess attenuation for the end of the 21st century, yet local increases in storm surge maxima around the Mediterranean coastal zone are also pinpointed. Moreover, a slight reduction of average storm-induced Mean Sea Level (MSL; component attributed solely to the meteorological residual of SSH) is also apparent towards the end of the 21st century (Makris et al. 2023). The produced results can be used in focused studies for integrated hydrologic/hydrodynamic modelling and coastal management under projected climate change conditions until 2100 (e.g., Katirtzidou et al. 2023).

References

Androulidakis Y, Kombiadou K, Makris C, Baltikas V, Krestenitis Y (2015) Storm surges in the Mediterranean Sea: variability and trends under future climatic conditions. Dyn Atmos Oceans, 71:56–82. doi:10.1016/j.dynatmoce.2015.06.001

Androulidakis Y, Makris C, Mallios Z, Pytharoulis I, Baltikas V, Krestenitis Y (2023) Storm surges and coastal inundation during extreme events in the Mediterranean Sea: the IANOS Medicane. Nat Hazards, 117:939–978. doi:10.1007/s11069-023-05890-6

Boyes S, Elliott M (2019) European Challenges to Coastal Management from Storm Surges: Problem-Structuring Framework and Actors Implicated in Responses. In: La Jeunesse I, Larrue C (ed) Facing Hydrometeorological Extreme Events: A Governance Issue, Wiley, NY, p 339-361.

Katirtzidou M, Skoulikaris Ch, Makris C, Baltikas V, Latinopoulos,D, Krestenitis Y (2023) Modeling stakeholders' perceptions in participatory multi-risk assessment on a deltaic environment under climate change conditions. Env Mod Assess, 1-22. doi:10.1007/s10666-023-09890-5

Krestenitis Y, Androulidakis Y, Kombiadou K, Makris C, BaltikasV (2014) Modeling storm surges in the Mediterranean Sea under the A1B climate scenario. Paper presented at the 12th International COMECAP, Heraklion (Crete), Greece, 28-31 May 2014, 91-95.

Laloyaux P et al. (2018) CERA-20C: A coupled reanalysis of the twentieth century. J Adv Mod Earth Sys, 10(5):1172-1195. doi:10.1029/2018MS001273

Lionello P, Conte D, Reale M (2019) The effect of cyclones crossing the Mediterranean region on sea level anomalies on the Mediterranean Sea coast. Nat Hazard Earth Syst Sci, 19(7):1541-1564. doi:10.5194/nhess-19-1541-2019

Makris C, Androulidakis Y, Baltikas V, Kontos Y, Karambas T, Krestenitis Y (2019) HiReSS: Storm Surge Simulation Model for the Operational Forecasting of Sea Level Elevation and Currents in Marine Areas with Harbor Works. Paper presented at the 1st International Scientific Conference DMPCO, Athens, Greece, 8-11 May 2019, 1:11-15.

Makris C, Tolika K, Baltikas V, Velikou K, Krestenitis Y (2023) The impact of climate change on the storm surges of the Mediterranean Sea: coastal sea level responses to deep depression atmospheric systems. Ocean Mod, 181:102149. doi:10.1016/j.ocemod.2022.102149

Makris CV, Androulidakis YS, Krestenitis YN, Kombiadou KD, Baltikas VN (2015) Numerical Modelling of Storm Surges in the Mediterranean Sea under Climate Change. Paper presented at the 36th IAHR World Congress, The Hague, The Netherlands, 28 June – 3 July, 2015.

Reale M, Cabos Narvaez WD, Cavicchia L, Conte D, Coppola E, Flaounas E, Giorgi F, Gualdi S et al. (2021) Future projections of Mediterranean cyclone characteristics using the Med-CORDEX ensemble of coupled regional climate system models. Clim Dyn, 1-24. doi:10.1007/s00382-021-06018-x

Ruti PM et al. (2016) MED-CORDEX initiative for Mediterranean climate studies. Bull Amer Meteo Soc, 97(7): 1187-1208. doi:10.1175/BAMS-D-14-00176.1

Skoulikaris C, Makris C, Katirtzidou M, Baltikas V, Krestenitis Y (2021) Assessing the vulnerability of a deltaic environment due to climate change impact on surface and coastal waters: the case of Nestos River (Greece). Env Mod Assess, 26:459-486. doi:10.1007/s10666-020-09746-2

DMPCO 2023

e-Proceedings of the 2nd International Scientific Conference on Design and Management of Port Coastal and Offshore Works Thessaloniki, Greece, May 24-27 2023

Circulation pathways in Thermaikos Gulf based on field and model Lagrangian experiments

Y. Androulidakis[1,2,*], C. Makris[1], Y. Krestenitis[1], V. Kolovoyiannis[2], V. Baltikas[1], Z. Mallios[1]

[1]Division of Hydraulics and Environmental Engineering, School of Civil Engineering, Aristotle University of Thessaloniki, Thessaloniki, Central Macedonia, 54124, Greece

[2]Laboratory of Physical and Chemical Oceanography, Department of Marine Sciences, University of the Aegean, Mytilene, Lesvos Island, 81100, Greece

[*]Corresponding author: iandroul@civil.auth.gr

Abstract

The Northern Thermaikos Gulf (NTG; Figure 1a) is a semi-enclosed coastal region of the Aegean Sea facing severe pollution events, characterized by anthropogenic and natural stresses such as intense industrial and agricultural activities, urban outflows, and several nutrient-rich river discharges. The hydrography and the hydrodynamic circulation patterns of NTG are revisited in this paper based on the findings of an integrated observational-modeling study, conducted during an annual cycle from June 2021 until May 2022. The main goal of the study is to investigate the environmental conditions that determine the renewal and water quality of the semi-enclosed basin. An operational system for predictions of ocean circulation and Lagrangian pathways to support search and rescue and first responders during pollution accidents over NTG was also developed providing daily 3-day forecasts.

Keywords Drifters, Hydrodynamic circulation, Delft3D, Operational system.

1 INTRODUCTION

The Northern Thermaikos Gulf (NTG) is located at the tip of the northwestern Aegean Sea (eastern Mediterranean Sea; Figure 1a). Thessaloniki, the second largest city in Greece with population of 1.1 million habitants, is located along the gulf's northern coast. Two large (Axios and Aliakmonas) and two smaller (Gallikos and Loudias) rivers (Figure 1a) supply freshwater into the NTG along its western coast, containing large quantities of nutrients (Karageorgis et al. 2005). Several smaller outflows (e.g., the Halastra irrigational drainage channel network and Anthemountas intermittent river; Figure 1a) periodically discharge overflowing waters, containing agricultural (drainage), urban (treated and untreated wastewater) and industrial (liquid chemicals and heavy metals) pollutants. The main pollution pressure of NTG, related to these inputs, is eutrophication, which is strongly controlled by the mesoscale circulation patterns and the renewal capability of the gulf (Androulidakis et al. 2021). The principal objective of this study is to describe the seasonal distribution of the water masses' physical properties, the main circulation patterns, and the variability of the physical connectivity pathways, based on a systematic observational approach (six field campaigns with a 2-monthly temporal step) supported by outputs from three-dimensional (3-d) numerical simulations combined with Lagrangian particle modeling, covering a recent annual cycle (June 2021 - May 2022).

Figure 1. (a) Location of NTG, river system, drainage basins, and Delft3D-Thermaikos model domain. Components of the observational platform: (b) "AEGEAN" drifter, (c) "CARTHE" drifter, (d) Workhorse ADCP, and (e) SBE 19plus CTD

2 METHODS AND DATA

2.1 Field observations

The monitoring period covered an annual cycle from June 2021 to May 2022 with a 2-monthly temporal step (6 campaigns). The near-surface circulation pathways investigation was based on 12 Lagrangian experiments with autonomous, satellite-tracked, and free-drifting floats (drifters) for the recording of ocean current velocities at different times and locations during the observational campaigns. Two types of drifters were used: a) nine AEGEAN drifters (Figure 1b; Zervakis et al. 2009), developed by the Laboratory of Physical and Chemical Oceanography in the Department of Marine Sciences (University of the Aegean; https://www.mar.aegean.gr/), and b) three CARTHE drifters, developed by the Consortium for Advanced Research on Transport of Hydrocarbon in the Environment (CARTHE; http://carthe.org; Novelli et al. 2017, Androulidakis et al. 2018). A network of seven measurement stations (temperature, salinity, density, and current velocity measurements; Figure 1) was also employed to investigate the distribution of physical properties over the NTG during the Lagrangian experiments.

2.2 Numerical simulations of meteorological, ocean and river conditions

The meteorological conditions were obtained from the operational system for met-ocean weather forecasts, Wave4Us (Krestenitis et al. 2017, http://wave4us.web.auth.gr). Simulations of regional-scale, high-resolution, atmospheric circulation are conducted with the Weather Research and Forecasting model's Advanced Research dynamic solver (Wang et al. 2010), developed in the Department of Meteorology and Climatology of the Aristotle University of Thessaloniki (WRF-ARW-AUTh; Pytharoulis et al. 2015). The ocean circulation conditions during 2021-2022 were reproduced by numerical hydrodynamic simulations with the Delft3D modeling system, implemented over the broader Thermaikos Gulf (Delft3D-Thermaikos; Androulidakis et al. 2021; Figure 1a). The boundary conditions along the open southern boundary of the model, are derived by the Mediterranean Forecasting System model (Clementi et al. 2019; http://medforecast.bo.ingv.it/) embedded into Copernicus CMEMS Mediterranean Sea Physical Reanalysis dataset (Simoncelli et al. 2019). Androulidakis et al. (2021) discuss in detail the model setup (e.g., initial, boundary, and forcing conditions; parameterization and river input) and its performance capabilities. The simulated current fields were used to support the prevailing circulation patterns derived from the drifter experiments and current measurements. The main freshwater NTG input comes from four rivers (Gallikos, Axios, Loudias, and Aliakmonas) *in tandem* with a complex system of irrigation canals and trench drains (e.g., Halastra, Anthemountas) (Figure 1a). The daily river outflow rates of the two large rivers of Aliakmonas and Axios (Figure 1a) were derived from available observational datasets. Daily discharges of the smaller rivers, canals and trenches were not available (Loudias, Gallikos, Halastra and Anthemountas; Figure 1a). Therefore, the Hydrologic Modeling System (HEC-HMS; https://www.hec.usace.army.mil/software/hec-hms/) was implemented to simulate the hydrologic processes of the river basins (Figure 1a) and their discharges into the NTG.

2.3 Lagrangian numerical experiments

The simulated fields of currents derived from the Delft3D-Thermaikos model were used to develop Lagrangian particle experiments based on an advection-dispersion model (TracerModel2D; Krestenitis et al. 2007). Nine sources of particles input (100 particles) were used, located at the mouths of the main freshwater discharges in the coastal zone of NTG: 1) Axios, 2) Aliakmonas, 3) Dendropotamos, 4) Loudias/Mylovou, 5) West Halastra, 6) Gallikos, 7) Anthemountas, 8) Rema Dikaston, 9) East Halastra. Twelve simulation cycles were executed associated to the 5-day periods of the maximum river discharges of each month during the annual cycle (June 2021 - May 2022). The results of the particle experiments were used to estimate the main connectivity pathways between the land pressure sources and the NTG sub-basins. Additional Lagrangian experiments were also executed covering the periods of the field drifter deployments and current measurements (ADCP) to compare the simulated trajectories to the realistic conditions (drifter tracks and measured currents).

3 RESULTS

3.1 Comparison between drifter and numerical experiments

The spreading of the simulated particles (TracerModel2D) agrees with the surface currents derived from the ADCP measurements and the overall drifter trajectories (Figure 2). Field and numerical experiments reproduced the prevailing circulation conditions over the NTG during 6 study periods of the annual cycle. The drifter trajectories show that the ocean currents may transfer the surface water masses at long distances in less than 10 days. For example, Drifter D8 moved cyclonically in the inner-Gulf (Gulf of Thessaloniki) in 8 days of March 2022, in agreement with the simulated particles that were confined in the Gulf of Thessaloniki. The particles moved around the coasts after their release in the same location with the drifter (eastern coast). This trajectory also highlights the

connectivity pathway between the most polluted area of NTG (northern tip) and the eastern coasts of the central-Gulf.

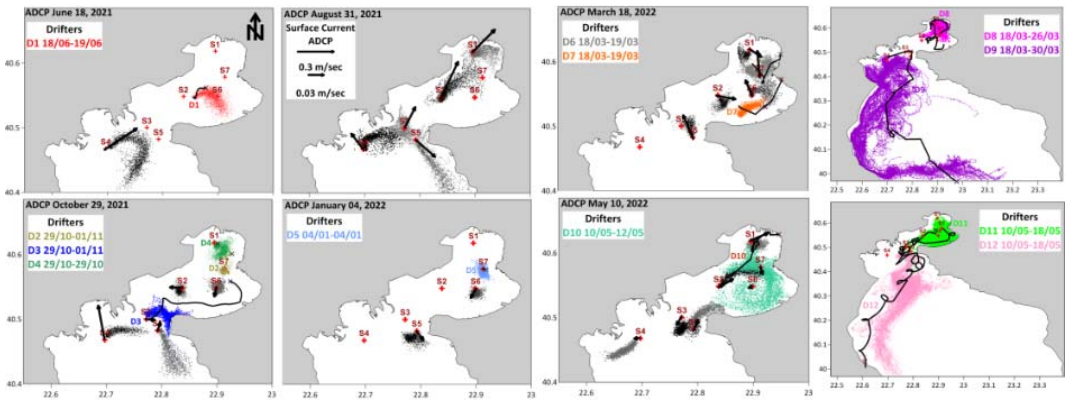

Figure 2 ADCP surface currents (vectors), trajectories of 12 drifters (black lines), and positions of 100 simulated particles (for each experiment) during the same periods

3.2 Distribution of Lagrangian particles over the NTG

The NTG was divided in 29 sub-areas to estimate each source impact at different parts of the Gulf. The June 2021 experiment is presented in Figure 3 showing the distribution of the particles spreading from each of the 9 potential coastal sources of seawater pollution.

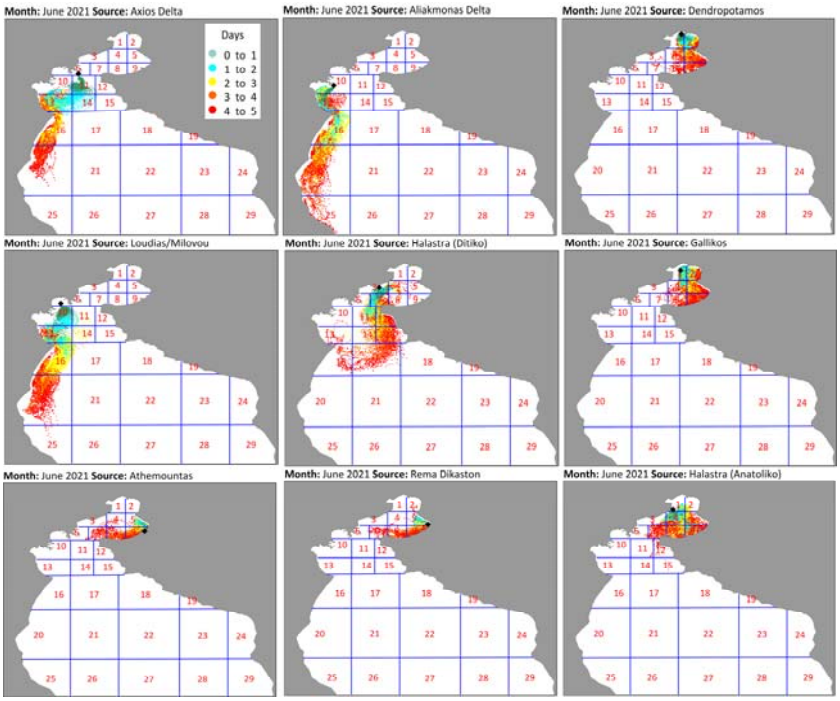

Figure 3 5-day distribution of simulated particles in NTG originated from the 9 sources during the maximum river discharge rates of June 2021

To compare the impact at each sub-domain that are characterized by different size, the number of particles ($N_{i,j}$) at each domain was weighted by the respective area ($A_{i,j}$). The impact percentage ($P_{i,j}$) of each source was then computed for all 29 sub-areas:

$$P_{i,j} = \widehat{N}_{i,j} \Big/ \sum_j \widehat{N}_{i,j} \times 100 \quad (1)$$

where $\widehat{N}_{i,j} = N_{i,j}/A_{i,j}$, $N_{i,j} = M_j \text{ x } t$, i=1,29 (areas), j=1,9 (sources), M_j=1,100 (particles), t=120 hours (5 days). The $P_{i,j}$ represents the impact of each source based on the prevailing circulation conditions derived from the Delft3D-

Thermaikos simulations. To take into account the discharge rate of each source as well, the R_D index was computed:

$$R_{Di,j} = P_{i,j} \times Q_j \Big/ \sum Q_j \quad (2)$$

where Q_j is the monthly maximum discharge rate of each j source. High (low) R_D values indicate strong (weak) impact of the source at each sub-domain (Figure 4). Due to the high discharge rates of Axios and Aliakmonas rivers, the respective R_D are significantly high along the western coasts and in the broader southwestern area of NTG. The stronger impact of the northern NTG areas is related to Gallikos and Dendropotamos sources, however it is restricted in the northern basin (Thessaloniki Bay) and is weaker than the impact of the large rivers in the southern areas of the gulf. At the coastal areas of the eastern NTG, which are characterized by urban facilities, sanitary utility infrastructure, and extensive touristic activities, the main impact is related to both more polluted northern sources (e.g., Dendropotamos, Gallikos) and the large deltas of the western coast (e.g., Axios).

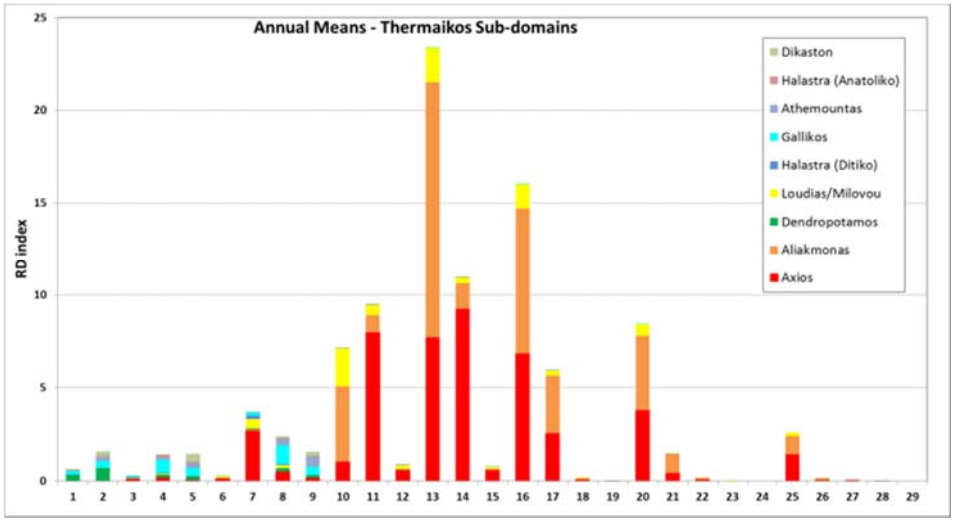

Figure 4. R_D index per source at the surface layer of the 29 sub-areas of NTG

3.3 Operational mode

The operational system Wave4us provides 3-day forecasts of sea level, wave conditions, temperature, salinity, density, and horizontal currents at different depths. The simulated forecasts are distributed freely to the general public through the system's website every day at 8:30 am after the preparation of the boundary and atmospheric conditions from the Copernicus service and the WRF-ARW-AUTh model, respectively. The system also includes the Lagrangian component that can quickly (in approximately half an hour) operate on demand to provide estimations of water mass spreading in the case of a polluting accident in the marine environment of Thermaikos Gulf. An example during a recent oil spill that was detected near the port of Thessaloniki (03/04/23; https://greekcitytimes.com/2023/04/07/thessaloniki-marine-pollution/) shows the theoretical spreading of the polluted water masses during the following hours after the accident, assuming that no clean-up countermeasures were taken (Figure 5).

4 CONCLUSIONS

An integrated observational and modeling study was conducted, with measurements of thermohaline and current profiles, drifter experiments, combined meteorological-river-ocean numerical simulations to describe the hydrography and the main circulation patterns of the Northern Thermaikos Gulf (NTG). It is the first time that drifter trajectories were used to describe the physical connectivity in NTG, representing the near-surface circulation pathways under variable wind regimes. The coupled meteorological, river, hydrodynamic and Lagrangian particle simulations provided information about the connectivity pathways between the environmental stress sources located along the NTG coastline and the several sub-basins of the Gulf. The spreading of the simulated particles (Delft3D-Thermaikos/TracerModel2D suite) agrees with the surface currents derived from the ADCP measurements and the overall drifter trajectories. Field and numerical experiments reproduced the prevailing circulation conditions over the NTG during 6 study periods of the annual cycle. The coupled model suite is also used in the operational system Wave4Us, providing daily forecasts of ocean conditions and spreading of water masses that can be used in the case of polluting accidents in the marine environment of NTG. Furthermore, the operational system, whose products are freely available to the public, is an important tool both for first-level

responders during a pollution incident or search-and-rescue teams during maritime transportation accidents, and for stakeholders and authorities responsible for the integrated management of the coastal zone.

Figure 5 Snapshots of particles´ spreading derived from the Wave4us forecast during an oil spill accident in the port of Thessaloniki (03/04/23)

References

Androulidakis Y, Kolovoyiannis V, Makris C, et al (2021) Effects of ocean circulation on the eutrophication of a Mediterranean gulf with river inlets: The Northern Thermaikos Gulf. Cont Shelf Res 221:104416. doi:10.1016/j.csr.2021.104416

Androulidakis Y, Kourafalou V, Özgökmen T, et al (2018) Influence of river-induced fronts on hydrocarbon transport: A multiplatform observational study. J Geophys Res Oceans, 123(5):3259-3285. doi:10.1029/2017JC013514

Clementi E, Pistoia J, Delrosso D, et al (2019) The Mediterranean analysis and forecasting physical system for the Copernicus Marine Service: description and skill assessment. Paper presented at the GODAE OceanView Symposium 2019 - OceanPredict'19, Halifax.

Karageorgis AP, Skourtos MS, Kapsimalis V, et al (2005) An integrated approach to watershed management within the DPSIR framework: Axios River catchment and Thermaikos Gulf. Reg Env Chang, 5(2):138-160. doi:10.1007/s10113-004-0078-7

Krestenitis Y, Pytharoulis I, Karacostas TS, et al (2017) Severe weather events and sea level variability over the Mediterranean Sea: The WaveForUs operational platform. In: Karakostas et al (ed) Perspectives on Atmospheric Sciences, Thessaloniki, Greece, p 63-68.

Krestenitis YN, Kombiadou KD, Savvidis YG (2007) Modelling the cohesive sediment transport in the marine environment: the case of Thermaikos Gulf. Ocean Sci 3(1):91-104. doi:10.5194/os-3-91-2007

Novelli G, Guigand CM, Cousin C, et al (2017) A biodegradable surface drifter for ocean sampling on a massive scale. J Atm Ocean Tech 34(11):2509-2532. doi:10.1175/JTECH-D-17-0055.1

Pytharoulis I, Tegoulias I, Kotsopoulos S, et al (2015) Verification of the operational high-resolution WRF forecasts produced by WAVEFORUS project. Paper presented at the 16th Annual WRF Users' Workshop, Boulder, Colorado, USA.

Simoncelli S et al. (2019) Mediterranean Sea Physical Reanalysis (CMEMS MED-Physics). Available via Copernicus Monitoring Environment Marine Service [Data set; accessed 21 Apr 2023]. https://doi.org/10.25423/MEDSEA_REANALYSIS_PHYS_006_004.

Wang X et al. (2010) WRF-Chem simulation of East Asian air quality: Sensitivity to temporal and vertical emissions distributions. Atm Env, 44(5):660-669. doi:10.1016/j.atmosenv.2009.11.011

Zervakis V, Kalampokis A, Kakagiannis G, et al (2009) Low-cost drifters for coastal use. Paper presented at the 9th Hellenic Symposium of Oceanography and Fisheries, Patra, Greece.

DMPCO 2023

e-Proceedings of the 2nd International Scientific Conference on Design and Management of Port Coastal and Offshore Works Thessaloniki, Greece, May 24-27 2023

On using submarine cables to monitor water transport: the case of intensely baroclinic oceanic flows

S. Vatitsis, I.G. Mamoutos, V. Zervakis*, E. Tragou, A.F. Velegrakis

Department of Marine Sciences, University of the Aegean, Mytilene, Lesvos, GR81100, Greece
*Corresponding author: zervakis@aegean.gr

Abstract

The use of submarine telephone cables for the assessment of net volume fluxes through marine Straits was first proposed by Michael Faraday in 1832 and since then it has been used in several oceanographic applications, the longest used one being the assessment of the Gulf Stream through the Florida Keys. In this method, the submarine cable is used as an extension of a voltmeter, enabling to measure the electric potential difference (voltage) between two opposing coasts induced by the flow of electrically charged ions of the seawater through the vertical component of the Earth's magnetic field. In a recent effort to use the method at the entrance of an island bay in the Aegean Sea, the recorded voltage did not exhibit any correlation with the water volume flux through the Strait. In this work we use two methods to investigate one of the possible causes of this lack of correlation, the intense baroclinic shear of the examined exchange flow. The first method corresponds to an electrical circuit analogous to the experimental design while the second method exploits a numerical simulation of the exchange flow to assess the expected voltage between the costs. Both methods converge to the conclusion that the intense shear could not be the source of the lack of correlation between the observed voltage and the water volume net flux through the Strait.

Keywords Submarine Telephone Cable, Exchange Flow, Semi-enclosed Basin, Kalloni Bay.

1 INTRODUCTION

Making measurements in the marine environment is generally very costly, due to the extreme and inhospitable conditions which impose very specific and demanding technical requirements that the equipment to be deployed needs to follow. However, there are few exceptions, which can provide long time-series at minimal investment and very low, if any, maintenance costs. One of these methods is the measurement of net volume flux between two opposing shores of a marine region via the use of a submarine telephone cable (Sanford 1971). This method was proposed by Michael Faraday in 1832, when he suggested that due to the Lorenz force acting on a charged particle moving within a magnetic field, an electric potential difference would be generated between two opposing shores of a marine Strait, due to the motion of the dissolved ions advected by the water in the presence of the vertical component of Earth's magnetic field. Despite Faraday's failure to measure the voltage between the opposing shores of Thames river via the deployment of two long cables (in the role of electrode extensions) in the water near the two landing sides of the Waterloo Bridge, the method has been adopted by the oceanographic community and used in several applications and scales ranging from salt marsh drainage channels (Sanford 1977) and estuaries (Swenson 1981) to oceanic sub-Basins (Larsen and Sanford 1985; Kim et al. 2004).

During the summer 2019, the method was applied on an active telephone cable laid on the seafloor across the narrow entrance of Kalloni Bay (Figure 1), in order to investigate the prospects of add the cable as a component of the AEGIS Coastal Environmental Observatory, capable of assessing in real-time the net water volume exchange rate between the Bay of Kalloni and the Aegean Sea (Petalas et al., 2020). The water budget of the Bay at timescales of the order of hours to days is controlled by the next water exchange through the Strait, thus Petalas et al. (2020) used sea-level measurements to provide the basis for validation and calibration of the cable method, in parallel with results of a numerical simulation model of the Bay's circulation. Both estimates of net water volume exchange through the Strait, arising from sea-level variability and the numerical simulations, exhibited a very good agreement. However, the temporal variability and the spectral density of the across-Strait voltage were quite different than

either of the sea-level-obtained or the simulated estimates, thus it was not possible proceed to calibrate the cable (Petalas et al., 2020).

In more detail, the power spectrum of the voltage time-series revealed a dominance of lower-than-daily frequencies, a diurnal spectral peak and a complete lack of a semi-diurnal signal, while both the sea-level-obtained Suspect sources of additional noise responsible for the failure of the cable method in the Kalloni Bay include the intense baroclinic shear of the flow, the potential role of the seafloor's conductivity, the distance of the grounding electrodes from the water, potential electromagnetic noise in the vicinity. The present work investigates whether the low correlation between the electrical voltage across the opposing shores of the Kalloni Strait and the assessed net water volume flux through it could be attributed to the highly baroclinic nature of the exchange flow.

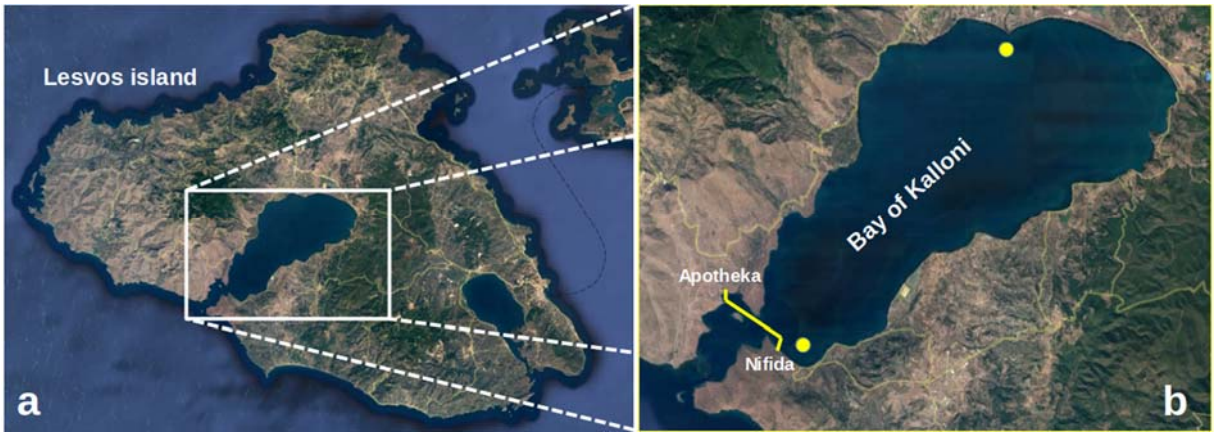

Figure 5 (a) map of Lesvos Island. The rectangle inset identifies the position of Kalloni Bay on the island and is expanded in (b) to the right. **(b)** map of Kalloni Bay, identifying the position of the submarine cable (yellow solid line) and of the two sea-level gauges (yellow dots) used in this study

2 METHODOLOGY AND DATA

Two methods were applied in order to seek an answer to the potential impact of baroclinicity on the recorded voltage between the two coasts. The first method is a theoretical approach of examining an electrical circuit that consists of the electromotive force generated on the seawater charged particles moving in Earth's magnetic field and the resistors that water and seabed constitute, given their finite conductivity. The second method proceeds to estimate the actual variability of the expected voltage between the two coasts, exploiting the numerically simulated velocity and conductivity fields for the period of the voltage observations.

2.1 Theoretical Electrical Circuit Approach

The temporal variability of the voltage recorded on the opposing coasts across the Strait exchange can be modeled as an electrical circuit (Figure 2).

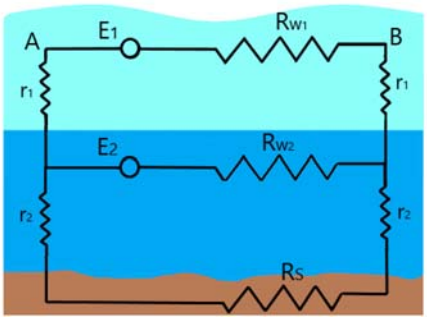

Figure 6 Idealized electrical circuit of a two-layer flow across a channel, where each layer has a different conductivity

Assuming the motion of the *i* layer's charged particles within the vertical component of Earth's magnetic field induces an electromotive force E_i, and the finite conductivity of the water and seabed sediment the corresponding resistors R_{wi}, r_i and R_s respectively, the voltage V_{AB} measured between the opposing coasts at point A and B should be:

$$V_{AB} = \frac{E_1\left(R_{w2}+2r_1-\frac{4r_1^2}{R_{w1}}\right)+E_2(2r_1-R_{w1}-R_{w2})}{\frac{R_{w2}^2-R_{w1}^2-4r_1^2}{R_{w1}}+\frac{R_{w1}R_{w2}+R_{w2}^2+2r_1R_{w2}}{R_S+2r_2}} \quad (1)$$

2.2 Estimation of the voltage induced by the numerically simulated exchange flow

2.2.1 Cable Voltage Measurements

The collection and processing of the voltage data is presented by Petalas et al. (2020). The power spectrum of the voltage time-series revealed a dominance of lower-than-daily frequencies, a diurnal spectral peak, and a complete lack of a semi-diurnal signal (Petalas et al., 2020).

2.2.2 Simulated Water Volume

Results from the Kalloni Bay numerical model described in Petalas et al. (2020) are exploited to estimate the conductivity flux through the Strait, an analogous quantity to the voltage induced across it (Kim et al., 2004). From the model output, the zonal (u) and meridional (v) components of velocity, temperature, salinity, and pressure variables from the transect across the Strait between the cable landing sites of Apotheka and Nifida have been retrieved. The velocity components have been projected to a Cartesian system aligned with the Strait. Furthermore, the simulated temperature, salinity and pressure have been used to provide conductivity, and then the conductivity flux time series has been estimated:

$$Q_{cu}(t) = \int_{y_1}^{y_2}\int_{-H(y)}^{0} C\,(y,z,t)u(y,z,t)dzdy, \quad (2)$$

where $C(y,z)$ and $u(y,z)$the conductivity and along-channel velocity component at at across-channel coordinate y and depth z, $H(y)$ the depth at y, and y_1, y_2 the across-channel coordinates of the two sides of the cross-channel transect.

For comparison, the net volume flux through the Strait was also estimated:

$$Q_u(t) = \int_{y_1}^{y_2}\int_{-H(y)}^{0} u\,(y,z,t)dzdy, \quad (3)$$

as well as the mean conductivity of the water column along the Strait:

$$\bar{C}(t) = \frac{\int_{y_1}^{y_2}\int_{-H(y)}^{0} C(y,z,t)dzdy}{\int_{y_1}^{y_2}\int_{-H(y)}^{0} dzdy} \quad (4)$$

3 RESULTS

3.1 Theoretical Electrical Circuit Approach

Examination of Equation (1) reveals that the voltage V_{AB} varies proportionally to the electromotive forces E_1 and E_2 of the two layers. In other words, in this simple circuit, the resistors are not capable to act as a damping or delaying factor on the voltage between the points A and B, thus, if both layers exhibit a similar temporal variability (which for this application corresponds mainly to the diurnal and semidiurnal tides), the same variability is expected to be shown by the voltage. However, there is a special case in which the two electromotive forces would cancel each other, in which case $V_{AB} = 0$. If we assume that the vertical dimension of the channel is very small compared to the horizontal one, this would take place when $E_1R_{w2} \simeq E_2(R_{w1} + R_{w2})$, or

$$\frac{E_1}{E_2} \simeq \frac{(R_{w1}+R_{w2})}{R_{w2}} \quad (5)$$

So, it appears that the voltage induced by some motions may be minimal depending on the relative strength and conduction of the two layers. We could assume that this is the case for the lack of spectral signature of the semidiurnal tide in the case of Kalloni Bay. This is investigated by the second method hereby used, the exploitation of the numerically simulated flows.

3.2 Estimation of the voltage induced by the numerically simulated exchange flow

The estimation of the time-series of net water volume flux (Q_u), conductivity flux (Q_{cu}), and an approximate conductivity flux ($\bar{C}Q_u$), estimated by multiplying the net water volume flux by mean conductivity, exhibit almost identical temporal variability (Figure 3a, b).

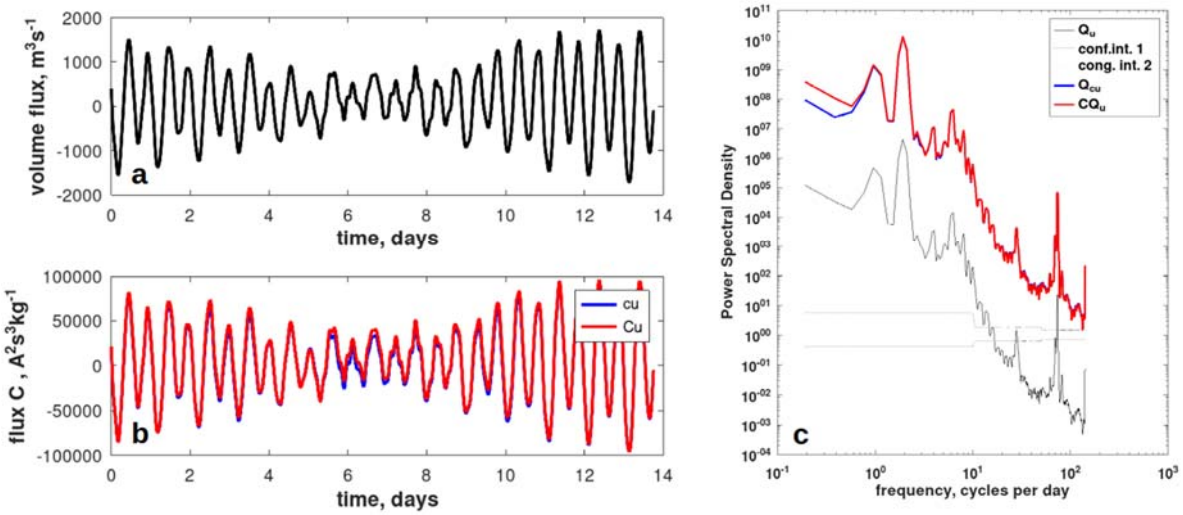

Figure 7 Time series of net volume flux **(a)** and conductivity flux **(b)** estimated both as (blue line) and (red line). The power spectra of the three time-series are presented in **(c)**

It is even visually obvious that all the time-series are dominated by the semidiurnal tide, thus the voltage induced at the two sides of the Strait will have also to be dominated by it. This result is also certified by the power spectra of the three above-mentioned time series, which have an almost identical shape, dominated by the semi-diurnal peak, and secondarily by a diurnal peak (Figure 3c).

Thus, it is clear that the special conditions which lead to Equation (5) do not apply in the case of Kalloni Bay, since the strong semi-diurnal tidal signal that dominates the net volume flux time-series remains dominant also in the conductivity flux time-series, thus the parameter that determines the variability of the voltage between the two opposing coasts of the Strait (Kim et al., 2004).

4 CONCLUSIONS AND DISCUSSION

The expected impact of a strongly baroclinic flow through the connecting Strait of a semi-enclosed basins is hereby investigated through the application of two methods. The first method, a purely analytical approach treating the Strait as an electrical circuit, reveals that in general the voltage would have an immediate linear response to the electromotive Lorenz force induced by the flow, however it is possible that under special conditions the two layers would counter-balance their impact and minimize their response. The second method, exploiting numerically simulated conductivity flux through the Strait in realistic conditions, showed that in the Kalloni Bay case the expected voltage induced between the coasts should be directly proportional to the net water volume flux, contrary to the observed voltage. Thus, the lack of correlation identified by Petalas et al. (2020) is probably related either to another environmental source of electromagnetic signal in the vicinity or inappropriate application of the method (distance of electrodes to the beach, bad grounding, loss of continuity of the cable's shield).

Acknowledgements

This work has taken place in the framework of the Project "Coastal Environment Observatory and Risk Management in Island Regions AEGIS+" (MIS 5047038), implemented within the Operational Programme "Competitiveness, Enterpreneurship and Innovation" (NSRF 2014-2020), co-financed by the Hellenic Government (Ministry of Development and Investments) and the European Union (European Regional Development Fund).

References

Faraday (1932) The Bakerian Lecture – Experimental Researches in Electricity. Philos Trans R Soc London, 122:174-176.

Kim K, Lyu SJ, Kim YG, Choi BH, Taira K, Perkins T, Teague WJ, Book JW (2004) Monitoring Volume Transport through Measurement of Cable Voltage across the Korea Strait. J Atmos Ocean Tech, vol. 21(4):671-682. doi:10.1175/1520-0426(2004)021<0671:MVTTMO>2.0.CO;2

Larsen, JC, Sanford, TB (1985) Florida current volume transports from voltage measurements, Science, 227(4684): 302-304. doi: 10.1126/science.227.4684.302

Petalas S, Mamoutos I, Dimitrakopoulos AA, Sampatakaki A, Zervakis V (2020) Developing a Pilot Operational Oceanography System for an Enclosed Basin. J Mar Sci Eng 8 (5):336. doi:10.3390/JMSE8050336

Sanford TB (1971) Motionally induced electric and magnetic fields in the sea, J Geophys Res, 76: 3476–3492. doi: 10.1029/jc076i015p03476

Sanford TB (1977) Measurements by geomagnetic induction of volume transport in a salt marsh drainage channel, Limnol Oceanogr, 22 (6): 1082-1089. doi:10.4319/lo.1977.22.6.1082

Swenson EM (1981) Electromagnetic measurements of tidal transports in estuaries, Estuaries 4: 161–166. doi:10.2307/1351471

e-Proceedings of the 2nd International Scientific Conference on
Design and Management of Port Coastal and Offshore Works
Thessaloniki, Greece, May 24-27 2023

Optimizing the parameterization of a high resolution numerical simulation of the Saronikos Gulf hydrodynamics

V. Kolovoyiannis[1*], S. Petalas[1], I. Mamoutos[1], E. Krasakopoulou[1], V. Zervakis[1], E. Tragou[1], H. Kontoyiannis[2]

[1]Department of Marine Sciences, University of the Aegean, Lesvos, 81100, Greece
[2]Hellenic Center for Marine Research, Institute of Oceanography, Athens, 19013, Greece.
*Corresponding author: vkol@marine.aegean.gr

Abstract

The performance of a high-resolution coastal ocean hydrodynamic model (Delft3D-FLOW) implemented in Saronikos Gulf (Eastern Mediterranean) is examined in a number of numerical experiments forced with various open boundary data sources and using different vertical discretization configurations. Model output is validated against field observations – monthly CTD casts in the inner Saronikos and oceanographic buoy time series- and satellite sea surface temperature for the Nov 2009-Oct 2010 annual cycle. It is found that the way the property exchanges through the Dardanelles Strait are described by the Aegean-resolving 'wider' model that provides boundary data, plays a crucial role in improving reproduction of salinity within the high-resolution domain of Saronikos model that does not receive large freshwater volumes from the watershed.

Keywords Coastal hydrodynamic circulation, Modelling, Delft3D, Saronikos Gulf

1 INTRODUCTION

Implementing reliable quantitative tools for the investigation of coastal dynamics is crucial in the effort to understand and preserve these highly dynamic marine environments that are under constant environmental pressure from human activities. In the work at hand, a high-resolution coastal hydrodynamic model is implemented in the busy Saronikos Gulf (Eastern Mediterranean, Fig. 1), and its performance under various open boundary datasets and vertical discretization configurations is evaluated, aiming to optimize its setup. Model output covering the annual cycle of November 2009-Oct 2010 is compared to (a) monthly CTD data by the Hellenic Center for Marine Research (HCMR) from a network of ten (10) stations located in inner Saronikos Gulf and Elefsina Bay (Fig. 1), (b) HCMR oceanographic buoy records of temperature, salinity and current speed/direction (Fig. 1) and (c) satellite sea surface temperature (SST) by the Copernicus Marine Service.

2 METHODS AND DATA

2.1 Model implementation

The FLOW module of Delft3D modelling system (Delft3D-FLOW, 2023) is implemented in a 3D configuration to simulate the hydrodynamics of Saronikos Gulf. The system of non-linear equations solved by the model consists of the horizontal equations of motion, the continuity equation, and the transport equations for conservative constituents. They are derived from the three-dimensional Navier-Stokes equations for incompressible, free surface flow.

The 83x101 *curvilinear grid* developed, with resolution varying from about 1400m offshore (open boundaries), to less than 300m off Piraeus, resolves the water exchanges at the straits connecting Elefsis subbasin with Saronikos (Fig. 1). In the vertical, numerical experiments have been conducted using two separate configurations with 15 and 20 σ-layers (terrain following), for the discretization of the water column. Also, σ-layers vertical distributions both as even and uneven percentages of the total depth (i.e., variable layer thickness) are considered. In the latter case, model resolution is very high near the sea surface: 1%, 1.5%, 2% of grid cell depth for the top, second, third σ-layer respectively, and increasing towards the mid-column (denoted with '-s' in the acronym of the experiment). Simulations are forced with hourly *atmospheric data* from the ECMWF ERA5 reanalysis database (Hersbach et al., 2018): air temperature, air pressure, relative humidity, precipitation, cloudiness, net shortwave radiation, and x-

and y- components of wind velocity on a 0.25° x 0.25° grid are used to quantify the atmosphere-sea interaction and exchange of heat, water and momentum.

To optimize model performance, three sets of *open boundary conditions* data are used to drive simulations, through time series of sea surface height, daily temperature and salinity profiles. Initially, a subset of the Mediterranean Sea Physics Reanalysis product by Copernicus Monitoring Environment Marine Service is used (operational product MEDSEA_MULTIYEAR_PHY_006_004; Med MFC physical reanalysis; Escudier et al. 2021). Boundary conditions are also derived from two implementations of the free–surface, hydrostatic, primitive equation Regional Ocean Modelling System (Shchepetkin et al. 2005): a 30-years hindcast study of the coupled Eastern Mediterranean-Black Sea system (ROMS-EMBS, Petalas et al. 2022) and a 2008-2017 hindcast of the Aegean Sea (ROMS-AEG, inhouse development). Details on the implementation of these models (scope, domain, setup, parameterization and validation) are given in the respective references, while herein, key features are summarized in Table 1.

Table 1. Information on modelling datasets used as boundary conditions for the Saronikos Gulf Delft3d-FLOW comparative simulations

	Modelling system		
	Mediterranean Sea Physics Reanalysis (Med MFC, Copernicus Marine Service) MEDSEA_MULTIYEAR_PHY_006_004 Escudier et al. 2021	**ROMS-EMBS** Petalas et al. 2022	**ROMS-AEG**
Domain / scope	Mediterranean Sea, operational product	Eastern Mediterranean and Black Sea, 1985-2015 hindcast	Aegean Sea 2008-2017 hindcast
Horizontal resolution	orthogonal, 1/24˚ in both directions (ca. 4-5 km)	curvilinear grid variable resolution, ~1.2 km @ Dardanelles-Bosporus straits, 2-4 km in Aegean and the open seas, up to ~6 km @ western boundaries	orthogonal, 1.9 km in both directions, Marmara Sea is included.
Vertical resolution	141 unevenly spaced z levels	30 terrain-following, sigma-coordinate layers, high near-surface resolution (stretching function, Shchepetkin et al. 2005)	30 terrain-following, sigma-coordinate layers, high near-surface resolution for better representation of SST (Souza et al. 2015)
Atmospheric forcing	ECMWF ERA-5 reanalysis	ECMWF ERA Interim	ECMWF ERA-5 reanalysis
Freshwater discharges	monthly climatological datasets	SHMI E-HYPE hydrological model	SHMI E-HYPE hydrological model
Open boundaries	Atlantic global reanalysis	Med MFC	Med MFC
Dardanelles / Bosphorus Straits parameterization	as river runoff	dynamical resolution of Black Sea water input in the Aegean Sea domain	parameterized with data from Maderich et al. (2015)

The annual *freshwater inflow* is considered: Kifisos river discharge, as well as discharges from two intermittent water streams (Mandra and Sarantapotamos) flowing into Elefsis bay, are evaluated from data provided by the Swedish Meteorological and Hydrological Institute (SHMI E-HYPE hydrological model; Lindstrom et al., 2010). The discharges from the Wastewater Treatment Plants (WWTP) of Psittaleia are also accounted for. Information on the mean daily volume outflow is retrieved from the Greek Special Secretariat for Water WWTP monitoring database. The November 2009-October 2010 annual cycle is simulated, with a time step of 0.5 min. Turbulent processes are parameterized with the *k-e* turbulence closure model. Simulations are free (no data assimilation or relaxation to climatological or other observed quantities), in a parallel implementation of the Delft3D code on multiple cores utilizing the HPC facilities of the University of the Aegean.

2.2 Validation data

Temperature and salinity CTD profiles from a network of ten stations (Fig. 1) collected monthly by the Hellenic Centre for Marine Research during the study period (HCMR, 2011) are used to assess model performance. Time series of temperature, salinity and current speed/direction from HCMR's Saronikos Gulf buoy (WMO platform number 6101001, Fig 1a.) are also utilized. Lastly, the 'Mediterranean Sea

High Resolution and Ultra High Resolution Sea Surface Temperature Analysis' dataset (Copernicus Marine Service product SST_MED_SST_L4_NRT_OBSERVATIONS_010_004_c_V2; Buongiorno Nardelli et al., 2013) is used in the model validation procedure. It consists of daily mean, gap-free, optimally interpolated maps of foundation SST at ultra-high spatial resolution of 0.01° (~1 km).

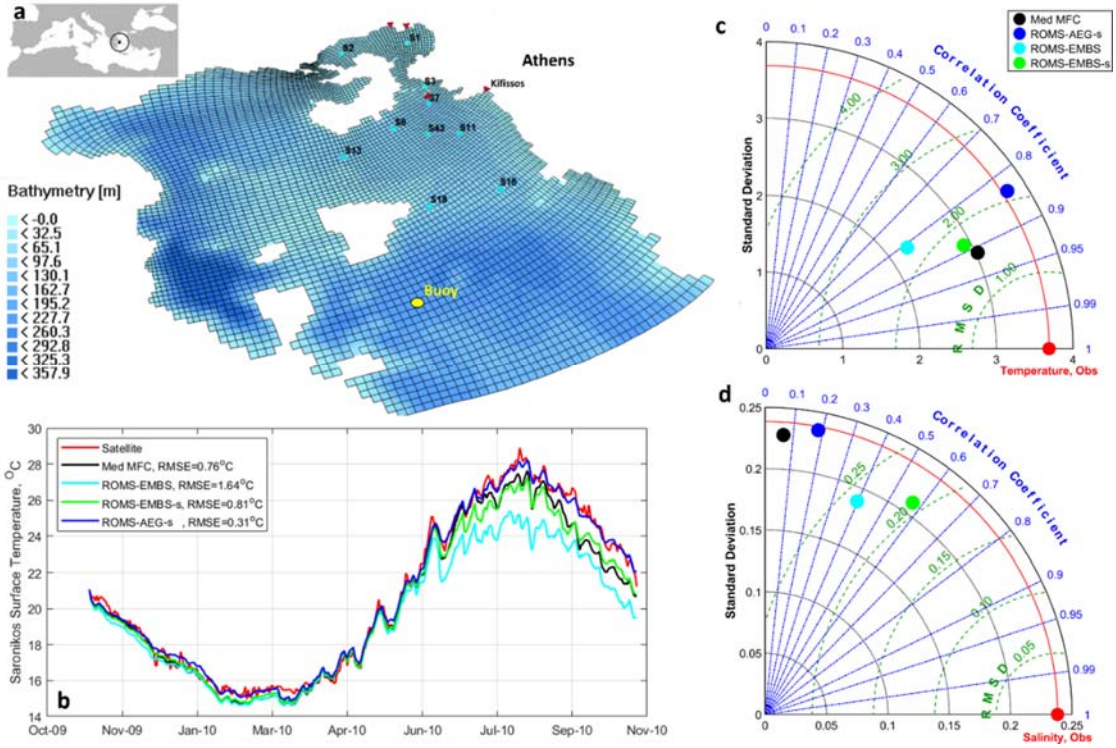

Figure 1. **(a)** Saronikos Gulf computational domain, model bathymetry, Hellenic Center for Marine Research sampling stations network (cyan points) and oceanographic buoy location (yellow), locations of freshwater input (magenta), **(b)** satellite derived sea surface temperature (red) and Delft3D-FLOW surface layer temperature for various open boundary data sources, spatially averaged for the whole Saronikos Gulf domain, for the Nov 2009-Oct 2010 annual cycle. The RMS error in each case is reported, **(c, d)** evaluation of Delft3D Saronikos simulation performance under various open boundary datasets, using Taylor diagrams for temperature (c) and salinity (d). 'Obs' refers to the observational annual dataset from HCMR stations of inner Saronikos (Fig 1a)

3 RESULTS

In Fig. 1(c, d), the performance of the Delft3D Saronikos gulf model forced with various open boundary data is summarized using Taylor diagrams. For salinity, the use of output from the ROMS-EMBS model that resolves the coupled Black Sea – Eastern Mediterranean system, describing dynamically the exchanges through the Dardanelles Strait, produces overall better results comparatively to other sources. Quantitative skill metrics further improve when higher near-surface resolution is employed. The ROMS-EMBS simulation produces overall the lowest centered RMS error (~0.21), the highest correlation coefficient (~0.58) and standard deviation close to that of the observational dataset of HCMR stations in inner Saronikos, while buoy salinity data are also better reproduced (Fig 2b, rmse=0.71 psu). For temperature, the ROMS-EMBS and the Mediterranean Forecasting System forced simulations produced better overall metrics (Fig. 1c) for the whole column of inner Saronikos.

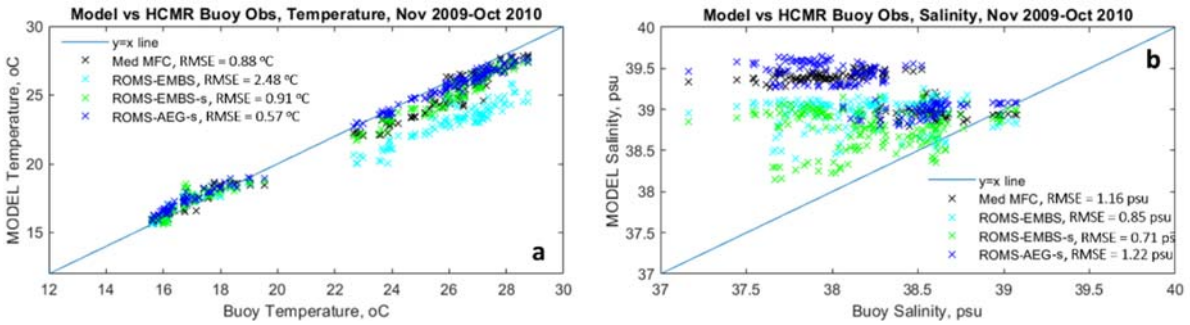

Figure 2. Saronikos HCMR buoy observations at 3m depth vs model runs under various open boundary data sources for (a) temperature (n=164 obs) and (b) salinity (n=163 obs) for the Nov 2009-Oct 2010 annual cycle. Missing temperature values between 20 – 23 ºC correspond to the March-June 2010 period where no data were recorded. The RMS error for each model run is reported

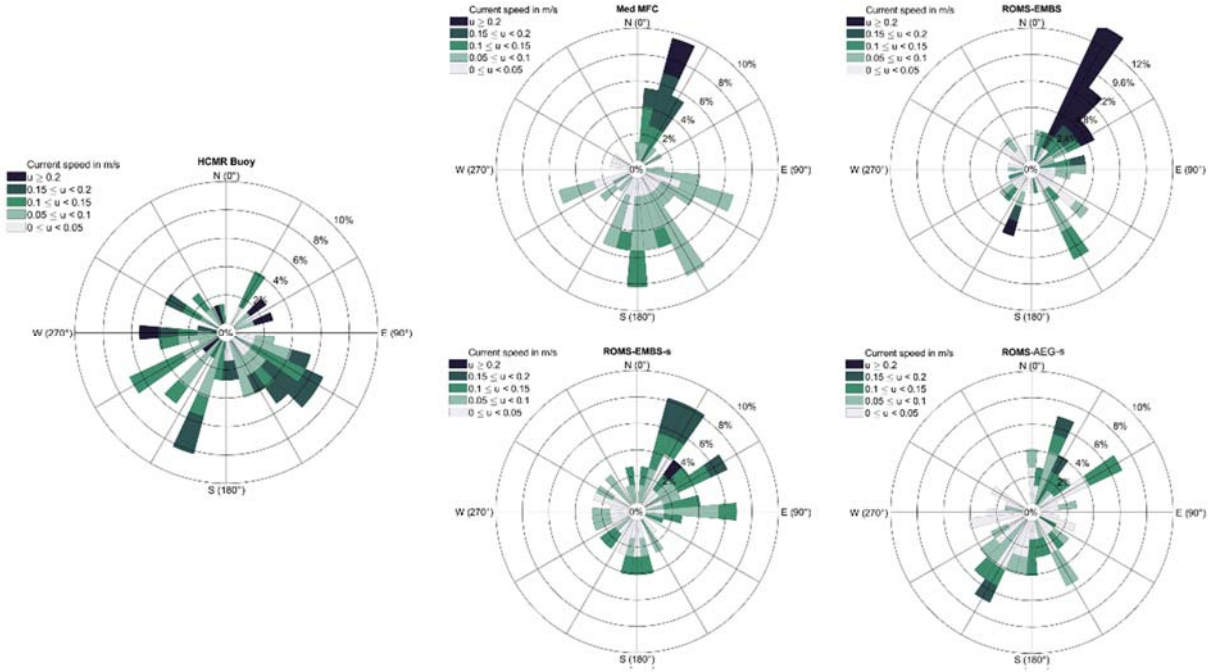

Figure 3. (a) Rose diagrams for current speed and direction from Saronikos HCMR buoy observations (3m depth) and model runs for the 1 Dec 2009 – 5 Mar 2010 period (n=73 available observations at 00:00)

There is a notable capability of the ROMS-AEG forced experiment to reproduce the spread of temperature values, as the standard deviation indicates (Fig. 2). Also, this forcing dataset leads to quite good simulation of surface temperature, as Fig. 1b (whole domain) and Fig. 2a (buoy) demonstrate. This is attributed to the near-surface, high-resolution configuration of the ROMS-AEG model which, in combination with the 30 sigma layers, manages to accurately quantify air-sea heat exchange processes. In Fig. 3, for the 1 Dec 2009 – 5 Mar 2010 period (buoy data availability, 73 data points), observations indicate prevailing W-SW-S-SE currents with speed ranging between 0-0.2 m/s. In model runs, while speed is in general adequately reproduced, deviations can be seen in the simulated current directions. However, point-by-point comparison, especially for an offshore buoy, is a process that requires studying longer periods to result in a reliable correlation, due mostly to smaller scales of velocity fields relative to sea-surface temperature or salinity ones. Also, a comparative study between buoy wind measurements and ERA5 wind forcing could reveal discrepancies between the two series of data and help in interpreting the above findings.

4 CONCLUSIONS

The validation exercise described in this work demonstrates the effect different open boundary datasets and vertical discretizations can have in the performance of a high-resolution, coastal ocean

hydrodynamic model and can help optimize its parameterization. Comparison of model output with monthly CTD profiles, buoy observations and satellite SST has been employed in the process. For Saronikos Gulf, an Eastern Mediterranean embayment that does not receive large freshwater volumes from the watershed, the modelling system that resolves dynamically Black Sea water (BSW) input in the Aegean domain, provides improved lateral boundary conditions in terms of volume variability and water characteristics when compared to models that parameterize the flow, and manages to convey a clearer BSW signal to the downscaled coastal model open boundaries. This is critical in improving reproduction of salinity within the high-resolution domain of the Saronikos model. Near-surface temperature is better simulated when the water column is resolved with model sigma layers distributed vertically as an uneven percentage of total depth (variable layer thickness) with very high resolution near the sea surface, for both the coastal and the boundary forcing models. The optimized hydrodynamic model is currently being used to force water quality simulations to study ecosystem and pollution processes.

Acknowledgements

This project has received funding from the European Union's Horizon 2020 Research and Innovation Program under Grant Agreement No 874990" (EMERGE project).

References

Buongiorno Nardelli, B., C. Tronconi, A. Pisano, and R. Santoleri (2013) High and Ultra-High resolution processing of satellite Sea Surface Temperature data over Southern European Seas in the framework of MyOcean project. Remote Sens Environ., 129: 1-16, doi:10.1016/j.rse.2012.10.012

Delft3D-FLOW (2023) Simulation of multi-dimensional hydrodynamic flows and transport phenomena, including sediments. User manual, v4.05, Deltares.

Escudier, R., Clementi, E., Cipollone, A., Pistoia, J., Drudi, M., et al. (2021) A High-Resolution Reanalysis for the Mediterranean Sea. Frontiers in Earth Science, 9, 1060, doi:10.3389/feart.2021.702285

Hersbach, H., Bell, B., Berrisford, P., Biavati, G., Horányi, A., et al. (2023) ERA5 hourly data on single levels from 1940 to present. Copernicus Climate Change Service (C3S) Climate Data Store (CDS), doi:10.24381/cds.adbb2d47

HCMR (2011) Monitoring of the Inner Saronikos Gulf ecosystem under the influence of the Psittalia Wastewater Treatment Plant. Final report. Hellenic Centre for Marine Research, pp217 (in Greek)

Lindstrom, G., Pers, C., Rosberg, J., Strömqvist, J. and Arheimer, B. (2010) Development and testing of the hype (hydrological predictions for the environment) water quality model for different spatial scales. Hydrology Research, 41(3-4):295–319, 04.

Maderich, V., Ilyin, Y. and Lemeshko, E., (2015) Seasonal and interannual variability of the water exchange in the Turkish straits system estimated by modelling. Med Mar Sci, 16(2).

Petalas, S., Tragou, E., Mamoutos I.G., and Zervakis, V. (2022) Simulating the Interconnected Eastern Mediterranean – Black Sea System on Climatic Timescales: A 30-Year Realistic Hindcast. J Mar Sci Eng 10, 11:1786. doi:10.3390/jmse10111786

Shchepetkin, A.F., Mc Williams, J.C. (2005) The regional oceanic modeling system (ROMS): A split-explicit, free-surface, topography-following-coordinate oceanic model. Ocean Model., 9, 347–404.

Souza, J. M., B. Powell, A. C. Castillo-Trujillo, and P. Flament (2015) The Vorticity Balance of the Ocean Surface in Hawaii from a Regional Reanalysis, J Phys Oceanogr, 45, 424-440, doi:10.1175/JPO-D-14-0074.1

An expanded harmonic separation method to showcase the effects of nonlinearity on extreme irregular sea waves

G. Spiliotopoulos[1], V. Katsardi[1*]

[1]Department of Civil Engineering, University of Thessaly, Volos, Pedion Areos, 38334, Greece
[*]Corresponding author: vkatsardi@civ.uth.gr

Abstract

This work highlights the effects of nonlinearity on extreme sea wave events that rise during directional focused wave simulations in finite water depths. For this purpose, the fully nonlinear model "HOS-Ocean" by Ducrozet et al. (2016) is considered and compared with linear simulations. Nonlinear wave harmonics were extracted combining methods by Fitzgerald et al. (2014) and Hann et al. (2014), while expanding up to the 6th harmonic order, showing the contribution of various orders of nonlinearity on the formation of extreme wave crests. The results aim to offer transparency in understanding the physics underlying such extreme events.

Keywords Extreme Ocean Waves, Nonlinear Waves, Wave Crest Shape, Harmonic Separation

1 BACKGROUND

For the construction of nearshore and offshore structures, the prediction of the largest crest elevations is very important for the determination of any overtopping and the calculation of the wave loads acting on these structures. The affected area hit by an extreme event, is associated both with the crest height and width, affecting the stability and resilience of a structure or ship.

Previous work by Spiliotopoulos and Katsardi (2022) has investigated the crest shapes formed during nonlinear simulations. It was shown that "walls of water" are also formulated in finite water depth, as is the case for deep water extreme events (Adcock et. al., 2015). Indeed, the sea-state becomes more long-crested during the formulation of the extreme events in both focused and random simulations; all highly dependent on the directionality of the wavefield. The above is highlighted in the substantially increased crest width measured in the nonlinear simulations despite the decreased maximum crest elevations in intermediate water depths.

2 WAVE MODELLING AND SETUP

This section describes the theory behind the nonlinear model used in the simulations, how the model was set up to run and the choices behind the formation of the initial conditions for each simulation.

2.1 HOS-Ocean

HOS-Ocean is an open-source fully nonlinear model focused on simulating the evolution of a realistic wavefield incorporating the wave energy spread both in the various frequencies and the various directions, without any narrow-banded assumptions. It is based on the High-Order Spectral method, presented in the original work of West et al. (1989) and Dommermuth and Yue (1989).

2.2 Initial Conditions

The initial conditions for the simulations involved a JONSWAP amplitude spectrum with a peak period of T_p=10s, a peak enhancement factor of γ=2.5 and a linear amplitude sum of the frequency components equal to $A=\Sigma_{\alpha i}$=9.5m for perfectly focused wave events. The focused wave event simulated here is based on the averaged shape of a large linear wave event, which is the result of the dispersive and directional focusing of the underlying wave components, the celebrated quasi-determinism or *NewWave* theory (Boccotti, 1983, Lindgren, 1970, Tromans et al., 1991) and then directionally spread with the directional distribution by Mitsuyasu et al. (1975).

The frequency spectrum is used as an input into HOS-ocean and then converted to a wavenumber spectrum; an example presented in Figure 1 along with the evolved spectrum at η_{max}. The simulations were first conducted for infinite water depth conditions (Case *A9.5s45d*) and then for finite water depth

(15m, Case *A9.5s45d15*), keeping every other parameter the same. Every run was backward propagated linearly for 500s or $50T_p$ before being run forward nonlinearly. Due to the phase separation that was employed each simulation was re-run with 11 different phase-shifts.

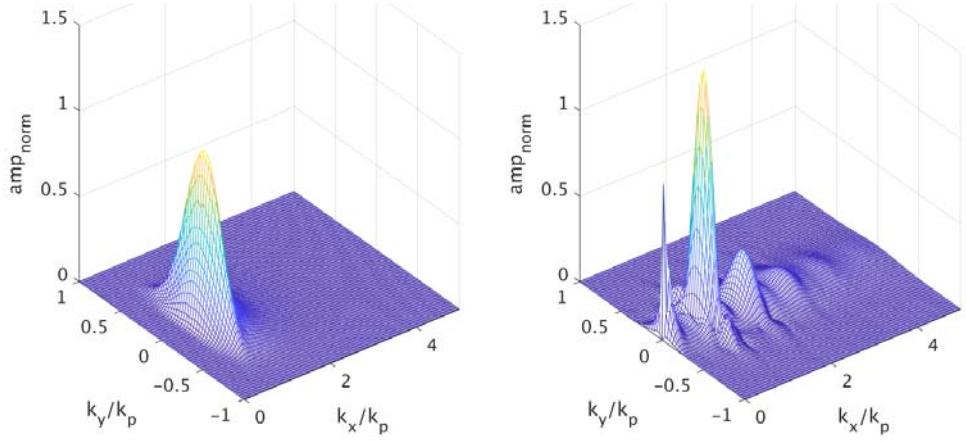

Figure 8. Input (left) and evolved at η_{max} (right) JONSWAP wavenumber spectra for case *A9.5s45d15*

2.3 Setting up the model

In the initial run consisting of all combinations of water depth and directionality, the discretization of the domain was N_x=512 and N_y=128 for the x and y directions respectively corresponding to *256* and *128* wave frequency and directional frequency components. The linear simulations were performed by compiling and running a binary of HOS-Ocean with HOS order M=1, while all nonlinear propagation was performed using a binary with HOS order M=5.

3 NONLINEAR HARMONIC SEPARATION

By combining the phase separation methods of Fitzgerald et al. (2014) and Hann et al. (2014), a more detailed method for expanding up to the 6th order harmonic is derived; according to Fenton (1990) the Stokes expansion up to 6th order expansion is as follows:

$$\eta(\theta) = f_{11}Acos(\theta) + f_{20}A^2 + f_{22}A^2cos(2\theta) + f_{31}A^3cos(\theta) + f_{33}A^3cos(3\theta) + f_{40}A^4 + f_{42}A^4cos(2\theta) + f_{44}A^4cos(4\theta) + f_{51}A^5cos(\theta) + f_{53}A^5cos(3\theta) + f_{55}A^5cos(5\theta) + f_{60}A^6 + f_{62}A^6cos(2\theta) + f_{64}A^6cos(4\theta) + f_{66}A^6cos(6\theta) + O(A^7) \quad (1)$$

This harmonic separation uncovers the underlying physics behind the nonlinear evolution of extreme waves, showing the effect each harmonic has on the formation of the extreme crest. Spiliotopoulos and Katsardi (2023) provides more details on the way the nonlinear harmonics are derived, with separation of the linear record ($\eta_{11}Acos(\theta)$) from the whole first order harmonic ($\eta_{11}Acos(\theta) + \eta_{31}A^3cos(\theta) + \eta_{51}A^5cos(\theta)$) as well.

4 DISCUSSION OF RESULTS

4.1 Crest and wave group shape

The most tangible method of measuring crest width is by viewing the front of the wave group and showing the difference in width between linear and nonlinear propagation. To further show these differences pseudocolor plots of the free surface elevation (Figure 2) are employed.

The crest differences can be described by the measurements of crest height, width and area. All measurements (Table 1) provide with the conclusion of a very significant increase in crest area in both deep and intermediate water. The total crest area increase is close to 50% for both cases, but the way it increases is drastically different. The crest width, or the total width of the disturbance in the wavefield of a focused wave is increased slightly in deep water conditions, while in intermediate water it is almost doubled. Due to the reduction in maximum crest height though, the total crest area increase is quite similar.

The nonlinear surface at η_{max} (Figure 2) shows the significant differences arising in the largest wave in deep water, which are consistent with the results of Adcock et al. (2015). Going into the intermediate

water surface, the trend of the wider crest is maintained, but the energy is spread more in the wavefield. The crest height is reduced compared to linear (Figure 3) but the maximum crest is even wider. The side slices show significant decrease in the maximum wave height in intermediate water while in deep water it remains similar with little reduction. This is consistent with the energy being distributed more widely across the wavefield, and it is also consistent with the results of Katsardi and Swan (2005, 2011) where the nonlinear propagation of both unidirectional and directional wavefields lead to large nonlinear "focused" waves with a significant decrease in maximum crest height compared to linear theory depending on the directionality of the wavefield.

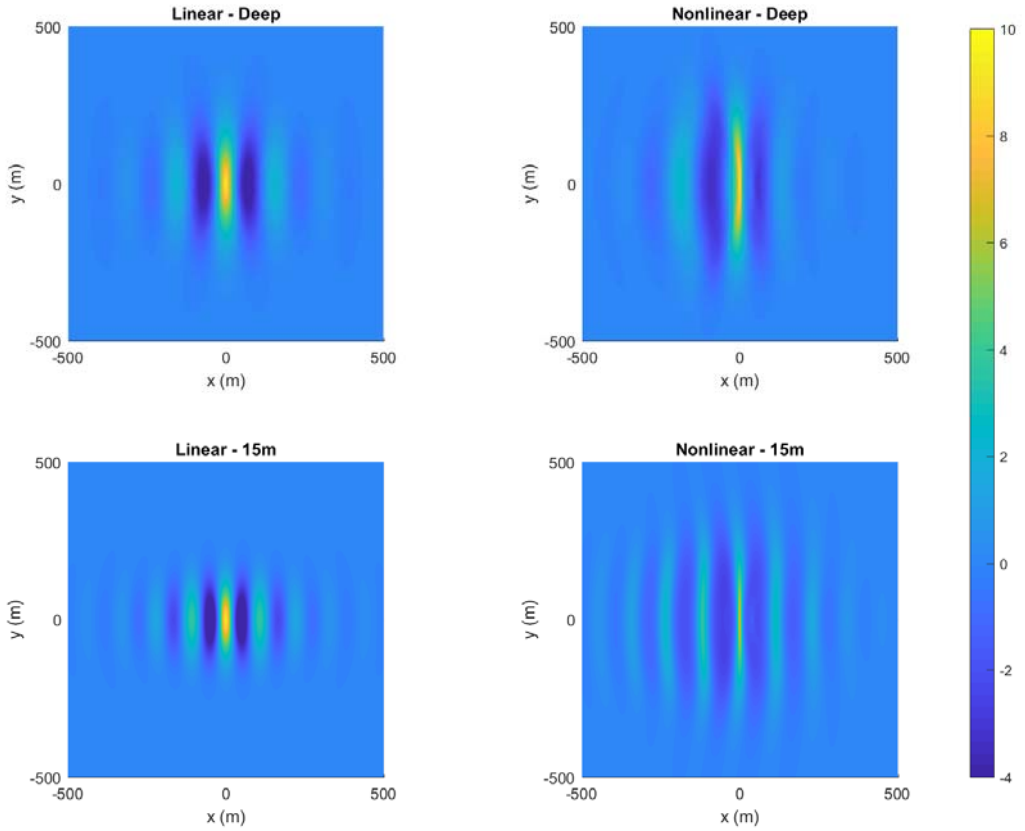

Figure 9. Linear and nonlinear simulations of the free surface elevation, $\eta_{max,}$ centred at the point of η_{max}.

Table 1. Crest Height, Width and Front Area

	Linear	Nonlinear	Change in %
Crest Height in m (Deep)	9.5000	9.7761	**+2.91**
Crest Width in m (Deep)	805.055	912.395	**+13.33**
Crest Area in m^2 (Deep)	2359.8	3474.1	**+47.22**
Crest Height in m (15m)	9.5000	7.1793	**-24.43**
Crest Width in m (15m)	490.721	926.921	**+88.89**
Crest Area in m^2 (15m)	1683.4	2548.1	**+51.37**

4.2 Harmonic Separation and Spectral Analysis

To further delve into the physical background, the harmonic separation method is employed and highlights the reasons behind the significant differences in intermediate water nonlinear propagation. In Figure 4 the contribution of each harmonic that was separated is shown as it relates to crest width/area. It is evident that the 1st order harmonic is responsible for the widening of the crest beyond its linear limits, while the other harmonics are mostly adding crest height at the point of η_{max}. What also causes a significant effect though, is the contribution of the 2nd and 4th order difference terms or "0th" harmonic, where it is the principal cause of crest height decrease, due to it being out of focus.

Figure 5 examines the energy transfers that occur during the formulation of the large "focused" wave event, comparing the separated first-order harmonic order, $\eta_{11} = f_{11}Acos(\theta)$, of the evolved nonlinear wavefield with the linear underlying spectrum. The narrowing on the *y*-axis of the evolved spectrum compared to linear indicates a decrease in directionality and a crest width increase for deep water. This narrowing is much more significant in intermediate water depth, where energy is transferred towards the peak of the spectrum while moving away from the more directional field.

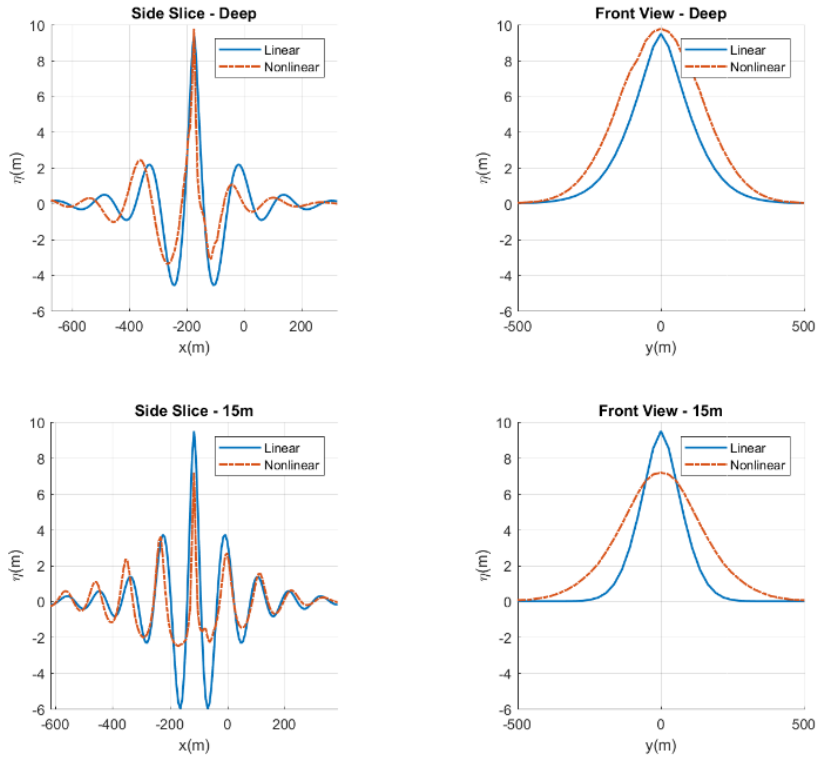

Figure 10. Side and Front views of the free surface elevation, η_{max}, comparing linear vs. nonlinear simulations. *Note:* the linear field is shifted at the point of the occurrence of the nonlinear η_{max}.

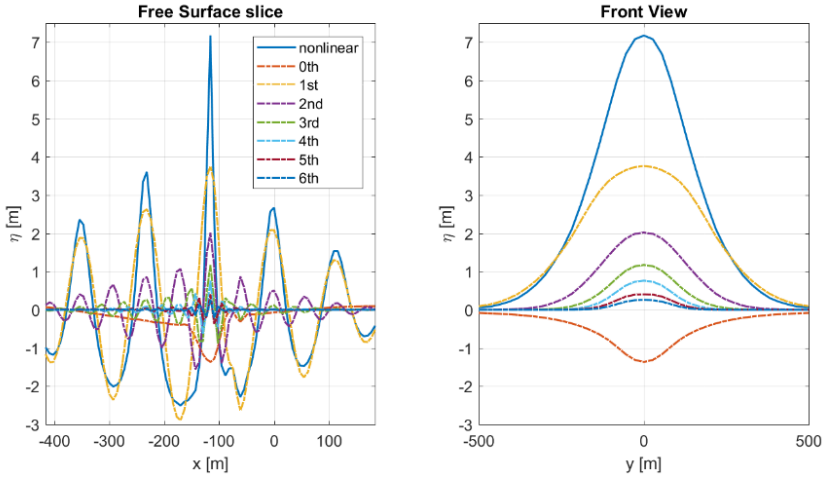

Figure 11. Phase separation of up to 6th order harmonics of case *A9.5s45d15* at η_{max}.

5 CONCLUSIONS

The harmonic separation uncovers the underlying physics during the nonlinear evolution of extreme waves, showing the effect each harmonic has on the formation of the extreme crest. The results show the pre-eminent effect of the free wave regime into the formation of the crest shape. This method, allows

firstly to highlight that the differences that arise during nonlinear formulation of extreme events between intermediate and deep water, can be attributed to the effects of wave energy transfers associated with the evolved underlying spectrum. Moreover, the method allows to understand which harmonics are responsible for the severe changes on the crest shape compared to linear simulations.

In all, the ability to separate nonlinear harmonics to a higher degree, allows the better understanding of the nonlinear wave dynamics, particularly in shallower water where the effects of higher order harmonics are more pronounced. The gradual effect of each separate harmonic during changes in the effective water depth, steepness and directionality has been now made clear. These findings will work towards a better prediction of the extreme waves in any sea-state leading to a more effective design of sea structures.

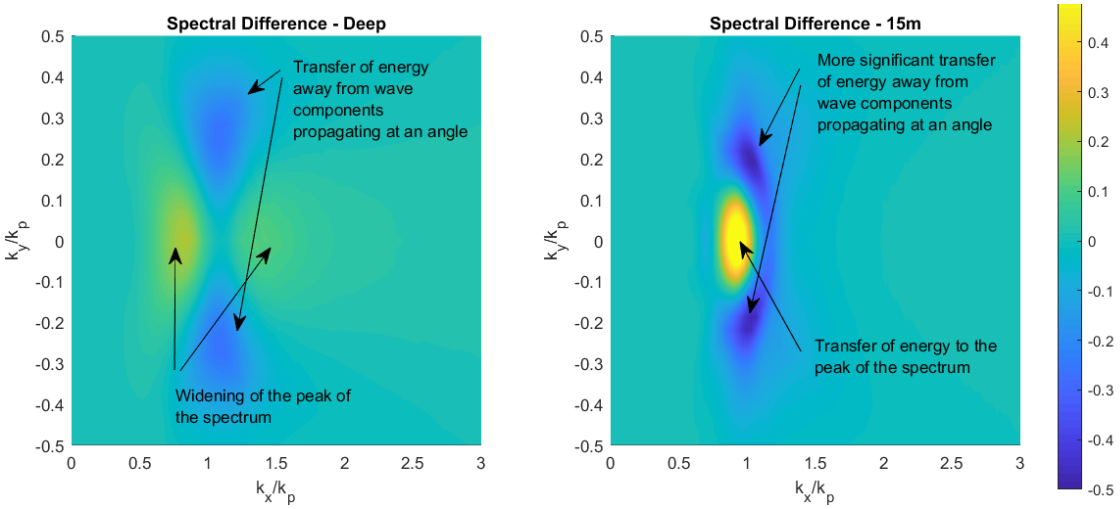

Figure 12. Energy transfers: the separated first-order harmonic order, η_{11}, of the evolved nonlinear wavefield with the linear underlying spectrum

References

Adcock TAA, Taylor PH, Draper S (2015) Nonlinear dynamics of wave-groups in random seas: unexpected walls of water in the open ocean, Proceedings of the Royal Society A, 471, 20150660.

Dommermuth D, Yue D. 1987 A high-order spectral method for the study of nonlinear gravity waves. Journal of Fluid Mechanics 184, 267–288.

Ducrozet G, Bonnefoy F, Le Touzé D, Ferrant P (2016) HOS-ocean: Open-source solver for nonlinear waves in open ocean based on High-Order Spectral method. Computer Physics Communications, 203, pp. 245–254.

Fenton JD (1990) Nonlinear wave theories, In B. Le Méhauté & D. M. Hanes, eds, The Sea – Ocean Engineering Science, Part A, pp. 3–25.

Fitzgerald CJ, Taylor PH, Eatock Taylor R, Grice J, Zang J (2014) Phase manipulation and the harmonic components of ringing forces on a surface-piercing column, Proc. R. Soc. A 470, 20130847.

Hann M, Greaves D, Raby A (2014) A new set of focused wave linear combinations to extract non-linear wave harmonics, In Proceedings of 29th Int. Workshop on Water Waves and Floating Bodies.

Katsardi V, Swan C (2005) An experimental study of shallow water wave statistics on mild bed slopes, Proceedings of the 30th International Conference on Offshore Mechanics and Arctic Engineering, OMAE2011, Rotterdam, The Netherlands.

Katsardi V, Swan C (2011) The evolution of large non-breaking waves in intermediate and shallow water. Part I: Numerical Calculations of Uni-Directional Seas. Proc. R. Soc. A 467, 778–805.

Spiliotopoulos G, Katsardi V (2022) Effects of Nonlinearity on the formulation of the Crest Elevation and the Crest Width of Extreme Waves in Random Seas, Proceedings of the 41st International Conference on Offshore Mechanics and Arctic Engineering, OMAE2022, Hamburg, Germany.

Spiliotopoulos G, Katsardi V (2023) Effects of Nonlinearity on the Crest Shape of Extreme Irregular Sea Waves Part 1: Nonlinear Harmonic Separation and Analysis, Submitted to Proc. R. Soc. A

West B, Brueckner K, Janda R, Milder M, Milton R (1987) A new numerical method for surface hydrodynamics. Journal of Geophysical Research 92, 11803–11824.

DMPCO 2023

e-Proceedings of the 2nd International Scientific Conference on Design and Management of Port Coastal and Offshore Works Thessaloniki, Greece, May 24-27 2023

Improved crest height predictions for nonlinear and breaking waves in large storms

I.Karmpadakis[1*], C. Swan[1]

[1]Department of Civil and Environmental Engineering, Imperial College London, SW7 2AZ, U.K.
[*]Corresponding author: i.karmpadakis@imperial.ac.uk

Abstract

The statistical distribution of zero-crossing crest heights represents a critical design input for a wide range of engineering applications. The present paper describes the development and validation of a new crest height model, suitable for application across a broad range of water depths. The purpose of this model is two-fold: first, to describe the amplifications of the largest crest heights arising due to nonlinear interactions beyond a second-order of wave steepness, and second, to incorporate the dissipative effects of wave breaking. Although these two effects act counter to each other, there is substantial evidence to suggest departures from existing models based upon weakly nonlinear second order theory; the latter corresponding to current design practice. The proposed model has been developed based on a significant collection of experimental results and a small subset of field measurements. It incorporates effects arising at different orders of nonlinearity as well as wave breaking in a compact formulation and covers a wide range of met--ocean conditions. Importantly, the new model has been independently validated against a very extensive database of experimental and field measurements. Taken together, these include effective water depths ranging from shallow water ($k_p d \sim 0.5$) to deep water ($k_p d > 3$) and sea-state steepnesses covering mild, severe and extreme conditions. The new model is shown to provide a significant improvement in crest height predictions over existing methods. This is particularly evident in the steepest, most severe sea--states which inevitably form the basis of design calculations.

Keywords extreme waves, nonlinearity, wave breaking, wave statistics.

1 INTRODUCTION

Traditional oil & gas applications, the rapidly expanding offshore wind energy sector, and different types of marine renewable devices are all examples for which accurate crest height calculations are essential. Importantly, such applications occur in a wide variety of deep, intermediate, and shallow water depths. As such, successful crest height predictions must be achievable across the full range of effective water depths.

In this context, the success of a crest height distribution is defined by its potential to incorporate both the amplifications associated with fully nonlinear wave-wave interactions and the dissipative effects of wave breaking. Evidence of the importance of these effects is given in Latheef and Swan (2013) and Karmpadakis et al. (2019); the former relating to deep water and the latter intermediate water depths. Whilst the findings in these studies were largely based upon laboratory data, Figure 13 provides characteristic examples based upon water surface elevations recorded in the field. In both subplots, the exceedance probability (Q) of the normalised crest heights (η_c / H_s) is compared to the most widely applied models in engineering design. These models include effects arising either at the first (linear) or second--order of wave steepness (Forristall, 2000); the latter representing the recommended practice in most design codes. Figure 13(a) shows data recorded at a deep-water location ($d = 110$ m), in which the largest crest heights are notably larger than the design (second order) predictions. In this case, design predictions appear to align with the lower bound of the 95% confidence intervals of the data. In contrast, Figure 13(b) shows measurements at a shallow water location $d = 7.7$ m). In this case the largest measured crest heights lie between the linear and second-order predictions; both models clearly misrepresenting the measured field data.

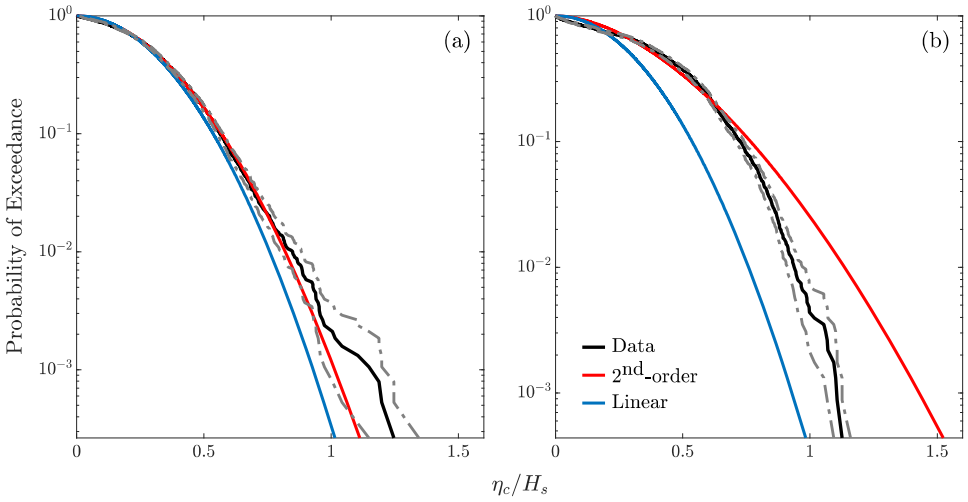

Figure 13: Examples of normalised crest height distributions, η_c/H_s recorded in the field and showing comparisons to linear and second-order predictions. The data relate to: **(a)** $H_s = 8\,m,\ T_p = 10\,s, d = 110\,m$ and **(b)** $H_s = 4.5\,m,\ T_p = 9.5\,s, d = 7.7\,m$. The 95% confidence intervals have been added for reference.

2 BACKGROUND

Having noted the practical importance of crest height predictions, it is not surprising that several studies have addressed their short-term distribution. Among these, the Rayleigh (Longuet-Higgins, 1952), Tayfun (Tayfun, 1980), Forristall (Forristall, 2000) and Tayfun & Fedele (Tayfun and Fedele, 2007) distributions are the most widely applied. These models cover effects arising at increasing orders of nonlinearity; the latter being expressed in terms of effective wave steepness (αk), where α represents the wave amplitude and k the wavenumber. Taken together, these models cover the first three orders of wave steepness and have been extensively validated and assessed using a wide range of wave conditions (Karmpadakis et al., 2019; Latheef and Swan, 2013) The key characteristics of the models are summarised below:

(a) Rayleigh distribution (Longuet-Higgins, 1952)

This is the first-order (linear) model that describes crest heights arising in a Gaussian sea-state. Its functional form is defined as:

$$Q(\eta_c) = \exp\left[-8\left(\frac{\eta_c}{H_s}\right)^2\right], \tag{1}$$

where Q is the exceedance probability, η_c the crest heights and H_s the significant wave height. The significant wave height is calculated using its spectral definition as

$$H_s = 4\sqrt{m_0} = 4\sigma_\eta, \tag{2}$$

where σ_η is the standard deviation of $\eta(t)$ and m_0 is the zeroth spectral moment. Using the variance spectrum, $S_{\eta\eta}(f)$, the spectral moments of order n are described by:

$$m_n = \int_0^\infty f^n S_{\eta\eta}(f)\mathrm{d}f \tag{3}$$

where f represents the frequency of individual wave harmonics. Bound by the assumption of linearity, the Rayleigh distribution is known to significantly under-estimate the largest crests, or those arising at small exceedance probabilities.

(b) Tayfun distribution (Tayfun, 1980)

Considering nonlinear effects arising at a second-order of wave steepness and a narrowband approximation, Tayfun (1980) derived an analytical model to describe the crest height distribution. This is given by:

$$Q(\eta_c) = \exp\left[-\frac{\left(-1+\sqrt{1+8\mu\frac{\eta_c}{H_s}}\right)^2}{2\mu^2}\right], \quad (4)$$

where μ is a measure of wave steepness that accounts for second-order nonlinearities. In its original form, μ was related to the sea-state skewness, λ_3 (Fedele and Tayfun, 2009).

(c) Forristall (3D) distribution (Forristall, 2000)

This model is the most widely applied in engineering practice. It has been derived as a fit to numerical simulations of second-order random wave theory (Sharma and Dean, 1981). Its functional form is a two-parameter Weibull distribution, defined as:

$$Q(\eta_c) = \exp\left[-\left(\frac{\eta_c}{\alpha H_s}\right)^{\beta}\right] \quad (5)$$

where the scale, α, and shape, β, can be found in Forristall (2000).

(d) Tayfun & Fedele distribution (Tayfun and Fedele, 2007)

This is a third-order model derived on the basis of a GramCharlier series expansion. This method of representation has previously been applied in the description of water surface elevations and related wave statistics by Longuet-Higgins (1963) and Bitner (1980), as well as wave envelopes and phasing by Tayfun and Lo (1990). The functional form of the model is given by:

$$Q(\eta_c) = \exp\left[-\frac{\left(-1+\sqrt{1+8\mu\frac{\eta_c}{H_s}}\right)^2}{2\mu^2}\right]\left\{1+\Lambda\left(\frac{\eta_c}{H_s}\right)^2\left[4\left(\frac{\eta_c}{H_s}\right)^2-1\right]\right\}, \quad (6)$$

where μ and Λ can be found in the original paper.

3 NEW MODEL

A vast dataset of experimental and field measurements has been analysed and employed in the development of a new model. For brevity these are not discussed here, but can be found in Karmpadakis and Swan (2022) The proposed model aims to:

- be applicable across a wide range of effective water depths extending from relatively shallow $(k_p d \approx 0.5)$ to deep $(k_p d > 3)$ conditions;
- capture the amplifications beyond the second order of wave steepness that have been observed in steep sea-states in both field and experimental measurements; and
- incorporate the effects of wave breaking, limiting the largest crest heights.

To achieve this, the new model has been formulated using the latest understanding of the physical processes that contribute to the formation of the largest crest heights. Any empirical coefficients included in the model have been calibrated using data from 2 experimental campaigns and a small subset of field measurements.

The proposed model is formulated by incrementally including the relevant physical processes that define the largest crest heights. As such, the development of the model begins with the most fundamental assumption of linear wave theory, with additional terms progressively added to represent nonlinear contributions and wave breaking. In adopting this approach, the validity of the model can be assessed at each step and further parametrisations can easily be achieved. The proposed model has the following form:

$$\eta_M = \left(\eta^{(1)} + \eta^{(2)} + \eta^{(NL)}\right) \cdot f_{Br}, \tag{7}$$

where η_M represents the crest heights predicted by the new model, $\eta^{(1)}$ is the linear contribution, $\eta^{(2)}$ is the second order contribution and $\eta^{(NL)}$ is the higher-order nonlinear contribution including all effects above second-order. The additional scaling term f_{Br} incorporates the effects of wave breaking. The parametrisation of the model can be found in Karmpadakis and Swan (2022).

Evidence of the success of the new model is provided in Figure 2. Each plot compares the distribution of measured crest heights with the predictions of the new model, the Forristall and Rayleigh distributions. All the sea-states considered belong to the calibration dataset and have been selected to represent the widest range of effective water depths. Figure 2(a) relates to a deep-water case with effective water depth $k_p d = 3.5$ and sea-state steepness $S_p \approx 0.04$. The observed amplifications above the Forristall model for $Q < 10^{-2}$ are well described by the proposed model. Figure 2(b) shows that the new model is equally successful for an intermediate water depth case with $k_p d = 1.53$ and $S_p = 0.03$. In both cases, the key feature of the sea-states is the increase of the measured crest heights above from the second order model.

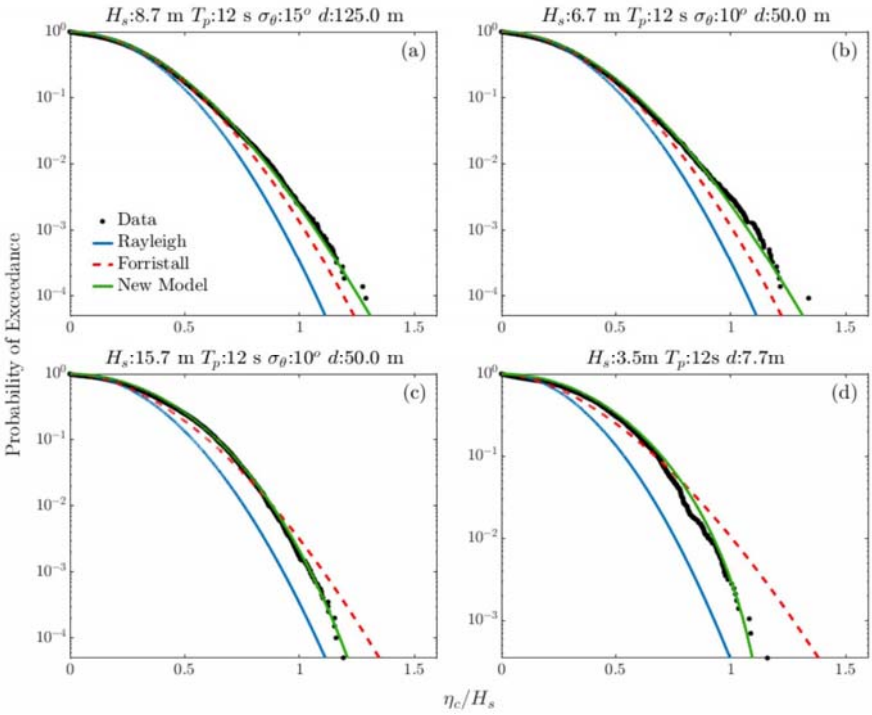

Figure 14: Normalised crest height distributions, η_c/H_s, showing comparisons to linear (Rayleigh), second-order (Forristall) and proposed model predictions. Subplots **(a)-(c)** correspond to experimental cases, while subplot **(d)** to field data.

Considering sea-states that are characterised by extensive wave breaking, Figure 2 (c) concerns an intermediate water depth case with $k_p d = 1.53$ and $S_p = 0.07$. In this case, the observed reduction in the tail of the distribution compared to second-order predictions is well described by the new model. Finally, Figure 2(d) presents results arising in a single storm event recorded at the shallowest measuring location in the field. The data correspond to a sea-state with $k_p d = 1.5$ and $S_p = 0.015$. Considering the shallow depth and the severity (steepness) of this case, it is clear that wave breaking plays a significant role. This becomes apparent by noting the large reductions in crest heights for $Q < 10^{-1}$ when compared to second-order predictions. More importantly, it is clear that the new model is successful in capturing this behaviour.

4 CONCLUSIONS

The new model has been shown to provide considerable improvements over existing models in the vast majority of cases considered. Most importantly, it has been shown to successfully predict the changes in the crest height distribution arising due to the nonlinear amplifications and the dissipative effects of wave breaking. The latter incorporating both steepness-induced wave breaking in deeper water and depth induced wave breaking in shallower water. Importantly, the proposed model is directly relevant to design calculations, being no more difficult to apply than the existing design standard. Moreover, the model is presented in a modular form in the sense that it parametrically describes individual physical processes separately before bringing everything together. In this respect, each component of the model can be assessed individually and improved (if necessary) as more data become available.

References

Bitner, E.M., 1980. Non-linear effects of the statistical model of shallow-water wind waves. Applied Ocean Research 2, 63–73.

Fedele, F., Tayfun, M.A., 2009. On nonlinear wave groups and crest statistics. J Fluid Mech 620, 221–239.

Forristall, G.Z., 2000. Wave Crest Distributions: Observations and Second-Order Theory. J Phys Oceanogr 30, 1931–1943.

Karmpadakis, I., Swan, C., 2022. A new crest height distribution for nonlinear and breaking waves in varying water depths. Ocean Engineering 266.

Karmpadakis, I., Swan, C., Christou, M., 2019. Laboratory investigation of crest height statistics in intermediate water depths. Proceedings of the Royal Society A: Mathematical, Physical and Engineering Sciences 475, 20190183.

Karmpadakis, I., Swan, C., Christou, M., 2019. Wave Height and Crest Height Distributions in Shallow Water: Analysis of Field Data. In: Goseberg, N., Schlurmann, T. (Hg.) (Eds.), Coastal Structures 2019. Bundesanstalt für Wasserbau, Karlsruhe, pp. 642–651.

Latheef, M., Swan, C., 2013. A laboratory study of wave crest statistics and the role of directional spreading. Proceedings of the Royal Society A: Mathematical, Physical and Engineering Sciences 469, 20120696–20120696.

Longuet-Higgins, M.S., 1952. On the statistical distribution of the heights of sea waves. J Mar Res 11, 245–266.

Longuet-Higgins, M.S., 1963. The effect of non-linearities on statistical distributions in the theory of sea waves. J Fluid Mech 17, 459.

Tayfun, M.A., 1980. Narrow-band nonlinear sea waves. J Geophys Res 85, 1548.

Tayfun, M.A., Fedele, F., 2007. Wave-height distributions and nonlinear effects. Ocean Engineering 34, 1631–1649.

Tayfun, M.A., Lo, J., 1990. Nonlinear Effects on Wave Envelope and Phase. J Waterw Port Coast Ocean Eng 116, 79–100.

DMPCO 2023

e-Proceedings of the 2nd International Scientific Conference on Design and Management of Port Coastal and Offshore Works Thessaloniki, Greece, May 24-27 2023

Statistical distribution of free water surface over a mild bed slope for extreme wavefields

I. Karmpadakis[1*], V. Katsardi[2], C. Swan[1], M.A. Tayfun[3]

[1]Department of Civil & Environmental Engineering, Imperial College London, SW7 2AZ, U.K.
[2]Department of Civil Engineering, University of Thessaly, Volos, 38334, Greece
[3]Independent researcher, Williamsburg, 23185, USA
[*]Corresponding author: i.karmpadakis@imperial.ac.uk

Abstract

This paper examines the probability density function (PDF) of free water surface elevations in coastal areas. The functional form and properties of PDFs of extreme storms propagating over a mildly sloping bathymetry are investigated. This is facilitated through comparisons between experimental measurements and a wide range of probability models; the latter including both analytical and empirical distributions. The incident wave conditions correspond to realistic storm spectra (JONSWAP) and have been simulated as long random timeseries of 60-hour duration. The length of the records is sufficient to provide an accurate description of distribution tails. Six sea-states with varying offshore steepness have been generated and measured at different cross-shore locations. The cross-shore evolution of the wavefield initially leads to the development of nonlinear harmonics, both at low and high frequencies, and a broadening of the wave spectrum. This is enhanced by wave breaking particularly at shallower water depths or steeper sea-states. These result in rapid deviations from Gaussian theory with respect to the PDFs of surface elevations. Available models are generally successful in capturing nonlinear evolution arising at a second order of wave steepness but cannot model the probability structure once a significant proportion of waves are breaking. In comparing the deviations between experimental data and model predictions, the best performing model is identified.

Keywords PDF, extreme waves, statistics, nonlinear waves, wave breaking.

1 INTRODUCTION

The efficient design of coastal and offshore structures directly depends upon the appropriate description of the design wavefield. Most commonly, the statistical distributions of zero-crossing quantities, such as wave heights and crest heights, are used to infer relevant kinematics and calculate design wave loads and responses. The PDF of water surface elevations provides the means to derive the distributions of zero-crossing waves. While Gaussian theory has been traditionally applied to approximate the PDF of water surface elevations, waves in coastal regions have a strong nonlinear behaviour and are prone to breaking. As such, more advanced models are required to provide an accurate representation of measured PDFs. Such models are discussed in the present paper and their accuracy is assessed on the basis of experimental data.

2 BACKGROUND AND EXPERIMENTAL SETUP

The vast majority of models used to describe the statistical distribution of these zero-crossing quantities (e.g., Boccotti, 1989; Forristall, 2000; Longuet-Higgins, 1952; Tayfun, 1980, 1990) are formulated on the assumption of a linear or weakly nonlinear wave field. In the former case, the probability density function (PDF) of the free water surface elevation, $\eta(t)$, assumes a Gaussian form. In the latter case, a variety of models provide corrections to the Gaussian structure based on finite wave steepness. Most of these models are based on a description of the wave field correct to a second order of wave steepness (Sharma and Dean, 1981). These clearly provide an improvement over linear predictions for sea-states in relatively deep water and moderate steepness. However, once increased wave nonlinearity and breaking become important, noteworthy deviations from the models are observed. Considering moderate deviations from Gaussian, Longuet-Higgins (1963) proposed the use of the Edgeworth series expansion

for the description of the PDF of the free water surface. This is a similar approximation to the Gram-Charlier but considering statistical cumulants rather than moments (Ochi, 1986). It was shown that an improved description of the PDF could be obtained for sea-states of larger steepness. Bitner (1980) followed the same approach and applied the Edgeworth series approximation for nonlinear waves in shallow water.

In adopting a Hermite moment model, Winterstein (1988) proposed to use response moments (e.g., skewness, kurtosis) to capture the non-Gaussian response contributions. These were made Orthogonal using the Hermite series. The hypothesis of this model is that the response of interest is conveniently related to a Gaussian process. Later, Winterstein et al. (1994) proposed some improvements in the model coefficients that reflect skewness and kurtosis minimising lack-of-fit errors.

Another alternative to model the PDF of $\eta(t)$ is to use the Gamma (Γ) distribution. This has the required properties in terms of skewness and tail behaviour to capture the shape of the observations. Again, this applies to non-breaking, moderately nonlinear wavefields. In fact, Bolles et al. (2019) and Majda et al. (2019) have used the Gamma distribution to provide comparisons between experimental and numerical data over abrupt bathymetric changes. A more systematic approach is the Exponential-Gamma distribution (Kobayashi et al., 1998). This model was derived to switch between a Gamma distribution in the surf zone to an exponential distribution in the swash zone. In the case of linear waves, it defaults to the standard Gaussian distribution. Laboratory measurements using random waves propagating up a 1/16 bed slope showed better agreement in the surf zone which deteriorated as the water depth was reducing.

More recently, (Tayfun and Alkhalidi, 2020)derived a PDF model appropriate to waves in the coastal zone following second order narrow-banded theory. It is known that the perturbation series expansion using wave steepness ($\epsilon = \alpha\kappa$) as an ordering parameter is no longer valid when the water depth becomes very shallow. This results in increased contribution of second-order terms in the surface elevation which is typically demonstrated as artificial secondary peaks on wave troughs. The emergence of these spurious peaks makes the standard second-order PDF (e.g., Socquet-Juglard et al., 2005; Tayfun, 1980) unusable in shallow water and its predictions potentially misleading. The model proposed by Tayfun and Alkhalidi (2020) hereafter called the M-NB model, proposes a correction to these effects and leads to a semi-closed form of the PDF. Comparisons between M-NB model with laboratory and field measurements showed that the model can accurately describe surface elevations in the shoaling and surf zones, despite the theoretical challenges.

In the present paper, we provide comparisons between the models described above and the experimental measurements of Katsardi et al. (2013). Details about the models can be found in the respective papers and Karmpadakis et al. (2023) - in press. Considering the experimental setup, measurements of free-water surface elevations are conducted at 11 location the wave flume shown on Figure 15. The seabed had a slope of 1:100 and the wave conditions corresponded to JONSWAP spectra. Each test condition was simulated for the equivalent of 60 hours in field scale, adopting Froude similarity scaling of 1:100. The test cases considered herein represent steep and extreme sea-states generated offshore at a water depth of $d = 50$ m, and are shown on Table 1. Details about the generation and analysis of measurements can be found in Katsardi et.al., (2013).

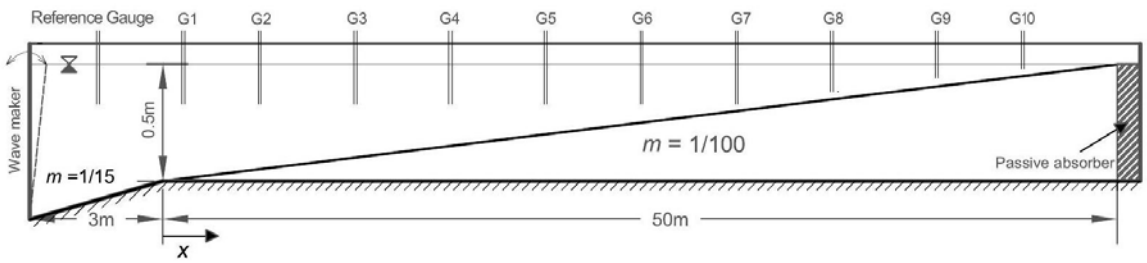

Figure 15. Schematic of the experimental apparatus

Table 1. Test cases considered in the experimental campaign. Conditions refer to the offshore boundary (G1).

Case	T_p [s]	H_s	$k_p d$	$1/2 H_s k_p$
Tp12s	12	7.5	1.53	0.115
Tp12m	12	11.9	1.53	0.183
Tp12l	12	14.7	1.53	0.225
Tp15s	15	7.9	1.11	0.088
Tp15m	15	12	1.11	0.133
Tp15l	15	14.7	1.11	0.163

3 RESULTS

Figure 15 shows comparisons of 4 models to laboratory measurements from the shallow end of the flume. We consider case Tp15s and cover effective water depths $k_p d \in (0.4, 0.7)$ to show nonlinear and breaking effects in a series of subplots. It is clear that in the deepest location, the PDF is positively skewed and deviates from the Gaussian model. All the models can capture these nonlinearities well.

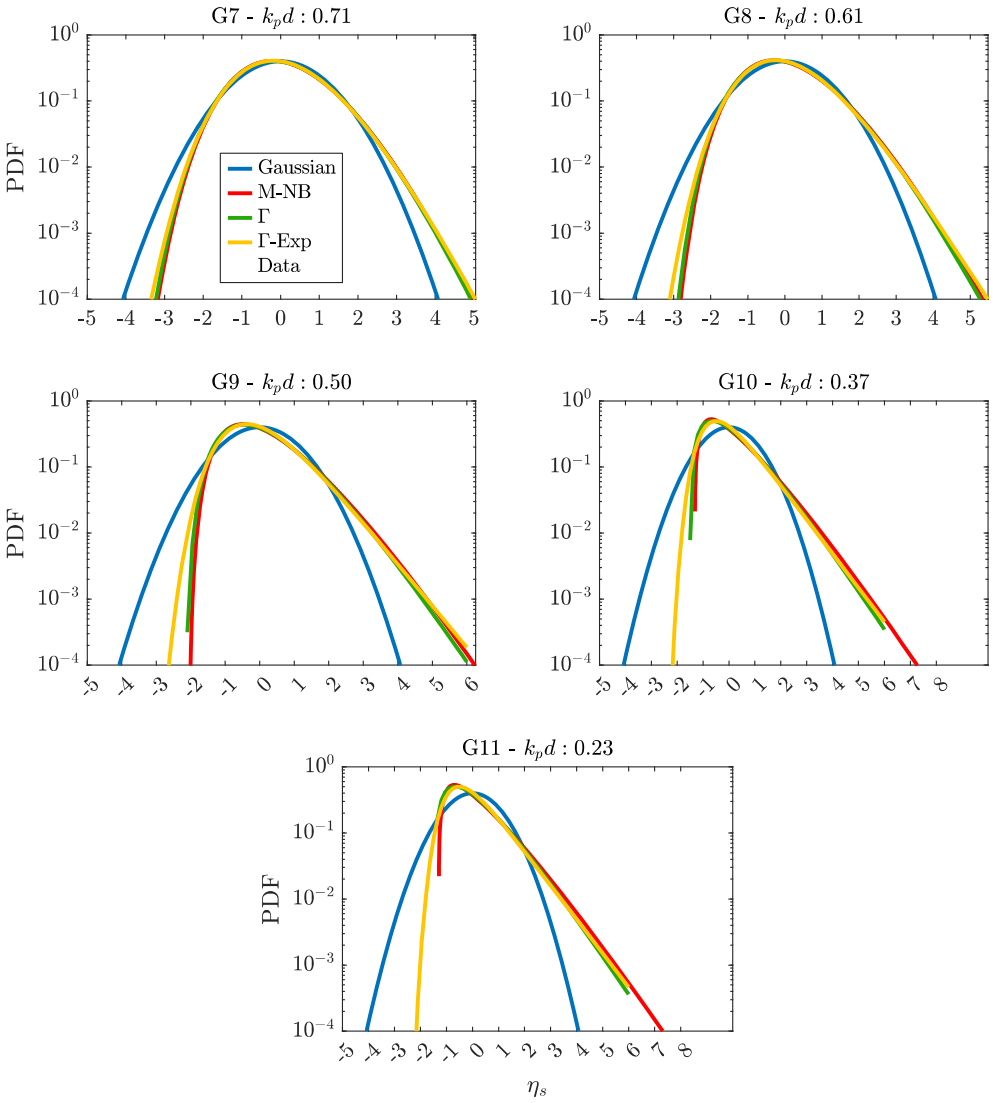

Figure 16: PDF of measured data with comparisons to the Gaussian, M-NB, Gamma, Gamma-Exponential models. The sublots correspond to wave gauges 7-11 in the shallow end of flume for case Tp15s.

Considering the steepness of this case, these are predominantly second order effects. Similar situations arise across the deeper end of the full dataset. As the water depth reduces, waves break and therefore their crest heights are reduced. This is manifested in all subsequent subplots as reductions in the positive displacement of η. None of the models is capturing these effects. Considering he negative displacements, we observe and increase in the elevations which is generally well captures by the M-NB and Gamma models.

With the aim to collect results presented in Figure 2 across all cases, we use the Kullbach-Leibler divergence to measure the deviation between models and data. The results are presented on Figure 17. The x-axis represents water depth and the error of each model in shown by a different color in the bar plots. These core results indicate that the error from the Gaussian distribution progressively increases as (a) water depth reduces and (b) steepness increases. Errors are much reduced when considering nonlinear models compared to the Gaussian and all models show similar magnitude in their errors. Errors are increasing with increasing steepness across all models. The M-NB and Winterstein models show the smallest error overall.

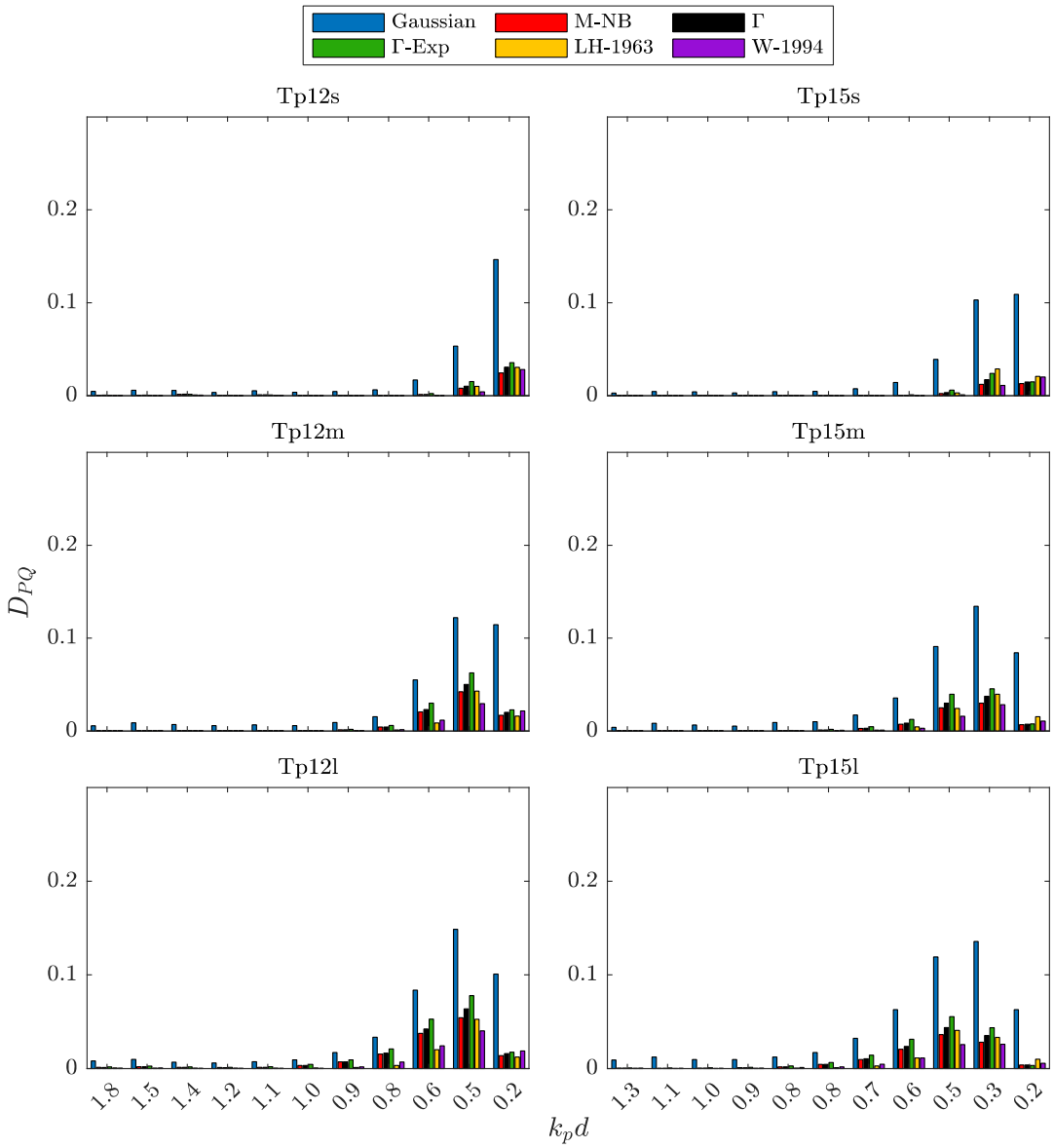

Figure 17: Divergence of each model against all experimental data.

4 CONCLUSIONS

The present paper has provided an analysis of the PDF of surface waves on a mild slope. The most appropriate theoretical models have been introduced and compared to extensive laboratory measurements of steep and extreme storms.

We find that the deviations from the Gaussian distribution in the shoarling and surf zone are noteworthy and should be taken into account. For moderately steep sea-states the M-NB model provides an easy-to-implement alternative. It shows similar errors as the Hermite model (Winterstein, 1994) but its functional form is much more amenable to extensions and manipulations. The Gamma distribution provides good results as well, but marginally increase errors compared to the two models above. The Gamma-Exponential and LH models showed larger deviations from measurements. Overall, the differences between the models are relatively small in terms of accuracy.

While part of the nonlinearity can be captured by the models presented herein, once extensive breaking is observed none of the models provides reasonable approximations. The errors are typically found in the positive displacements and have a profound effect of the sea-state statistics.

References

Bitner, E.M., 1980. Non-linear effects of the statistical model of shallow-water wind waves. Applied Ocean Research 2, 63–73.

Boccotti, P., 1989. On mechanics of irregular gravity waves. Atti della ASccad. naz. dei Lincei; A 386. Memorie/Classe di scienze fis., mat. e naturali. 19, 111–170.

Bolles, C.T., Speer, K., Moore, M.N.J., 2019. Anomalous wave statistics induced by abrupt depth change. Phys Rev Fluids 4, 1–8.

Forristall, G.Z., 2000. Wave Crest Distributions: Observations and Second-Order Theory. J Phys Oceanogr 30, 1931–1943.

Karmpadakis, I., Katsardi, V., Swan, C., Tayfun, M.A., 2023. Statistical distribution of free water surface over a mild bed slope for extreme wavefields. Coastal Engineering.

Katsardi, V., de Lutio, L., Swan, C., 2013. An experimental study of large waves in intermediate and shallow water depths. Part I: Wave height and crest height statistics. Coastal Engineering 73

Kobayashi, N., Herrman, M.N., Johnson, B.D., Orzech, M.D., 1998. Probability Distribution of Surface Elevation in Surf and Swash Zones. J Waterw Port Coast Ocean Eng 124, 99–107.

Longuet-Higgins, M.S., 1952. On the statistical distribution of the heights of sea waves. J Mar Res 11, 245–266.

Longuet-Higgins, M.S., 1963. The effect of non-linearities on statistical distributions in the theory of sea waves. J Fluid Mech 17, 459.

Majda, A.J., Moore, M.N.J., Qi, D., 2019. Statistical dynamical model to predict extreme events and anomalous features in shallow water waves with abrupt depth change. Proc Natl Acad Sci U S A 116, 3982–3987.

Ochi, M.K., 1986. Non-Gaussian random processes in ocean engineering. Probabilistic Engineering Mechanics 1, 28–39.

Sharma, J.N., Dean, R.G., 1981. Second-Order Directional Seas and Associated Wave Forces. Society of Petroleum Engineers Journal 21, 129–140.

Socquet-Juglard, H., Dysthe, K., Trulsen, K., Krogstad, H.E., Liu, J., 2005. Probability distributions of surface gravity waves during spectral changes. J Fluid Mech 542, 195–216.

Tayfun, M.A., 1980. Narrow-band nonlinear sea waves. J Geophys Res 85, 1548.

Tayfun, M.A., Alkhalidi, M.A., 2020. Distribution of sea-surface elevations in intermediate and shallow water depths. Coastal Engineering 157, 103651.

Tayfun, M.A.M., 1990. Distribution of large wave heights. J Waterw Port Coast Ocean Eng 116, 686–707.

Winterstein, S.R., 1988. Nonlinear Vibration Models for Extremes and Fatigue. J Eng Mech 114, 1772–1790.

Winterstein, S.R., Ude, T.C., Gudmud, K., 1994. Springing and slow-drift responses: Predicted extremes and fatigue vs. simulation. In: Proc., BOSS-94. pp. 1--15.

DMPCO 2023

e-Proceedings of the 2nd International Scientific Conference on Design and Management of Port Coastal and Offshore Works Thessaloniki, Greece, May 24-27 2023

Spatial evolution of wave height and crest height distributions of waves propagating over sloping coastal bathymetry

V. Bellos[1*], I. Karmpadakis[1], C. Swan[1]

[1]Department of Civil Engineering and Environmental Engineering, Imperial College London, SW7 2AZ, UK
[*]Corresponding author: vasileios.bellos18@imperial.ac.uk

Abstract

This paper concerns the cross-shore evolution of the statistical distributions of zero-crossing wave heights and crest heights associated with surface waves propagating over sloping beds. These are investigated through the analysis of laboratory data involving long random wave simulations in realistic sea-state conditions. Specifically, experimental simulations have been designed to isolate the contributions of key met-ocean parameters, such as the incident wave steepness, effective water depth and seabed slope. These results provide in-depth insights regarding the effects of nonlinearity, reduced water depth, bathymetric configuration, and the dissipative effect of wave breaking on the statistical behaviour of wave heights and crest heights. Their distributions are subsequently assessed against some of the most widely applied statistical models in engineering practice. The range of applicability of the models is investigated, and key deviations are observed. Taken together, the results presented herein have important practical implications for the design of coastal structures and operation of marine vessels.

Keywords Wave heights, Crest heights, Sloping bathymetry, Laboratory experiments.

1 INTRODUCTION

The short-term statistical distributions of wave heights and crests heights arising within specific sea-state conditions represent key inputs for the design and the reliability assessment of marine structures. Knowledge of the representative heights is imperative to a multitude of marine design calculations, such as designing to avoid wave-in-deck loading and wave overtopping. However, the distributions of wave heights and crest heights in extreme sea-states across a broad range of effective water depths and incident wave conditions has traditionally been notoriously challenging to capture, due to the competing physical mechanisms of nonlinear interactions and wave breaking. This has resulted in large uncertainty in the estimation of design conditions for many offshore and coastal installations. This paper aims to address these challenges, by providing a comprehensive laboratory investigation of wave height and crest height distributions across a wide range of water depths, incident wave conditions and bed slope configurations.

2 BACKGROUND

The two most commonly applied statistical models for crest heights are the Rayleigh (Longuet-Higgins, 1952) and Forristall (2000) distributions. The functional form of these models is given by:

$$Q(\eta > \eta_c) = \exp\left[-\frac{1}{a}\left(\frac{\eta_c}{H_s}\right)^{\beta}\right], \quad (1)$$

where Q is the probability of exceedance of the crest height η_c, H_s is the significant wave height and α and β are the scale and shape parameters of the distributions. These parameters have fixed values (α=1/8, β=2) for the Rayleigh model, while they vary as a function of the mean sea-state steepness and the Ursell number for the Forristall model; their exact description can be found in Forristall (2000).

The Rayleigh distribution is based on the assumption that a sea-state can be described using linear random wave theory, with a relatively narrow spectral bandwidth. As such, it tends to underpredict the largest waves in the ocean. In contrast, the Forristall model was developed based on a large set of numerical simulations using second-order random wave theory, enabling it to capture nonlinear changes in crest heights arising at a second order of wave steepness. While the latter has been extensively validated and is presently recommended practice (DNV 2010), recent findings (e.g. Karmpadakis et al. 2019) suggest that noteworthy discrepancies between the model predictions and real seas can arise.
The Rayleigh (Longuet-Higgins, 1952) distribution for wave heights is given by:

$$Q(h > H) = \exp\left[-2\left(\frac{H}{H_s}\right)^2\right], \quad (2)$$

where Q is the probability of exceedance of the wave height H. However, wind seas are naturally broad-banded. In practice, a broader spectral bandwidth leads to a de-correlation between the wave crests and troughs and, consequently, reduced wave heights. As such, the Rayleigh distribution has been shown to overestimate the measured wave heights (Forristall 1978). In addition, the increase in sea-state steepness leads to progressively larger deviations from the Rayleigh distribution. This is attributed to the occurrence wave breaking. Overall, the Rayleigh model appears to lack the essential physical input to describe the measured data.

To address some of the issues associated with shallow-water wave breaking, Battjes and Groenendijk (2000) proposed a composite Weibull distribution for wave heights. Its functional form is given by:

$$Q(h > H) = \begin{cases} \exp\left[-\left(\frac{H}{H_1}\right)^2\right] \; for\; H \leq H_{tr} \\ \exp\left[-\left(\frac{H}{H_2}\right)^{3.6}\right] \; for\; H > H_{tr}, \end{cases} \quad (3)$$

$$H_{tr} = (0.35 + 5.8\, tan\, \alpha)d, \quad (4)$$

where tan α is the average bed slope in the cross-shore direction and d is the local water depth. The normalising wave heights H_1 and H_2 can be obtained from Table 2 of Battjes and Groenendijk (2000).

Despite significant contributions of proposed wave height models in the literature, multiple issues remain unresolved. Particularly, Karmpadakis et al. (2020) highlighted that no single wave height model provides the best statistical description across a wide range of effective water depths and incident wave steepnesses. In addition, Katsardi et al. (2013) argued that none of the existing models can accurately describe the distribution of wave heights for the shallowest water depths. Building upon these results, the present study aims to provide physical insights into the evolution of the distributions of waves as they propagate towards the shoreline.

3 METHODOLOGY

The experiments presented herein were conducted in the Coastal Flume at the Hydrodynamics Laboratory of Imperial College London. All experimental test cases were generated using a JONSWAP spectral shape (Hasselmann et al. 1973) with a peak enhancement factor γ=2.5. These were chosen to represent realistic storm conditions in intermediate water depths (Jonathan and Taylor 1997), aiming to capture the stochastic nature of water waves. To investigate the effect of sea-state steepness on the wave height and crest height distributions, sea-states with varying significant wave height H_s, but constant peak period T_p were simulated. For each test case, 20 seeds with individual duration of 1024 s were generated. Adopting a scaling of 1:100, each random seed relates to a sea-state of approximately 3 hours at full scale. Each individual wave component was assigned an initial phase, chosen randomly from a uniform distribution lying in the range of [0,2π]. The methodology follows the phase-alignment approach described by Karmpadakis et al. (2019). This enables direct comparisons between individual waves in sea-states of different offshore wave steepness S_p and increases confidence in the description of the largest waves. The list of experimental cases is presented in Table 1. These correspond to 6 sea-states of increasing steepness propagating over 3 seabed configurations. The water depth regime ranges from intermediate to shallow, and the sea-states cover near-linear to highly nonlinear storms.

Table 1 List of experimental cases

Sea-state	T_p [s]	H_s [m]	$1/2H_sk_p$ [-]	s [-]	Wave gauges	k_pd [-]
A1	1.4	0.029	0.035	0	40	1.22
A2		0.057	0.070			
A3		0.086	0.105	1/15	40	⋮
A4		0.115	0.140			
A5		0.139	0.170	1/50	80	0.47
A6		0.156	0.190			

The unidirectional random waves were allowed to propagate over the uniform bed slopes while being sampled using a densely packed array of sensors. The fine spatiotemporal resolution of the measurements is paramount to the quantification of the competing physical mechanisms of nonlinear amplification and wave breaking, as well as their dependence on the investigated parameters. A zero-

crossing analysis was performed on the time-histories of each random simulation. The results for each sea-state were concatenated and re-ordered to derive probability distributions extending to $Q \approx 10^{-4}$.

4 RESULTS

4.1 Effects of Nonlinearity and Effective Water Depth

To isolate the individual contributions, comparisons are performed between cases while varying the parameter of interest. This is presented in Figure 1. For a single bed slope case and individual S_p cases, the wave height and crest height distributions for different k_pd values are compared.

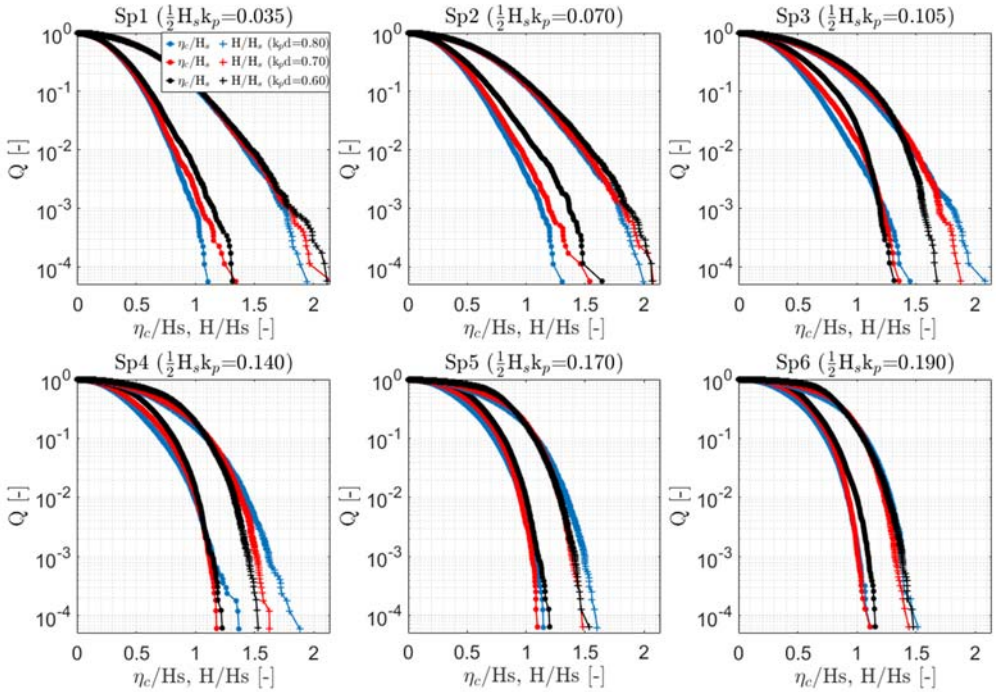

Figure 1 Normalised crest height (η_c/H_s) (•) and wave height (H/H_s) (+) distributions for selected k_pd values. Each subplot corresponds to gradually increased S_p. All cases refer to bed slope s=1/50

An overall increase in crest heights is observed as k_pd reduces. This is particularly prominent for S_p1:2 where there is no or very limited wave breaking. This is explained by the enhancement of the nonlinear characteristics of waves, manifesting as higher and steeper crests and shallower and flatter troughs. Conversely, we see a downward shift with a reduction in the largest crest heights in the tail of the distributions for S_p3:4. This is attributed to the occurrence of wave breaking. However, this trend reverses for S_p5:6 at the shallowest k_pd region. This is explained by the relatively larger reduction in H_s with which the distributions are normalised, compared to the crest heights of the surviving waves.

A similar limiting trend is observed for wave heights. However, its onset occurs at progressively higher Q, leading to a substantial reduction in the tail of the distributions. The wave heights only seem to increase in the tail of the distributions for S_p1:2. For higher S_p, the distributions fall back as k_pd reduces, as the effect of wave breaking becomes more prominent. This occurs progressively earlier as S_p increases. However, they eventually reach a point where they fall on top of each other and no longer reduce, barring small differences in the tail of the distributions. This is explained by the relative balance between the wave heights throughout the corresponding Q range and the overall H_s evolution.

By extending this analysis to the full range of effective water depths, and for different sea-state steepness and bed slope combinations, the relative importance of each individual parameter can be determined.

4.2 Spatial Evolution

In order to investigate the spatial evolution of the distributions, the crest heights and wave heights at the representative $Q=10^{-3}$ are normalised by their corresponding offshore values. This is demonstrated in

Figure 2. The relative increase and decrease are represented by the blue and red bars respectively. We observe that the crest heights increase as k_pd reduces for S_p1 where there is no wave breaking. This trend persists up to S_p4, until a balance is reached between nonlinear amplifications and wave breaking; after which they start to decrease. This equilibrium point occurs progressively earlier for increasing S_p. For S_p5:6 where there is excessive wave breaking, the crest heights are consistently lower than their corresponding offshore. The crest height evolution generally follows the trend of the H_s evolution; however, their ratios can vary significantly depending on the steepness, particularly for the shallowest locations. For S_p1 and reduced k_pd, the increase in crest heights is significantly larger than the increase in H_s. Conversely, for S_p5:6 and reduced k_pd, H_s is further reduced compared to the reduction in crest heights. This has significant implications for the normalised distributions.

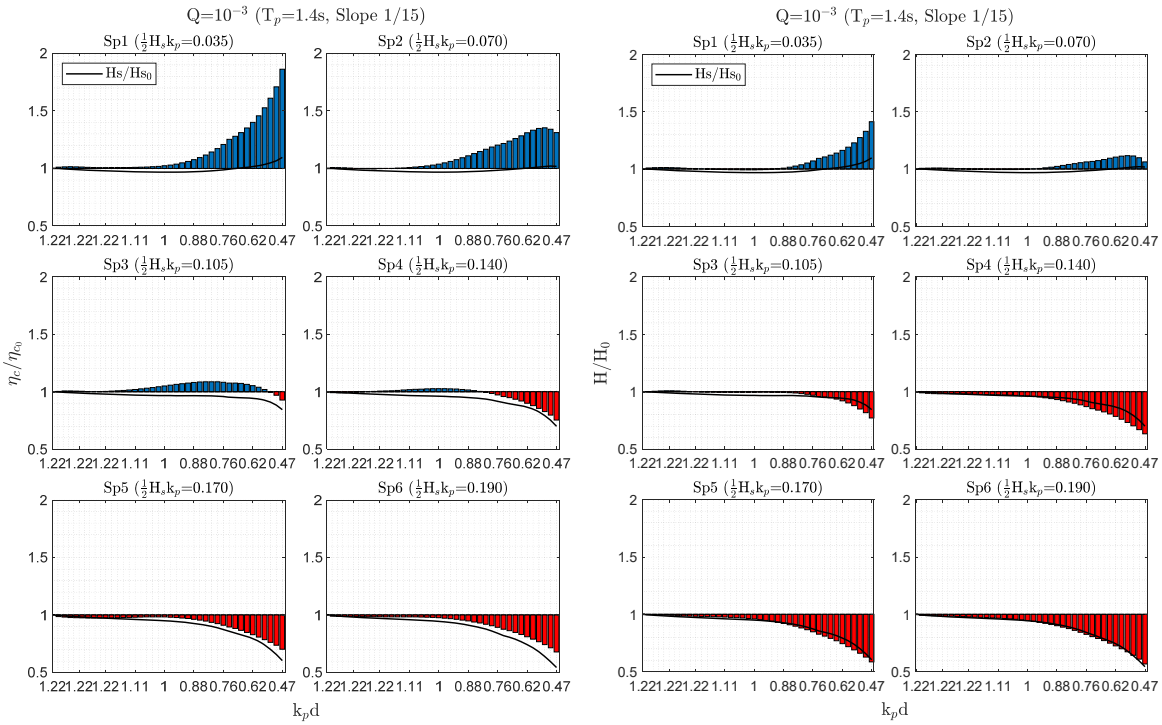

Figure 2 Spatial evolution of η_c, H and H_s. Each subplot corresponds to gradually increased S_p

The wave heights increase as k_pd reduces for S_p1 where there is no wave breaking. This is attributed to wave shoaling. However, we also note the largest relative increase of wave heights compared to H_s for S_p1 and reduced k_pd. The wave heights also increase as k_pd reduces for S_p2, until they start decreasing due to the onset of wave breaking. A relative equilibrium occurs for most of the slope for S_p3, until they start reducing at the shallowest-depth region. The reduction trend is consistent throughout the rest of the higher S_p. The wave height evolution generally follows the trend of the H_s evolution.

4.3 Assessment of Statistical Models

In order to assess the range of applicability and the accuracy of the existing statistical models, the wave height and crest height distributions of the experimental data are compared against the corresponding model predictions. Figure 3(a) shows the normalised crest height distributions compared to the Rayleigh and Forristall distributions, for k_pd=0.60. For S_p1, the models underestimate the data, indicating amplifications above second order of wave steepness. For S_p3, the Forristall model overpredicts the data for the tail of the distribution, owing to the increased influence of wave breaking. To investigate this further, Figure 3(b) shows the cross-shore evolution of crest heights at selected Q levels with comparisons to the corresponding second order Forristall predictions. Significant deviations are observed for S_p1 as k_pd reduces, as the data increase at a faster rate compared to the model predictions. However, this trend reverses for S_p3, as the increase is limited by the dissipative effect of wave breaking. This occurs progressively earlier for lower Q, resulting in the data falling below the model predictions for low k_pd values. Similarly, Figure 3(c) compares the corresponding wave height distribution to the

Rayleigh and the Battjes & Groenendijk model predictions. The latter appears to be very successful for both S_p cases. Upon closer examination of the cross-shore evolution in Figure 3(d), it is shown that while the model can adequately incorporate the effect of wave breaking, some deviations still occur. This is not surprising, as the model is calibrated to experimental data involving specific combinations of offshore steepness and bed slope angle.

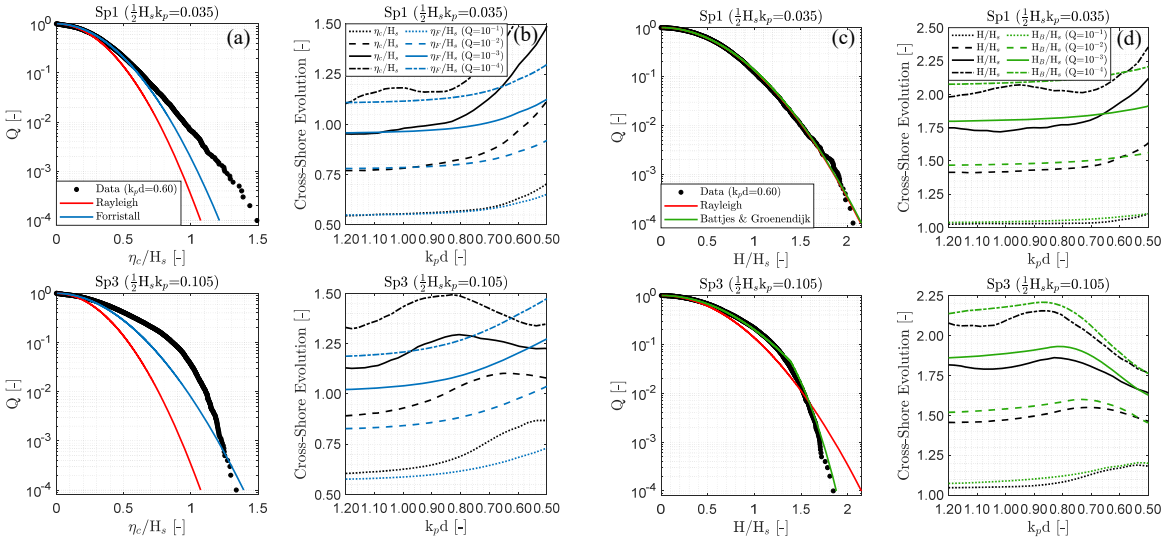

Figure 3 (a,c) n_c/H_s and H/H_s (•) at k_pd=0.60, (b,d) Cross-shore evolution of n_c/H_s and H/H_s (—). Comparisons to the corresponding Rayleigh (—), Forristall (—) and Battjes & Groenendijk (—). Top/bottom rows: S_p1/S_p3

5 CONCLUDING REMARKS

Taken together, the results presented herein provide important physical insights into the spatial evolution of the wave height and crest height distributions as the waves propagate towards the shoreline. Importantly, they demonstrate the relative effects of the competing mechanisms of nonlinear amplifications and wave breaking, and their dependence on the effective water depth, bed slope angle and incident wave conditions. Finally, assessment of some of the most widely applied statistical models reveals their range of applicability, as well as significant deviations as the effective water depth reduces.

References

Battjes JA, Groenendijk HW (2000) Wave height distributions on shallow foreshores. Coast Eng 40 (3):161–182. doi:10.1016/S0378-3839(00)00007-7

DNV (2010) DNV-RP-C205 Environmental Conditions and Environmental Loads. Det Norske Veritas

Forristall GZ (1978) On the statistical distribution of wave heights in a storm. J Geophys Res 83 (C5):2353. doi:10.1029/JC083iC05p02353

Forristall GZ (2000) Wave Crest Distributions: Observations and Second-Order Theory. J Phys Oceanogr 30 (8):1931–1943. doi:10.1175/1520 0485(2000)030,1931:WCDOAS.2.0.CO;2

Hasselmann K et al. (1973) Measurements of Wind-Wave Growth and Swell Decay during the Joint North Sea Wave Project (JONSWAP). Ergnzungsheft Dtsch Hydrogr Z R, A(8) (12):95

Jonathan P and Taylor PH (1997) 'On Irregular, Nonlinear Waves in a Spread Sea', J Offshore Mech Arctic Eng.119 (1):37. doi:10.1115/1.2829043

Karmpadakis I, Swan C and Christou M (2019) Laboratory investigation of crest height statistics in intermediate water depths. Proc R Soc A 475 (2229). doi:10.1098/rspa.2019.0183

Karmpadakis I, Swan C and Christou M (2020) Assessment of wave height distributions using an extensive field database. Coast Eng 157. doi:10.1016/j.coastaleng.2019.103630

Katsardi V, de Lutio L and Swan C (2013) An experimental study of large waves in intermediate and shallow water depths. Part I: Wave height and crest height statistics. Coast Eng 73:43–57 doi:10.1016/j.coastaleng.2012.09.007

Longuet-Higgins MS (1952) On the Statistical Distribution Of Sea Waves. J Mar Res 11 (3):245–266

Assessment of extreme sea state conditions for offshore aquaculture projects

T.H. Soukissian[1*], F. Karathanasi[2,3], C. Zeri[1], S. Zervoudaki[1]

[1] Institute of Oceanography, Hellenic Centre for Marine Research, 46.7 km Athens-Sounio Ave., 190 13 Anavyssos, Greece

[2] Hellenic Hydrocarbons and Energy Resources Management Company, Dim. Margari 18, 115 25, Athens, Greece

[3] Cyprus Marine and Maritime Institute, Vasileos Pavlou Square, 6023, Larnaca, Cyprus

[*]Corresponding author: tsouki@hcmr.gr

Abstract

In this work, the estimation of design sea states is performed for an offshore area in the Evoikos Gulf, Greece. This area was selected for the development of an offshore aquaculture farm in the framework of the MATISSE project, whose aim is to design offshore fish cage nets, made of innovated materials that operate safely under extreme sea conditions. In this context, the wind and wave climate analysis and the estimation of extreme wave heights is of utmost importance for the rational design of the fish cages. Since the dynamic behaviour of any marine structure, and especially of the non-symmetric ones, strongly depends on the directional characteristics of sea states, directionality is taken into account as a covariate in the estimation of the n −year ($n = 10,20, \ldots ,100$) design value of significant wave height, H_S. The wind and wave climate analysis is based on long-term time series of wind speed and direction at 10 m above sea level and high spatial and temporal resolution wave spectral parameters data. A comparison between the extreme values obtained from the directional and the non-directional extreme value analysis of H_S revealed important differences, rendering the offshore fish cage design a very delicate procedure, especially in non-unidirectional sea states.

Keywords: directional extremes, design sea state, offshore aquaculture, peak-over-thresholds.

1 ENVIRONMENTAL CONDITIONS AT THE STUDY AREA

The wider study area refers to the southern part of Evoikos Gulf, see Figure 18a. In the northern part, it is connected to the North Evoikos Gulf through the Euripus Strait, while in the southern part it is directly connected to the Aegean Sea. The bottom slopes of the area are relatively mild with intermediate water depths. In particular, the central and northern parts of N. Evoikos Gulf have a maximum depth around 70 m, while the deeper parts are located in the southern part (towards the Aegean side) with depths up to 90 m (Petalioi and Marmari Bay). At distances closer to the Aegean Sea, the depths increase smoothly, while in the area of the islet of Mantilos the depths range between 90 m and 110 m; see also Figure 18b. The wider climatic conditions in the region do not deviate from the Mediterranean characteristics of the country. In the maritime activities of the area (and especially in the southernmost part of it), there is relatively intense tourist activity especially during the summer season. In addition, the South Evoikos Gulf is a characteristic fishing ground with a long tradition, while at the same time, due to the relatively mild wave climate and the favorable hydrodynamic conditions, it presents aquaculture activities, which in the past were a source of conflicts. For more details, see also Mente et al. (2007).

HCMR has carried out field studies of the hydrodynamic regime of the wider region. Coastal traffic is mainly shaped by the wind and, the occasional strong, inflow sea currents that enter this area from the channel between Kea and Makronissos Isl. In contrast to the N. Evoikos Gulf, tidal circulation is very weak, with current velocities of the order of 0.01-0.02 cm/s. Seasonal variability is characterized by homogeneous flows during winter, spring, and strongly stratified in summer and autumn. Thermocline extends to depths from 20 m to 50 m.

There is a limited number of publications on the environmental/ecological conditions of the southern Evoikos Gulf. On the other hand, in the northern part of the gulf, the environmental conditions are well-known; the wider area lacks significant sources of pollution, while there is a significant dispersion of potential pollutants combinational with the hydrodynamic regime of the study area. In the southern

opening of the bay (known as Cavo D'Oro straits), the environmental conditions are considered to resemble the state of the open sea (Aegean Sea) due to the strong channel effect. See also Sustainable Mediterranean, Special Issue 71, (2015). Proceedings of the International Conference "Environmental Perspectives of the Gulf of Elefsis. A Mediterranean case study where Science meets the Society", Stamou, et al. (1999), Angelidis, Aloupi, (2000), Valavanidis (2018), http://www.fao.org/3/S6087E/S6087E03.htm, Tsirogiannis, et al. (2019).

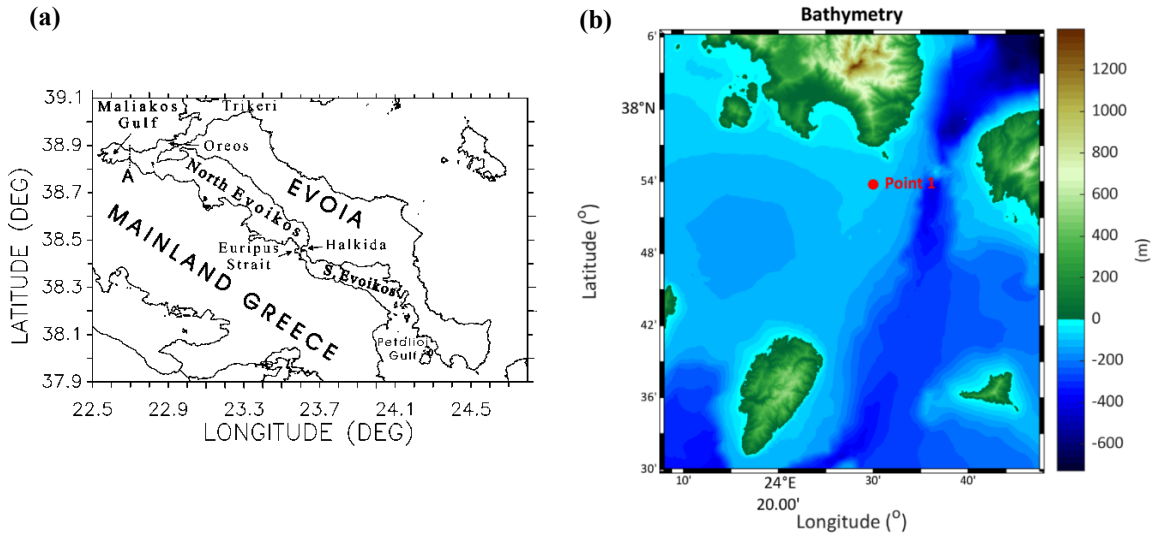

Figure 18. **(a)** The wider area of interest, **(b)** bathymetry of the examined area

The geographical coordinates of Point 1 are (24.50° E, 37.90° N), and it is located at the south of the uninhabited islet of Mantilou; see also Figure 18b. The depths in the study area vary between 95 m and 100 m, with relatively smooth bathymetry within a radius of 5 km from this point. The area is characterized by key geographical and environmental features that are important when considering the installation of offshore fish cages. In particular, it is close to important transit centers (e.g., the port of Karystos is 14.5 km away and the port of Lavrio about 45 km) and it is very close to the important fish auction of Keratsini (Piraeus). In addition, the examined point is located away from the passenger ship routes, while the wider area is characterized by a relatively mild to moderate wave and wind climate. Moreover, there is no other intense or competitive use of maritime space in the region, so there are not expected to be significant socio-economic impacts due to conflicts of other marine uses.

2 WIND AND WAVE DATA AND CLIMATE ANALYSIS

2.1 Wind data and wind climate

The wind data (wind speed and direction at 10 m above sea level) that are used in the present analysis were derived from the ERA5 reanalysis product of the European Centre for Medium-Range Weather Forecasts (ECMWF) and is the most up-to-date reanalysis available today in long-term reanalysis data. The associated atmospheric numerical model uses historical records and 4D-Var data assimilation in order to produce estimates of the climate and its various parameters, on a global scale. ERA5 data is generated by the ECMWF, and currently dates back to 1959. The data are available and freely accessible from the Copernicus website https://cds.climate.copernicus.eu/#!/home. Compared to the previous ERA-Interim analysis, ERA5 is based on improved numerical models and data assimilation schemes, has a more sophisticated resolution with ~30 km for the horizontal dimension, 137 levels in the vertical dimension and 1 hour time step, that renders this data source very adequate for this study. ERA5 wind data have been validated by a number of studies. Wind speeds have been compared with lidar measurements at different heights with very good results. ERA5 wind and wave data have also been validated after comparison with ERA-Interim data and advanced measurements from offshore platforms (Soukissian and Sotiriou, 2022). In this work, the time series of wind speed at a height of 10 m above sea level is analyzed. The duration of the wind time series covers a period of 16 years (2005–2020). Let

us note that the statistical estimation of the wind speed in the study area was based on spatial interpolation where the inverses of the squares of the distances of the six nearest points from the study site were used as weights. To this end, the whole analysis was carried out on components u and v of wind speed in order to correctly estimate the wind direction θ_U at the point of interest as well. The wind climate of the area is relatively intense (Table 3). The most intense wind speeds occur during January, February and August. The prevailing wind directions are NNW and SE, while the strongest winds in the area blow from the N, NW, NW and SW directions. See also Figure 19a. On a monthly basis, wind climate is affected by the etesian winds during summer. The maximum value of U_W is ~19.14 m/s, while the long-term mean value is ~5.79 m/s. See also Figure 19b.

Table 3. Long-term wind speed statistics at Point 1

	Descriptive statistics									
Variable	N	m	min	max	5% $quant.$	95% $quant.$	s	CV	Sk	Ku
U_W	140256	5.789	0.023	19.138	1. 436	11.072	3.056	52.788	0.412	0.479

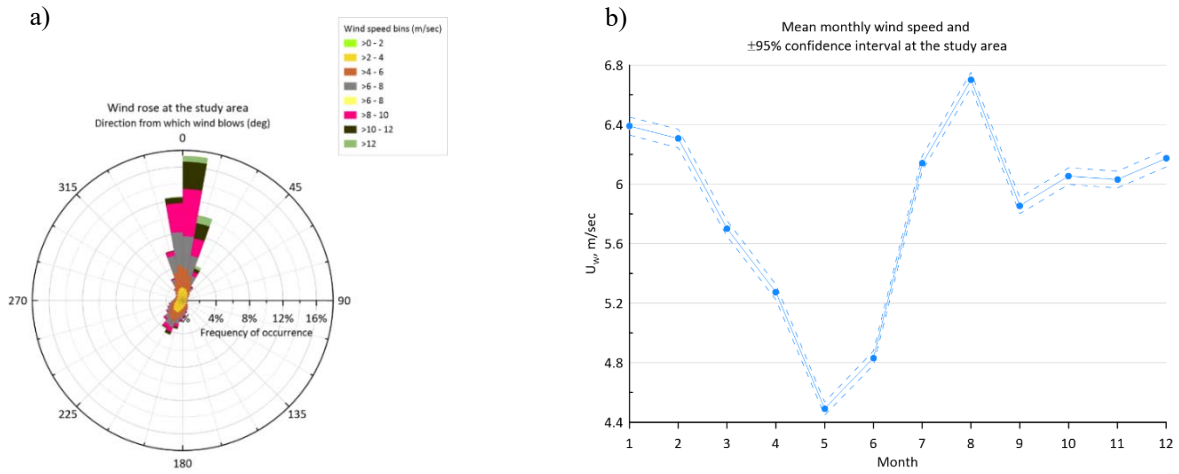

Figure 19. **(a)** Wind rose, **(b)** mean monthly wind speed at the study area

2.2 Wave data and wave climate

The wave data is a hindcast product of the Mediterranean Sea Waves forecasting system, which is based on the third-generation WAM Cycle 4.5.4 wave model, covering the period 2006–2018, Korres et al. (2021), http://marine.copernicus.eu/services-portfolio/access-to-products/. Wave parameters are provided every hour in a grid of spatial horizontal resolution of 1/24° x 1/24° for the Mediterranean Sea region, an analysis suitable for describing the wave potential in the Aegean Archipelago, a semi-enclosed basin with geographical and topographical peculiarities. The WAM model fully resolves the wave energy equation including refraction and breaking due to bathymetry and the presence of sea currents, wave breaking, wind influence on wave generation, bottom friction effect, nonlinear four-way wave interactions and wave propagation in space and time.

Table 4. Main linear wave statistical characteristics at Point 1

	Descriptive statistics									
Variable	N	m	min	max	5% $quant.$	95% $quant.$	s	CV	Sk	Ku
H_S	113220	0.613	0.078	4.177	0.116	1.562	0.484	78.988	1.549	3.147
T_P	113220	4.707	1.000	12.285	2.209	7.628	1.677	35.624	0.275	-0.467

At each grid point, the wave spectrum is solved in 24 directions and 32 frequencies. The wave climate of the area is rather mild, with mean significant wave height $\boldsymbol{H_S}$ 0.6 m and mean spectral peak period

$\boldsymbol{T_P}$ 4.7 s. The examined area is dominated mainly by wind waves (Table 4). The prevailing sea state directions are NNW and SW, see Figure 20a. During winter, the highest values of mean $\boldsymbol{H_S}$ and $\boldsymbol{T_P}$ occur, exceeding 0.7 m and 5 s, respectively, while the lowest values occur during May and June, where the mean values of $\boldsymbol{H_S}$ do not exceed 0.4 m and the mean values of $\boldsymbol{T_P}$ range between 4 s and 4.2 s. See also Figure 20b.

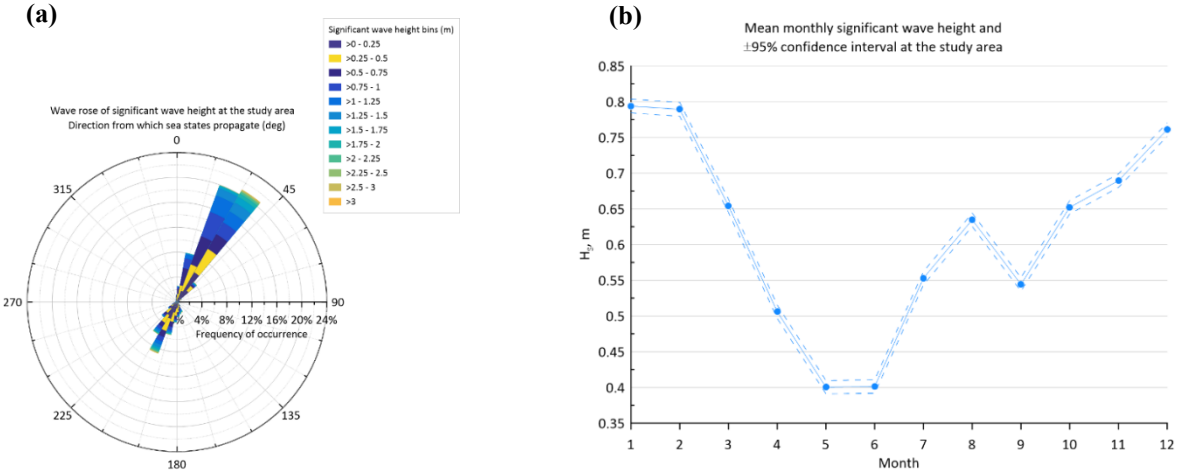

Figure 20. **(a)** Wave rose, **(b)** mean monthly significant wave height at the study area

3 DIRECTIONAL EXTREME VALUE ANALYSIS OF SEA STATES

Since the dynamic behaviour of marine structures strongly depends on the directional characteristics of sea states, directionality is taken into account as a covariate in the estimation of the n −years design value of H_S, see e.g., Philippe et al. (2013). The modelling of the extreme values of H_S is based on the Generalized Pareto (GP) distribution with its unknown parameters expressed as a function of sea-state direction θ, as proposed by Jonathan & Ewans (2007). In this context, the form of the GP distribution is as follows:

$$G(y;\xi,\sigma^*) = 1 - \left[1 + y\frac{\xi(\theta)}{\sigma^*(\theta)}\right]^{-1/\xi(\theta)}, \sigma^* > 0, \tag{1}$$

for $y > 0$, $1 + y\frac{\xi}{\sigma^*} > 0$ and $\sigma^* = \sigma + \xi(u - \mu)$, when $\xi \neq 0$. In the above relation ξ and σ^* are the shape and scale parameters, respectively. u is an appropriately defined threshold value that allows the GP distribution to be used to describe extremes. To describe the directional dependence of the unknown σ^* and ξ parameters, a Fourier series extension was applied, which ensures a relatively smooth periodic behavior of these estimates with respect to wave direction θ. The general form of the Fourier series for the parameters ξ and σ^* is given as follows:

$$\sum_{k=0}^{p}\sum_{b=1}^{2} A_{bk}t_b(k\theta) \text{ and } \sum_{k=0}^{p}\sum_{b=1}^{2} B_{bk}t_b(k\theta), \tag{2}$$

respectively, where $k = 0, \dots, p$ denotes the order of the Fourier model, A, B are the unknown coefficients for the parameters ξ and σ^*, respectively, and t_1, t_2 are the functions of sine and cosine, respectively. Indicatively, for the Fourier 1st order model, six unknown coefficients should be estimated. The unknown coefficients A_{bk} and B_{bk}, $b = 1,2$, $k = 0, \dots, p$, are estimated by applying a penalized maximum likelihood method, proposed by Karathanasi et al. (2020). The use of a variable threshold in the application of the peaks-over-threshold method is considered reasonable. For the estimation of the threshold in this case, an automated method proposed by Thompson et al. (2009) was chosen. The rationale of this method is based on the use of a range of threshold values and the study of its behavior

in relation to the actual threshold value. In Figure 21, the design values of 20, 50 and 100 years for H_S in relation to the wave direction θ are presented. For a return period of 50 years, the highest design value of H_S (5.82 m) corresponds to the SSW sector [183°,190°] and the second highest value (5.39 m) to the NNE sector [26°,30°].

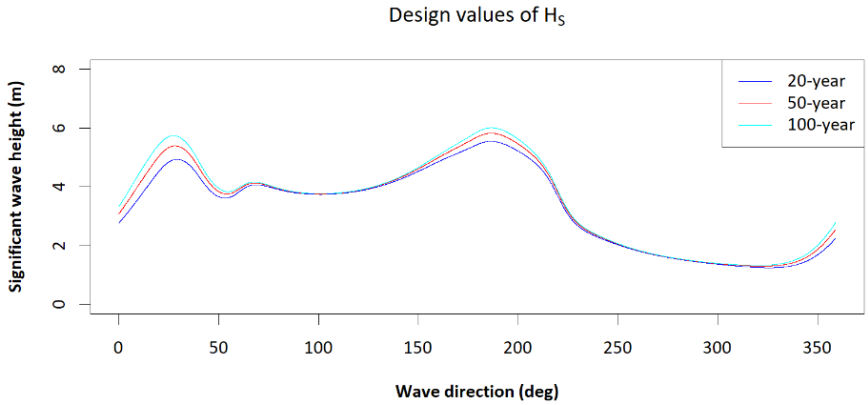

Figure 21. Directional design values of H_S

Acknowledgements

This work received funding in the context of the project "Feasibility Study of Innovated Materials for Offshore Fish Cage Nets – Numerical and Experimental Investigation Under Realistic Loading Conditions, MATISSE" (2019-2022) with reference code MIS 5045859, funded by the Hellenic General Secretariat of Research and Technology.

References

Angelidis MO, Aloupi M (2000) Geochemical Study of Coastal Sediments Influenced by River-Transported Pollution: Southern Evoikos Gulf, Greece, Marine Pollution Bulletin, 40(1), 77-82

Philippe M, Babarit A, Ferrant P (2013) Modes of response of an offshore wind turbine with directional wind and waves. Renewable Energy, 49: 151-155.

Jonathan P, Ewans K (2007) The effect of directionality on extreme wave design criteria. Ocean Engineering, 34(14-15), 1977-1994.

Karathanasi F, Soukissian T, Belibassakis K (2020) Directional Extreme Value Models in Wave Energy Applications. Atmosphere, 11, 274.

Korres G, Ravdas M, Zacharioudaki A, Denaxa D, & Sotiropoulou M (2021) Mediterranean Sea Waves Reanalysis (CMEMS Med-Waves, MedWAM3 system) (Ver. 1) Data set. Copernicus Monitoring Environment Marine Service (CMEMS).

Mente E, Pantazis P, Neofitou C, Aifanti S, Santos MB, Oxouzi E, Bagiatis V, Papapanagiotou E, Kourkouta V, & Soutsas K (2007) Socioeconomic interactions of fisheries and aquaculture in Greece: A case study of South Evoikos Gulf, Aquaculture Economics & Management, 11:3, 313-334.

Soukissian T, Sotiriou M-A (2022) Long-Term Variability of Wind Speed and Direction in the Mediterranean Basin, Wind, 2, 513-534.

Stamou AI, Noutsopoulos C, Pipilis KG, Gavalaki E, Andreadakis A (1999) Hydrodynamic & water quality modelling of southern Evoikos Gulf, Greece, Global Nest: the Int. J., 1(2), 131-141.

Thompson P, Cai Y, Reeve D, Stander J (2009). Automated threshold selection methods for extreme wave analysis, Coastal Engineering 56, 1013–1021.

Tsirogiannis E, Angelidis P, Kotsovinos N (2019) Mixing Characteristics under Tide, Meteorological and Oceanographic Conditions in the Euboean Gulf Greece. Computational Water, Energy, and Environmental Engineering, 8, 99-123.

Valavanidis A (2018) Environmental Pollution of Marine and Costal Areas in Greece. Review on marine pollution, monitoring and quality of seawater.

Simulation of wave time series with a vector autoregressive method

A. Valsamidis[1*], D.E. Reeve[2], Y. Cai[2]

[1] Aktomechanics, 38 Olympiados Street, Postcode 54633, Thessaloniki, Greece
[2] College of Engineering, Swansea University, Swansea SA1 8EN, Wales, United Kingdom
[*]Dr Antonios Valsamidis : valsanton@hotmail.com

Abstract

Joint time series of wave height, period and direction are essential input-data to computational models which are used to simulate beach evolution that occurs diachronically at specific case studies. Here, an innovative vector autoregressive, (VAR), stochastic model is presented which may be applied for the simultaneous simulation of wave height, period and direction time series which extend over a specific time span; the output times series having the similar average value, marginal distribution, autocorrelation and cross-correlation structure as the original. To this end, nearshore wave records offshore of Littlehampton in south-east England over the period from 01/07/ 2003 to 30/06/2016 were used to test the method. Results showed a satisfactory degree of stochastic agreement between original and simulated time series.

Potential applications of the current research work include the creation of multiple realisations of wave time series for Monte Carlo modelling of shoreline evolution, thereby allowing ensemble prediction of shoreline response to a variable wave climate. Importantly, our method recreates both the correct marginal and joint statistics, as well as the lag correlation properties of the original multi-variate time series.

Keywords VAR model, wave time series, autocorrelation, cross-correlation.

1 INTRODUCTION

Bivariate autoregressive models were used to simulate time series of significant wave height and mean period (C. G. Soares and C. Cunha 2000). Borgman and Scheffner (1991) introduced a technique for simulating time series of wave height period and direction, accounting for seasonality on a monthly mean basis. Recently, Cai (2011) and Cai et al. (2008) generalized the work of Cario and Nelson (1998) and Biller and Nelson (2003) in order to obtain simulated multivariate time series. However, these methods are suitable for stationary time series only, and hence, they cannot be used to generate the non-stationary wave conditions observed widely in practice. Although Cai et al. (2014) developed a simulation method for non-stationary time series, this method is suitable only for short non-stationary time series due to relatively high computational cost, and therefore is not suitable for wave time series corresponding to long-term measurements.

The purpose of this paper is to present a method that can recreate both the statistics and lag correlation properties of a non-stationary, multivariate wave record spanning many years. The data used here are multivariate and nonstationary. The work of Cai (2011) is generalized so that non-stationary sea condition data of any required length can be obtained.

2 METHODOLOGY

Let $E_t = (E_{1t}, E_{2t}, E_{3t})$ denote observed sea condition data, where E_{1t} is wave height, E_{2t} is wave period and E_{3t} is wave direction. As discussed in the previous section, the main objective of this research is to obtain simulated sea condition data, denoted by $\tilde{E}_t = (\tilde{E}_{1t}, \tilde{E}_{2t}, \tilde{E}_{3t})$, such that the simulated data will have similar trend, seasonality, autocorrelation structures and marginal distributions with those of the observed E_t. This is a very challenging task due to the fact that the sea condition data are non-stationary, and three sea condition variables need to be dealt with simultaneously.

To achieve this, the work of Cai (2011) has been generalized so that the non-stationarity of the data could also be dealt with. The basic idea of the proposed approach includes the following steps: (i) Remove the trend and seasonality from the observed data to produce stationary series; (ii) Apply the method of Cai (2011) to the series obtained from step (i); (iii) Include the trend and seasonality into the simulated data obtained from step (ii) to generate the final simulated data that we require. Fig. 1 illustrates the methodology that was followed for the simulation of the wave data:

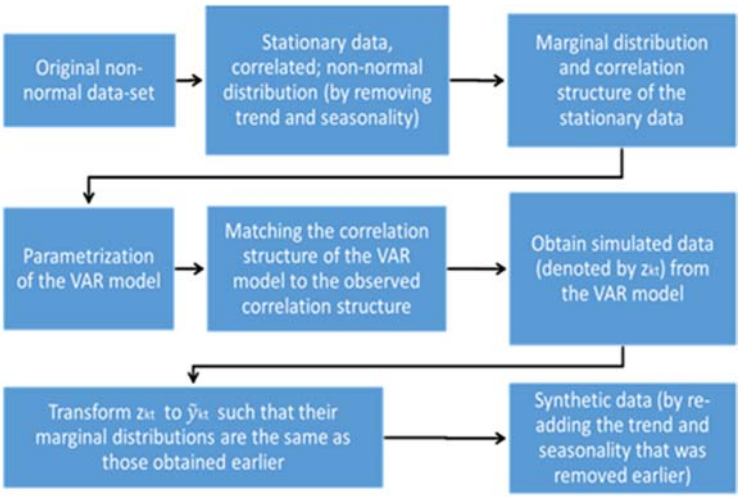

Figure 1. Schematic representation of wave data generation according to the methodology presented in this study

3 CASE-STUDY

Our case study is Littlehampton in south-east England (Fig. 2).

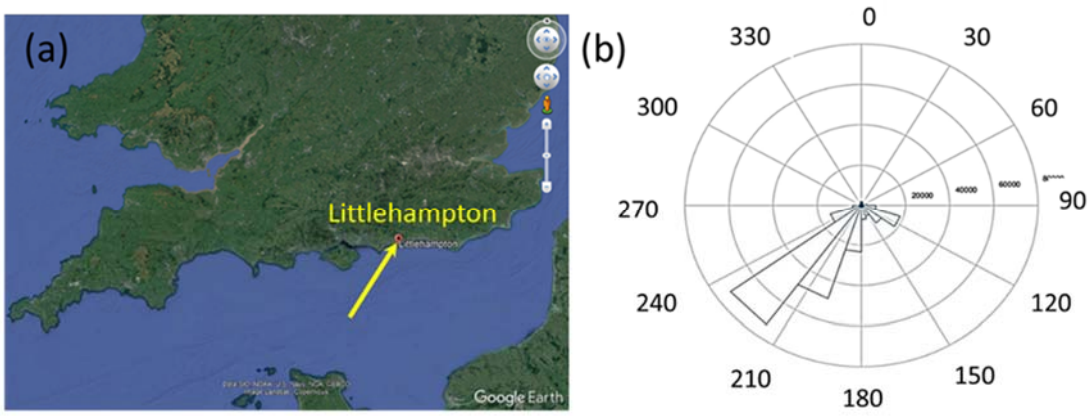

Figure 2. Littlehampton beach lies in south-east England; (b) A rose diagram illustrating the predominant wave direction from southwest to northeast

Wave-data near Littlehampton beach were available from the Channel Coastal Observatory, a UK organization which collects and archives coastal field-data. Specifically, recorded time series of significant wave height (Hs), peak wave period (T_p) and wave direction (α) between the 1st of July 2003 and the 30th of June 2016 were available every 30 minutes at a location 4 miles SSE of Littlehampton harbour entrance with a Datawell Directional WaveRider Mk III buoy moored in approximately 10m water.

The wave records were averaged to create a time series of daily wave conditions, as our focus is on storm events rather than wave by wave fluctuations. The daily data are shown in Fig. 3, in which seasonality is visually evident.

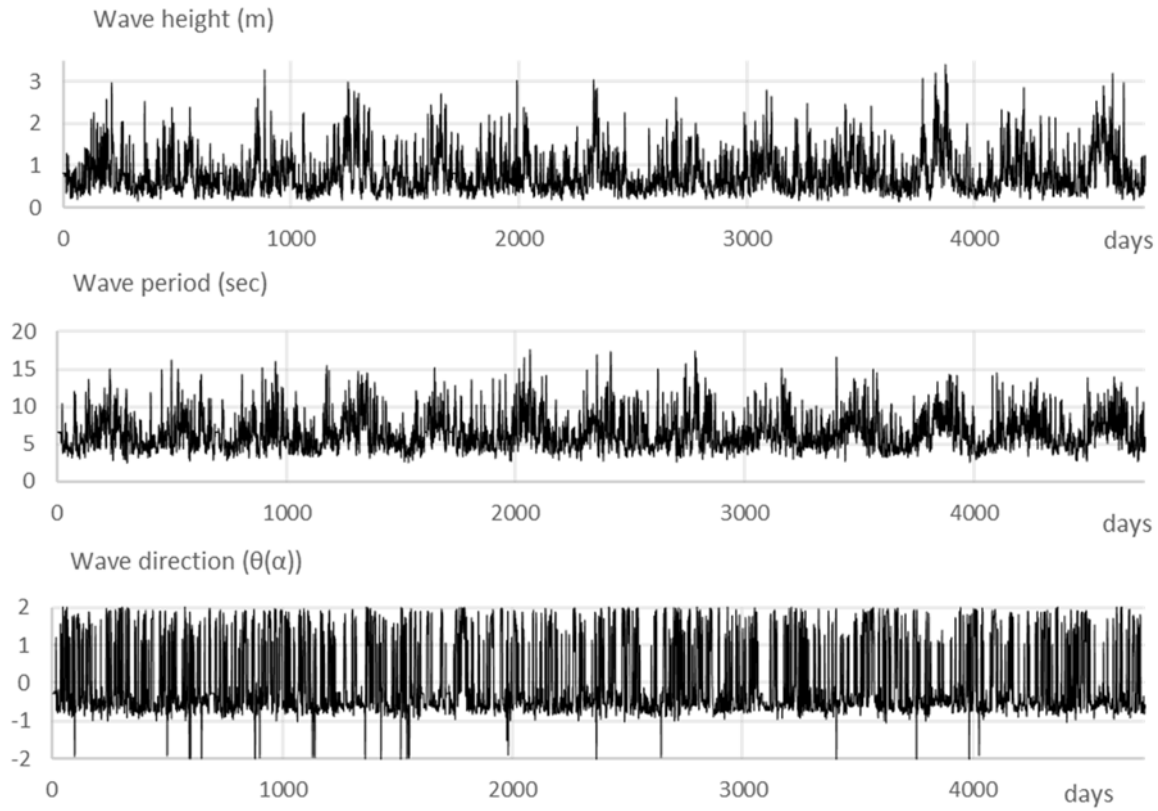

Figure 3. Time series of the observed daily wave-data

4 RESULTS

Following detrending and deseasonalizing of the original wave data, the stochastic trend was removed as well to achieve data stationarity. Then, the marginal distribution and the autocorrelation and cross-correlation structure of the stationary data was calculated. This information was used to assess the correlation matrices *Γ(h)* of the VAR stochastic model, considering standard normal distribution for each one of the three VAR time series corresponding to the original wave time-series. These correlation matrices were used for yielding the other parameters of the VAR model (by solving the system of equations denoted as Equation 2). Then, the VAR time series were produced. Consequently, the Rackwitz-Fiessler method (Rackwitz and Fiessler 1978) was applied to derive the detrended and deseasonalized synthetic data. Finally, statistical trend, stochastic trend and seasonality which were initially removed, were re-added to create the output synthetic time-series $\tilde{E}_t$. The latter had the same length in time with the original data, covering this way, the same time period. The whole process of wave data simulation is schematically described in Fig. 1.

If the method is working well the simulated data $\tilde{E}_t$ should have similar statistical properties as those of observed data E_t . To check the distributions, we estimated the marginal distributions of the observed and simulated data respectively by using the non-parametric kernel estimation method (Silverman 1986). The estimated marginal density functions are given in Fig. 4, where the black curves correspond to the observed data and the red curves correspond to the simulated data. It can be seen that the two density functions are very close for all three sea condition variables. Specifically, the values of each estimated density function at equally spaced 40 points in the range of the estimated distributions was calculated. The Mean Square Error (MSE) was used to measure the difference between the two density functions for each variable and was found that the MSE values for wave height, wave period and wave direction are: 0.0099, 0.0000 and 0.0010, respectively. All these results suggest that the simulation results are satisfactory. Moreover, the estimated means of the observed and simulated data are shown

by using the black and red vertical lines respectively. It is seen that they are also very close, suggesting that the simulation results are satisfactory.

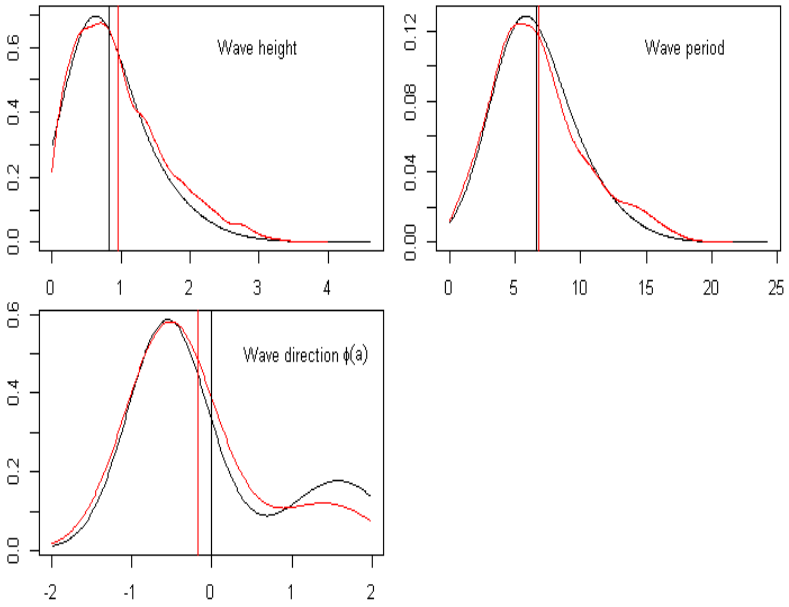

Figure 4. Marginal density function plots for all sea condition variables. Black curves correspond to observed data and red curves correspond to simulated data. Continuous and dashed vertical lines correspond to the means of the observed and simulated data respectively.

Recall that H is a fixed number that defines the maximum lag value we would like to consider for matching the autocorrelation structures between the simulated and the observed data. For illustration purposes, we let $H=4$, i.e. we consider the correlation up to four days. We also estimated the autocorrelation structures of the observed and simulated data respectively. Fig. 5 shows the estimated autocorrelation and cross-correlation between variables.

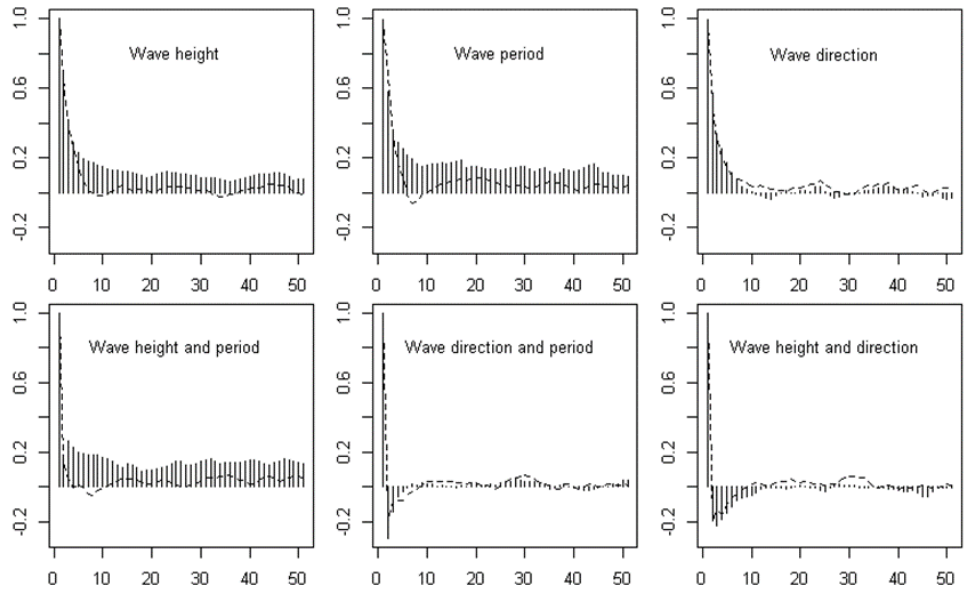

Figure 5. First row: autocorrelation up to 50 lags for each sea condition variable. Second row: cross-correlation between pairs of sea condition variables. Vertical lines are the acf for the observed data and the dashed curves correspond to those of the simulated data.

It is seen that the autocorrelations over the first four lags, (0 to 3 days), agree very well, with the exception of wave period, where the autocorrelation function drops a bit faster than in the original series. The cross-correlations show a similar level of agreement over the first four lags; again, with the possible exception of wave height-wave period in which the correlation in the simulated data drops faster than in the original. The shape and curvature of the correlations for small lags is well-captured by the method and, overall, show a satisfactory agreement.

5 DISCUSSION AND CONCLUSION

Removing trend and seasonality from the original data is a crucial step to achieve stationarity and consequently, make the VAR stochastic model applicable to a particular case-study. We found that using an AR model and a linear trend for the trends and using different formulations for the seasonal components of the variables have led to satisfactory simulation results. Our results show that we are able to generate simulated non-stationary wave data for three variables simultaneously, and the simulated and observed data have similar statistical properties including the marginal distributions and auto- and cross-correlation structures.

It is worth noting that the approaches we took for removing trend and seasonality from the original data are data dependent. This is because different data may have different types of trends and seasonality, and hence different approaches may need to be adopted. However, once the trends and seasonality have been removed from the original data, the simulation procedures are generally the same as discussed in Section 2.

In this study, a methodology was introduced for the reconstruction of three non-stationary wave time-series, namely, significant wave height H_s, peak wave period T_p, and wave direction a. The goal was to simulate wave time series that preserved the statistical characteristics of the corresponding original time series such as the mean value, the marginal distribution, and the auto- and cross- correlation structures. The method was tested for a 13-year sequence of wave measurements recorded off Littlehampton in southern England and provided satisfactory results.

References

Biller B, Nelson BL 2003 Modeling and generating multivariate timeseries input processes using a vector autoregressive technique. ACM Transactions on Modeling and Computer Simulation (TOMACS). 13, 211-237.

Borgman LE, Scheffner NW 1991 Simulation of time sequences of wave height, period, and direction. Technical Report DRP-91-2, USACE-WDC, Coastal Engineering Research Center, Vicksburg, Mississippi.

Cai Y, 2011 Multivariate time series simulation. Journal of Time Series Analysis. 32, 566-579.

Cai Y, Gouldby B, Hawkes P, Dunning P 2008 Statistical Simulation of Flood Variables: Incorporating Short-Term Sequencing. Journal of Flood Risk Management. 1, 1-10.

Cai Y, Huang J, Tang Y, Zhou G 2014 A simulation method for finite non-stationary time series. Journal of Statistical Computation and Simulation. 84, 1563-1579.

Cario MC, Nelson BL 1998 Numerical methods for fitting and simulating autoregressive-to-anything processes. Journal on Computing. 10, 72-81.

Soares CG, Cunha C 2000 Bivariate autoregressive models for the time series of significant wave height and mean period. Journal of Coastal Engineering. 40, 297-311.

DMPCO 2023

e-Proceedings of the 2nd International Scientific Conference on Design and Management of Port Coastal and Offshore Works Thessaloniki, Greece, May 24-27 2023

Hydrodynamic loads and fatigue design of large rated fixed bottom offshore wind turbines

C. Michailides[1*], W. Shi[2]

[1]Department of Civil Engineering, International Hellenic University, Serres University Campus, Greece
[2] Deepwater Engineering Research Center, Dalian University of Technology, Dalian, China
[*]Corresponding author: cmichailides@ihu.gr

Abstract

In the present paper the responses and fatigue damage of two large-rated monopile OWTs (5MW and 10MW) due to environmental loadings are investigated using a coupled analysis tool and the time until failure is compared. Fatigue damage is estimated based on the internal loads of the OWTs in the monopile base and tower base. The fluctuating responses obtained from the analysis tool are broken down into individual stress cycles using the rain flow counting approach. Three different efficient engineering methods for computing hydrodynamic loads are considered and compared. Fatigue life of the OWTs is estimated for a specific site in the Aegean Sea, Greece. The importance of including diffraction effects in the fatigue design calculation is emphasized with the present comparative study especially when the diameter of the monopile increases and monopile base is examined.

Keywords Offshore Wind Turbines, Monopiles, Hydrodynamic Loads, Fatigue Analysis.

1 INTRODUCTION

Rapid development and readiness boost in Offshore Wind Turbines (OWTs) technology have occurred over the past ten years globally. OWTs technology can be considered as the leading technology in the offshore renewable energy sector and have the largest potential of becoming the backbone of the energy system by 2030. OWTs technology already is considered as a fully developed commercial solution. By the end of 2021 the global cumulative offshore wind power capacity has reached 56 GW. A year-over-year increase growth equal to 58% has been achieved within 2021 and 21.1 GW of new installations have connected to the grid globally (GWEC 2022).

Up to now, the use of fixed bottom OWTs dominates against the use of floating OWTs mainly due to the lower Levelized Cost of Energy that fixed bottom OWTs present and due to engineering issues related to smaller number of uncertainties in their design. Different possible types of foundations (e.g., monopiles, jackets, tripods) can be used to support wind turbines depending mainly on the water depth but also on the local site environmental conditions. Monopiles are the most widely used foundations for fixed bottom OWTs and intermediate waters because of low cost, as well as easy installation and maintenance processes. Monopiles remain the most frequently installed foundation, with more than 90% of the total installed foundation to date in Europe (WindEurope 2022).

Similarly to 2021 and following this marvelous trend, the contribution of offshore wind power to the energy mix is expected to boom significantly by 2030. Fixed bottom OWTs and monopiles will remain as the dominating utilized technology for the years to come. Relevant reports (GWEC 2022; WindEurope, 2022) are highlighting the need for parallel technological advancement in fixed bottom OWTs accompanied by an increase in the capacity of OWTs targeting to ultra-large OWTs with capacity larger than 5 MW. This need already results to a relevant huge challenge for the design and maintenance of large diameter monopiles for serving as foundations to the ultra-large, fixed bottom OWTs. Currently, with the increasing rated power capacity of the OWTs, it is very common the need for utilization of monopiles larger than 10 m diameter.

As moving from shallow to deeper waters in connection with larger turbines and supporting infrastructures the technical feasibility of the monopile will be challenged, particularly, as wave loads increasingly interact with the response and integrity of the OWTs. The diameter of fixed bottom monopile OWTs is one of the important factors affecting their hydrodynamic performance, while, the

interaction between nonlinear waves and the monopile is particularly prominent. The effect of diffraction of waves will become increasingly important.

Support structures of OWTs are extremely vital components in their design, as damage or failure of them can lead to the loss of the complete OWT. The slenderness of monopile OWTs combined with the highly dynamic environmental loadings have resulted in structures which must be carefully designed against ultimate and fatigue failure. Even when the wave and wind loads are resulting to lower than the yield stress response, the sheer number of load cycles over the lifetime of an OWT may lead to failure. For this reason, it is important to consider the fatigue damage when designing OWTs and evaluate their Fatigue Limit State.

The effect of the method used for computing hydrodynamic loads on the fatigue design of a large diameter fixed bottom OWT is examined in the present paper. Three different efficient methods for computing hydrodynamic loads are considered and compared. Those methods are (a) the Morison's equation (Morison and Johnson 1950) with undisturbed linear wave kinematics, (b) Morison's equation with undisturbed second order Stokes wave kinematics and (c) the MacCamy-Fuchs model (MacCamy and Fuchs 1954) which is able to account for diffraction in waves. Initially the models are compared in terms of the hydrodynamic loading calculation against relevant experimental data and wave conditions. Afterwards, the hydrodynamic loads models are integrated within a software tool for solving the fully coupled dynamic equation of the OWT.

The responses and fatigue life of the large-rated OWT due to environmental loadings are investigated using the coupled analysis tool and compared. Fatigue damage is estimated based on the internal loads in the monopile and tower. The fluctuating responses obtained from the analysis tool are broken down into individual stress cycles using the rain flow counting approach. The fatigue damage is assumed to accumulate linearly with each of the load cycles and calculated according to Miner's rule with thickness effects included. Fatigue life of the OWT is estimated for a specific site in the Aegean Sea, Greece. The importance of including diffraction effects in the fatigue design calculation is emphasized with the comparative study.

2 NUMERICAL ANALYSIS

2.1 Fully coupled numerical analysis model of the fixed bottom offshore wind turbine

Numerical analysis for fixed bottom OWTs is suggested to be performed in different standards (e.g., DNV-OS-J101, IEC61400-3) in order to secure different levels of design limit states requirements, namely, ultimate analysis, extreme response analysis, serviceability analysis, fatigue analysis, natural frequency analysis, accidental analysis and vortex shedding analysis. Very commonly and since advanced and highly accurate loading and interaction methods that exist (e.g., Computational Fluid Dynamics methods) require large amount of computational resource demands, fully coupled time domain analysis of fixed bottom OWTs is performed with widely used numerical methodologies and tools (commercial and/or open source). The numerical models are used for solving Eq. 1 below and for performing time domain dynamic analysis integrating together all possible loads (e.g., hydrodynamics, aerodynamic, currents, seismic, etc.) with flexible finite element beam-based or flexible multibody elements and structural components in order to calculate the position at any point of the structure as well as any possible internal load responses (e.g. axial force, moments, stresses) of the fixed bottom OWT:

$$M\ddot{X} + B\dot{X} + KX = F_H + F_A + F \tag{1}$$

where M and K are the mass and stiffness of the structural components, B is any possible source of damping coefficients, F_H is the hydrodynamic load, F_A is the aerodynamic load, F is any other possible source of external loading and $\ddot{X}, \dot{X}, \text{and } X$ are the acceleration, velocity, and displacement at any point of the structure.

In the present paper the responses are obtained using the coupling tool F2A (Yang et al. 2020). F2A performs the fully coupled time domain analysis by integrating the aero-servo-elastic simulation tool FAST (Jonkman and Buhl 2005) with ANSYS/AQWA. The implementation of the F2A coupling

framework is achieved by modifying the source codes of FAST and the built-in dynamic link library of AQWA for calculating the external forces in a time-domain analysis; the responses of the structure (AQWA) are used (FAST) to correct the positions and kinematics of the wind turbine's components for solving the equation of motions iteratively in every time step of the analysis. FAST is a fully coupled aero-hydro-servo-elastic code developed at the National Renewable Energy Laboratory, which can model the dynamic response and simulate loads of three-bladed, conventional, horizontal-axis wind turbine.

Fixed bottom OWTs are subjected to significant cyclic hydrodynamic loading throughout their service life. Wide applicable engineering models for estimating the hydrodynamic loadings on circular cylinders have been studied and used extensively in the past. An initial critical component for estimating the hydrodynamic loading is the wave kinematic theory that is applied, since the velocity and acceleration components of the water particles may differ depending to the theory used. Very commonly Linear wave theories (e.g., Airy wave theory) are used for small wave heights while Higher order theories may be applied (e.g., Stokes 2nd order theory).

Different methods exist (spanning from simple analytical formulations to the complete set of Navier-Stokes equations) in order to calculate the hydrodynamic loading acting on an offshore slender structural component. The most applicable model, and maybe the simplest one that is allowed to be used from relevant standards for the design of OWTs, for calculating the wave force on slender members is the Morison's equation which can be used when the dimensions of the structure are small with respect to the wavelength and the diffraction effects can be neglected. The hydrodynamic force normal to each strip of the monopile can be calculated by Morison's equation, which consists of a drag and an inertia component as below:

$$F_H(x,y,t) = \rho C_M \frac{\pi D^2}{4} \dot{u}(x,y,t) + \frac{1}{2}\rho D C_D |u(x,y,t)| u(x,y,t) \quad (2)$$

where C_M and C_D are the inertia and drag coefficients, ρ is the water density, D is the monopile diameter, u is the wave velocity and $\dot{u}$ is the wave acceleration at specific point.

On the other hand, and when the structure's dimensions become very large (e.g., like the case of large diameter fixed bottom OWTs) and comparable to the wavelength, then the viscous effects are negligible and the diffraction effects should be accounted with relevant methods. MacCamy and Fuchs' analytical solution integrates the first order diffraction problem for the hydrodynamic loads on monopile cylinders extending from the seabed to mean free surface. MacCamy and Fuchs is based on diffraction theory and can be used when considering very large structures with a ratio of diameter to wavelength being larger than 0.2. The relevant to Eq. 2 hydrodynamic loading is as below:

$$F_H(x,y,t) = \frac{2\rho\rho g}{k} \frac{\cosh(k(h+z))}{\cosh(kh)} A(kr)\cos(\omega t - \alpha(kr)) \quad (3)$$

$$\text{with } A(kr) = \frac{1}{\sqrt{\left(J_1'(kr)\right)^2 + \left(Y_1'(kr)\right)^2}} \quad (4) \text{ and } \alpha(kr) = \arctan\left(\frac{J_1'(kr)}{Y_1'(kr)}\right) \quad (5)$$

where H is the wave height, h the total depth, z the vertical position, k the wave number, ω the wave frequency, r the radius of the cylinder and J_1' and Y_1' are the differentiated Bessel functions of the first and second kind, respectively. It should be stated that for the purposes of the present paper the calculation of the MacCamy and Fuchs hydrodynamic loads with Eqs. 3~5 has been modeled with a developed script that can be incorporated in the F2A tool as well as can be used with rest software tools.

2.2 Fatigue damage evaluation

Fatigue occurs over cyclic loading in time and is a common source of failure in OWTs; minor faults, such as cracks, grow when subject to repeat cyclic loading. Time domain approaches are recommended by industry guidelines for the evaluation of the fatigue damage as they are considered the most reliable for the case of OWTs. This is because non-linear and stochastic load effects from environmental loads

(e.g., hydrodynamic and aerodynamic) and soil interaction can be accounted for. Several fatigue analysis approaches are available, such as notch stress, nominal stress, hot spot stress and crack propagation approaches (Hobbacher 2009). The time series of the response quantities generated with use of F2A are used to calculate the fatigue design life of the OWT. Initially aggregate statistics (e.g., mean values) are calculated from the time series. With use of the rain flow counting method the fatigue cycles for each time series are determined and short term damage rates are computed. By summing the damage contribution from each time series, the short term aggregate damage rates are calculated and all damage contributions across the systems design life are extrapolated in order to predict lifetime damage and predict the time until failure. The fatigue damage evaluation is performed based on the recommendations described in Annex G of IEC61400-3 (IEC 2009). Fluctuating loads over the design life of the turbine are accumulated and binned into individual cycles using rain flow counting. The cycles are characterised by load-mean and range. Following Miners rule, it is assumed that damage occurs linearly thus lifetime damage is given as:

$$D = \sum_i \frac{n_i}{N_i\left(L_{i,RF}\right)} \tag{6}$$

where D is the total fatigue damage, N_i is number of cycles to failure due to the cycle load range over a fixed load-mean value, n_i is the cycle count and $L_{i,RF}$ the cycles load range about a fixed load-mean value. In order to estimate the number of cycles per bin, an effective S-N curve based on the load range Ni can be estimated as below:

$$N_i = \left(\frac{L^{ult} - \left|L^{MF}\right|}{0.5L_{i,RF}} \right)^m \tag{7}$$

where L^{ult} is the component's response ultimate design load, L^{MF} the load-mean which is calculated by aggregating all of the time series of the load cases and m the Whöler exponent (equal to 5 in this study study to account for the increased effective density of the material). S-N curves express fatigue resistance of a structural component or structure by specifying the number of cycles to failure against stress range. Finally, the Goodman correction is applied to adjust the cycle load range since load cycles occur over a spectrum of mean loads rather than a fixed mean load. For the case of OWTs the expected design life of the OWT is set to 20 years as recommended by relevant standards.

3 RESULTS AND DISCUSSION

In the present paper the fatigue damage is estimated for three different methods as far as the hydrodynamic loading method that is utilized, namely, MEL, MES and MCF. The fatigue damage is calculated for two different positions of the OWT system, namely, the tower base and monopile base at the seabed. The monopiles are considered to have fixed boundary conditions at the seabed and as a result no soil-monopile interaction is considered within the presented results. Two different wind turbines are examined: (a) the reference NREL 5 MW wind turbine (Jonkman et al. 2009) and (b) the DTU 10 MW baseline wind turbine (Bak et al. 2012).

With regards to the environmental conditions, a site off the north-east coasts off Samothraki Island, Greece has been selected with water depth equal to 40.0 m. Hub mean wind speed, significant wave height and wave peak period long-term joint probability distributions are used for obtaining the most probable sea states associated with the relevant wind turbine operational conditions and environmental contours. Five years data from a numerical hindcast model have been used for the estimation of the distributions. It is stated that in order to simulate realistic conditions, wind speeds are extrapolated to the wind turbine hub height. Both distributions of the one-hour mean wind speed at 10 m height and of the significant wave height are assumed to follow a two-parameter Weibull distribution, while, the distribution of the wave peak period is assumed to follow a log-normal one.

In Table 1 the fatigue damage predictions are presented for the examined cases and the specific site. Differences exist between the fatigue damage with loads estimated by Morison's equation and the loads with MacCamy and Fuchs theory. Differences are larger moving from 5MW to the 10MW wind turbine due to the increase of the monopile diameter and significance of the diffraction loads. Contrary to the

importance of the diffraction effects for fatigue damage levels the higher order waves do not show a significant increase. Fatigue damage is larger in the monopile base compared to the tower base due to the systems natural frequencies corresponding to the first fore-aft and side-side eigenmodes falling within the blade pass frequency.

Table 1. Results of lifetime fatigue damage analysis for the two examined OWTs

Wind turbine	Position of fatigue calculation	Lifetime damage			Time until failure (years)		
		MEL	MES	MCF	MEL	MES	MCF
5MW OWT	Tower base	0.794	0.795	0.804	23.08	23.05	22.96
	Monopile base	0.904	0.906	1.013	20.95	20.93	19.78
10MW OWT	Tower base	0.918	0.920	1.005	20.72	20.66	19.90
	Monopile base	0.987	0.990	1.228	20.12	20.09	18.38

4 CONCLUSIONS

In the present paper the effects of the method used for computing hydrodynamic loads on the fatigue design of a large diameter fixed bottom OWTs is examined. Three different efficient engineering methods for computing hydrodynamic loads are considered and compared. Initially the diffraction hydrodynamic load method is integrated with a fully coupled analysis tool. The fatigue damage is calculated for two different positions of the OWT system and two different large-rated reference wind turbines for a specific site. Fatigue damage is estimated based on the internal loads in the monopile and tower bases. Differences exist for the fatigue damage with hydrodynamic loads estimated with the MacCamy and Fuchs theory that takes into consideration the diffraction effects especially when the diameter of the monopile increases and monopile base fatigue damage is examined.

References

Bak C, Bitsche, Yde A, Kim T et al. (2012). Light Rotor: The 10-MW reference wind turbine. In EWEA 2012-European Wind Energy Conference & Exhibition. European Wind Energy Association.

Global Wind Energy Council (2022) Global offshore wind report, 2022.

Hobbacher A. (2009). Recommendations for Fatigue Design of Welded Joints and Components, IIW doc.1823-07, Welding Research Council Bulletin 520. International Institute of Welding, New York.

International Electrotechnical Commission (2009), IEC 61400-3 Ed. 3 Design requirements for offshore wind turbines. International Standards. Geneva.

Jonkman JM, Buhl MLJ (2005). FAST user's guide, National Renewable Energy Laboratory, U.S. Department of Energy Office of Energy Efficiency & Renewable Energy, Report no. NREL/TP-500-38230.

Jonkman JM, Butterfield S, Musial W, Scott G (2009). Definition of a 5-MW reference wind turbine for offshore system development. Golden, CO, National Renewable Energy Laboratory, NREL Report TP-500-38060.

MacCamy RC, Fuchs RA (1954) Wave Forces on Piles: A Diffraction Theory. Technical Report; The Institute of Engineering Research, University of California: Los Angeles, CA, USA, 1954.

Morison JR, Johnson JW, Schaaf SA (1950) The force exerted by surface waves on piles. J. Pet. Technol. 2, 149–154.

Naess A, Moan T (2013) Stochastic Dynamics of Marine Structures, Cambridge University Press.

Wind Europe (2022) Wind Energy in Europe: 2021 Statistics and the outlook for 2022-2026.

Yang Y, Bashir M, Michailides C, Li C, Wang J (2020). Development and application of an aero-hydro-servo-elastic coupling framework for analysis of floating offshore wind turbines. Renewable Energy, 161, 606-625.

e-Proceedings of the 2nd International Scientific Conference on Design and Management of Port Coastal and Offshore Works Thessaloniki, Greece, May 24-27 2023

Numerical investigation of wave-induced seabed response around a monopile foundation

Gkougkoudi-Papaioannou M.[1,*], Stuyts B.[1,2], and Troch P.[1]

[1]Ghent University, Department of Civil Engineering, Technologiepark 60, Zwijnaarde, 9052, Belgium
[2]Vrije Universiteit Brussel, OWI-Lab, Pleinlaan 2, Elsene, 1050, Belgium

*corresponding author: Maria.GkougkoudiPapaioannou@UGent.be

Abstract

In the present study, a 3D integrated numerical model is developed to investigate the wave-induced seabed response around a monopile foundation. The coupled hydrodynamic-geotechnical model consists of two sub-models; the wave model is based on the Volume Averaged Reynolds Averaged Navier-Stokes (VARANS) equations which are solved within the OpenFOAM® framework. The poro-elastic seabed is modelled using ABAQUS finite element software. The excess pore water pressure development around the monopile foundation and the accompanying changes in the effective stress of the seabed soil under wave loads are investigated. One way coupling is adopted in this study by transferring the wave induced pressure at the seabed surface to the seabed model. The present model is validated against analytical solutions and laboratory experiments and good agreements for the seabed response are obtained. In addition to the coupled hydrodynamic-geotechnical analyses, in-situ monitoring data are available to the SOILTWIN research project, which can provide better insight in the soil behaviour around the monopile and will lead eventually to an improved calibrated numerical model.

Keywords Wave loading, Seabed response, Monopile foundation.

1 INTRODUCTION

Offshore wind has favoured the use of monopile foundations due to the simplicity in design, construction, and industrial scalability. The stability of the monopile foundation can be affected not only by the direct wave action but also by the response of the surrounding seabed. When waves are propagating over a porous seabed, the excess pore pressure may increase and the effective stress within the seabed soil decreases accordingly (Sumer, 2014). This can result in a stiffness reduction of the seabed soil around the monopile foundation or even liquefaction under the action of the waves. Therefore, an accurate evaluation of the wave-induced hydro-mechanical soil response is of high significance for the design of the monopile foundations. Numerical modelling can be used to simulate the wave-structure-seabed interaction and provide a better understanding of the mechanisms involved in wave-induced seabed response around the monopile foundation. Within this context a coupled hydrodynamic-geotechnical numerical model is developed using OpenFOAM® and ABAQUS software to investigate the fluid-structure-seabed interaction, based on Stokes wave theory and poro-elastic Biot soil theory. The unique aspect of this research is the availability of a dataset with in-situ pore pressure measurements for a field-scale monopile. This dataset is available to the SOILTWIN project and can provide insight in the actual pore pressure distribution for various wave loading conditions. The comparison of the numerical results with in-situ monitoring data is essential for an improved calibration of the soil response to the observed behaviour in-situ.

2 NUMERICAL MODEL

In this section, the governing equations of both the wave model and the seabed model adopted in the numerical simulations are described in detail.

2.1 Wave model

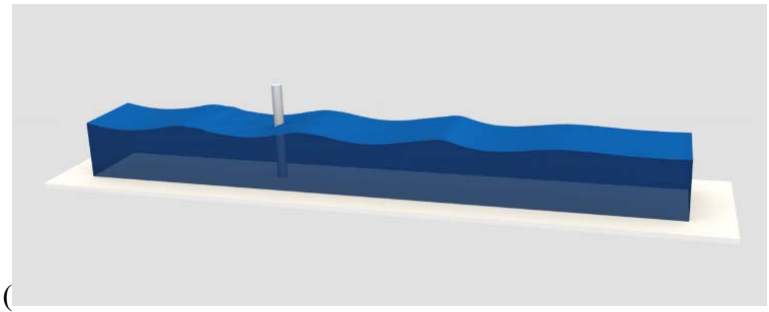

The hydrodynamic numerical model (Figure **22**) is developed using OpenFOAM®, an open source Computational Fluid Dynamics (CFD) software. OlaFlow solver is implemented for the wave generation and absorption at the boundaries. The wave domain is governed by the VARANS equations for the two-phase incompressible fluid, using the volume of fluid (VOF) method. In this study the k-ω-SST turbulence model is adopted. The mass and momentum conservation governing equations can be expressed as follows:

$$\nabla \boldsymbol{U} = 0, \quad (1)$$

$$\frac{\partial \rho \boldsymbol{U}}{\partial t} + \nabla(\rho \boldsymbol{U}\boldsymbol{U}) - \nabla\left(\mu_{eff} \nabla \boldsymbol{U}\right) = -\nabla p^* - \boldsymbol{g}\boldsymbol{X}\nabla\rho + \nabla \boldsymbol{U} \nabla \mu_{eff} + \sigma\kappa\nabla\alpha_1, \quad (2)$$

in which $\boldsymbol{U}$ = the velocity vector, ρ = the density of the fluid, $p*$ = the pseudo-dynamic pressure ($p^* = p - \rho \boldsymbol{g}\boldsymbol{X}$, where p = the total pressure, $\boldsymbol{g}$ = the gravitational acceleration, $\boldsymbol{X}$ = the position vector), μ_{eff} = the efficient dynamic viscosity, where the molecular dynamic viscosity plus the turbulent effects are taken into account, σ = the surface tension coefficient, and κ = the curvature of the interface, which are used for indicating the effect of surface tension. Using the volume fraction index (α_1), the mixture properties are computed as:

$$\Phi = \alpha_1 \Phi_w + (1 - \alpha_1)\Phi_\alpha, \quad \alpha_1 = \begin{cases} 1, \ water \\ 0, \ air \\ 0 < \alpha_1 < 1, \ free\ surface \end{cases} \quad (3)$$

in which Φ_w and Φ_α is any kind of property of water and air, respectively.

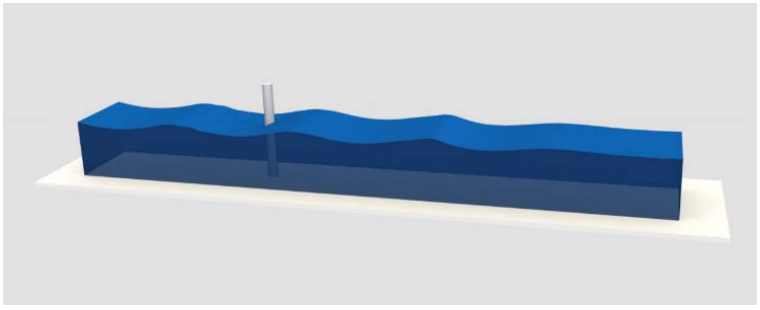

Figure 22. The hydrodynamic numerical model developed in OpenFOAM®

2.2 Seabed model

The seabed model is developed within ABAQUS finite element software. In ABAQUS, the SOILS analysis solves the equations related to the behaviour of porous media under mechanical and hydraulic loads. More specifically, ABAQUS uses Biot's consolidation theory to model the coupling between the solid and fluid phases of the porous media, which includes continuity and momentum balance equations for the fluid and the solid phase, constitutive equations for the solid phase which depend on the specific material properties as well as equations for the boundary conditions at the model interfaces. In this study, an elastic porous soil material is adopted. The elastic soil material has been widely used in numerical modelling due to its simplicity and various successful validation cases in engineering practice (Lin et al., 2017; Sui et al., 2019).

The flow and soil equations are solved iteratively to obtain the pressure, velocity, and displacement fields of the fluid and solid phases, as well as other properties such as effective stress, permeability, and

porosity. The solution process involves discretizing the model domain into finite elements, applying appropriate numerical methods, and using iterative solution techniques to converge on the final solution.

2.3 Integrated process

In this study, one-way coupling process is adopted for the integrated numerical model i.e. the effect of the movement of the seabed and the structure on the wave progression is considered to be negligible. This one-way coupling process has been extensively used in previous studies (Sui et al., 2015; Zhao et al., 2018). The model coupling is achieved by computing the wave induced pressure field at the seabed surface using the wave model and by transferring it as an initial boundary condition to the seabed model. It is noted that the element size in the fluid domain is very small relative to that in the solid domain. Using the same element size in the soil domain would lead to huge CPU computation and memory costs. Therefore a non-matching mesh interface system is adopted in this study.

3 MODEL VALIDATION

In this section, the model validation with both an analytical solution and experimental data is presented. In the first validation case the vertical pore pressure distribution along the seabed soil is examined (p_f is the maximum pore water pressure, p_0 is the pore water pressure at the seabed surface, z is the seabed depth and h is the seabed thickness). Figure 23 shows the comparison of the maximum pore water pressure between numerical results and the analytical solution of Wang et al. (2018) for the wave induced dynamic response in a poro-elastic seabed without a monopile. The calculation parameters adopted for this validation case are: wave height H=1m, wave period T=5sec, water depth d=8m, seabed thickness h=25m, soil shear modulus $G=5\times10^7$ Pa, Poisson's ratio $\mu=0.333$, porosity n=0.4 and mass density of solid grain $\rho_s=2.65\times10^3$ kg/m^3. The maximum pore water pressure shows a sharp decrease over the top 10m, which corresponds to z/h=0.4, and then gradually subsides. A similar behaviour is shown in Figure 24, which presents the comparison of the maximum pore water pressure distribution between the present numerical results, the experimental data of Maeno and Hasegawa (2018) and the numerical results of Zhang et al. (2015). The wave conditions and soil properties used for this validation case are: wave height H=0.0368m, wave period T=0.96sec, water depth d=4.1m, seabed thickness h=0.36m, soil shear modulus $G=2\times10^6$ Pa, Poisson's ratio $\mu=0.495$, porosity n=0.4, and permeability $K=2.3\times10^{-4}$ m/s. Summarizing, it is evident that the numerical results agree well with both the analytical solution and experimental data, demonstrating the accuracy of the present numerical model.

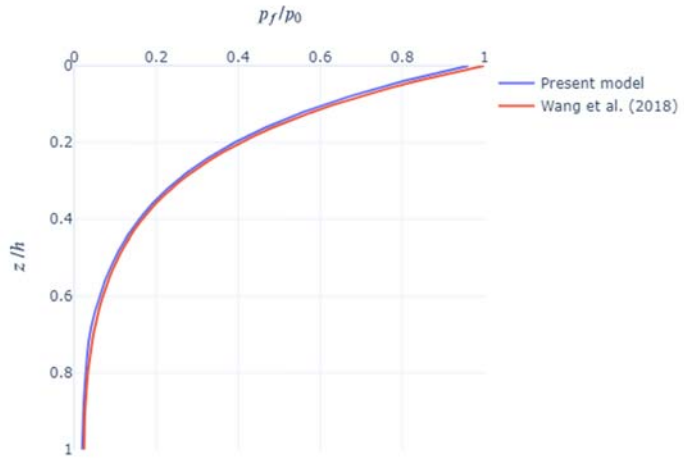

Figure 23. Comparison of the maximum pore water pressure p_f between present model (blue solid line) and the analytical solution of Wang et al. (2018) (red solid line).

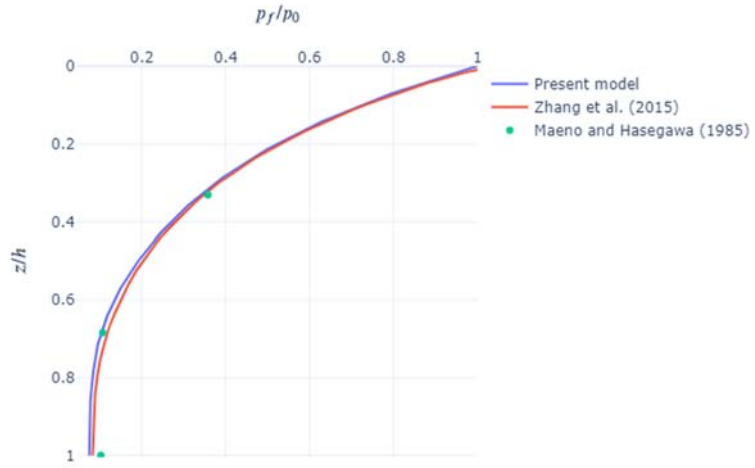

Figure 24. Comparison of the maximum pore water pressure p_f between present model (blue solid line), the numerical results of Zhang et al. (2015) and the experimental data (circles) of Maeno and Hasegawa (1985).

4 APPLICATIONS

Figure 4 shows the wave induced pressure at the seabed surface $p_0(t)$ for a study case with wave height H=1m, wave period T=5sec and water depth d=8m. As an example, two different locations are presented, in front and behind the monopile (Figure 4 (a) and (b) respectively) and a comparison is made with the pressures of a wave domain without a monopile foundation. It is clear that the presence of the monopile causes an increase of the wave induced pressure in front of the monopile (Figure 4(a)) which is expected to lead to an increased pore water pressure distribution in the seabed foundation. As shown in Figure 4(b) the pressure behind the monopile shows a minor decrease compared to the case without the monopile. The first results obtained using the 3D integrated numerical model show that the inserted pile foundation modifies the distribution of pore water pressures in the seabed considerably; namely, the maximum pore water pressure increases near the front and near the sides of the monopile foundation compared to the case without the monopile. This is mainly because the wave loading in front of the monopile is larger due to wave reflection and refraction as a result of the wave-structure interaction. Furthermore, the possible comparison of the numerical results with in-situ monitoring data can provide a better understanding of the mechanisms of wave induced soil response around the monopile foundation and result in a high fidelity, calibrated numerical model. This is ongoing research within the SOILTWIN project.

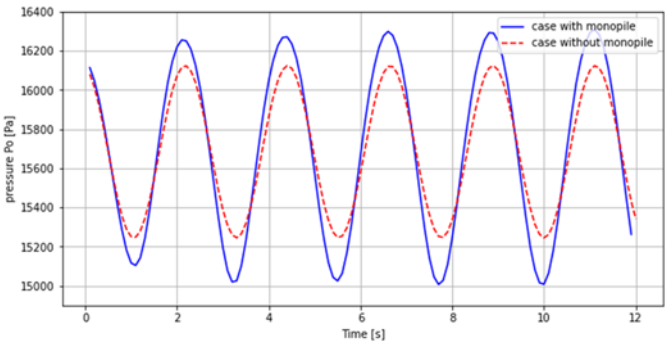

(a)

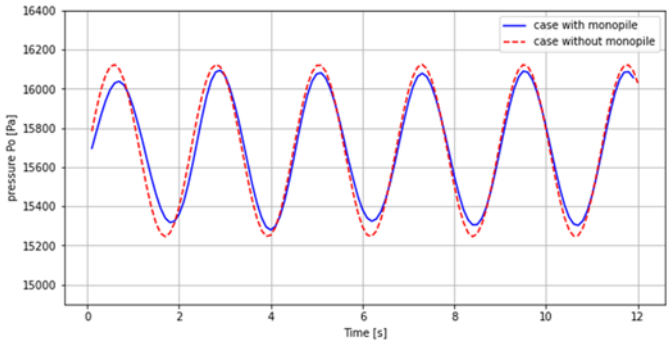

(b)

Figure 4. Comparison of the wave induced pressure at the seabed surface for cases with and without the monopile foundation at two positions: (a) in front of the monopile, (b) behind the monopile

5 CONCLUSIONS

In this study, a three-dimensional numerical model is developed based on a VARANS wave model and a poro-elastic seabed model using one-way coupling. The wave induced seabed response and, more specifically, the pore pressure development around the monopile foundation is investigated. The model is validated against analytical solutions and experimental data and promising results are obtained. The unique datasets available to this project will further allow for a data-driven approach which is built up around in-situ monitoring data of the foundation piles.

Acknowledgements

The authors would like to acknowledge the support of the Belgian Ministry of Economic Affairs through the ETF project WINDSOIL project. The support of VLAIO through the De Blauwe Cluster SBO SOILTWIN project is also acknowledged.

References

Berberović, E., Van Hinsberg, N. P., Jakirlić, S., Roisman, I. V., Tropea, C. (2009) Drop impact onto a liquid layer of finite thickness: Dynamics of the cavity evolution. Physical Review E, Statistical, Nonlinear, and Soft Matter Physics, 79, 036306.

Biot, M.A. (1941) General theory of three-dimensional consolidation. J. Appl. Phys. 26 (2), 155–164. doi:10.1063/1.1712886.

Higuera, P. (2020) Enhancing active wave absorption in RANS models. Appl. Ocean Res. 94, 102000. doi:10.1016/j.apor.2019.102000.

Higuera, P., Lara, J.L., Losada, I.J. (2013) Realistic wave generation and active wave absorption for Navier-Stokes models: Application to openfoam. Coast. Eng. 71, 102–118. doi:10.1016/j.coastaleng.2012.07.002.

Lin, Z., Pokrajac, D., Guo, Y., Jeng, D.-s., Tang, T., Rey, N., Zheng, J., Zhang, J. (2017) Investigation of nonlinear wave-induced seabed response around monopile foundation. Coast. Eng. 121, 197–211. doi:10.1016/j.coastaleng.2017.01.002

Maeno, Y., Hasegawa, T. (1985) Evaluation of wave-induced pore pressure in sand layer by wave steepness. Coastal Engineering Journal, 28, 31-44.

Stuyts, B., Weijtjens, W., Gkougkoudi-Papaioannou, M., Devriendt, C., Troch, P., Kheffache, A. (2023) Insights from in-situ pore pressure monitoring around a wind turbine monopile. Ocean Eng. 269, 113556.

Sui, T., Zhang, C., Guo, Y., Jeng, D., Zhang, J., Zhang, W. (2015) Three-dimensional numerical model for wave-induced seabed response around mono-pile. Ships and Offshore Structures. 11. 1-12. doi:10.1080/17445302.2015.1051312.

Sui, T., Zhang, C., Jeng, D.-S, Guo, Y., Zheng, J., Zhang, W., Shi, J. (2019) Wave-induced seabed residual response and liquefaction around a mono-pile foundation with various embedded depth. Ocean Eng. 173, 157-173. doi:10.1016/j.oceaneng.2018.12.055.

Sumer, B.M. (2014) Liquefaction Around Marine Structures. World Scientific Publishing, Singapore.

Wang, G., Chen, S., Liu, Q., Zhang, Y. (2018) Wave-induced dynamic response in a poroelastic seabed. Journal of Geotechnical and Geoenvironmental Engineering, 144, 06018008.

Yamamoto, T., Koning, H., Sellmeijer, H., Hijum, E.V. (1978) On the response of a poro-elastic bed to water waves. J. Fluid Mech. 87 (1), 193–206. doi:10.1017/S0022112078003006.

Zhang, Q., Zhai, H., Wang, P., Wang, S., Duan, L., Chen, L., Liu, Y., Jeng, D.-S. (2020) Experimental study on irregular wave-induced pore-water pressures in a porous seabed around a mono-pile. Appl. Ocean Res. 95, 102041. doi:org/10.1016/j.apor.2019.102041

Zhang, C., Zhang, Q., Wu, Z., Zhang, J., Sui, T., Wen, Y. (2015) Numerical study on effects of the embedded monopile foundation on local wave-induced porous seabed response. Mathematical Problems in Engineering, 2015, 1-13.

Zhao, H.Y., Jeng, D.S., Liao, C.C., Zhang, J.S., Guo, Z., Chen, W.Y. (2018) Numerical modelling of liquefaction in loose sand deposits subjected to ocean waves. Appl. Ocean Res. 73, 27-41. doi:10.1016/j.apor.2018.01.011.

DMPCO 2023

e-Proceedings of the 2nd International Scientific Conference on Design and Management of Port Coastal and Offshore Works Thessaloniki, Greece, May 24-27 2023

Design and time-domain analysis of a 10 MW semi-submersible floating offshore wind turbine

L.A. Vagenas[1*], M. Panagiotidou[1*], E. Loukogeorgaki[1], C. Michailides[2]

[1]Department of Civil Engineering, Aristotle University of Thessaloniki, Thessaloniki, 54124, Greece
[2]Department of Civil Engineering, National University of Greece, Serres, 62124, Greece
[*]Corresponding author: lewn300slash@gmail.com, panagiotidou.mariaa@gmail.com

Abstract

Floating Offshore Wind Turbines (FOWTs) play a key role in the renewable energy sector, providing access to deep water depths, where stronger winds exist. Aiming at reducing FOWT costs, the deployment of large capacity WTs is desired. Thus, the design of adequate floating platforms to support those WTs is required. Motivated by this, the present paper focuses on the design and the preliminary time-domain analysis of a new 10 MW semi-submersible FOWT. The semi-submersible platform is designed to support the DTU 10 MW reference WT by upscaling an existing 5 MW FOWT. A three-leg catenary mooring system for 100 m installation water depth is considered. The fully coupled, integrated time-domain analysis of the proposed FOWT is conducted in OpenFAST and aims at: (a) identifying important static and intrinsic dynamic features of the FOWT and (b) assessing the FOWT's performance under various wind and wave load cases. The results demonstrate an efficient design of a new 10 MW semi-submersible FOWT that meets main design requirements of this kind of floating systems (e.g., natural frequencies within required limits, anticipated dynamic responses and power production).

Keywords Floating offshore wind turbine, Semi-submersible, Upscaling, Numerical simulation.

1 INTRODUCTION

Floating Offshore Wind Turbines (FOWTs) play a leading role in the renewable energy technology towards a low-carbon future in Europe. Those structures are designed to operate at large water depths, where stronger winds exist, while, furthermore, implications related to visual disturbance, ecosystems degradation and scarcity of available shallow water sites can be efficiently overcome. Despite all those advantages, the deployment of FOWTs is still economically challenging due to various cost raisers, including for example the scale of development, the balance of plant and grid costs (OREC, 2021), as well as installation and O&M costs (Leimeister et al., 2016). One of the most promising approaches to reduce the relevant levelized cost of energy is the deployment of WTs of large capacity. Accordingly, the design of adequate floating platforms to support those WTs is required.

Along these lines, many researchers have developed various concepts of floating platforms for the DTU 10 MW reference WT (Bak et al., 2013) and they have investigated their performance numerically and/or experimentally. Due to the inherent flexibility of the semi-submersible platform to adapt to a wide range of water depths, most of those investigations focus on this type of floating platform, including for example the LIFES50+ OO-Star (Yu et al., 2017; Pegalajar-Jurado, et al., 2018) and NATILUS-10 (Yu et al., 2017) semi-submersible platforms, the DUT platform (Zhao et al., 2021), the SPIC concept of a semi-submersible with three partially inclined side columns (Cao et al., 2021). All these platforms have been developed from scratch, while Zhao et al. (2019) upscaled the design of an existing 5 MW braceless semi-submersible platform to support the DTU 10 MW turbine. It is straightforward, however, that FOWTs irrespectively of their floating platform concept correspond to multi-body systems with rigid and flexible components (wind turbine, tower, floating platform, mooring lines) and complex interactions (e.g., aerodynamic-hydrodynamic coupling), which makes the analysis of the dynamic characteristics and behaviour of the FOWT system greatly complex and challenging (Zhao et al., 2019).

The present paper focuses on the design of a new 10 MW semi-submersible FOWT and its preliminary time-domain analysis. The examined FOWT consists of the DTU 10 MW reference WT with the relevant tower, a semi-submersible floating platform, which is designed by upscaling an existing 5 MW

FOWT and a three-leg catenary mooring system designed for an installation water depth of 100 m. A fully coupled time-domain simulation analysis is performed using OpenFAST (NREL, 2023) for various design load cases of increasing complexity.

2 DESIGN OF THE FOWT

2.1 Superstructure and floating platform

The examined FOWT consists of the DTU 10 MW reference WT with the relevant tower (Yu et al., 2017) and a semi-submersible floating platform. The tower of the DTU 10 MW WT has been appropriately modified in order to be adjusted to the new geometry of the floating platform. The platform consists of a central column, 3 side columns and 3 interconnected submerged pontoons (Figure 1). It is noted that the pontoons and the 3 side columns can be filled with ballast up to a specific height. The design of the platform is based on the upscaling of an existing 5 MW FOWT (Michailides et al., 2014), by using the following scaling factor:

$$k = \sqrt[3]{m_{WT,10MW}/m_{WT,5MW}} \tag{1}$$

where $m_{WT,10MW}$ and $m_{WT,5MW}$ are the mass of the 10 and the 5 MW WT respectively.

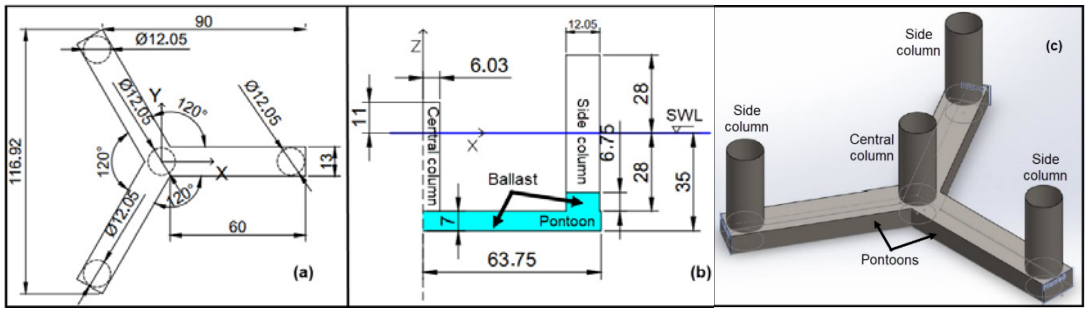

Figure 1. The proposed platform **(a)** Top view, **(b)** Half side view, **(c)** 3D view (all units are in m)

In order to fit, though, the central column to the tower base, the k_M scaling factor has been used for this column, as defined by Eq. 2 below:

$$k_M = D_{tower,10MW}/D_{tower,5MW} \tag{2}$$

In Eq. 2, $D_{tower,10MW}$ and $D_{tower,5MW}$ are the diameter of the tower base for the 10 and the 5 MW WT respectively. It is noted that some geometrical arrangements required the consideration of k_M also for the side columns.

The final draft of the FOWT was selected equal to 35 m. To achieve this value, the pontoons were fully filled with water ballast, while for the three side columns a ballast height of 6.75 m was selected (Figure 1). The geometrical characteristics of the platform are included in Figure 1, while some of its main technical characteristics are cited in Table 1.

Table 1. Main characteristics of the semi-submersible platform

Draft (m)	Mass (tn)	V_{disp} (m^3)	Ballast height (m)	C.G. (m)	C.B. (m)	ρ_{steel} (tn/m^3)	I_{XX}, I_{YY} (m^4)	I_{ZZ} (m^4)
35	28470.2	29665	6.75	-19.26	-23.98	7.85	1.56E+10	1.85E+10

2.2 Mooring System

The mooring system is designed for 100 m water depth and consists of three catenary mooring lines of studless chains and submerged weight, w_o, of 5.33 kN/m with the layout shown in Figure 2. The geometrical characteristics of each mooring line have been defined using the well-known catenary equations (Faltinsen, 1993). More specifically, the total minimum required length, $L_{tot,min}$, of each

mooring line is calculated by using Eq. 3, while Eq. 4 is deployed for determining the horizontal distance between the fairlead and the anchor, l_A:

$$L_{tot,min} = d\left(2\frac{\left(T^{top}_{BreakingLoad}\right)}{w_o d} - 1\right)^{0.5} \quad (3)$$

$$l_A = \frac{H}{w_o}\left\{sinh^{-1}\left[\frac{w_o L_{catenary}}{H}\right]\right\} + (L_{tot,min} - L_{catenary}) \quad (4)$$

In Eq. 4, $T^{top}_{BreakingLoad}$ is the breaking load of the selected studless chain and d is the vertical distance between the fairlead and anchor point, while in Eq. 5, H is the horizontal force applied on the mooring line and $L_{catenary}$ is the lift-off length of the mooring line. The application of the above equations has resulted to $L_{tot,min}$ and l_A equal to 771 m and 800.83 m respectively. It is noted that the design of the mooring lines has been made at a preliminary stage and it is based on quite conservative calculations.

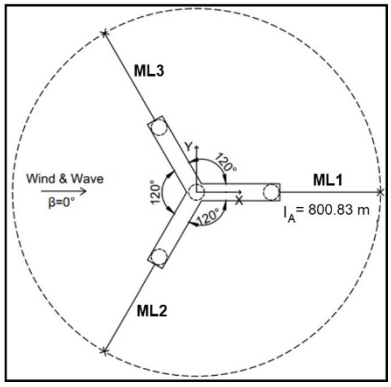

Figure 2. Top view of the mooring system

3 TIME-DOMAIN ANALYSIS OF THE FOWT

The integrated coupled time-domain analysis of the proposed FOWT is conducted using OpenFAST (NREL, 2023) and has a twofold objective. Specifically, it aims at: (a) identifying important static and intrinsic dynamic features of the FOWT (Load Cases LC1 and LC2 in Table 2) and (b) assessing the FOWT's performance under various wind and wave load cases (Load Cases LC3-LC7 in Table 2). The required for OpenFAST tower mode shapes are obtained by performing a modal analysis of the modified tower of the DTU 10 MW WT in BModes (Bir, 2007). Furthermore, WAMIT (Lee, 1995) has been used to acquire the required for the time-domain analysis frequency-dependent quantities (exciting forces and hydrodynamic coefficients) as well as the hydrostatic-gravitational coefficients.

Table 2. Examined load cases in OpenFAST

		$t_{simulation}$ (s)	$U_{w,RNA}$ (m/s)	H_s (m)	T_p (s)	WT condition
Static Equilibrium	LC1	1000	-	-	-	Parked
Free Decay	LC2	1000	-	-	-	Parked
Real conditions	LC3	5400	5.00 (cut-in)	0.52	3.11	Operating
	LC4	5400	10.30	1.10	3.98	
	LC5	5400	13.90 (rated)	1.55	4.50	
	LC6	5400	17.90	1.95	4.86	
	LC7	5400	25.00 (cut-out)	3.03	5.65	

For LC1 and LC2 (Table 2) the WT is parked, and the simulations are conducted in the absence of wind and waves. For LC3-LC7 (Table 2) the WT is fully operational. The action of turbulent wind with mean wind velocity at the hub, $U_{w,RNA}$, is taken into account together with irregular waves of significant wave height, H_s, and peak period, T_p. The latter characteristics have been defined by using the Jonswap spectrum for a fetch of 100 km. Head wind and waves (Figure 2) are considered.

4 RESULTS AND DISCUSSION

Table 3 shows the static offset of the FOWT (LC1, static equilibrium tests). The results demonstrate a good model stability, with very small static offsets in surge and pitch. Similar conclusion can be derived for heave; however, the corresponding offset is a bit larger due to the conservative design of the mooring system, as noted above. Moving on to LC2, the natural frequencies of the platform as resulted from the corresponding free decay simulations are cited in Table 4. Those values are within the range of other semi-submersible floating platforms, and they do not fall close to the 1P and 3P frequencies.

Table 3. Static offset of the FOWT (LC1)

Surge (m)	Heave (m)	Pitch (deg)
0.0203	-0.1909	-0.0728

Table 4. Natural frequencies (Hz) of the FOWT (LC2)

Surge	Sway	Heave	Roll	Pitch	Yaw
0.0049	0.0049	0.0433	0.4028	0.4028	0.0055

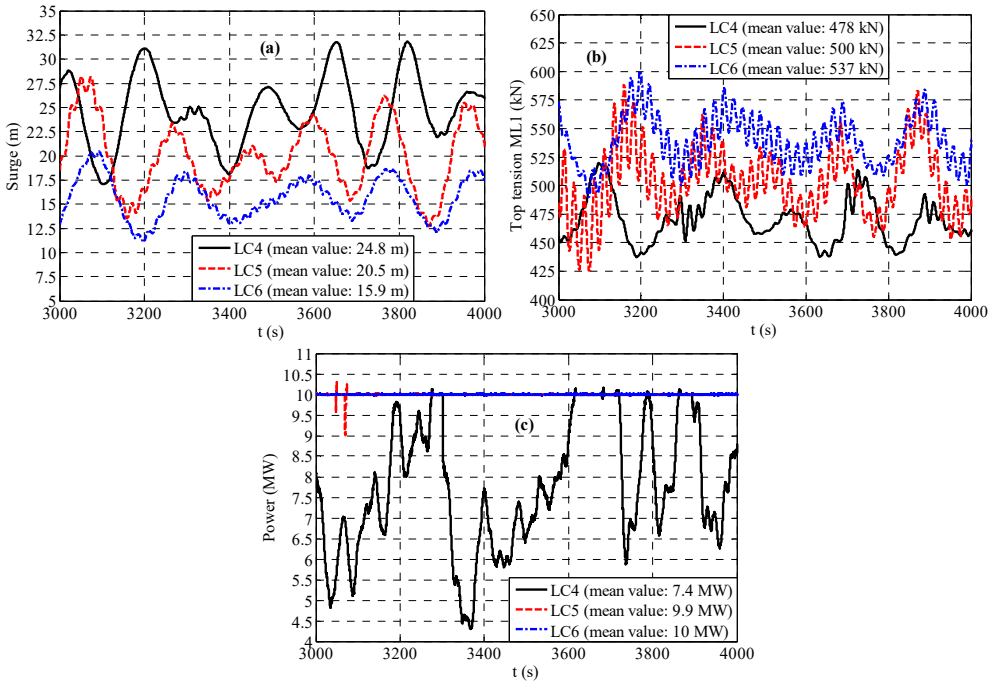

Figure 3. FOWT surge response, ML1 top tension and power for LC4, LC5 and LC6

Finally, in Figure 3 part of the time-series of some representative quantities (surge response, ML1 top tension and power) describing the FOWT's performance are shown indicatively for LC4, LC5 and LC6. For all cases, the surge response (Figure 3(a)) is dominated by the corresponding natural frequency, and it is mainly excited by the wind forcing. Similar is the variation of the ML1 top tension Figure 3(b)). By increasing the wind and the wave forcing (transition from LC4 to LC5 and, finally, to LC6), the platform's surge response decreases successively due to the decrease of the thrust force (results are not

included here due to space constraints). The opposite holds true for the tension of ML1 (Figure 3(b)) lying in the leeward side of the platform (Figure 2). Finally, regarding the produced power (Figure 3(c)), the WT for a given LC operates as anticipated.

5 CONCLUSIONS

The results of the present paper indicate an efficient design of a new 10 MW semi-submersible FOWT that meets some of the main design requirements of this kind of floating systems. More specifically, the natural frequencies of the FOWT lie within the required limits for this type of structures, while the power production as well as the dynamic responses of the FOWT are as expected compared to similar studies (e.g., Yu et al. 2017; Zhao et al. 2021). Further work is required including a more detailed mooring system design and an extensive assessment of the FOWT's performance under various load cases for different limit states in accordance with relevant standards.

References

Bak C, Zahle F, Bitsche R, Kim T, Yde A, Henriksen L, Natarajan A, Hansen M (2013) Description of the DTU 10 MW reference wind turbine vol. 5. DTU Wind Energy Report-I-0092.

Bir GS. (2007) User's guide to BModes (Software for Computing Rotating Beam Coupled Modes). National Renewable Energy Laboratory, USA.

Cao Q, Xiao L, Cheng Z, Liu M (2021) Dynamic responses of a 10 MW semi-submersible wind turbine at an intermediate water depth: A comprehensive numerical and experimental comparison. Ocean Eng 232: 109138. doi:10.1016/j.oceaneng.2021.109138

Faltinsen O (1993) Sea loads on ships and offshore structures. Cambridge Ocean Technology Series, Cambridge University Press.

Lee CH (1995) WAMIT theory manual. MIT Report 95-2, Department of Ocean Engineering, MIT.

Leimeister M, Bachynski EE, Muskulus M, Thomas P (2016) Rational upscaling of a semi-submersible floating platform supporting a wind turbine. Energy Procedia 94: 434–442. doi:10.1016/j.egypro.2016.09.212

Michailides C, Luan C, Gao Z, Moan T (2014) Effect of flap type wave energy converters on the response of a semi-submersible wind turbine in operational conditions. Paper presented at the 33rd International Conference on Ocean, Offshore and Arctic Engineering, San Francisco, California, USA, V09BT09A014.

National Renewable Energy Laboratory (NREL) (2023) OpenFAST Documentation - Release 3.4.1. Available at https://openfast.readthedocs.io/en/main/. Accessed 27 April 2023

Offshore Renewable Energy Catapult (OREC) (2021) Floating offshore wind: Cost reduction pathways to subsidy free. Floating Offshore Wind Centre of Excellence. Available via https://ore.catapult.org.uk/wp-content/uploads/2021/01/FOW-Cost-Reduction-Pathways-to-Subsidy-Free-report-.pdf. Accessed 27 April 2023

Pegalajar-Jurado A, Bredmose H, Borg M, Straume J, Landbø T, Andersen HS, Yu W, Müller K, Lemmer F (2018) State-of-the-art model for the LIFES50+ OOStar wind floater semi 10MW floating wind turbine. J Phys: Conf Ser IOP Publ 104 (1): 012024. doi:10.1088/1742-6596/1104/1/012024

Yu W, Müller K, Lemmer F, et al. (2017) D4.2 Public definition of the two LIFES50+ 10MW floater concepts. Deliverable of LIFES50+ project.

Zhao Z, Li X, Wang W, Shi W (2019) Analysis of dynamic characteristics of an ultra-large semi-submersible floating wind turbine. J Mar Sci Eng 7(6): 169. doi:10.3390/jmse7060169

Zhao Z, Shi W, Wang W, Qi S, Li X (2021) Dynamic analysis of a novel semi-submersible platform for a 10 MW wind turbine in intermediate water depth. Ocean Eng 237: 109688. doi:10.1016/j.oceaneng.2021.109688

DMPCO 2023

e-Proceedings of the 2nd International Scientific Conference on Design and Management of Port Coastal and Offshore Works Thessaloniki, Greece, May 24-27 2023

Wave trapping phenomena in an array of bottom-seated surface-piercing porous cylinders

D.N. Konispoliatis[1*], I.K. Chatjigeorgiou, V. Bougiouri

[1]School of Naval Architecture and Marine Engineering, National Technical University of Athens, Greece
[*]Corresponding author: dkonisp@naval.ntua.gr

Abstract

This work deals with the investigation of the interaction phenomena of regular waves with arrays of porous vertical cylinders. The acting loads on the array have been modelled using an analytical solution for the diffraction problem under the assumptions of potential flow and linear wave theory, whereas the multiple scattering approach is applied to describe the hydrodynamic wave interactions among the members of the array. Focus is placed on the so called "nearly trapped" mode phenomena, created by an array of multiple bodies, supplemented by representative numerical results for various porosity parameters and distances between the bodies concerning the exciting loads on the porous cylinders. The reduction of the wave amplitude around adjacent bodies is shown which is strongly affected by the porosity of the cylinders' side surface.

Keywords Trapping modes, Trapped waves, Porous cylindrical bodies, Darcy's law.

1 INTRODUCTION

Porous structures have been widely studied due to their effectiveness at dissipating the unwanted wave energy (Sollitt & Cross, 1972, 1976; Madsen 1972; Sulisz 1985). By comparing with the impermeable bodies, both the transmitted and reflected wave heights are relatively reduced, whereas the wave loads on porous structures are decreased. Hence, they become preferable due to their porosity, for applications such as harbor and shore protection. To raise some of them as examples, Williams & Li, (2000) studied the effect of various wave and structural parameters of arrays of porous cylinders on the hydrodynamic loads and the diffracted wave field. Also, Park et al. (2010) examined an array of truncated porous circular cylinders for the determination of the heave as well as the surge and the sway forces for various values of porosity rates. Zhao et al. (2011) presented a theoretical and experimental study on the interaction of water waves with a cylinder which is made of porous materials, whereas Park & Koo (2015) examined the wave interactions with multi-bodied partial porous cylinders under linear potential theory. Recently, Konispoliatis et al. (2021) presented a theoretical hydrodynamic analysis of a surface-piercing porous cylinder for the evaluation of the wave elevation around the body and the acting hydrodynamic loads for various values of porosity coefficients.

At the same time, there is a considerable interest in determining the hydrodynamic interactions between multibody impermeable arrangements due to the diffracted and the scattered waves that create the so called trapped-mode phenomenon (Ursell, 1951; Callan et al., 1991). The latter is related to the wave trapping in the fluid region between adjacent bodies, forming a near-standing wave with much larger amplitude compared to the waves at other wave frequencies, whose energy slowly leaks away to infinity. Maniar & Newman (1997) associated the existence of trapped waves in a channel with near-resonant modes occurring between neighborhood impermeable bodies with critical spacing. In these modes the diffraction loads are remarkably increased compared to the forces on a body in isolation. Evans & Porter (1999) investigated the trapping and near-trapping phenomena by a variety of bottom mounted vertical circular cylinder array, whereas in Kagemoto et al., (2002) the developed trapped waves in an array of cylinders have been experimentally investigated. Also, Konispoliatis et al. (2020) investigated the near trapped wave phenomena in an array of truncated cylinders in a perpendicular arrangement in front of a vertical breakwater.

The present paper takes a further step dealing with the same problem, enhanced however, with the existence of porous structures in the vicinity of the array. The 3D water-wave diffraction problem by

arrays of bottom-seated and surface piercing porous cylinders is formulated and solved, whereas the existence of trapped waves is studied against the porosity parameter.

2 HYDRODYNAMIC FORMULATION

An array of N porous vertical cylinders is assumed to be placed on the seabed and extend beyond the undisturbed free surface (see Figure 1). The sidewall of each cylinder is porous and thin. The bodies are exposed to the action of a plane incident wave train of frequency ω and amplitude A, propagating over a constant water depth d, at an angle θ with respect to the positive x-axis. The array bodies are assumed similar with a radius a, whereas the distance between the center of two adjacent cylinders is ℓ. Also, N local cylindrical coordinate systems $(r_q, \theta_q, z_q), q = 1, \ldots, N$ are considered with origin at the seabed and their vertical axes pointing upwards and coinciding with the vertical axis of symmetry of the q body.

A theoretical formulation is presented, which is suitable for solving the linearized diffraction problem around the array in the frequency domain. Specifically, the solution is based on the eigenfunction expansion method, in which analytical representations of the velocity potential are derived through the idealization of the flow field around each body. The condition on the porous boundary is defined by applying the Darcy's law, whereas the fluid velocity and its derivatives are matched at the common boundaries of adjacent fluid domains by enforcing appropriate continuity conditions. The fluid is assumed non viscous and incompressible and the flow irrotational, so that linear potential theory can be employed. The water domain is subdivided into two regions: (a) fluid region $I: r \geq a, 0 \leq z \leq d$, and (b) fluid region $II: 0 \leq r \leq a, 0 \leq z \leq d$.

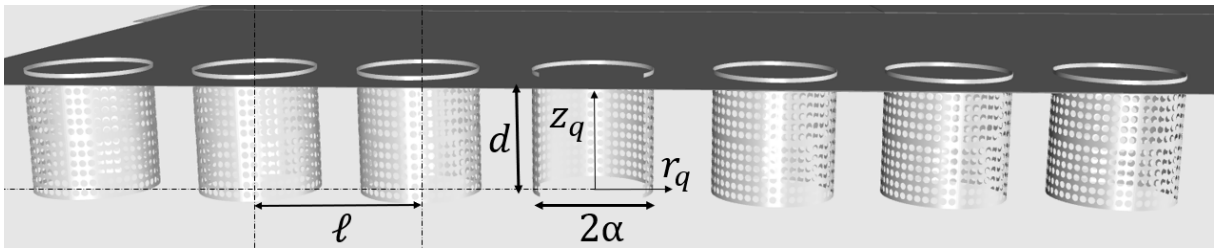

Figure 1. 3-D representation of the examined array of permeable cylindrical bodies

The velocity and the pressure fields are distributed due to the diffraction of the incoming waves. Both fields are described by the velocity potential, $\Phi^{q,l}(r_q, \theta_q, z_q; t) = \mathrm{Re}\left(\varphi^{q,l}(r_q, \theta_q, z_q)\mathrm{e}^{-\mathrm{i}\omega t}\right)$, $q = 1, \ldots, N$, $l = I, II$ which satisfies the Laplace equation; the combined linear kinematic and dynamic condition on the free surface; and the zero condition on the flat bottom (Konispoliatis et al., 2021). Also, the following Darcy's condition on the vertical boundaries of the q body should be satisfied, i.e.:

$$\frac{\partial \varphi^{q,II}}{\partial r_q} = ikG(\varphi^{q,II} - \varphi^{q,I}), r = a, 0 \leq z \leq d \tag{1}$$

In Equation (1) G denotes a dimensionless porous coefficient (Sankar and Bora, 2020); k is the wave number and $\frac{\partial()}{\partial r_q}$ stands for the derivative over r_q. Finally, a radiation condition must be imposed which states that propagating disturbances must be outgoing.

The diffraction potential $\varphi^{q,l}, l = I, II$, can be written as:

$$\varphi^{q,l}(r_q, \theta_q, z_q) = -i\omega A \sum_{m=-\infty}^{\infty} i^m \Psi_{D,m}^{q,l}(r_q, z_q) e^{im\theta_q} \tag{2}$$

The unknown potential functions $\Psi_{D,m}^{q,l}, q = 1, \ldots, N,\ l = I, II$, can be established through the method of matched axisymmetric eigenfunction expansions in which analytical representations of the velocity potential are derived through the idealization of the flow field around each body (Mavrakos & Koumoutsakos, 1987).

Regarding the wave interaction phenomena between the array's members and the incoming waves, the multiple scattering approach has been applied. The latter is based on the superposition of the incident wave potential and various orders of propagating and evanescent modes that are scattered and radiated

by the array members. The method has been thoroughly presented in Mavrakos & Koumoutsakos, (1987) hence it is no further elaborated here.

3 NUMERICAL RESULTS

3.1 Validation

In this section the validity of the presented theoretical method is confirmed. The results from the present methodology are compared with corresponding data, which are available in the literature. In Figure 2 the horizontal exciting forces, normalized by $2\rho g A a^2$, acting on a four porous cylinder array (see Figure 2a) are presented. The term ρ stands for the water density and g for the gravity acceleration. Here the radius of the examined porous bodies equals to $a = d/5$, the distance between the center of adjacent bodies is $\ell = 4d/5$, and θ is assumed equal to zero. Also, several porous coefficients are examined, i.e., $G = 0, 1, 2$. The results are compared with the outcomes from Williams & Li (2000). From the figure (see Figure 2b) it can be seen a favorable agreement between the calculation obtained by the present method and the results reported in Williams & Li work. Therefore, it can be concluded that the present model can effectively solve the diffraction problem for an array of porous cylindrical bodies.

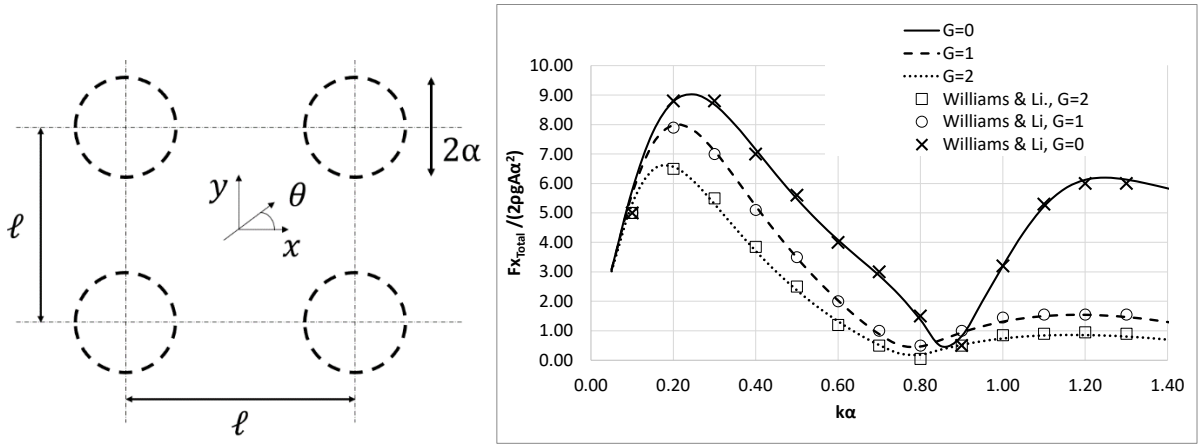

(a) (b)

Figure 2. Horizontal exciting forces on an array of four porous bottom-seated cylindrical bodies. The results are compared against those reported in Williams & Li (2000). The dashed circles in the left figure denote the four porous bodies of the array.

3.2 Test cases

The presented analysis is applied for the case of an array of nine bottom-seated, surface-piercing porous cylinders (see Figure 3). The nine bodies are identical, and their geometric characteristics are $a/d = 1/8$, $a/\ell = 1/8$. Also, several porous coefficients are examined $G = 0, 0.1, 0.25, 0.5, 1, 2$. The bodies are considered placed in a row, in the direction of the incoming wave train (hence $\theta = 0$). In Figure 4α the wave loads acting on the middle cylinder of the array (i.e., the fifth cylinder) are depicted for different values of porous coefficients versus $k\ell/(2\pi)$. The exciting forces are normalized by the term $\rho g A a d$.

In the sequel, the effect of the distance between the porous bodies on the exciting forces is examined. Here the geometric characteristics of the nine porous bodies are: $a/d = 1/8$, $a/\ell = 1/4, 1/6, 1/8, 1/10, 1/12$ for $G = 0.25$. Similarly to the above configuration, the bodies are considered placed in a row, whereas $\theta = 0$. Figure 4b depicts the exciting forces on the middle cylinder of the array (i.e., the fifth cylinder) for different values of distances ℓ versus $k\alpha$.

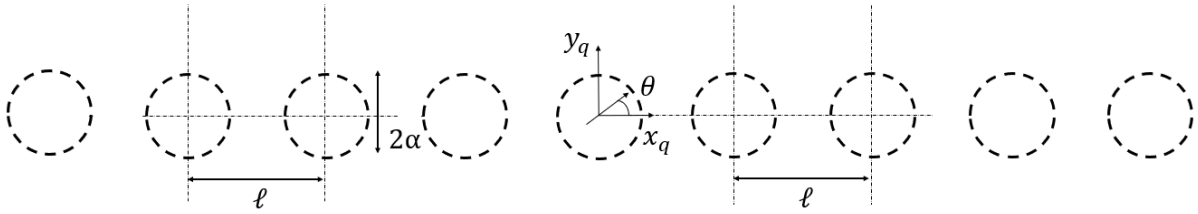

Figure 3. Plan view of the multi-body array of nine bottom-seated and surface piercing porous cylinders.

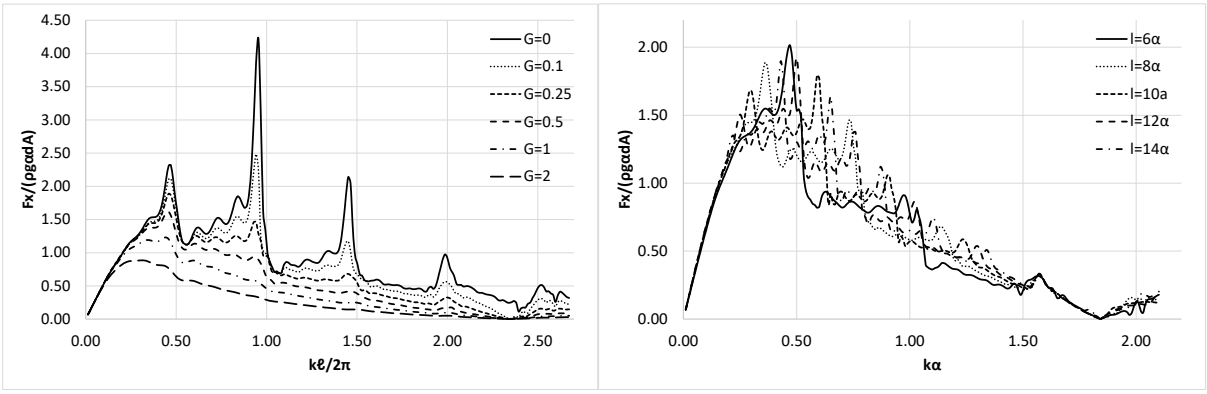

(a) (b)

Figure 4. Dimensionless horizontal exciting forces on the middle porous cylinder of a nine bottom-seated cylinder array: (a) plots for various porous coefficients $G = 0, 0.1, 0.25, 0.5, 1, 2$; (b) plots for various distances between the porous bodies $a/\ell = 1/6, 1/8, 1/10, 1/12, 1/14$.

4 CONCLUSIONS

This study dealt with the water wave diffraction problem of arrays of circular porous cylinders. Two different configurations were investigated (i.e., an array of nine porous cylinders with a constant distance between adjacent bodies and various porous coefficients; and a similar porous array with a constant porous coefficient and various distances between neighborhood bodies) based on the hydrodynamic loading exerted on the constituent modules. By comparing the results from the theoretical formulation, the following conclusions were drawn:

- The "Dirichlet" and "Neumann" trapped waves (for wave numbers $k\ell = \pi$ and $k\ell = 2\pi$, respectively) and the "nearly trapped waves" (local resonances at remaining wave numbers) occur at the same frequency regardless the examined porous coefficients. Nevertheless, as G increases, the exciting forces on the body decrease since the incident wave energy is absorbed by the pores of the cylindrical surface. In the figures $G = 0$ means impermeable surface, whereas for $G \gg 0$, the sidewall is completely permeable to fluid.
- The exciting forces on the porous body attain an increased oscillating behavior as the distance between adjacent bodies increases. An important feature that should be observed is that the exciting forces zero at $ka \sim 1.85$, regardless the distance between the bodies. This wave number corresponds to the first root of Bessel function $J_1'(ka)$ which is applied in the solution procedure for the determination of the fluid's velocity potential (see Mavrakos & Koumoutsakos, 1987).

Summarizing, it can be seen that the forces on the multi-body array can be reduced significantly by the porosity and the forces tend to decrease as the porosity parameter increases. On the other hand, placing the bodies at a greater distance does not seem to cause a reduction of the exerted loads on the examined body. Hence, the depicted results allow us to conceive the examined configuration as a section of a system for an alternative application, say a breakwater.

Acknowledgements

This research received financial support by Greek national funds through the Operational Program "Competitiveness, Entrepreneurship & Innovation" of the National Strategic Reference Framework (NSRF) – Research Funding Program: "MATISSE: Study of the appropriateness and the adequacy of modern materials for offshore fish cage – numerical and experimental investigation in realistic loading conditions".

References

Callan M, Linton C, Evans D (1991) Trapped modes in two dimensional waveguides. J Fluid Mech., 1991; 229:51-64

Evans D, Porter R (1999) Trapping and near-trapping by arrays of cylinders in waves, J. Engng. Math.; 35: 149-179

Kagemoto H, Murai M, Saito M, Molin B, Malenica S (2002) Experimental and theoretical analysis of the wave decay along a long array of vertical cylinders. J. Fluid Mech.;456: 113-135

Konispoliatis D, Chatjigeorgiou I, Mavrakos S (2020) Near trapped wave phenomena in an array of truncated cylinders in a perpendicular arrangement in front of a vertical breakwater. Appl. Math. Mod.; 83: 497-525

Konispoliatis D, Chatjigeorgiou I, Mavrakos S (2021) Theoretical hydrodynamic analysis of a surface-piercing porous cylindrical body. Fluids, 6 (9), 320

Madsen O (1972) Wave transmission through porous structures. Journal of Waterways, Ports, Coastal Ocean Engineering Division; ASCE, 100: 169-188

Maniar H.D.; Newman, J.N. Wave diffraction by a long array of cylinders. Journal of Fluid Mechanics, 1997, 339: 309-330

Mavrakos SA, Koumoutsakos P (1987) Hydrodynamic interaction among vertical axisymmetric bodies restrained in waves. Appl. Oc. Res., 9: 128–140

Park MS, Koo W, Choi Y (2010) Hydrodynamic interaction with an array of porous circular cylinders. Inter. J. Nav. Archit. Oc. Engng. 2: 146-154

Park MS, Koo W (2015) Mathematical modeling of partial-porous circular cylinders with water waves. Hindawai Publishing Corp. Math. Problems Engng; 903748.

Sankar A, Bora SN (2020) Hydrodynamic coefficients for a floating semi-porous compound cylinder in finite ocean depth. Marine Syst. Oc. Techn.; 15: 270-285

Sollitt C, Cross R (1972) Wave transmission through permeable breakwaters. Proceedings of the 13th Coast. Engng. Conf.; Vancouver, Canada

Sollitt C, Cross R (1976) Wave reflection and transmission at permeable breakwaters. Tech. Paper 76-8. US Army Corps of Engineers, Coast. Engng. Res. Centre

Sulisz W (1985) Wave reflection and transmission at permeable breakwaters of arbitrary cross section. Coast. Engng; 9: 371-386

Ursell F (1951) Trapping modes in the theory of surface waves. Mathematical Proceedings of the Cambridge Philosophical Society; 47 (2): 347-358

Williams A, Li W (2000) Water wave interaction with an array of bottom-mounted surface-piercing porous cylinders. Oc. Engng.; 27: 841-866

Zhao F, Bao W, Kinoshita T, Itakura H (2011) Theoretical and experimental study on a porous cylinder floating in waves. ASME J. Offsh. Mech. Arctic Engng,; 133 (1): 011301

DMPCO 2023

e-Proceedings of the 2nd International Scientific Conference on Design and Management of Port Coastal and Offshore Works Thessaloniki, Greece, May 24-27 2023

Numerical modelling of a floating hybrid offshore wind and wave energy system by utilizing the generalized modes approach

N. Mantadakis[*1], E. Loukogeorgaki[1], C. Michailides[2], P. Troch[3]

[1]Department of Civil Engineering, Aristotle University of Thessaloniki, Thessaloniki 54124, Greece
[2]Department of Civil Engineering, International Hellenic University, Serres 62124, Greece
[3]Department of Civil Engineering, Ghent University, Ghent B-9052, Belgium
[*]Corresponding author: mantadaki@civil.auth.gr

Abstract

In the present paper, a generic numerical tool for the time-domain analysis of a floating Hybrid Offshore Wind and Wave Energy System (HOWiWaES), consisting of a Floating Offshore Wind Turbine (FOWT) and several Wave Energy Converters (WECs) is developed and is preliminary validated. The floating platform and the WECs are modeled as one multi-component floating structure with six rigid-body Degrees of Freedom (DoFs), while the motions of the WECs relatively to the FOWT are described as additional DoFs by utilizing the generalized modes concept. The tool is developed by modifying and extending appropriately the aero-hydro-servo-elastic open-source code Open-FAST. The frequency-dependent exciting forces and hydrodynamic coefficients, as well as the hydrostatic coefficients are, initially, calculated in the frequency domain using the traditional boundary integral equation method. The required for this calculation mode shapes of the generalized DoFs are determined by developing appropriate vector shape functions. The numerical tool is validated by comparing results with the numerical ones of other investigators, who utilized the multi-body approach, for the case of a 5 MW OWT with a spar floating platform and a conic WEC buoy hinged on it via a mechanical arm. A quite good agreement is obtained, indicating the potential of the developed tool to model floating HOWiWaESs efficiently.

Keywords Floating hybrid wind and wave energy systems, Offshore wind turbines, Wave energy converters, Generalized modes approach.

1 INTRODUCTION

Offshore wind and wave energy are two of the most important renewable energy sources in the marine environment. Their efficient exploitation, directly related to the EU energy policies, can contribute to energy security enhancement, economic growth, and reduction of greenhouse gas emissions. Accordingly, many large-scale commercial offshore wind farms have been installed and are operating in Europe, while, during the last years, the Floating Offshore Wind Turbines' (FOWTs) technology is rapidly growing, giving access to deep waters, where stronger and more consistent winds exist. Regarding wave energy, a variety of Wave Energy Converters (WECs) with different working principles have been investigated, developed, and tested so far aiming to overcome existing technological barriers and achieve competitiveness with other renewable energy sources. Irrespectively of the above developments, costs reduction still presents a challenge that both the offshore wind and the wave energy sectors share. It may, thus, be beneficial to deploy floating Hybrid Offshore Wind and Wave Energy Systems (HOWiWaESs) that enable the simultaneous exploitation of the corresponding energy potentials in deep waters by combining in one structure an offshore wind turbine with WECs. Up to now, different concepts of HOWiWaESs have been proposed by various researchers, who investigated their performance (dynamic behavior and power production) numerically (e.g., Muliawan et al. 2013, Karimirad and Michailides 2018, Bachynski and Moan 2013, Luan et al. 2014) and experimentally (e.g., Gao et al. 2016, Michailides et al. 2016, Armesto et al. 2016). In all the above investigations adequate, case-specific, time-domain numerical models have been developed based on the multi-body approach.

In the present paper, a generic numerical tool for analyzing in time-domain the performance of floating HOWiWaESs under the combined wind and wave action is developed and is preliminary validated. Contrary to existing studies, the floating platform and the WECs are modeled as one multi-component

floating structure with six rigid-body Degrees of Freedom (DoFs), while the motions of the WECs relatively to the FOWT are described as additional DoFs by utilizing the generalized modes concept (Newman 1994). The numerical tool is applied for a HOWiWaES consisting of a spar floating platform and a conic WEC buoy hinged on it via a mechanical arm, and results are compared with the corresponding numerical ones of other investigators.

2 NUMERICAL MODELLING

The proposed in the present paper numerical tool for the time-domain analysis of a floating HOWiWaES is developed by deploying the numerical modelling framework shown in Figure 1. The whole framework is based on a "dry" mode superposition approach, where the generalized modes concept is utilized for describing the relative to the FOWT motions of the WECs, additionally to the six rigid-body modes of the multi-component floating structure. It is noted that the generalized modes concept can take advantage of the layout's symmetry, providing a faster and more effective way for obtaining results.

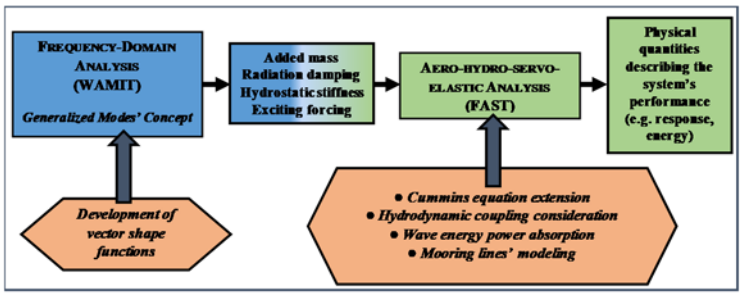

Figure 1. Outline of the present numerical modelling framework

Initially, the multi-component floating structure (floating platform and WECs) is modeled in the frequency domain in order to calculate the required for the time-domain analysis physical quantities (i.e., frequency-dependent exciting forces and hydrodynamic coefficients, as well as hydrostatic coefficients). The frequency-domain analysis relies on the boundary integral equation method and is numerically realized using the WAMIT© software (Lee, 1995). The 3D linear potential theory is utilized, where the multi-component floating structure is assumed to undergo small oscillations in all six DoFs corresponding to the rigid-body modes, while, moreover, the relative to the platform motions (translations and/or rotations) of the WECs are taken into account through the inclusion of N additional DoFs (generalized modes). The required mode shapes of the generalized modes are determined in the present paper in vacuum ("dry" mode superposition approach), through the derivation of appropriate 3D vector shape functions.

The solution of the 1st order boundary value problem is based on the 3D panel method by utilizing Green's theorem and by imposing the appropriate boundary conditions on the free surface, the sea bottom and the bodies (Lee 1995; Newman 1994; Lee and Newman 2004). Having solved the boundary value problem, the generalized exciting forces, F_i, $i = 1, \dots N + 6$, and generalized added mass and damping coefficients, A_{ij}, B_{ij}, $i,j = 1, \dots, N + 6$, are calculated as follows:

$$F_i = -i\omega\rho \iint_{S_B} n_i \, \varphi_D dS, \; i = 1, \dots, N + 6 \tag{1}$$

$$A_{ij} - \frac{i}{\omega} B_{ij} = \rho \iint_{S_B} n_i \, \varphi_j dS, \; i,j = 1, \dots, N + 6 \tag{2}$$

where S_B is the wetted surface of the floating structure, ρ is the sea water density, φ_D is the diffracted potential, φ_j, $j = 1, \dots, N + 6$, is the unit radiation potential of the j^{th} DoF respectively, n_i is the unit normal vector of the i^{th} DoF, ω is the frequency of the unit-amplitude incident waves and $i^2 = -1$.

As for the hydrostatic restoring coefficients C_{ij}, $i,j = 1, \dots, N + 6$, those are obtained according to Newman (1994).

Having calculated the required for the time-domain analysis physical quantities, the modeling and the analysis of the HOWiWaES in time domain follows (Figure 1). This is achieved by modifying and extending appropriately the aero-hydro-servo-elastic open-source code Open-FAST (NREL, 2023). More specifically, the equation of motion in Open-FAST, which is formed based on the Newton's second law by deploying the Cummins time-domain formulation (Cummins 1962), is appropriately extended to account for the additional N generalized DoFs as well as for the Power Take-Off (PTO) mechanisms of the WECs. Accordingly, and taking into account that a FOWT is modelled in Open-FAST using up to 24 DoFs, the equation of motion for a HOWiWaES with $M = 24+N$ DoFs can be written as follows:

$$\boldsymbol{mX}\ddot{(t)} = \boldsymbol{F_{exc}}(t) + \boldsymbol{F_{rad}}(t) + \boldsymbol{F_{hs}}(t) + \boldsymbol{F_{aer}}(t) + \boldsymbol{F_{cont}}(t) + \boldsymbol{F_{moor}}(t) + \boldsymbol{F_{PTO}}(t) + \boldsymbol{F_{rest}}(t) \quad (3)$$

where t is time, $\ddot{\boldsymbol{X}}(t)$ is the M X 1 vector of the HOWiWaES accelerations, $\boldsymbol{m}$ is the M X M structural mass matrix, $\boldsymbol{F_{exc}}(t)$ is the M X 1 vector of the wave exciting forces, $\boldsymbol{F_{rad}}(t)$ is the M X 1 vector of the wave radiation forces, $\boldsymbol{F_{hs}}(t)$ is the M X 1 vector of the hydrostatic-gravitational forces, $\boldsymbol{F_{aer}}(t)$ is the M X 1 vector of the aerodynamic forces, $\boldsymbol{F_{cont}}(t)$ is the M X 1 vector of the forces resulting from the controller, $\boldsymbol{F_{moor}}(t)$ is the M X 1 vector of the mooring lines' forces, $\boldsymbol{F_{PTO}}(t)$ is the M X 1 vector of the forces originating from the PTO mechanisms and $\boldsymbol{F_{rest}}(t)$ is the M X 1 vector of other forces (e.g., viscous forces). Under the action of irregular waves, $\boldsymbol{F_{rad}}(t)$ is calculated using Eq. 4, where $\boldsymbol{A}_\infty$ is the added mass matrix at infinite frequency, $\boldsymbol{K_{rad}}$ is the matrix of the impulse response functions (retardation functions), $\dot{\boldsymbol{X}}$ is the vector of the HOWiWaES velocities and τ is a dummy variable.

$$\boldsymbol{F_{rad}}(t) = -\boldsymbol{A}_\infty \ddot{\boldsymbol{X}}(t) - \int_0^t \boldsymbol{K_{rad}}(t-\tau)\dot{\boldsymbol{X}}(\tau)d\tau \quad (4)$$

The hydrodynamic coupling between the FOWT and the WECs is taken into account through the inclusion of relevant non-zero terms in the $\boldsymbol{F_{rad}}(t)$ and $\boldsymbol{F_{hs}}(t)$ matrices of Eq. 3 (A_{ij}, B_{ij} and C_{ij} for $i \neq j = 1, \dots, N+6$ in the frequency domain analysis). Finally, it is noted that for deploying Eq. 3 in Open-FAST, extensive modifications of the source-code subroutines have been conducted.

3 VALIDATION OF THE NUMERICAL TOOL

The numerical tool is validated by comparing results with the numerical ones obtained by Karimirad and Michailides (2018) for the case of the so-called "Wind-WEC" hybrid system (Figure 2). The examined system consists of the NREL 5 MW FOWT with a spar floating platform of 8,216,000 kg total mass and a conic heaving WEC buoy of 10 m diameter, 180,509 kg mass, hinged on the platform via a mechanical arm of 20 m length. The PTO of the device is modelled as a linear damping system with damping coefficient 14,409 kg/s. The hub of the FOWT is located 90 m above Mean Water Level (MWL) and the platform's draft is 120 m. The FOWT is moored to the seabed floor via a 3-leg catenary delta segment system of 902 m length in total (900 m of 42.5 kg/m mass plus the 2 m with clump mass of 17,253 kg/m) and axial stiffness of 384,243 kN. The whole system is located in an area of 320 m water depth.

Based on the above, the numerical tool developed herein is applied for a 7 DoFs multi-component floating structure (i.e., $N = 1$) with the additional generalized DoF denoting the heave motion of the WEC relative to the spar platform. Accordingly, the whole floating system has a displaced volume of 8,160.8 m^3, while the Center of Gravity (COG) and the Center of Buoyancy (COB) in the global coordinate system lying on the MWL at the center of the FOWT are (-0.44, 0.0, -76.84) and (-0.45, 0.0, -60.7) respectively.

Validation is performed for an operating, near rated wind profile of 11.0 m/s average velocity, with shear and normal turbulence model for class B wind turbines together with Kaimal wind spectra and for irregular waves (Jonswap spectrum) of significant wave height $H_s = 3.6$ m and peak period $T_p = 10.2$ s. Four different Loading Cases (LCs) are simulated by modifying the wind and the wave direction with respect to the X-surge axis. In LC1 both the wind and the wave direction are equal to 0 deg, while in LC4 the action of wind and waves with 30 deg direction is taken into account. LC2 and LC3 correspond

to misaligned wind and wave conditions (0 deg wind and 30 deg wave direction in LC2, 30 deg wind and 0 deg wave direction in LC3). The simulation duration has been set to 1000 s, while the frequency domain analysis has been implemented for ω varying between 0.5 rad/s and 3.0 rad/s.

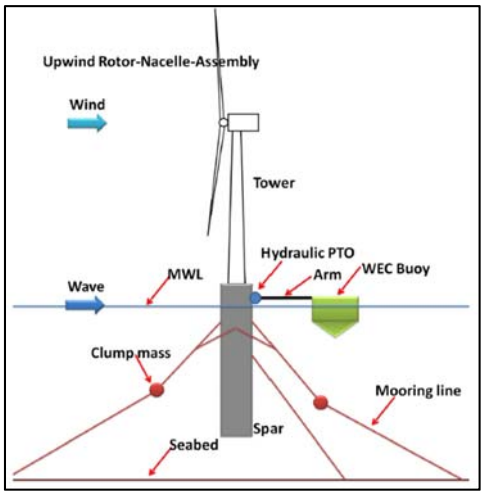

Figure 2. The "Wind-WEC" system (Karimirad and Michailides 2018)

Figure 3 shows indicatively part of the time series of the WEC's absorbed power as obtained from the developed in the present paper numerical tool for the 4 examined LCs, while in Figure 4 the mean value, P_{mean}, and the standard deviation, P_{std}, of those time series are compared with the corresponding statistical quantities obtained from Karimirad and Michailides (2018). It is worth to note that for LC1 and LC3 (Figure 3(a)), as well as for LC2 and LC4 (Figure 3(b)) the results are almost the same. This indicates that the WEC's performance is mainly affected by the wave direction and not by the wind direction.

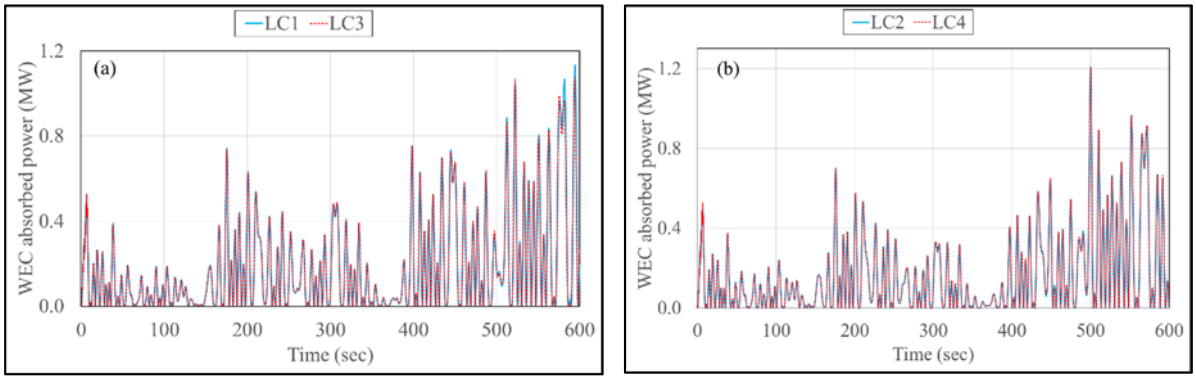

Figure 3. WEC's absorbed power for: **(a)** LC1 and LC3 and **(b)** LC2 and LC4

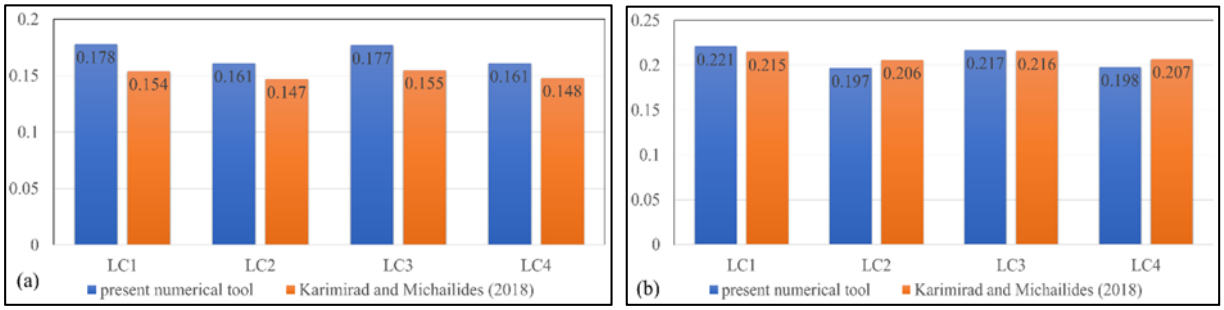

Figure 4. Comparison of the present numerical tool with Karimirad and Michailides (2018) for LC1-LC4 in terms of: **(a)** P_{mean} and **(b)** P_{std} (values are given in MW)

The results of Figure 4a illustrate that the present numerical tool slightly overestimates the mean values of the WEC's absorbed power, P_{mean}, for all examined LCs compared to the results of Karimirad and Michailides (2018). As for the P_{std} (Figure 4b), quite small differences are observed between the two numerical models/approaches.

4 CONCLUSIONS

In the present study, a generic numerical tool for conducting aero-hydro-servo-elastic analysis of a HOWiWaES by utilizing the generalized modes approach was developed. The tool was preliminary validated by comparing results with the numerical ones of other investigators, who utilized the multi-body approach, for the case of a FOWT with a spar platform and a heaving buoy hinged on it under several wind and wave conditions. A quite good agreement between the two numerical tools/approaches has been obtained. Differences do exist attributed to the different assumptions of the two numerical tools/approaches, related mainly to the WEC modeling. Specifically, Karimirad and Michailides (2018) modelled a mechanically rotating joint between the WEC's arm and the FOWT's platform, while in the present numerical tool we considered the WEC as a purely heaving device. The consideration of a generalized DoF resembling in a more accurate manner the motion of the device and relevant comparisons, as well as the inclusion of multiple WECs around the platform present items for future research.

References

Armesto JA, Sarmiento J, Ayllón V, Iturrioz A, Jurado A, Guanche R, Losada IJ (2016) Numerical and experimental study of a multi-use platform. Paper presented at the 35th International Conference on Ocean, Offshore and Arctic Engineering (OMAE2016), June 19-24, 2016, Busan, South Korea.

Bachynski EE, Moan T (2013) Point absorber design for a combined wind and wave energy converter on a tension-leg support structure. Paper presented at the 32nd International Conference on Ocean, Offshore and Arctic Engineering (OMAE2013), June 9-14, 2013, Nantes, France.

Cummins WE (1962) The impulse response function and ship motions. Report 1661, Department of the Navy David Taylor Model Basin.

Gao Z, Moan T, Wan L, Michailides, C (2016) Comparative numerical and experimental study of two combined wind and wave energy concepts. J Ocean Eng Sci 1:36-51. doi: 10.1016/j.joes.2015.12.00

Karimirad M, Michailides C (2018) Effects of misaligned wave and wind action on the response of the combined concept WindWEC. Paper presented at the 37th International Conference on Ocean, Offshore and Arctic Engineering (OMAE2018), June 17-22, 2018, Madrid, Spain.

Lee CH (1995) WAMIT theory manual. Massachusetts, USA.

Lee CH, Newman JN (2004) Computation of wave effects using the panel method. In: Chakrabarti S (ed) Numerical Models in Fluid–Structure Interaction. WIT Press, p 1–41.

Luan C, Michailides C, Gao Z, Moan T (2014) Modeling and analysis of a 5 MW semi-submersible wind turbine combined with three flap-type wave energy converters. Paper presented at the 33rd International Conference on Ocean, Offshore and Arctic Engineering (OMAE2014), June 8-13, 2014, San Francisco, California, USA.

Michailides C, Gao Z, Moan T (2016) Experimental and numerical study of the response of the offshore combined wind/wave energy concept SFC in extreme environmental conditions. Mar Struct 50:35-54. doi:10.1016/j.marstruc.2016.06.005

Muliawan MJ, Karimirad M, Gao Z, Moan T (2013) Extreme responses of a combined spar-type floating wind turbine and floating wave energy converter (STC) system with survival modes. Ocean Eng 65:71-82. doi:10.1016/j.oceaneng.2013.03.002

National Renewable Energy Laboratory (NREL) (2023) OpenFAST Documentation - Release 3.4.1. Available at https://openfast.readthedocs.io/en/main/. Accessed 27 April 2023.

Newman JN (1994) Wave effects on deformable bodies. Appl. Ocean Res. 16(1):47-59. doi:10.1016/0141-1187(94)90013-2

DMPCO 2023

e-Proceedings of the 2nd International Scientific Conference on Design and Management of Port Coastal and Offshore Works Thessaloniki, Greece, May 24-27 2023

2D Numerical hydrodynamic validation of very flexible floating solar platforms

R. Ioannou[1*], V. Stratigaki[1], E. Loukogeorgaki[2], P. Troch[1]

[1]Department of Civil Engineering, Ghent University, Ghent, Flanders, 9052, Belgium
[2] Department of Civil Engineering, Aristotle University of Thessaloniki, Thessaloniki, Macedonia, 54124, Greece
[*]Corresponding author: rafail.ioannou@ugent.be

Abstract

In this paper numerical modelling of thin and very flexible offshore floating photovoltaic (OFPV) platforms is conducted using the coupling between DualSPHysics, a smoothed particle hydrodynamics (SPH) solver, and the finite element analysis (FEA) module of Project Chrono. This framework allows non-linear time-domain hydroelastic phenomena to be investigated for various fluid-structure interaction (FSI) applications due to the meshfree nature of the fluid solver. Furthermore, the structural flexibility of the floating platform can be described by the rigid finite element method (RFEM), using the mechanical joints provided by the existing coupling. However, due to the computational demanding costs of the SPH solver only a two-dimensional (2D) formulation is developed. The proposed numerical model is validated against physical data from wave flume testing and at this stage a reasonably high accuracy and good agreement with the numerical predictions are achieved.

Keywords FSI, SPH, RFEM, Floating solar platforms, Hydroelasticity.

1 INTRODUCTION

Scaling up energy production from renewable resources is an imperative need to meet future energy demands. A novel approach to ramp up production of renewable energy is the use of offshore floating photovoltaics (OFPVs), deploying land-based renewable solar technologies on offshore platforms. The current state of the art OFPVs prototypes lack any design standards for environmental loads, while they employ as proxy the design basis of the offshore oil and gas (ONG) industry. Contrary to the very large and stiff offshore ONG structures, OFPVs conceptual designs use thin, lightweight, and very flexible materials (Trapani and Millar 2014), leading to design inefficiencies when adapting ONG standards to capture device specific behaviours. OFPVs are characterized by structural flexibility and large deformations which are dominant in comparison to the rigid body motions. Thus, significant consequences are introduced on the overall structural robustness and fatigue integrity of the floating structure (Loukogeorgaki et al. 2014).

In order to design and assess the survivability of flexible OFPVs, the related wave-induced hydrodynamic forces, the floating body motions and the structural deformations have to be modelled. Simplistic approaches based on linear models and analytical equations to determine the hydrodynamic forces on the floating structure, disregard the hydroelastic performance of the OFPVs. Such approaches may be based on the Morrison equation and on potential flow theory to model the hydrodynamic flow (Al-Yacouby et al. 2020; Ikhennicheu et al. 2021). The hydroelastic response of the OFPVs needs to be addressed with fully rotational time-domain non-linear models both for structural dynamics and hydrodynamics.

To address the described knowledge gaps, the current research employs the coupling of a smoothed particle hydrodynamics (SPH) model (DualSPHysics), to account for non-linear hydrodynamic effects, with a finite element analysis (FEA) library (Project Chrono), to account for the elastic response of the structure. Capasso et al. (2022) employed the same coupling to accommodate flexible elements through a co-rotational formulation of rigid bodies, while Martínez-Estévez (2023) further developed the existing coupling to simulate an Euler-Bernoulli beam. Furthermore, O'Connor and Rogers (2021) described a unified SPH formulation in DualSPHysics, solving both the fluid and the structural domain, to handle fluid-structure interaction (FSI) applications. However, all prementioned approaches simulate flexible beams which are fixed to solid boundaries, while their numerical setup is limited in terms of

domain size. Thus, the current research aims to extend the existing coupling, by simulating flexible floating structures with no constraints and validating the numerical setup against experimental cases with greater domain size at a two-dimensional (2D) formulation.

2 DUALSPHYSICS: SMOOTHED PARTICLE HYDRODYNAMICS METHOD

DualSPHysics employs the SPH method, which is a well-established computational fluid dynamics (CFD) approach, to simulate fluid flow. SPH is a fully meshfree method replicating fluid as a set of discrete particles moving in a Lagrangian manner. Particle properties are computed individually based on their interactions with neighboring particles, governed by the Navier-Stokes equations. In the DualSPHysics formulation (Domínguez et al. 2021), the area of influence for each particle is determined based on a Kernel function, specified by a smoothing length and defined by the initial inter-particle distance (dp). This meshless nature of the numerical formulation allows DualSPHysics to solve complex fluid dynamic problems, such as free surface flow and FSI applications.

2.1 Fundamental equations

For each time step and for each individual particle the Navier–Stokes equations are applied in a Lagrangian formulation. Therefore, the conservation of momentum and continuity are herein described in Eqs. 1 – 2 respectively, as they are applied in DualSPHysics. Within this formulation the physical properties of position r, velocity u, pressure P, mass m and density ρ of particle a are calculated with respect to its neighboring particles $b = 1,\dots,Np$, where Np is the total number of particles within the area of influence of particle a:

$$\frac{du_a}{dt} = -\sum_{b=1}^{Np} m_b \left(\frac{P_b + P_a}{\rho_b \rho_a} + \Pi_{ab}\right)\nabla_a W_{ab} + g \tag{1}$$

$$\frac{d\rho_a}{dt} = \sum_{b=1}^{Np} m_b \,(u_a - u_b)\nabla_a W_{ab} + \delta h c_0 \sum_{b=1}^{Np} \Psi_{ab}\nabla_a W_{ab}\frac{m_b}{\rho_b} \tag{2}$$

with g denoting acceleration of gravity and W_{ab} a Quintic Kernel function (Wendland, 1995).

Since in DualSPHysics a weakly-compressible fluid is defined, a density diffusion term (DDT) is also introduced in Eq. 2 to filter the noisy pressure field (Antuono et al. 2012). For fluid – boundary interaction a DDT is selected based on Fourtakas et al. (2019), with $\delta = 0.10$ and Ψ_{ab} given by:

$$\Psi_{ab} = 2(\rho_b^D - \rho_a^D)\frac{r_{ab}}{\|r_{ab}\|} \tag{3}$$

where $r_{ab} = r_a - r_b$ is the in-between distance of the particles and $\rho^D = \rho^T - \rho^H$ is the dynamic density, with superscript T denoting the total density and superscript H the hydrostatic density. A numerical dissipation is also added to the pressure term in the form of artificial viscosity as indicated in Monaghan (1992). Thus, a tuning coefficient is applied for tuning the dissipation process (Domínguez et al. 2021). Finally, an equation of state is introduced to the fluid pressure calculation as function of the fluid density in order to ensure that a weakly compressible fluid formulation is maintained with less than 1% density variations (Liu and Liu 2003).

2.2 Boundary conditions and floating bodies

Within DualSPHysics the dynamic boundary conditions (DBC) treatment is applied to define boundary conditions, as described by Crespo et al. (2007). Solid boundaries are described as particles subjected to the same equations of momentum and continuity (Eqs. 1 - 2) as fluid particles, but with their velocities fixed to zero or with a pre-defined velocity profile (e.g., wave paddle movement). However, this formulation leads to a small gap between the fluid and the solid boundaries due to repulsive forces exerted on the moving particles from the artificially fixed boundary particles, resulting to misprediction of pressures on solid boundaries. To anticipate this issue a modified DBC (mDBC) framework (English et al. 2020) is recruited for the floating bodies, where boundary particles receive properties of

neighboring fluid particles to achieve accurate pressure prediction. DualSPHysics allows the simulation of fluid-driven floating bodies, by calculating forces acting on each boundary particle k, f_k, as a summation of exerted forces per unit mass from all fluid particles in its area of influence. However, only rigid body dynamics equations are employed to simulate their motion:

$$M\frac{dV}{dt} = \sum_{k\in body} m_k f_k \tag{4}$$

$$I\frac{d\Omega}{dt} = \sum_{k\in body} m_k(r_k - R)\times f_k \tag{5}$$

where M is the mass, I is the pitching moment of inertia, V is the linear velocity, Ω the angular velocity and R the center of mass for the floating body.

2.3 Coupling DualSPHysics with Project Chrono

Project Chrono is an open-source numerical framework designed to simulate complex and multibody mechanical systems. The DualSPHysics framework utilizes the FEA module from Project Chrono to handle mechanical joints connecting rigid bodies. When floating objects interact with fluid particles, DualSPHysics calculates their linear and angular accelerations and passes that information to the Chrono module. Chrono calculates the mechanical joint reaction forces and the dynamic responses of the floating bodies over time using smaller time steps. The resulting positions, angular velocities, and linear velocities for the floating bodies are then used by DualSPHysics to update the data of the floating particles.

2.4 Rigid finite element method

The rigid finite element method (RFEM) proposed by Wittbrodt et al. (2006) is employed to discretize the flexible floating body into multiple rigid bodies interconnected with spring-damping elements. These links contain the inertial properties of the floating bodies to account for the structural flexibility. Thus, for the current research the link between the floating rigid bodies is managed by a rotational hinge, where a bending moment is applied according to:

$$M(t) = \zeta\dot{\theta}(t) + k\theta(t) \tag{6}$$

where ζ is the structural rotational damping, θ is the relative rotation angle between the connected floating bodies, k is the structural rotational stiffness and t the current timestep. The term ζ is assigned based on material properties, while k is calculated as:

$$k = \frac{EI}{\Delta x} \tag{7}$$

where E the Young's modulus of the material and $\Delta x = L/N$, with L corresponding to the total length of the floating body in the longitudinal dimension and N the number of the rigid bodies recreating the flexible body.

3 VALIDATION

The described approach proposed for modeling flexible OFPV platforms in DualSPHysics is validated using experimental data obtained from physical wave flume tests, for very flexible floating structures, conducted by Brown et al. (2022). The silicone-type material properties of the tested structure correspond to a Young's modulus $E = 5.65 \text{ x } 10^5$ Pa, a Poisson's ratio $v = 0.49$ and a density $\rho = 369 \text{ kg/m}^3$. Furthermore, the structure has a length of $L = 0.960$ m, a width of 0.146 m and a thickness of $\Delta_z = 0.025$ m. The hydrodynamic response of the structure was measured under regular wave attack with wave height $H = 0.018$ m and wave period $T = 1.04$ s, generated by a piston-type wave paddle at a water depth of 0.75 m. The physical experiment is numerically replicated in a 2D numerical SPH formulation. The structure is discretized to multiple rigid elements interconnected with rotational hinges according to Figure 1a, with a stiffness coefficient calculated based on Eq. 7. A sensitivity analysis was

conducted to select the optimal number of rigid bodies representing the flexible element, where a number of $N = 24$ rigid bodies was selected. To ensure accurate wave generation, a numerical wave flume was initially recreated and tested without the implementation of the floating structure. Wave calibration was achieved with less than 3% error in wave height and wave period at the location of the floating structure ($x = 0$). After a convergence analysis, a very high particle resolution was selected, with a ratio of H/d_p equal to 18. At the end of the numerical wave flume, from $x_0 = L + 0.50$ to $x_1 = L + 0.50 + L_{wav}$ (where L_{wav} is the generated wavelength), a damping zone was implemented to absorb incident waves. The damping system gradually reduces the velocity of particles from point x_0 to point x_1 at every time step, for all particles at z direction. A zero velocity is enforced to all particles reaching point x_1.

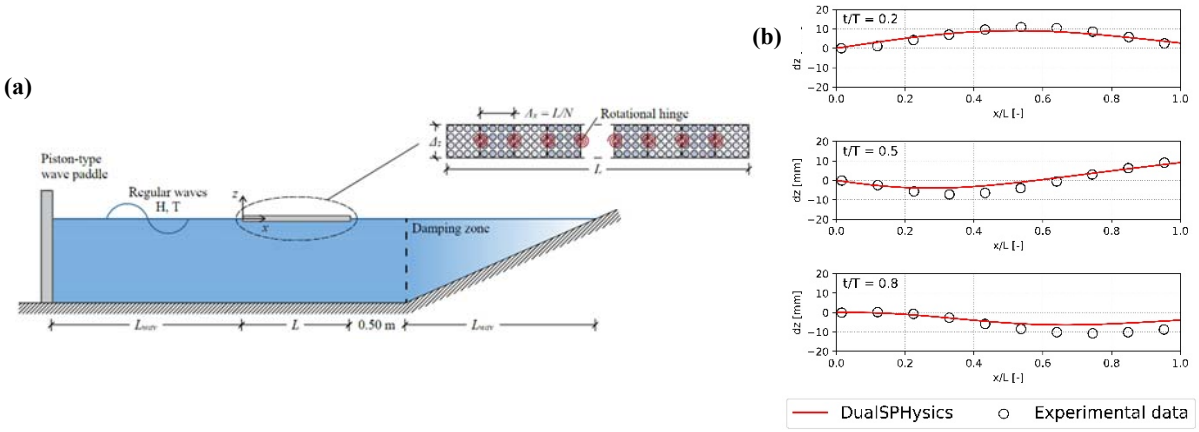

Figure 1. (a) Schematic view of the numerical SPH setup, **(b)** Comparison of numerical prediction (—) with experimental data (○) in terms of vertical displacement of the structure (dz), as a function of x normalized by the structure's length (L) and different wave phases during one wave period (T)

Figure 1b depicts a comparison of the numerical SPH prediction with experimental data in terms of vertical displacement of the structure, dz, for various points x in the longitudinal dimension of the structure normalized by L, as a function of different wave phases during one wave period. Overall, good agreement is observed between the numerical prediction and the physical data. However, the numerical magnitude of the vertical displacement is slightly underestimated at locations where the section is near its minima. This under-estimation is hypothesized to be caused by the neglection of three dimensional (3D) hydrodynamic effects, wave reflection and wave abosrption from the structure, in the numerical method. Since the structure in the physical model test does not span on the entire width of the flume, the related 3D effects are considered to be more significant and therefore cause inacuracies in the numerical output.

4 CONCLUSIONS

Flexible floating structures described by the RFEM have been numerically developed and succesfully applied into the coupling of DualSPHysics with Project Chrono. The model has been validated to properly simulate the motion of very flexible floating box-type structures, making it feasible to analyse deflections due to time-domain non-linear wave dynamics. Furthermore, the described approach is efficient and easy to implement, requiring no modifications to the source codes. It is suitable for reproducing extreme hydroelastic phenomena and can handle large deformations with ease due to the meshfree nature of the SPH method. Thus, the current research proposes a novel and validated framework to numerically simulate and assess very flexible solar platforms. However, the results only indicate the potential of the numerical framework in a 2D formulation. Future work should focus on overcoming computational limitations in a 3D formulation, taking into account wave induced 3D effects, such as directional waves and 3D diffraction effects. In addition, complex geometries with various material properties could be investigated.

ACKNOWLEDGEMENTS

This research was funded by FWO (Fonds Wetenschappelijk Onder-zoek - Research Foundation Flanders), Belgium. The first author, Rafail Ioannou, is a recipient of the PhD Fellowship for Fundamental Research from FWO (application number 1184622N).

REFERENCES

Monaghan JJ (1992) Smoothed particle hydrodynamics. Annual Review of Astronomy and Astrophysics 30(1):543–574. doi:10.1146/annurev.aa.30.090192.002551

Wendland H (1995) Piecewise polynomial, positive definite and compactly supported radial basis functions of minimal degree. Advances in Computational Mathematics 4(1):389–396. doi:10.1007/BF02123482

Liu GR, Liu MB (2003) Smoothed particle hydrodynamics. World Scientific, Singapore.

Trapani K, Millar DL (2014) The thin film flexible floating PV (T3F-PV) array: The concept and development of the prototype. Renewable Energy 71:43–50. doi:10.1016/j.renene.2014.05.007

O'Connor J, Rogers BD (2021) A fluid–structure interaction model for free-surface flows and flexible structures using smoothed particle hydrodynamics on a GPU. Journal of Fluids and Structures 104:103312. doi:10.1016/j.jfluidstructs.2021.103312

Wittbrodt E, Adamiec-Wójcik I, Wojciech S (2006) Dynamics of Flexible Multibody Systems Rigid Finite Element Method. Foundations of engineering mechanics

Crespo AJ, Gómez-Gesteira M, Dalrymple RA (2007) Boundary conditions generated by dynamic particles in SPH methods. Computers, Materials & Continua 5(3):173–184. doi:10.3970/cmc.2007.005.173

Antuono M, Colagrossi A, Marrone S (2012) Numerical diffusive terms in weakly-compressible SPH schemes. Computer Physics Communications 183(12):2570–2580. doi:10.1016/j.cpc.2012.07.006

Loukogeorgaki E, Michailides C, Angelides DC (2014) "Dry" and "wet" mode superposition approaches for the hydroelastic analysis of floating structures. Paper presented at the 9th international conference on structural dynamic, University of Porto, Porto

Fourtakas G, Dominguez JM, Vacondio R, Rogers BD (2019) Local uniform stencil (LUST) boundary condition for arbitrary 3-D boundaries in parallel smoothed particle hydrodynamics (SPH) models. Computers and Fluids 190:346–361. doi:10.1016/j.compfluid.2019.06.009

Al-Yacouby AM, Halim ERBA, Liew MS (2020) Hydrodynamic Analysis of Floating Offshore Solar Farms Subjected to Regular Waves. Advances in Manufacturing Engineering Springer 375-390. doi:10.1007/978-981-15-5753-8_35

English A, Dominguez JM, Vacondio R, Crespo AJC, Stansby PK, Lind SJ, Chiapponi L, Gomez-Gesteira M (2020) Modified dynamic boundary conditions (mDBC) for general purpose smoothed particle hydrodynamics (SPH): application to tank sloshing , dam break and fish pass problems. Computational Particle Mechanics 9(5):911-925. doi:10.1007/s40571-021-00403-3.

Ikhennicheu M, Danglade B, Pascal R, Arramounet V, Trebaol Q, Gorintin F (2021) Analytical method for loads determination on floating solar farms in three typical environments. Solar Energy 219:34–41. doi:10.1016/j.solener.2020.11.078

Domínguez JM, Fourtakas G, Altomare C, Canelas R, Tafuni A, Feal OG, Martínez-Estévez I, Mokos A, Vacondio R, Crespo AJC, Rogers B, Stansby PK, Gómez-Gesteira M (2021) DualSPHysics: from fluid dynamics to multiphysics problems. Computational Particle Mechanics Altomare 9(5):867–895. doi:10.1007/s40571-021-00404-2

Capasso S, Tagliafierro B, Martínez-Estévez I, Domínguez JM, Crespo AJC, Viccione G (2022) A DEM approach for simulating flexible beam elements with the Project Chrono core module in DualSPHysics. Computational Particle Mechanics 9(5):969–985. doi:10.1007/s40571-021-00451-9

Brown SA, Xie N, Hann MR, Greaves DM (2022) Investigation of wave-driven hydroelastic interactions using numerical and physical modelling approaches. Applied Ocean Research 129:103363. doi:10.1016/j.apor.2022.103363

Martínez-Estévez I, Tagliafierro B, El Rahi J, Domínguez JM, Crespo AJC, Troch P, Gómez-Gesteira M (2023) Coupling an SPH-based solver with an FEA structural solver to simulate free surface flows interacting with flexible structures. Computer Methods in Applied Mechanics and Engineering 410:115989. doi:10.1016/j.cma.2023.115

DMPCO 2023

e-Proceedings of the 2nd International Scientific Conference on Design and Management of Port Coastal and Offshore Works Thessaloniki, Greece, May 24-27 2023

Time-domain performance of an array of heaving wave energy converters in front of a vertical wall

A. Papadopoulou[1*], E. Loukogeorgaki[1]

[1]Department of Civil Engineering, Aristotle University of Thessaloniki, Thessaloniki, 54124, Greece
[*]Corresponding author: aristipapad@gmail.com

Abstract

The present paper focuses on the time-domain performance analysis of a linear array of three oblate spheroidal heaving Wave Energy Converters (WECs) in front of a bottom-mounted vertical wall of finite length. The modeling and the analysis of the examined multi-body arrangement are realized using the WEC-Sim open-source code, where the equation of motion is solved by deploying the Cummins time-domain formulation. The required for the analysis frequency-depended quantities are obtained from the solution of the corresponding diffraction/radiation problem in the frequency domain, taking into account all hydrodynamic interactions among the devices and between the wall and the WECs. The action of both regular and irregular waves is considered, while emphasis is given on the effect of the array's distance from the wall on the the power absorption ability and hydrodynamic behavior of the array. The results demonstrate that the placement of the array at a large distance from the wall leads to hydrodynamic interactions that improve the behavior of the array and, thus, its power absorption ability at the period range where resonance phenomena occur. However, the placement of the array close to the wall imposes restrictions on this amplification, leading to enhanced power absorption ability of the array at incident wave periods far from resonance.

Keywords Heaving wave energy converter, Vertical wall, JONSWAP spectrum, Absorbed power.

1 INTRODUCTION

Wave energy corresponds to a vast and abundant renewable energy source in the marine environment characterized by multiple benefits such as higher energy density, compared to other ocean renewable energy forms, limited negative environmental impact and larger consistency due to natural seasonal variability (Guo and Ringwood, 2021). Currently the wave energy sector is rapidly developing, and various types of Wave Energy Converters (WECs) have been designed and developed, aiming at the realization of efficient and commercially competitive solutions (e.g., Guo and Ringwood, 2021). Among those types, heaving WECs with the "one-mode" operation simplicity correspond, nowadays, to one of the most technologically advanced WECs type (Guo et al., 2022).

Large-scale commercial exploitation of wave energy requires the deployment of multiple WECs in the form of arrays, which can be installed and operate either in offshore areas or at near-shore locations. In the latter case, arrays of heaving WECs may be combined with existing wall-type (vertical) breakwaters, facilitating the exploitation of both the incident and the scattered from the wall waves (Loukogeorgaki et al., 2021), while contributing to reduction of costs and advancement of the WECs' maturity. To support the successful design of WECs arrays, frequency or time domain analysis can be implemented by deploying relevant numerical tools. Considering the presence of a leeward vertical wall, arrays of oblate spheroidal or cylindrical heaving WECs have been extensively modeled so far in the frequency domain aiming at: (a) assessing the effect of various design parameters (e.g., array-wall distance, layout of the array) on the performance of the array (e.g. Loukogeorgaki et al., 2020; Konispoliatis and Mavrakos, 2020) or (b) optimizing the array's layout (e.g. Loukogeorgaki et al., 2021). Although frequency-domain numerical tools are characterized by low computational time, they do not enable the adequate inclusion of non-linear effects resulting from different sources (e.g., existence of complex Power-Take-Off (PTO) systems and highly non-linear relevant control strategies). For overcoming this barrier, time-domain numerical tools should be deployed. Along these lines, Kara (2021) and Kara (2022) have assessed in time domain the hydrodynamic behavior and the power absorption ability of heaving WECs arrays in front of a vertical wall by developing and applying an in-house transient wave-

multi body numerical tool. Devices of cylindrical shape have been taken into account, while the method of images was deployed to account for the wall, assuming, unavoidably, a "pure" wave reflecting leeward boundary of infinite extent.

In this paper, we investigate and assess in time domain the performance of a linear array of oblate spheroidal heaving WECs in front of a bottom-mounted vertical wall of finite length under the action of both regular and irregular waves. The modeling and the analysis of the examined multi-body arrangement is realized using the WEC-Sim open-source code (Yu et al., 2014). The equation of motion is formed and solved by deploying the Cummins time-domain formulation (Cummins, 1962), while the required for the analysis frequency-depended quantities are obtained from the solution of the corresponding diffraction/radiation problem in the frequency domain, including all hydrodynamic interactions among the WECs and between the wall and the WECs. Emphasis is given on the effect of the array's distance from the wall on its performance under different wave conditions.

2 NUMERICAL MODELLING

A linear array of M hydrodynamically interacting, semi-immersed heaving WECs is placed in front of a vertical, bottom-mounted wall of finite length l_w and of thickness t at an area of finite and constant water depth d (Figure 1). The array consists of identical WECs, which have an oblate spheroidal geometry of equatorial radius a and polar radius b (Figure 1b). Each WECi, $i = 1, \dots, M$, absorbs power through a linear PTO mechanism, which is schematically represented in Figure 1b as a linear damping system, with damping coefficient b_{PTOi}, $i = 1, \dots, M$. All the WECs of the array are situated at a perpendicular distance c from the wall and they are distributed uniformly within the array having a center-to-center spacing equal to l_{bet} (Figure 1a).

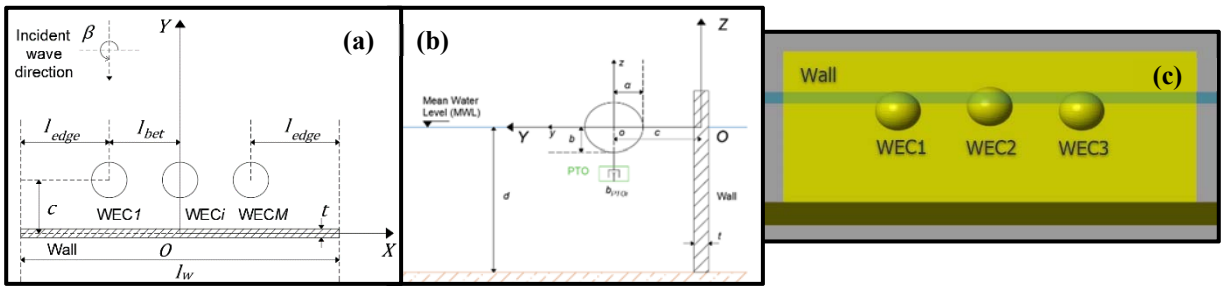

Figure 1. Geometry of the examined problem: **(a)** $X-Y$ plane, **(b)** $Y-Z$ plane, **(c)** Front view of an array with $M = 3$ WECs as modelled in WEC-Sim

The whole arrangement is, initially, modeled in the frequency domain in order to calculate the required for the time-domain analysis physical quantities (i.e., frequency-dependent wave exciting forces and hydrodynamic coefficients, as well as hydrostatic coefficients). The relevant analysis, including hydrodynamic interactions among the WECs and between the wall and the devices, relies on the boundary integral equation method and is numerically realized using the WAMIT© software (Lee, 1995). The 3D linear potential theory is utilized, where the wall is taken fixed at its position and all the devices are assumed to oscillate freely only along their working direction, i.e., along their local vertical oz axis. The action of unit amplitude regular incident waves with circular frequency ω that propagate at an angle β relatively to the global horizontal OX axis (Figure 1a) is taken into account. The solution of the 1st order boundary value problem is based on the 3D panel method by utilizing Green's theorem and by imposing the appropriate boundary conditions on the free surface, the sea bottom and the bodies (Lee, 1995). The exciting forces, $F_{exc}^{i}, i = 1, \dots, M$, the added mass, $A_{ij}, i, j = 1, \dots, M$, and the radiation damping, $B_{ij}, i, j = 1, \dots, M$, coefficients are then calculated as follows:

$$F_{exc}^{i} = -i\omega\rho \iint_{S_b^i} n_3^i \varphi_D ds\,,\ i = 1, \dots, M \tag{1}$$

$$A_{ij} - \frac{i}{\omega} B_{ij} = \rho \iint_{S_b^i} n_3^i \varphi_j ds\,,\ i, j = 1, \dots, M \tag{2}$$

where φ_D is the diffracted potential, $\varphi_j, j = 1, \dots, M$ is the unit-amplitude radiation potential of the j^{th} WEC, n_3^i and S_b^i denote respectively the normal unit vector in the vertical direction and the wetted surface of WECi, while ρ is the water density.

Having calculated the required for the time-domain analysis physical quantities, the modeling and the analysis of the examined multi-body arrangement in time domain follows using the WEC-Sim open-source code (Yu et al., 2014). In WEC-Sim, the equation of motion is formed based on the Newton's second law by deploying the Cummins time-domain formulation (Cummins, 1962). The latter formulation, which corresponds to a vector integro-differential equation, takes into account the interaction of the wave exciting forces with the radiation forces induced by the motions of the floating bodies themselves, also known as fluid memory effects. Based on the above and assuming M WECs oscillating only in heave (i.e., M degrees of freedom), the equation of motion the case of the array shown in Figure 1 can be written as follows:

$$\boldsymbol{m}\ddot{\boldsymbol{X}} = \boldsymbol{F_{exc}}(t) + \boldsymbol{F_{rad}}(t) + \boldsymbol{F_{PTO}}(t) + \boldsymbol{F_{rest}}(t) + \boldsymbol{F_{moor}}(t) \quad (3)$$

where t is time, $\ddot{\boldsymbol{X}}(t)$ is the M X 1 vector of the WECs' accelerations, $\boldsymbol{m}$ is the M X M structural mass matrix of the array, $\boldsymbol{F_{exc}}(t)$ is the M X 1 vector of the wave exciting forces, $\boldsymbol{F_{rad}}(t)$ is the M X 1 vector of the wave radiation forces, $\boldsymbol{F_{PTO}}(t)$ is the M X 1 vector of the forces originating from the PTO mechanism, $\boldsymbol{F_{rest}}(t)$ is the M X 1 vector of the net buoyancy restoring force and $\boldsymbol{F_{moor}}(t)$ is the M X 1 vector of the mooring lines' forces. Under the action of irregular waves, $\boldsymbol{F_{rad}}(t)$ is calculated using Eq. 4, where $\boldsymbol{A}_\infty$ is the M X M added mass matrix at infinite frequency, $\boldsymbol{K_{rad}}$ is the M X M matrix of the impulse response functions (retardation functions), $\dot{\boldsymbol{X}}$ is the M X 1 vector of the WECs' velocities and τ is a dummy variable. On the other hand, the simplified expression (Eq. 5) corresponding to a sinusoidal steady-state approach is deployed for regular waves, with $\boldsymbol{A}$ and $\boldsymbol{B}$ denoting the M X M added mass and radiation damping matrices respectively.

$$\boldsymbol{F_{rad}}(t) = -\boldsymbol{A}_\infty \ddot{\boldsymbol{X}}(t) - \int_0^t \boldsymbol{K_{rad}}(t-\tau)\dot{\boldsymbol{X}}(\tau)d\tau \quad (4)$$

$$\boldsymbol{F_{rad}}(t) = -\boldsymbol{A}(\omega)\ddot{\boldsymbol{X}}(t) - \boldsymbol{B}(\omega)\ddot{\boldsymbol{X}}(t) \quad (5)$$

The mean power absorbed by the whole array, $P_{array}(t)$, at a specific t is, finally, calculated as follows:

$$P_{array}(t) = \sum_{i=1}^{M} P_i(t) = \sum_{i=1}^{M} b_{PTOi}\dot{X}_i^{\,2}(t) \quad (6)$$

where $P_i(t), i = 1, \dots, M$, is the power absorbed by the i^{th} WEC and $\dot{X}_i(t)$ is the velocity of the specific device.

3 CHARACTERISTICS OF THE PHYSICAL PROBLEM EXAMINED

The numerical model described in Section 2 is applied for an array of $M = 3$ identical, semi-immersed oblate spheroidal WECs (Figure 1c), with a =2.0 m, b =1.7 m, submerged mass and volume equal to 14,597.9 kgr and 14.24 m^3 respectively, and heave hydrostatic coefficient of 125.6 kN/m (Tzellos et al., 2020). All three WECs are considered to have the same PTO characteristics, with a constant PTO damping coefficient selected, so that power absorption is maximized at the heave natural frequency, ω_{n3}, of a single, isolated device (Falnes and Kurniawan, 2020). Therefore, b_{PTOi}, $i = 1, \dots, M$, is set equal to the heave radiation damping of a single isolated WEC at its heave natural frequency, i.e., $b_{PTOi} = B_{33}^{ISO}(\omega = \omega_{n3}^{ISO})$. For the examined geometry, $\omega_{n3} = 2.4$ rad/s, resulting to $b_{PTOi} = 10{,}312.81$ Ns/m. The array is selected to be installed in a liquid region of $d = 10$ m in front of a vertical wall of l_w =36.0 m and t =1.0 m. Two different values of the WECs' distance from the wall, c, are investigated corresponding to c = 1.5a (Case 1 hereafter) and c = 3.0a (Case 2 hereafter). For both cases, the WECs are distributed uniformly within the array with center-to-center spacing l_{bet} equal to 4.0a.

Regarding the environmental conditions, the action of perpendicular to the arrangement waves is taken into account (i.e., $\beta = 270°$, Figure 1a). Regular waves with height, H, equal to 1.0 m and period, T,

equal to 2.8 s, 3.0 s, 4.0 s, 5.0 s and 6.0 s are being examined, while for irregular waves, the JONSWAP spectrum is deployed with significant wave height, H_s, varying between 0.5 m and 5.0 m with a 0.5 m step and peak period, T_p, between 2 s and 6 s with a 1 s step.

4 RESULTS AND DISCUSSION

Figure 2a shows the effect of c on the maximum value of the power absorbed by each WEC, P_i^{max}, under the action of regular waves with $H = 1.0$ m and different T values. Due to the symmetry of the array with respect to the incident wave direction, the same power is being absorbed by WEC1 and WEC3 (outer devices). The placement of the array close to the wall (Case 1) leads to less power absorption at T =2.8 s and 3.0 s, i.e., at periods close to the devices' heave natural period (equal to 2.6 s), while the action of regular waves with larger period increases the power absorption ability of the devices. By increasing c to $3.0a$ (Case 2), the opposite holds true, with the power absorption ability of the array being enhanced at the period range where resonance phenomena occur. Additionally, it is observed that for T values larger than 4.0 s the difference of P_j^{max} between Cases 1 and 2 decreases with the increase of T. As for the effect of c on the maximum value of the power absorbed by the whole array, P_{array}^{max}, (Figure 2b), it is clear that Case 1 array performs better at the three largest examined periods, while the opposite holds true for the periods closer to devices' heave natural period.

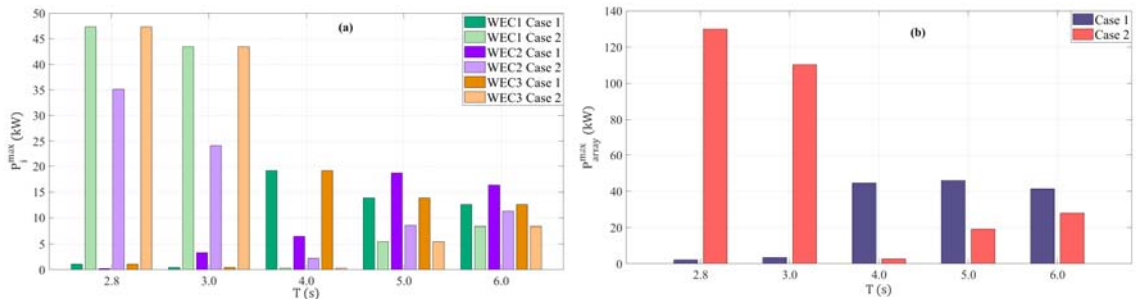

Figure 2. Effect of c and T on: **(a)** P_i^{max}, **(b)** P_{array}^{max}

For the case of irregular waves, the effect of the array's distance from the wall on the maximum value of the absorbed power is illustrated in Figure 3, where the contours of P_{array}^{max} for the two examined c values as a function of H_s and T_p are plotted.

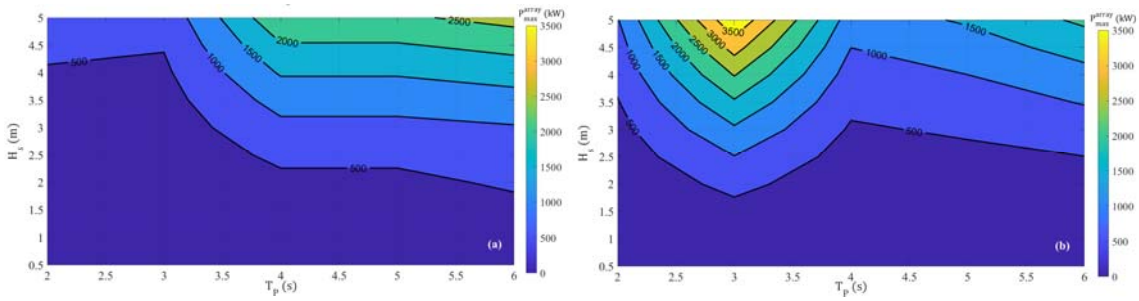

Figure 3. Contours of P_{array}^{max} under irregular waves: **(a)** Case 1, **(b)** Case 2

By placing the array close to the wall (Figure 3a), significant power absorption occurs at $T_p > 4.0$ s. On the other hand, the placement of the array at $c = 3a$ (Figure 3b) leads to a shift of the P_{array}^{max} peak values at a smaller T_p equal to 3.0 s and to a reduced power absorption ability at $T_p > 4.0$ s. This is in absolute accordance with the WECs responses, as shown in Figure 4, where parts of the time-series of the WECs' heave velocities are cited indicatively for sea states with H_s= 4.0 m and $T_p = 3.0$ s and 5.0 s. Furthermore, in Case 2 quite larger P_{array}^{max} values are observed compared to Case 1; thus, the power absorption ability of the array is significantly enhanced in the former case. Finally, for both examined c values, significant power absorption occurs at $H_s > 4.0$ m.

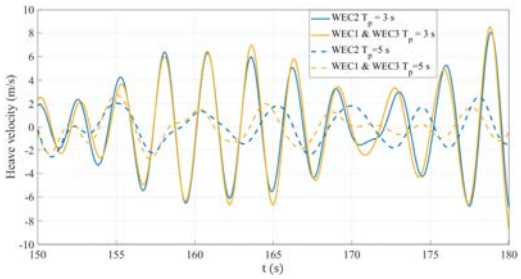

Figure 4. WECs response for Case 2 array and sea states with H_s= 4.0 m and T_p = 3.0 s and 5.0 s

5 CONCLUSIONS

In the present paper, the performance of a linear array of three semi-immersed oblate spheroidal heaving WECs in front of a bottom-mounted, vertical wall of finite length and thickness under the action of perpendicular to the wall regular and irregular waves is investigated in the time domain. The results demonstrate that when the WECs are situated close to the wall, the power absorption ability of the array is not driven by resonance phenomena, since the power absorbed by the WECs individually and, subsequently, by the whole array shows larger values at wave periods outside the range, where resonance phenomena occur. The opposite holds true when the array is placed further from the wall, advocating that the presence of the leeward boundary does not impose any restrictions on the amplification of the absorbed power due to resonance.

References

Cummins WE (1962) The impulse response function and ship motions. Report 1661, Department of the Navy David Taylor Model Basin.

Falnes J, Kurniawan A (2020) Ocean waves and oscillating systems: Linear interactions including wave-energy extraction. Cambridge University Press.

Guo B, Ringwood JV (2021) A review of wave energy technology from a research and commercial perspective. IET Renewable Power Generation 15:3065–3090. https://doi.org/10.1049/rpg2.12302.

Guo B, Wang T, Jin S, Duan S, Yang K, Zhao Y (2022) A review of point absorber wave energy converters. J Mar Sci Eng 10(10):1534. doi:10.3390/jmse10101534.

Kara F (2021) Hydrodynamic performances of wave energy converter arrays in front of a vertical wall. Ocean Engin 235:109459. doi:10.1016/j.oceaneng.2021.109459.

Kara F (2022) Effects of a vertical wall on wave power absorption with wave energy converters arrays, Renew Energ 196:812–823. doi:10.1016/j.renene.2022.07.046.

Konispoliatis DN, Mavrakos SA (2020) Wave power absorption by arrays of wave energy converters in front of a vertical breakwater: A theoretical study. Energies 13(8):1985. doi:10.3390/en13081985.

Lee CH (1995) WAMIT theory manual. MIT Report 95-2, Department of Ocean Engineering, MIT.

Loukogeorgaki E, Boufidi I, Chatjigeorgiou I. (2020) Performance of an array of oblate spheroidal heaving wave energy converters in front of a wall. Water 12(1):188. doi:10.3390/w12010188.

Loukogeorgaki E, Michailides C, Lavidas G, Chatjigeorgiou IK (2021) Layout optimization of heaving wave energy converters linear arrays in front of a vertical wall. Renew Energ 179:189–203. doi:10.1016/j.renene.2021.07.040.

Tzellos N, Loukogeorgaki E, Anastasiou E, Chatjigeorgiou IK (2020). Performance of an oblate spheroidal heaving wave energy converter. Paper presented at the 30th International Ocean and Polar Engineering Conference, Shanghai, China (virtual), 1:116–123.

Yu YH, Lawson M, Ruehl K, Michelen C (2014) Development and demonstration of the WEC-Sim wave energy converter simulation tool. Paper presented at the 2nd Marine Energy Technology Symposium (METS), Seattle, WA.

DMPCO 2023

e-Proceedings of the 2nd International Scientific Conference on Design and Management of Port Coastal and Offshore Works Thessaloniki, Greece, May 24-27 2023

Assessing the integration of an oscillating water column at the planned Genoa breakwater

George Lavidas[1*], Francesco De Leo[2], Giovanni Besio[2]

[1]Department of Civil Engineering and Geosciences, Delft University of Technology
[2]Department of Civil, Chemical and Environmental Engineering, University of Genoa, Italy
[*]Corresponding author: g.lavidas@tudelft.nl

Abstract

The option to have an WEC integrated breakwater at the port of Genoa ensures that the port will protect the area from harsh incoming waves, but also contribute towards the port decarbonization. However, for the solution to be viable, a first layer analysis must estimate its profitability. This works uses a long-term high fidelity wave numerical model from 1979-2018, estimating the potential energy production for an integrated OWC at the Port of Genoa.

Keywords Wave Energy, Oscillating Water Column, Capacity factor

1 INTRODUCTION

Coastal regions in the Mediterranean are in immediate risk of Climate Change, sea level rise driving increases in extreme events, potential flooding and erosion (Makris *et al.*, 2016). This can create severe problems for coastal populated areas, cities, and the security of operations for crucial sectors such as harbors. Indeed, the Mediterranean shores are densely populated and about 20% of the world's seaborn commerce passes through the Mediterranean Sea.

The increasing pressure at Mediterranean coastlines requires adaptation measures and rethink coastal infrastructure design, embedding policies that pursue sectoral decarbonization and carbon neutral operations. These have been particularly developed over the past years, with leading port infrastructure California, Shenzhen and the Port of Rotterdam (Samadi *et al.*, 2016). Most of the proposed solutions include photovoltaic and onshore wind as sources of renewable electricity. However, wave energy production remains one of the most overlooked and under-utilized resources, with high synergies at coastal locations for power production, and coastal protection.

The Italian energy mix is heavily dominated by oil and natural gas with net energy consumption≈315 TWh per year (IEA, no date). Italy has translated the aims for Blue Growth and further development of ocean energies into tangible targets, reducing greenhouse gas emissions by 40% (compared with 1990) and 30% of gross energy consumption from renewables by 2030 (European Commission, 2020). Focusing on a future perspective, the Italian National Energy and Climate Plan (NECP) has set ambitious goals for the development and regional Mediterranean cooperation for wave energy development. Wave energy is part of the Blue Growth agenda, and part of the technologies are represented in the SET-Plan.

An “hybrid maritime structures” is an innovative integration technique to combined WEC into existing or planned coastal structures with the purpose of the structure as a whole to maintain protection from metocean harsh events. It is, however, a logical evolution for someone to think that the integration of WECs into coastal structures will also benefit other sectorial developments. WECs are distinguished by their deployment applicability and are separated into shoreline, nearshore and deep-water devices (Rusu and Onea, 2018). However, knowledge of metocean conditions is vital to ensure the optimisation of any type of power take off for WEC.

2 MATERIAL AND METHODS

For the detailed characterization of the local wave climate, we took advantage of the hindcast data provided by the Department of Civil, Chemical and Environmental Engineering of the University of

Genoa (Mentaschi *et al.*, 2015). The data are defined on a hourly base over the period 1979–2018 in the node000230 at a depth of about 650 m (http://www3.dicca.unige.it/meteocean/hindcast.html), and were therefore subsequently downscaled in front of the dike with Simulating WAves Nearshore model (SWAN). The use of SWAN allows for higher fidelity simulation near shallow water, where oceanic models often use approximation for shallow water dynamics, thus allowing for properly accounting for the large depth variations the regional bathymetry is characterized by (see Figure 1).

Figure 25. Spatial representation of the domain used, indicating the point used for boundary information to propagate the high resolution SWAN model

Using a nearshore model driven by validated boundaries takes advantage of faster computation time and higher shallow water accuracy with similar model chains. Our boundary conditions are extracted by a validated and calibrated model, and considering the small fetch, validity of the underlying data benefits by the shallow water source terms of SWAN. The figure shows a close-up of the investigated area, highlighting the input and output wave data nodes, with the latter further used for the estimation of annual energy production.

3 RESULTS

The focus here is the integration and hybridization opportunities offered by an OWC converter to a harbour expansion. While OWC design has been installed and is operative (i.e., Mitruku) (Ibarra-Berastegi *et al.*, 2018), their power matrix is not available and, as mentioned in (Naty, Viviano and Foti, 2016), this can hinder development of studies. For the potential OWC, we have adopted the power matrix of an OWC and obtained the capacity factor (CF) based on a 40 years hindcast analysis, as indicated by other studies (Rusu and Onea, 2016; Lavidas and Venugopal, 2017).

The port of Genoa, comprised of the Genoa and Savona hubs, it is one of the busiest ports in Italy and Central Europe. The port encompasses several specialised terminals that can handle different types of cargo, from technological equipment to fresh produce. Operative versatility also means that energy requirements must be constantly met, especially in the case of sensitive produce.

The large traffic has increased requirements in cold ironing (i.e., berthing) for parked ships. It currently handles≈2.6 million TEUS, and this amount is expected to increase in the next future. As such, in 2018, the Port Authority launched a project for enlarging the port capacity, implying the building of a new

dike farther seaward with respect to the actual existing one. In addition, the Port Authority has set an ambitious plan for energy efficiency and production by renewable sources (Lavidas, De Leo and Besio, 2020)

The historical wave climate can be assumed to be representative of the future climatology of the area. Indeed, as far as wave parameters are concerned, the investigated location is not characterized by relevant historical trends, nor it is expected to be significantly affected by future variations. Annual energy performance of the OWC is given in Figure 2, along with the estimated Coefficient of Variation (CoV). At the port of Genoa, the mean value of CF is 8.85%, the CoV indicates a small level of variation expected annually, therefore showing little drops in performance.

As it can be seen in Figure 4, there seems to be a cyclic maxima performance every three years, followed by a decrease every two years. The energy analysis indicates that, through the region, performance and capacity factors are similar, with maximum value ≈11.5%. Surrounding the Ports of Genoa, the CF is ≈6–11%, with mean value of ≈8%. Focusing at the Port of Genoa, the specific location data representing 44◦24′N 8◦53′E were extracted. The analysis uses 40 years of data allowing for robust energy estimates, considering the effects of Climate variation on the OWC performance.

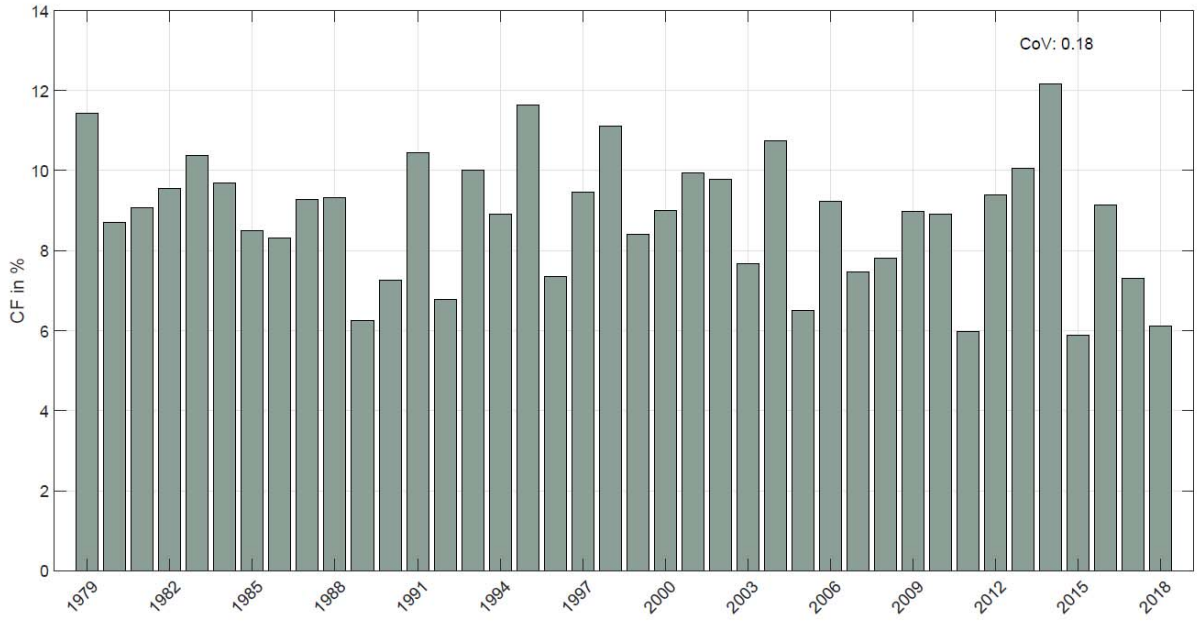

Figure 26. Annual estimated Capacity Factor for the location of the OWC in Genoa

A metric that can be used to compare different energy technologies is the Levelized Cost of Electricity (LCoE), regardless of their resource origin, the comparisons are expressed in currency per electricity produced. There are two main components for LCoE estimations, cost/expenditure, and energy production. LCoE does not indicate the economic viability, but it evaluates the probable aggregated energy cost. Avoided emission per fuel type and avoided energy imports are also estimated and used with the produced electricity to assess additional benefits by quantifying avoided emissions. The energy estimates and avoided emissions per fuel type, dominant in the Italian energy mix are given in Table 1.

Table 5. Performance in annual energy production and avoided emission from the potential installation(s) of the OWC proposed

	0.5 MW	1 MW	1.5 MW	2 MW	2.5 MW	3 MW
AEP (MWh/year)	387.55	775.11	1162.6	1550.21	1937.77	2325.32
Oil avoided Tn CO_2/year	293.92	587.85	881.77	1175.70	1469.62	1763.54
Natural Gas avoided Tn CO_2/year	199.52	399.05	598.57	798.10	997.62	1197.14

Given the fact that one specific device is proposed here, LCoE will be mostly a function of CapEx. As the installed capacity increases, the LCoE sees a reduction. The lowest LCoE 185.80 €/MWh is for 3 MW installed capacity, with a total CapEx 1,500,000 €. The highest LCoE is 627.05 €/MWh when the cost per MW is 3,000,000 €, and for a 0.5 MW configuration total costs scale to 10,800,000, see Figure 5.

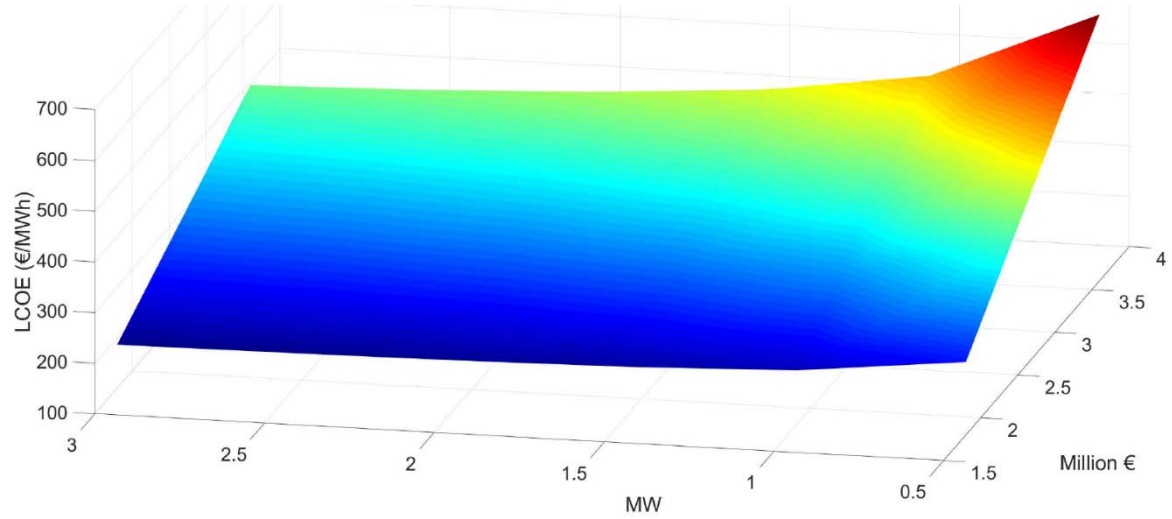

Figure 27. LCOE distribution of the OWC with regards to CAPEX (Million €) and installed capacity (MW)

4 CONCLUSIONS

Within this study determined the potential energy benefits and economic feasibility of an integrated OWC at the Port of Genoa. Through the coupling of multi-model nesting, energy analysis and utilizing a non-optimized WEC solution, ratios are proposed for which an investment would be feasible. Past studies indicated the possibility of tuning the converter behavior to local condition, hence scaling its performance is expected to increase the energy production by at least 50%. An integrated breakwater OWC operates at shallow water areas where surge and depth breaking will be more dominated, and thus simple Froude scaling is not possible.

Incorporating an OWC also offers significant benefits in offsetting carbon emissions by conventional sources, and hence increasing the sustainability of operation for the Port of Genoa. These values can be from ≈300–1763.54 Tn CO_2/year for oil-based electricity and ≈200–1200 Tn CO_2/year for Natural Gas (NG), effectively reducing the carbon budget and making the Port of Genoa highly competitive and sustainable regarding its emissions.

Another under-estimated characteristic is the beneficial mismatch of operation with other renewable energies. This in fact can enhance the utilisation of energy by renewables, whilst minimizing expensive solutions as batteries, which for industrial solution can be as high ≈1000 €/MWh (as stand-alone

solutions), and from ≈280–360 €/MWh (as part of storing electricity by photovoltaics). Besides the aggregated annual energy performance, the hourly power production was analysed, and a filter was applied to focus only on hours that photovoltaics does not produce (from 6:00 p.m.–8:00 a.m.). The minimum hours operated in this timeframe of non-sunshine, the lower value was in 2005 with 5.85% in total hours, the maximum was 10.72% in 2000, with mean power production in such hours representing 8.25%.

Acknowledgements

The work has received funding from EU-SCORES project under the European Union's Horizon 2020 research and innovation programme under grant agreement No 101036457.

References

European Commission (2020) National energy and climate plans (NECPs). Available at: https://ec.europa.eu/energy/topics/energy-strategy/national-energy-climate-plans_en#final-necps (Accessed: 3 September 2020).

Ibarra-Berastegi, G. et al. (2018) 'Electricity production, capacity factor, and plant efficiency index at the Mutriku wave farm (2014–2016)', Ocean Engineering, 147(September 2017), pp. 20–29. doi: 10.1016/j.oceaneng.2017.10.018.

IEA (no date) International Energy Agency. Available at: http://www.iea.org/.

Lavidas, G., De Leo, F. and Besio, G. (2020) 'Blue Growth Development in the Mediterranean Sea: Quantifying the Benefits of an Integrated Wave Energy Converter at Genoa Harbour', Energies, 13(16), p. 4201. doi: 10.3390/en13164201.

Lavidas, G. and Venugopal, V. (2017) 'A 35 year high-resolution wave atlas for nearshore energy production and economics at the Aegean Sea', Renewable Energy, 103, pp. 401–417. doi: 10.1016/j.renene.2016.11.055.

Makris, C. et al. (2016) 'Climate change effects on the marine characteristics of the Aegean and Ionian Seas', Ocean Dynamics, 66(12), pp. 1603–1635. doi: 10.1007/s10236-016-1008-1.

Mentaschi, L. et al. (2015) 'Performance evaluation of Wavewatch III in the Mediterranean Sea', Ocean Modelling, 90, pp. 82–94. doi: 10.1016/J.OCEMOD.2015.04.003.

Naty, S., Viviano, A. and Foti, E. (2016) 'Wave Energy Exploitation System Integrated in the Coastal Structure of a Mediterranean Port', Sustainability, 8(12), p. 1342. doi: 10.3390/su8121342.

Rusu, E. and Onea, F. (2018) 'A review of the technologies for wave energy extraction', Clean Energy, (March), pp. 1–10. doi: 10.1093/ce/zky003.

Rusu, L. and Onea, F. (2016) 'The performance of some state-of-the-art wave energy converters in locations with the worldwide highest wave power', Renewable and Sustainable Energy Reviews, (August 2015), pp. 0–1. doi: 10.1016/j.rser.2016.11.123.

Samadi, S. et al. (2016) Decarbonization Pathways for the Industrial Cluster of the Port of Rotterdam. doi: 10.13140/RG.2.2.35007.92325.

DMPCO 2023

e-Proceedings of the 2nd International Scientific Conference on Design and Management of Port Coastal and Offshore Works Thessaloniki, Greece, May 24-27 2023

Exploitation of marine wave energy: Application in selected Greek coastal areas

S. Ipodimatopoulou, M. Syrpi, Y Savvidis*

Department of Environmental Engineering, International Hellenic University, P.O. Box 141, 574 00 Sindos, Thessaloniki, Greece
*Corresponding author: savvidis@ihu.gr

Abstract

Sea wave energy is a purely renewable type of energy. The exploitation of this energy is therefore very significant. Coastal structures that aim to capture and utilize this kind of energy are of special value. The present study is focused on the harnessing of wave energy by structures which are parts of a port or a project that may simultaneously serve other purposes, like coastal protection. For the implementation of the study, three locations of Greek coasts were selected, which are exposed to waves that propagate on a long seaway distance. In particular, two coasts of southern Greece as well one of western Greece were selected. After the calculation of the wave characteristics by wave forecasting methods in combination with the wind climate of each region, a mathematical model is applied to simulate a suitable structural arrangement for capturing the wave energy and then calculating the ultimately produced energy. Particularly, the model simulates the propagation of a long linear wave along a one-dimensional channel from a left boundary to the right boundary where a caisson wall (a breakwater or a seawall) is located, absorbing the waves. The research leads to useful results for the exploitation of the seawaves' energy in Greece.

Keywords Wave energy, Coastal structures, Mathematical model.

1 INTRODUCTION

The exploitation and utilization of the sea waves' energy is of great value, since it refers to a purely renewable type of energy. The coastal structures aiming to capture and utilize this type of energy are extremely important, since these structures can satisfy two different goals, in parallel; firstly, the basic goal of protecting a harbours' basin from the sea waves or a coastal zone that suffers from erosion and secondly the goal of harnessing the wave energy and providing thereinafter the capability of electrical energy production. Many researchers studied this specific topic during last decades both experimentally and numerically (Stagonas 2010; Gravas et al, 2012; Sismani and Karampas 2015; Kralli et al. 2019). Stagonas et al. (2010) realized exploratory 2D model tests in the laboratory of a modified seawall and reached to a hydraulic power of 1.5 kW per m of the wall. Gravas et al. (2012) examined the exploitation of the sea waves' energy that attack coastal structures, in parallel to the conventional operation of these structures. The basic design of this structure was initially proposed by Koutitas and Savvidis (2008). The study was based on the development of mathematical models and investigated issues that concerned the height of the incident wave and various geometrical characteristics of the coastal structure so that the optimal amount of produced wave power can be harnessed. Sismani and Karambas (2015) studied the potential of wave energy conversion applying the Overtopping Breakwater for Energy Conversion (OBREC) system in an existing breakwater, at the north coastline of Crete, and specifically at Rethymno. They examined the possibility of improving the existing conventional operation in order to produce electrical power, in parallel with the wave protection. Kralli et al. (2019) focused their research on the optimal design of Overtopping Breakwater for Energy Conversion systems, known as OBREC, using a novel and very effective, meta-heuristic optimization technique, the Harmony Search Algorithm. The methodology was based on the combined application of wave propagation equations with an optimization algorithm, aiming at the identification of the optimal dimensions of an OBREC reservoir. For the effectiveness of the methodology, the port of Heraklion in the island of Crete in Greece was used as a case study, leading to very interesting results. In this paper, the coastal structure and numerical

model described by Gravas et al. (2012) is presented here with emphasis on the application at three selected places of Greek Coasts.

2 MATERIAL AND METHODS

2.1 Description of the study areas – Case studies

Three coastal areas that present a long effective wave fetch were initially selected. Aktio (coasts of west Greece), Heraklio (north coasts of Crete) and Ierapetra (south coasts of Crete) given in figure 1.

Figure 1. The wider field of Greek seas and the three selected coastal areas (A for Aktio, H for Heraklio and I for Ierapetra) (the figure drawn by the site below is slightly modified)

2.2 Description of the structure – device

A special coastal structure is proposed here for the parallel operation of power production together with the shore protection either as a part of a harbor or as an autonomous coastal defense structure. The process of wave propagation and incidence on a vertical of a seawall of this coastal structure as well as the process of harnessing the wave power for energy production is examined by the application of a numerical model. The initial version of the model was developed by Professor Koutitas, in the late 2000s (Koutitas and Savvidis 2008); later it was slightly modified by Gravas et al. (2012) who applied the model not only in one but also in two dimensions. In this research work, the simplest version of the one-dimensional model was used; this model describes the propagation of a linear long wave along a channel with depth d, ending at a specific type of coastal engineering structure (breakwater or seawall) for absorbing the waves and leading ultimately to electricity production. More specifically, there is an opening in the front of the structure's wall and a reservoir inside the structure which is filled with water while the height of the surface of the water column changes according to the incident waves and water that enters the tank; this reservoir is evacuated with the water abducting to the side of the port or the coastal zone behind the breakwater wall through a small opening and a pipeline (Figure 2).

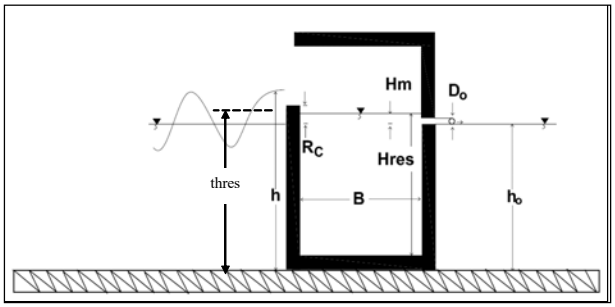

Figure 2. The system of a "wave harnessing" breakwater /seawall (Gravas et al. 2012)

Figure 2 contains the following symbols: D_o which is the diameter of the caisson evacuation orifice charging the low head turbine, h_o which is the water depth in the area (Mean Sea Level to Bottom), h which is the instantaneous water depth in front of the entrance of the reservoir (caisson) B: the width of the reservoir -tank R_c: the overtopped crest elevation, measured from the Mean Sea Level (MSL), H_{res} i.e. the depth of the water inside the reservoir (caisson), thres = $[h_o + R_c]$ i.e. the elevation of the

crest from the channel bed, Δ_{h2} or H_m i.e. the available pressure head e.g. [H_{res}-h_o], Δ_{h1} i.e. the overtopping water head from the crest of the structure, e.g. [h–R_c–h_o] = h –Thres.

2.3 Wave Forecasting

The wave heights H as well as the wave periods T, introduced in the model, are computed by prognostic methods. Initially the effective fetch is calculated. The wind data concerning the direction and intensity are taken from a long time period provided by the Hellenic National Meteorological Service (HNMS). Based on this available data the statistical average wind intensity is computed. Wave forecasting methods are then applied (JONSWAP and Pierson-Moskowitz), through which the significant wave height H_s and the period of maximum energy density T_p are calculated.

2.4 Description of the 1DV model

A 1DV mathematical model (x-z plane) is applied for the description of the propagation of a linear long wave along a channel with depth d = 4 m ending to a special type of a coastal structure (caisson type breakwater operating as a water collecting reservoir) for the harnessing of wave energy and the production of electric power. The model numerically resolves the equations (1) and (2) of mass and momentum conservation respectively (Gravas et al. 2012; Koutitas and Scarlatos, 2016):

$$\frac{\partial Q}{\partial t} + g \cdot h \cdot \frac{\partial \zeta}{\partial x} = 0 \qquad (1)$$

$$\frac{\partial \zeta}{\partial t} + \frac{\partial Q}{\partial x} = 0 \qquad (2)$$

where ζ(x,t) is the sea surface elevation from the MSL, h the water depth, Q(x,t) the specific water discharge, t is the time, and x is the distance from the wave generator on the left end of the channel.
At the entrance of the channel an incident sinusoidal wave signal is introduced while proper boundary conditions are applied i.e. superposition of the incoming wave signal and the reflected (Gravas et al., 2012). The model computes the elevation ζ as well as the total water depths h along the channel at each time step, from the left side up to right side of the flume which corresponds to the front of the structure with the hollow part of the caisson, leading to the overtopping water height.
The overtopping flow entering the reservoir is computed by the equation (3) (Chadwick, 1998),

$$Q_{in} = \mu \cdot b \cdot \Delta h_1^{1,5} \quad (3)$$

where μ is a discharge coefficient (1.6 to 2.3) and b is the width of the structure's front (here b=1). The discharge outflowing to the turbine, according to Gravas et al. (2012) is given by equation (4)

$$Q_{exit} = c \cdot A \cdot (2g \cdot \Delta h_2)^{0,5} \quad (4)$$

where c is a discharge coefficient ranging from 0.6 to 0.68, and A is the wet part of the orifice section. The harnessed power per meter of the front of the structure, P (in Watts), is given from equation (5):

$$P = \rho \cdot g \cdot Q_{exit} \cdot H_m \quad (5)$$

where Q_{exit} is the water discharge outflowing from the reservoir, H_m is the available pressure head in the reservoir, ρ is the water density and g is the gravity acceleration.

3 RESULTS –DISCUSSION

The computation of wind generated waves was based on the wind data that were kindly provided by the HNMS for a long period of recorded values. Statistical processing and analysis, based on the application of the well-known statistical pocket, SPSS, then followed and led to the values of wind intensity and direction of Tables 1, 2 and 3. It should be noted that, for the case of Ierapetra, there were many time periods with missing data, so the final values in Table 3 are presented with reservation. For each case study only the winds generating waves towards the study area were taken into account. The mean wind speed was used, and the wave characteristics H and T were then calculated based on the prognostic methods as mentioned above. Subsequently, the weighted average of these wave characteristics was calculated for each study area. For the simulation the conditions of (a) wind waves, (b) long waves and (c) nonbreaking waves were assumed; for the domain's discretization, a space step Δx= 2 m and a time

step Δt = 0.1 sec were selected. The computational field consisted of 200 cells and the model ran for 10000 time steps. The crest elevation (Thress) was changing with the wave characteristics. FORTRAN programming language was used. The model results concerning the wave power are given in Table 4 (where the available incident wave power refers to regular waves). It is obvious that among the three study cases, only the Heraklio can lead to worthy wave power. It should be noted that the model refers to the propagation and incidence of a wave train on a vertical front of a coastal structure. The values of wave power in Table 4 can be doubled if the proposed structure of wall presents an armored slope as Koutitas and Savvidis report (2008). Applying the model on a monthly basin, the simulations can lead to the harnessed power during the specific period.

Table 1 Wind direction and intensity (Aktio, 1990-2021) (%)

Frequency	N	NE	E	SE	S	SW	W	NW
Calm	0.189	0.595	0.586	0.164	0.131	0.112	0.239	0.125
Weak	3.521	26.298	9.979	2.694	3.370	6.810	16.143	2.440
Moderate	0.669	5.216	3.309	0.690	1.363	3.552	9.734	1.002
Strong	0.057	0.301	0.232	0.043	0.064	0.129	0.111	0.093
Gale/Rushing	0.003	0.011	0.006	0.008	0.001	0.003	0.006	0.006
Total	4.438	32.421	14.110	3.599	4.928	10.606	26.233	3.665

Table 2 Wind direction and intensity (Heraklio, 1990-2021) (%)

Frequency	N	NE	E	SE	S	SW	W	NW
Calm	0.886	0.511	1.966	0.417	2.203	0.473	0.254	0.383
Weak	8.979	3.228	2.207	1.690	22.458	2.741	3.474	9.995
Moderate	5.496	0.497	0.322	0.306	6.266	0.551	2.585	19.182
Strong	0.944	0.034	0.014	0.012	0.969	0.023	0.021	0.840
Gale/Rushing	0.023	0.000	0.003	0.000	0.030	0.000	0.002	0.013
Total	16.328	4.271	4.512	2.425	31.927	3.789	6.336	30.412

Table 3 Wind direction and intensity (Ierapetra, 1990-2010) (%)

Frequency	N	NE	E	SE	S	SW	W	NW
Calm	0.000	0.004	0.000	0.000	0.000	0.000	0.000	0.000
Weak	23.913	4.403	1.602	0.521	8.070	16.292	0.539	0.399
Moderate	22.194	2.697	0.386	0.108	1.566	4.897	0.117	0.283
Strong	7.845	0.426	0.031	0.004	0.355	0.785	0.723	0.126
Gale/Rushing	1.521	0.022	0.013	0.004	0.081	0.027	0.013	0.031
Total	55.473	7.554	2.033	0.637	10.071	22.001	1.391	0.839

Table 4 Wave characteristics, H, T and wave power, P for the three case studies.

	H (m)	T (s)	Thress (m)	Harnessed P (kW/m)	Incident P (H^2T) (kW/m)
Aktio	0.35	3.10	4.12	0.12	0.38
Heraklio	0.92	4.96	4.35	0.68	4.24
Ierapetra	0.23	2.91	4.04	0.023	0.12

Table 5 Harnessed Sea Wave Power P (kW/m). H (m) / T (s) / Thress (m)

	Aktio		**Heraklio**		**Ierapetra**	
	H. T. Thress	P	H. T. Thress	P	H. T. Thress	P
January	0.39/3.28 / 4.10	0.10	1.21/5.79 /4.50	1.16	0.37/3.18/ 4.15	0.12
February	0.41/3.38 / 4.10	0.10	1.35/6.12 /4.60	1.53	0.46/3.55 / 4.15	0.14
March	0.36/3.17 / 4.10	0.10	0.96/5.13 /4.35	0.68	0.28/2.78 / 4.10	0.07
April	0.34/3.05 / 4.10	0.10	0.77/4.52 /4.30	0.54	0.15/2.02 / 4.05	0.01
May	0.29/2.84 / 4.10	0.09	0.55/3.75 /4.20	0.24	0.12/1.80/ 4.05	0.00
June	0.35/3.12 / 4.10	0.10	0.69/4.23 /4.25	0.41	0.14/1.99/ 4.05	0.01
July	0.34/3.06 / 4.10	0.10	1.00/5.18 /4.45	0.90	0.15/2.06/ 4.05	0.00
August	0.34/3.05 / 4.10	0.10	0.98/5.14 /4.40	0.72	0.20/2.33/ 4.05	0.01
September	0.32/2.99 / 4.10	0.04	0.79/4.62 /4.30	0.54	0.13/1.88/ 4.05	0.00
October	0.24/2.58 / 4.05	0.03	0.72/4.43 /4.25	0.39	0.11/1.77 / 4.05	0.00
November	0.36/3.14 / 4.10	0.05	0.84/4.82 /4.35	0.68	0.20/2.35 / 4.05	0.03
December	0.46/3.55 / 4.15	0.14	1.22/5.81 /4.50	1.16	0.39/3.26 / 4.15	0.16

Focusing on the case of Heraklio and the operation of the structure for the period of February, the proposed wall can produce P=1.53 kW/m and energy equal to E_{Febr} =P·time=1.53·28·24=1028 kWh/m. The mean energy in the long period studied here is E_{an}= 0.68· 365·24 i.e., ~6000 kWh/m. However, it is well known that only a portion of this energy is converted to exploitable electricity production. The annual energy E_{100} produced by such an energy wall of 100 m length is E_{100}= 6000·100 = 600,000 kWh or 600 MWh while the produced electrical energy is E_{el100}=E_{100}· n_{gen}=270 MWh, where n_{gen} (= 0.45) defines the performance of the electric generator. This amount of energy may not be considered high; however, in case of a slope in front of the wall, the structure produces 540 MWh which is comparable with the values of energy produced by a breakwater of 100 m length as reported by Kralli et al. (2019).

5 CONCLUSIONS

The use of an energy wall, as breakwater or quay wall, in three selected Greek coastal areas, is presented in this paper. The study shows that Heraklio is proposed as an excellent place for constructing such an energy wall that can lead to a considerable amount of energy due to waves. The other two areas are obviously improper for such a structure. The study revealed the significance of the wind climate in relation to the geographical position and the effective wave fetch. So, although winds generating waves towards Aktio or Ierapetra coasts may present some important frequency, these winds present low intensity. Furthermore, an oriented study in specific time periods is needed so that the structure's design may lead to its optimal operation for specific periods. A moving stem, changing the level of the opening of the wall's front might be examined, so that the optimal performance of the wall could be achieved in relation to the time period and the corresponding changing wave conditions.

References

Sismani G, Karambas Th (2015). Wave energy Conversion in coastal constructions 11th Panhellenic Oceanography & Fisheries Symposium, University of the Aegean, Mytilini, Lesvos, Greece (in Greek)

Chadwick Andrew and Morfett John (1998). Hydraulics in Civil and Environmental Engineering, Third edition, E & FN SPON, An imprint of Routledge, London and New York

Christopher G. Koutitas, Panagiotis D. Scarlatos (2016). Computational Modelling in Hydraulic and Coastal Engineering, CRC Press

Koutitas C. G. and Y.G. Savvidis, (2008). Modeling of a Wave Energy Harnessing Breakwater. Proceeding of the Eighteenth International Offshore and Polar Engineering Conference Vancouver, Canada, July 6-11-2008

Stagonas D., G. Muller, N. Maravelakis and D. Warbrick (2010). "Composite Seawalls for wave energy production: 2D experimental results. Proceeding of the Third Conference on Ocean Energy, Bilbao, Spain

Athanasios Gravas, Yiannis Savvidis and Christopher Koutitas (2012) "Modelling study on wave energy harnessing port structures", Fresenius Environmental Bulletin, vol. 21, No 8, pp. 3069-3076

Vasiliki-Eleni Kralli, Nicolaos Theodossiou and Theophanis Karambas (2019) Optimal Design of Overtopping Breakwater for Energy Conversion (OBREC) Systems Using the Harmony Search Algorithm. Frontiers in Energy Research, doi: 10.3389/fenrg.2019.00080

DMPCO 2023

e-Proceedings of the 2nd International Scientific Conference on Design and Management of Port Coastal and Offshore Works Thessaloniki, Greece, May 24-27 2023

Mean drift forces on arrays of vertical porous cylindrical bodies

D.N. Konispoliatis[1*]

[1]School of Naval Architecture and Marine Engineering, National Technical University of Athens, Greece
[*]Corresponding author: dkonisp@naval.ntua.gr

Abstract

This work presents a theoretical investigation of the second-order steady horizontal drift forces acting on an array of bodies which are exposed to the action of regular waves propagating in finite depth waters. An array of vertical, surface piercing and bottom fixed porous cylindrical bodies are examined consisting of an inner impermeable cylindrical column. A three-dimensional solution based on the eigenfunction expansion is developed for the determination of the velocity potential of the flow field around each body. Numerical results are presented and discussed concerning the mean drift forces for various values of porosity coefficients. The results revealed that porosity plays a key role in reducing/controlling the wave loads on the bodies.

Keywords Mean drift forces, Porous cylindrical bodies, Array of floating bodies, Darcy's law.

1 INTRODUCTION

A floating body exposed to the action of incident waves experiences, apart from the oscillatory loading components which cause the first-order motions of the body, second order forces due to nonlinear effects. These forces which are derived by the solution of the linearized body-wave interaction problem, performs zero mean values over one period. These second-order force components are known as mean drift forces. They are generally small in magnitude compared to their first-order counterparts; however, they may cause large excursions of the body from its mean position, in situations where there is a lack or very small hydrostatic restoring forces (Mavrakos, 1988).

So far, two principally different approaches have been presented in the literature for the determination of the mean drift forces. One is based on the application of the momentum conservation principle (Sclavounos, 1987; Molin, 1983; Mavrakos, 1995 to name a few), while the other is based on the direct pressure integration over the instantaneous wetted surface of the body. The latter method is applied herein, keeping all relevant terms up to second order. It has been introduced by Pinkester & VanOortmersen (1977), whereas Molin (1983) and Papanikolaou & Zaraphonotis (1987) extended the method by adding some missing terms regarding the vertical drift components and the pitch and roll drift moments. Other similar studies on mean drift forces using the direct integration method are Konispoliatis & Mavrakos (2014, 2021) and Konispoliatis et al. (2021).

Porous-surfaced bodies constitute an important class of maritime structures since they can reduce the influence of wave -body interaction through pores on the body surface. Such structure formation is encountered in piles of floating islands, quay piles, connecting bridge columns, and columns of very large floating structures, i.e., floating airports. In addition, porous structures have been reported widely in the literature. To raise some of them as examples, Wang & Ren (1994) examined a concentric surface-piercing two-cylinder system, in which the exterior cylinder is permeable and the interior body is assumed impermeable, whereas Teng et al. (2001) studied the diffraction problem of a cylindrical body with upper porous outer wall and inner solid column. Williams et al. (2000) investigated water wave interactions with a floating porous cylinder embodying a permeable side surface and impermeable top and bottom. Other similar studies are those from Bao et al. (2009), Sankar & Bora (2019; 2020), Konispoliatis et al. (2021), Konispoliatis & Chatjigeorgiou (2022).

2 FORMULATION OF THE PROBLEM

2.1 Determination of the velocity potential

An array of N vertical, surface piercing and bottom fixed porous cylindrical bodies of radius a are examined consisting of an inner cylindrical impermeable column of radius b (see Figure 1). The array

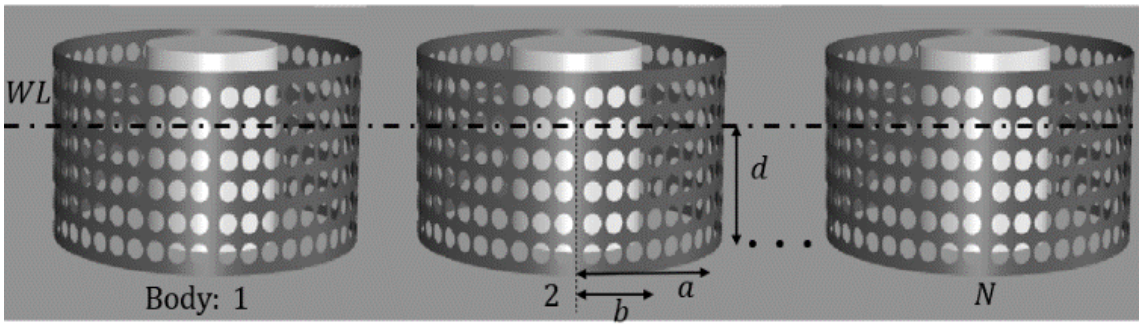

Figure 1: 3-D representation of the examined array of permeable cylindrical bodies

is exposed to the action of regular waves with amplitude $(H/2)$, wave number k and frequency ω, in a constant water depth d. A global Cartesian coordinate system O-XYZ with origin on the seabed and its vertical axis OZ directed positive upwards is used. In addition, N local cylindrical coordinate systems $(r_q, \theta_q, z_q), q = 1, \ldots, N$ are considered with origin at the seabed and their vertical axes pointing upwards and coinciding with the vertical axis of symmetry of the q body. The water domain is subdivided into two regions: (a) fluid region $I: r \geq a, 0 \leq z \leq d$, and (b) fluid region $II: b \leq r \leq a, 0 \leq z \leq d$. Also, viscous effects are neglected, and the fluid, which is assumed incompressible, can be represented in each fluid domain in terms of velocity potential, $\Phi^{q,l}(r_q, \theta_q, z_q; t) = \mathrm{Re}\left(\varphi^{q,l}(r_q, \theta_q, z_q)\mathrm{e}^{-\mathrm{i}\omega t}\right)$, $q = 1, \ldots, N,\ l = I, II$, where (Konispoliatis et al., 2021):

$$\varphi^{q,l} = \varphi_0^{q,l} + \varphi_7^{q,l} \tag{1}$$

Here, $\varphi_0^{q,l}$ is the velocity potential of the undisturbed incident harmonic wave; $\varphi_7^{q,l}$ is the scattered potential around the q body of the array.

The complex velocity potential $\varphi^{q,l}$, $q = 1, \ldots, N,\ l = I, II$, has to fulfill the Laplace differential equation in the entire fluid domain and the proper boundary conditions on the free surface and the seabed. Also, $\varphi_7^{q,I}$ has to satisfy an appropriate radiation condition at the far field. Furthermore, the following kinematic conditions on the vertical boundaries of the q body should be satisfied, i.e.:

$$\frac{\partial \varphi^{q,II}}{\partial r} = 0, r = b, 0 \leq z \leq d \text{ and } \frac{\partial \varphi^{q,II}}{\partial r} = ikG(\varphi^{q,II} - \varphi^{q,I}), r = a, 0 \leq z \leq d \tag{2}$$

In Equation (2) G denotes a dimensionless porous coefficient (Sankar and Bora, 2020).
Also, both the velocity potentials and their derivatives must be continuous at the vertical boundaries of neighboring ring elements.

The velocity potential of the undisturbed incident wave, $\varphi_0^{q,I}$, propagating at angle β, with respect to the positive x-axis can be expressed in the cylindrical coordinate frame of the q body as follows:

$$\varphi_0^{q,I}(r_q, \theta_q, z_q) = -\frac{i\omega H}{2} \sum_{m=-\infty}^{\infty} i^m \Psi_{0,m}^{q,I}(r_q, z_q) e^{im\theta_q} \tag{3}$$

where:

$$\frac{1}{d}\Psi_{0,m}^{q,I} = e^{ikl_{0q}\cos(\theta_{0q}-\beta)} \frac{Z_0(z_q)}{d\acute{Z}_0(d)} J_m(kr_q) e^{-im\beta} \tag{4}$$

In Equation (4) J_m is the m-th order Bessel function of first kind, (l_{0q}, θ_{0q}) are the polar coordinates of the q body's center relative to the origin O of the global coordinate systems O-XYZ, and $Z_0(z_q)$ is defined by:

$$Z_0(z_q) = \left[\frac{1}{2}\left[1 + \frac{\sinh(2kd)}{2kd}\right]\right]^{-1/2} \cosh(kz_q) \tag{5}$$

with $\acute{Z}_0(d)$ being its derivative at $z_q = d$.

In accordance to Equation (3), $\varphi^{q,l}$ can be written as:

$$\varphi^{q,l}(r_q, \theta_q, z_q) = -\frac{i\omega H}{2} \sum_{m=-\infty}^{\infty} i^m \Psi_{D,m}^{q,l}(r_q, z_q) e^{im\theta_q} \tag{6}$$

The unknown potential functions $\Psi_{D,m}^{q,l}, q = 1, \dots, N,\ l = I, II$, can be established through the method of matched axisymmetric eigenfunction expansions in which analytical representations of the velocity potential are derived through the idealization of the flow field around each body. Regarding the wave interaction phenomena between the array's members and the incoming waves, the multiple scattering approach has been applied. The latter is based on the superposition of the incident wave potential and various orders of propagating and evanescent modes that are scattered and radiated by the array members. The method of matched axisymmetric eigenfunction expansions as well as the multiple scattering approach have been thoroughly presented in Mavrakos and Koumoutsakos, (1987); Mavrakos, (1991), hence they are no further elaborated here.

2.2 Expression for the mean drift forces

In the present manuscript the mean drift forces are derived by the direct integration of the fluid pressure upon the instantaneous wetted surface of each porous body. Hence for the bottom seated array configuration, it holds:

$$\overline{F^{(2)}} = -\frac{1}{2}\rho g \int_{WL} \overline{\zeta_r^2} n dl + \frac{1}{2}\rho \iint_S \overline{|\nabla \Phi|^2} n dS \tag{7}$$

Here, ζ_r is the first-order relative wave elevation with respect to the transposed static water line WL of each body, S is the body's mean wetted surface, ρ and g denote the water density and the gravity acceleration, respectively, the term n is the unit normal vector pointing outwards of the body, and Φ is the velocity potential which describes the fluid flow around the array (see Section 2.1). The bars in the above equation denote the time average.

3 NUMERICAL RESULTS

3.1 Validation

This section is dedicated to confirming the validity of the presented theoretical method and its numerical implementation. The results from the present methodology are compared with corresponding data, which are available in the literature. In Figure 2 the mean drift forces, normalized by $\rho g b \left(\frac{H}{2}\right)^2$, acting on an isolated body are presented for three different porosity coefficients $G = 0, 0.075, 0.1$. The results are also compared with the outcomes from Cong & Liu (2020), concerning a porous, surface-piercing, cylindrical body of radii a and $b = 0.5a$, which is bottom seated in a fluid field of depth $d = 3b$. From the figure it can be seen a favorable agreement between the calculation obtained by the present method and the results reported in Cong & Liu work. Therefore, it can be concluded that the present model can effectively anticipate the mean drift forces associated with the concerned porous cylindrical body.

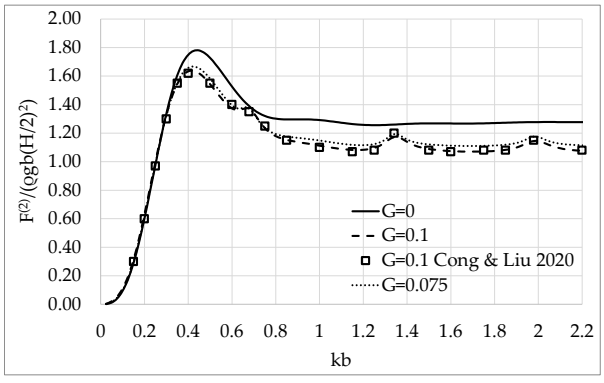

Figure 2: Horizontal mean drift forces on an isolated porous bottom-seated cylindrical body for $G = 0, 0.075, 0.1$. The results are compared against those reported in Cong & Liu (2020).

3.2 Test cases

The method developed in the present study is applied for an array of four bottom-mounted, surface-piercing impermeable cylinders, surrounded each one by an exterior porous cylindrical cell. The four

bodies are identical, and their geometric characteristics are presented above (see Section 3.1). The bodies are considered placed in a square arrangement and the distance between their vertical axes of symmetry is assumed constant and equal to $\ell = 10a$ (see Figure 3). In Figure 4 the mean drift wave forces on the 3rd body of the array are presented for various values of porosity coefficients $G = 0, 0.05, 0.1, 0.2, 0.5$ and directions of the incoming wave train (i.e., $\beta = 0, 20, 40, 60, 80$ degrees).

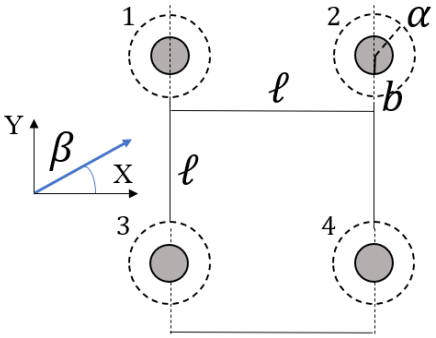

Figure 3. Definition sketch of the examined array configurations

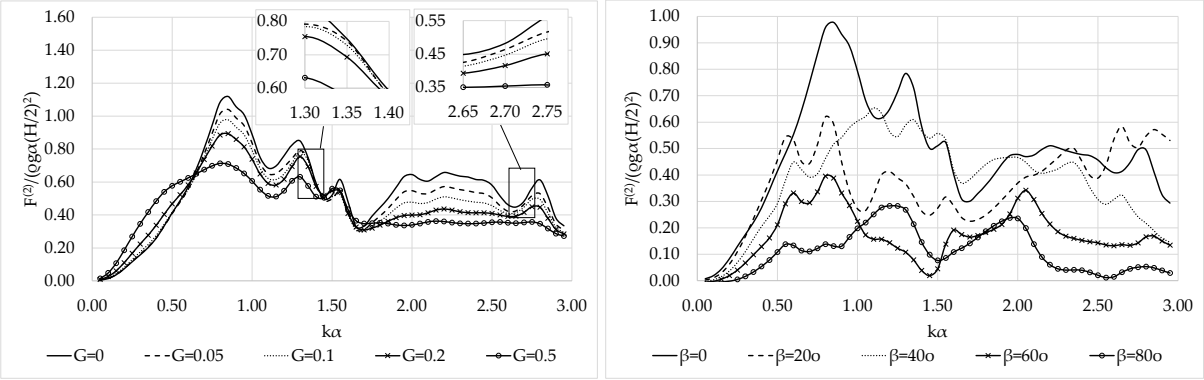

(a) (b)

Figure 4: Dimensionless horizontal mean drift wave forces on the porous structure: a) for different G values, b) for different ξ values

4 CONCLUSIONS

In the present work the direct integration method is applied for the evaluation of the mean drift wave forces on arrays of porous cylindrical bodies. In the framework of linear potential theory, the hydrodynamic interaction effects are determined through the first-order potential solutions by the use of the multiple scattering approach, whereas the hydrodynamic characteristics of the bodies are evaluated using the method of matched axisymmetric eigenfunction expansions. The porous surface is assumed to be inflexible with fine pores so that a linear pressure drop can be considered. From the presented theoretical formulation and the depicted results, the following conclusions are drawn.

The mean drift forces on the isolated body for $G \neq 0$ differ from those for $G = 0$. Specifically, the forces behave reverse proportionally with G. As the porosity coefficient increases the forces decrease, since the incident wave energy is absorbed by the side porous surface. Furthermore, a series of peaks is depicted at $ka \sim 1.35, 2.7$ (i.e., $kb \sim 0.67, 1.35$). At these wave numbers local enhancements of the mean drift wave forces are attained which decrease as G increases. Following the conclusions of Cong and Liu (2020) for an isolated porous vertical cylinder, at these kb the dissipation effect of the side porous surface is significantly weakened, thus the forces on the body tend to those on an impermeable cylinder, whereas as G increases this phenomenon is less pronounced.

Regarding the mean drift wave forces on the body when it is considered part of an array, it can be seen that their variation pattern differs from that for an isolated body. In particular, a large oscillatory behavior is appeared which is enhanced reverse proportionally with G. This can be attributed to the amplified wave field between the members of the array. Furthermore, the decrease of the dissipation

effect of the side porous surface seems also valid here. Nevertheless, the phenomenon is dominated by the large oscillatory behavior of the forces due to the wave interactions between the bodies of the array.

Finally, as the wave heading angle increases the tense oscillatory behavior of the mean drift forces on the presented configuration is reduced.

Summarizing, it can be seen that the mean drift wave forces on the multi-body array can be reduced significantly due to the porosity of the side surface. Hence this type of porous bodies can become preferable for applications such as the protection of a semi-submerged floating structure in severe wave conditions.

Acknowledgements

This research received financial support by Greek national funds through the Operational Program "Competitiveness, Entrepreneurship & Innovation" of the NSRF – Research Funding Program: "MATISSE: Study of the appropriateness and the adequacy of modern materials for offshore fish cage – numerical and experimental investigation in realistic loading conditions".

References

Bao W, Kinoshita T, Zhao F (2009) Wave forces acting on a semi submerged porous circular cylinder. Proc. of the Instit. Mech. Engin., Part M: J. of Eng. Maritime Envir., 223 (3): 349–360.

Cong P, Liu Y (2020) Local enhancement of the mean drift wave forces on a vertical column shielded by an exterior thin porous shell. J. Mar. Sci. Eng., 8, 349.

Konispoliatis D, Mavrakos S (2014) Mean drift loads on arrays of free floating OWC devices consisting of concentric cylinders. 29th IWWWFB, Osaka, Japan.

Konispoliatis D, Mavrakos S (2021) Mean drift forces on a vertical porous cylindrical body. 36th IWWWFB, Seoul, South Korea.

Konispoliatis D, Chatjigeorgiou I (2022) Theoretical hydrodynamic formulation for wave interactions with permeable cylindrical elements. 7th IAHR Europe Congress, Athens, Greece.

Konispoliatis D, Chatjigeorgiou I, Mavrakos S (2021) Theoretical hydrodynamic analysis of a surface-piercing porous cylindrical body. Fluids, 6 (9), 320.

Mavrakos SA, Koumoutsakos P (1987) Hydrodynamic interaction among vertical axisymmetric bodies restrained in waves. Appl. Oc. Res., 9: 128–140.

Mavrakos S (1988) The vertical drift force and pitch moment on axisymmetric bodies in regular waves. Appl. Ocean Res., 10: 207-218.

Mavrakos, S. (1991). Hydrodynamic coefficients for groups of interacting vertical axisymmetric bodies. Oc. Eng., 18: 485–515.

Mavrakos S (1995) Mean drift loads on multiple vertical axisymmetric bodies in regular waves. 5th ISOPE Conference, Hague, The Netherlands.

Molin B (1983) On second-order motion and vertical drift forces for three-dimensional bodies in regular waves. Intern. Works. on Ship and Platform Mot., Berkeley, USA.

Papanikolaou A, Zaraphonitis G (1987) On an improved near-field method for the evaluation of second order forces on 3D bodies in waves. 4th IMAEM Congress, Varna, Bulgaria.

Pinkster J, VanOortmersen G (1977) Computation of the first and second order wave forces on oscillating bodies in regular waves. 2nd Intern. Conf. Num. Ship Hydrod. Berkeley, USA.

Sankar A, Bora SN (2019) Hydrodynamic forces due to water wave interaction with a bottom-mounted surface-piercing compound porous cylinder. Oc. Eng., 171: 59–70.

Sankar A, Bora SN (2020) Hydrodynamic coefficients for a floating semi-porous compound cylinder in finite ocean depth. Marine Syst. Oc. Techn., 15: 270–285.

Sclavounos P (1987) The vertical wave drift force on floating bodies. 2nd IWWWFB, Bristol, UK.

Teng B, Zhao M, Li Y (2001) Wave diffraction from a cylinder with porous upper wall and an inner column. Acta Oceanologica Sinica, 23, 6.

Wang KH, Ren R (1994) Wave interaction with a concentric porous cylindrical system. Oc. Eng., 21 (4): 343–360.

Williams AN, Li W, Wang KH (2000) Water wave interaction with floating porous cylinder. Oc. Eng., 27: 1–28.

DMPCO 2023

e-Proceedings of the 2nd International Scientific Conference on Design and Management of Port Coastal and Offshore Works Thessaloniki, Greece, May 24-27 2023

Ocean Thermal Energy Conversion (OTEC) systems prospect in the eastern Mediterranean Sea

L. Aresti[1,3*], C. Michaelides[2], T. Onoufriou[1,3], P. Christodoulides[3]

[1]EMERGE CoE, Lemesos, Cyprus
[2]Department of Civil Engineering, International Hellenic University, Serres University Campus, Greece
[3]Faculty of Engineering and Technology, Cyprus University of Technology, Lemesos, Cyprus
[*]Corresponding author: lg.aresti@edu.cut.ac.cy

Abstract

Ocean Thermal Energy Conversion (OTEC), a renewable energy technology, has the potential to drastically lower greenhouse gas emissions while addressing the world's rising energy demand and may assist the European Union to reach its aim towards lower energy emissions. The Mediterranean Sea could be a viable area for the construction/ placement of OTEC systems, with reported high temperature values for the sea surface. An early analysis on the temperature difference (ΔT) between warm surface water and cold deep water indicates that the Mediterranean's Sea ΔT might not be adequate for the feasibility of the OTEC system. This research investigates the temperatures and location availability for installation of OTEC systems with the thermal parameters of the Mediterranean Sea and the effect of the positioning with the Cold Water Pipe. Based on the study findings, Cyprus in particular may have the potential for a successful hybrid OTEC system installation, albeit with an expected low efficiency. Overall, this study considers the OTEC systems in the Mediterranean Sea and emphasizes on the importance of location and the appropriate ΔT availability with the distance from shore. It is a fact that the potential availability of the desired ΔT is evident in many locations worldwide, allowing for OTEC system installation for electricity generation. However, in the case of the Mediterranean Sea, based on an initial evaluation, one would suggest that it is not sufficient. The present scientific paper aims to investigate such potentials in the Mediterranean Sea, specifically in the south-eastern Mediterranean area in the island of Cyprus, with the aim to identify how these systems, namely the OTEC systems, could be viable in order, through their possible use, to contribute towards the EU climate emissions neutrality.

Keywords Ocean Thermal Energy Conversion, Cold Water Pipe, OTEC Mediterranean Sea.

1 INTRODUCTION

Renewable Energy systems (RES) related to the ocean and marine environment have seen a significant advancement in recent years, due to the promotion of such RES for the reduction of fossil fuels and CO2 emissions in general. Ocean Thermal Energy Conversion (OTEC) systems can be categorized as RES, as they exploit the stored solar thermal energy in the ocean surface.

The natural temperature difference ΔT between the surface of the sea and the bottom, at great depths of about 1 km, gives rise to such exploitation potential. This capability can arise either for the generation of electricity or for the delivery of a by-product. The major disadvantage of OTEC systems lies in the availability and the location (i.e., distance from the equator), as the efficiency of the OTEC system depends on ΔT. A ΔT of 20°C or higher is recommended to provide a Carnot efficiency of 6.7%. OTEC systems aiming at the highest available ΔT, and hence a sufficiently high system efficiency, are suggested to be ideally placed in the tropical regions (or regions with ±20° from the Equator, including the Caribbean) where high ΔTs are recorded.

The current paper investigates possible locations and availability of the OTEC integration in the Eastern Mediterranean Sea, and more specifically in the island of Cyprus, where the water temperatures, salinity and the distance for shore are explored (see Section 2). Additionally, an initial investigation on the distance from shore is obtainable. In Section 3 the thermal potential of the Cold Water Pipe length is investigated. Furthermore, a discussion on the viability of such systems in presented in section 4.

2 MEDITERRANEAN SEA

The present study adopts the following methodology: (i) Firstly, thermal potential areas with high temperature difference (ΔT) are identified; (ii) the lowest horizontal distance from shore from the areas selected in (i) are recognized; (iii) it is checked whether these areas fall within protected areas; and (iv) the thermal potential based on the cold water pipe length in the specific areas is investigated.

The Mediterranean region (Sea), where OTEC systems are to be applied in this research, tell another story (Soukissian et al., 2017), compared to the Caribbean region. In particular, the sea surface temperature fluctuation is higher in the Mediterranean region (see Figure 1), with seasonal variation (i.e., winter or summer), with equally high mean values (CMEMS, 2022a; Darmaraki et al., 2019; Pastor et al., 2018). However, the temperatures at the seabed in the Mediterranean are higher, by approximately 5-10°C, yielding a lower ΔT compared to that of tropical regions (values of 20°C ΔT).

Estimations on the Mediterranean Sea temperature vertical profile in different sub-basins can be found in the literature (Carillo et al., 2012). Temperatures of approximately 13.6°C at 1 km depths can be observed, with no significant changes for depths of up to 4 km. Of note is that, from a 600m to up to 1km depth, similarly there is a minimum change in temperature, of approximately 0.2°C, as can be seen in the sea temperature depth profile of Figure 1. The EU Copernicus Marine Environment Monitoring Service reports similar findings (through the recorded date) (CMEMS, 2022b, 2022a). The rise of the sea surface temperature due to climate change, and the effect of the sources in the deep seawater, are aspects that researchers have considered and investigated (García-Monteiro et al., 2022; Lo Bue et al., 1990; Sakalli, 2017; Samuel-Rhoads et al., 2011).

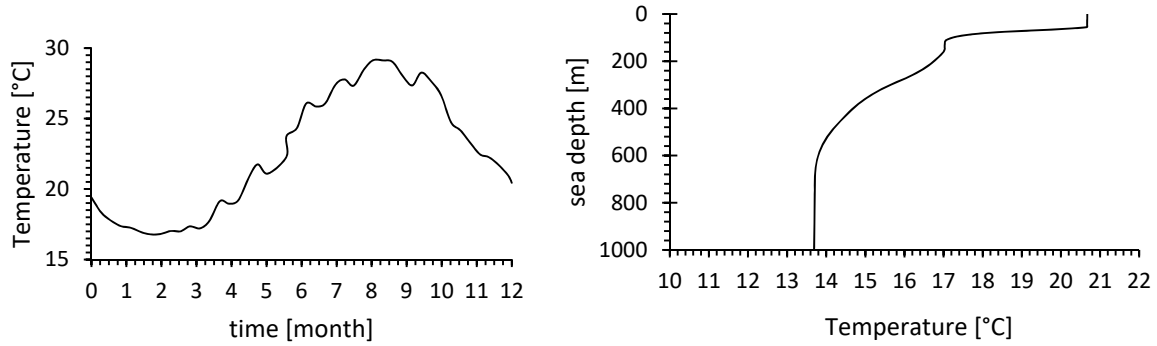

Figure 28 Surface sea temperature (left) and sea depth profile temperature (right) close to the Agia Napa Marina, Cyprus

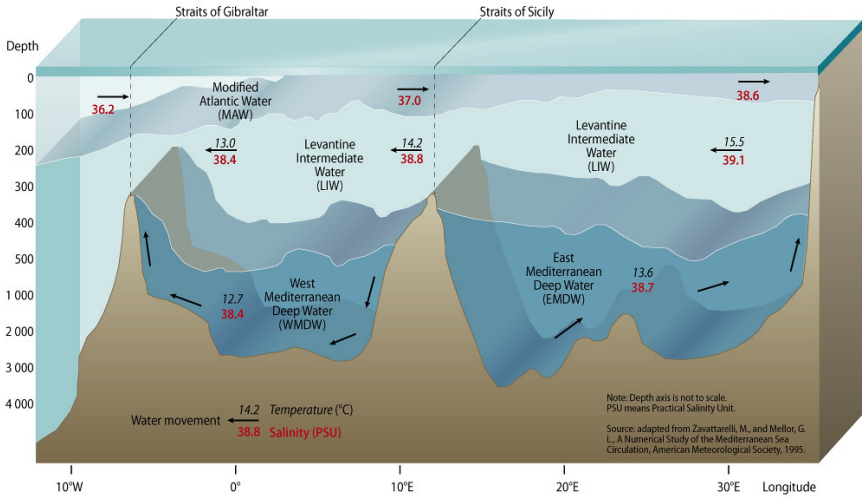

Figure 29 Mediterranean Sea water masses vertical distribution (GRID-Arendal, 2013)

The temperature profiles as well as salinity values vary in the Mediterranean Sea with the water masses are displayed in Figure 29**Figure *30***. The oceans' normal range of salinity is within the 33-37 psu

(practical salinity units), where the Eastern Mediterranean Deep Water (EMDW), compared to the Western basin, exhibits a higher deep seawater salinity of 38.6-38.7 psu (Zavatarielli and Mellor, 1995) at a depth of 1km. Of note is that the seawater salinity has a different behaviour depending on the depth and the mass of water. Additionally, in the EMDW the salinity does not have high fluctuations compared to the Levantine intermediate water and the surface seawater.

Further investigation was conducted in order to determine possible location around the island of Cyprus regarding the temperature availability and the distance from shore. Based on the shortest distance (horizontal) from shore temperature availability, three possible locations have been identified: (i) near the Xylofagou area (in Ammochostos District), (ii) the Akrotiti area (in Lemesos District), and near Peyia area (in Pafos District). The closest distance from shore (to reach the highest possible ΔT) is foundt to be in the Xylofagou area with a value of 6-6.5km (for a 600m depth) up to 7.5km (for a 1km depth). The other possible location would be the Akrotiri area with a similar distance of 6-6.5km, for a 600m depth, and a 9-9.5km, for a 1000m depth. For the Peyia area, distance from shore values of 8-10km are observed, which are much higher than the aforementioned ones. Figure 30 shows the two locations with the lowest distance from shore. Of note is that the distance from shore described here is a horizontal straight line, and it does not represent the actual cold water pipe (CWP) length, which will be higher and depend on the seabed morphology. It is important to stress that both locations happen to be under the British Overseas Territory and Sovereign Base Areas, and more specifically the Akrotiri area in Lemesos, is a closed area under the British military forces.

The seawater salinity on the given locations does not have any major variations, with values between 39.15-39.55 psu on the sea surface, and between 38.7-39.0 psu on the seabed (CMCC, 2021; Escudier et al., 2021). Similar finding was observed for the deep seawater temperature, with minimum variations, and values reported at 13.6-13.8°C. The sea surface variations vary depending on the season, with minimum and maximum values reported at 16.8°C and 29.2°C respectively.

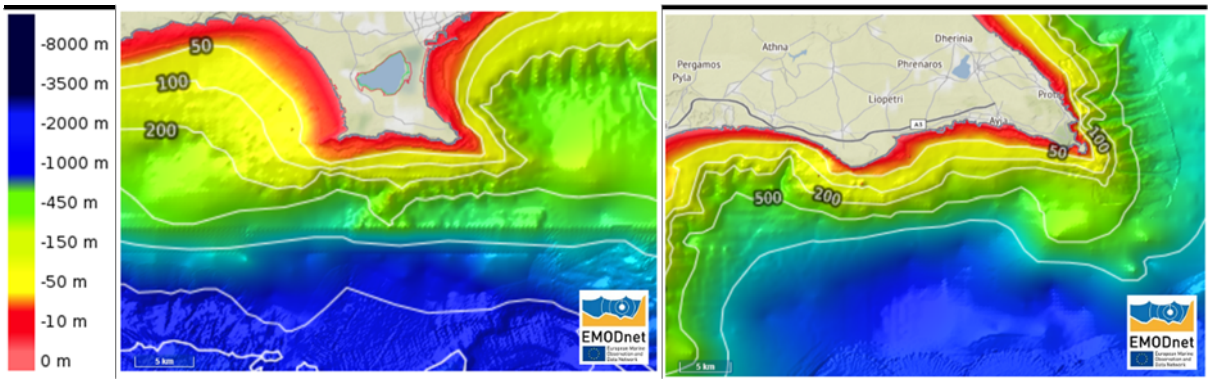

Figure 30 Bathymetry map of the island of Cyprus with bathymetry contours (EMOD, 2020) at different location: (left) the Akrotiti area (in Lemesos), and (right) Xylofagou area (near Ayia Napa).

Based on the initial evaluation of possible areas and physical water quality parameters, such as temperature and salinity, it can be clearly seen that the available ΔT (difference between the sea surface and the seabed temperatures) is fairly to very low, with a highest ΔT at 16°C (during the summer months) and a lowest ΔT at only 3°C (during the winter months), a fact making the systems not viable during the winter months. However, this shortcoming could be addressed, for example, by providing additional thermal energy from solar thermal systems, which will lead to an increase of the ΔT.

3 COLD WATER PIPE

A further examination/ investigation could be addressed on the ability of the CWP to transfer the temperature of the deep seawater (cold water) without losses and maintain the performance of the OTEC system. In order to estimate the heat transfer loss, between the cold water pipe and the temperature at the intake of the condenser, the convective and conductive heat transfer equation is used, as follows:

$$\rho A c_p \frac{\partial T}{\partial t} + \rho A c_p u e_t \cdot \nabla_t T = \nabla_t \cdot (Ak\nabla_t T) + \frac{1}{2} f_D \frac{\rho A}{d_i} |u^3| + Q_{wall} \quad (1)$$

where ρ is the density of the seawater fluid [kg m^{-3}], A is the pipe area [m^2], $\boldsymbol{c_p}$ is the specific heat capacity [J kg^{-1} K^{-1}], T is the temperature [K], t is time in [s], $\boldsymbol{ue_t}$ the tangential velocity of $\boldsymbol{u}$ inside the cold water pipe [m s^{-1}], $\boldsymbol{k}$ is the thermal conductivity [W m^{-1} K^{-1}], $\boldsymbol{f_D}$ is the Darcy's friction factor, $\boldsymbol{d_i}$ is the inner diameter of the cold water pipe [m], and $\boldsymbol{Q_{wall}}$ is the heat conduction [W m^{-1}].

The CWP length at the two investigated areas, presented in Section 2, is used as an input for initial investigation on the temperature at the intake of the condenser. The estimated horizontal distances from shore employed here are the 5km and 10 km lengths.

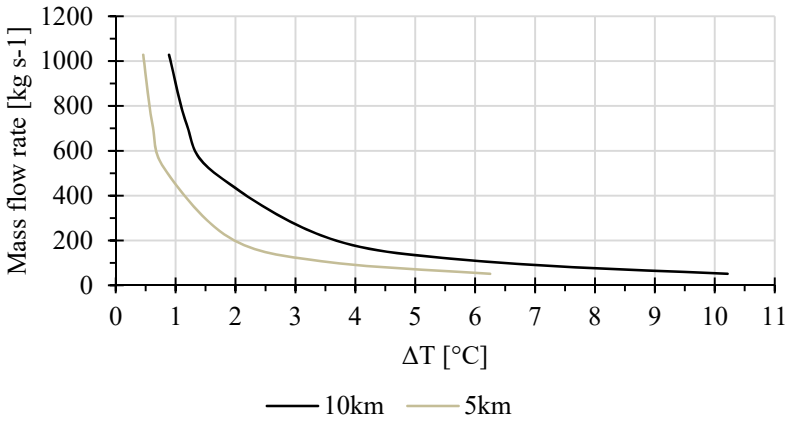

Figure 31 Mass flow rate effect on the ΔT at two different CWP lengths, 10km and 5km. with cold seawater density at 1028 kg m^{-3}.

The results are as predicted, with a higher heat transfer rate achieved with the reduction of the flow rate, and therefore a higher ΔT estimated. This would have a major effect on the performance of the OTEC system, as the temperature difference between the heat and cold source would be reduced. In terms of the length of the CWP to reach the desirable ΔT (for maximum system performance), with a shorter distance to shore, the resulting ΔT is also lower, thus having a significant effect on the performance and the costs of an OTEC system. However, a reduction in the length of the pipe is not a controllable parameter, as it depends on location, as described in Section 2.

4 DISCUSSION

The current study has investigated the potential use of OTEC (Ocean Thermal Energy Conversion) systems in the Eastern Mediterranean Sea, specifically in the island of Cyprus in the south-eastern Mediterranean area. The study firstly identified thermal potential temperature difference (ΔT), with a maximum ΔT estimated at approximately 16°C. Secondly, a possible area with the lowest horizontal distance from shore were identified in three locations, namely at the Xylofagou area, the Akrotiti area and the Peyia area, although two of these locations fall within protected or inaccessible locations. Based on the initial evaluation, performed for the case of the Eastern Mediterranean Sea, the temperature difference is not the optimum one for the efficient function of an OTEC system (as indicated from the difference between the hot and cold source temperatures) and possible types of hybrid use of OTEC should be explored.

Finally, the distance from shore was investigated, based on the thermal potential of the cold water pipe (CWP) length in the specific areas. The convection diffusion equation was used for the computational investigation, where the heat transfer loss was estimated based on the difference between the CWP intake at 1km depth, and at the intake of the condenser. The length of the CWP, as well as the selected flow rate, as expected, were verified to play a major role to the performance of the OTEC system.

References

Carillo, A., Sannino, G., Artale, V., Ruti, P.M., Calmanti, S., Dell'Aquila, A., 2012. Steric sea level rise over the Mediterranean Sea: Present climate and scenario simulations. Clim. Dyn. 39, 2167–2184.

CMCC, 2021. Mediterranean Sea Physics Reanalysis.

CMEMS, 2022a. Sea Surface Temperature extreme variability [WWW Document]. E.U. Copernicus Mar. Serv. Inf. URL https://resources.marine.copernicus.eu/product-detail/MEDSEA_OMI_TEMPSAL_extreme_var_temp_mean_and_anomaly/INFORMATION

CMEMS, 2022b. Baltic Sea Physics Reanalysis [WWW Document]. E.U. Copernicus Mar. Serv. Inf. URL https://resources.marine.copernicus.eu/product-detail/BALTICSEA_REANALYSIS_PHY_003_011/DATA-ACCESS

Darmaraki, S., Somot, S., Sevault, F., Nabat, P., Cabos Narvaez, W.D., Cavicchia, L., Djurdjevic, V., Li, L., Sannino, G., Sein, D. V., 2019. Future evolution of Marine Heatwaves in the Mediterranean Sea. Clim. Dyn. 53, 1371–1392.

EMOD, 2020. EMODnet-Bathymetry [WWW Document]. Eur. Mar. Obs. Data Netw. URL https://emodnet.ec.europa.eu/en/bathymetry

Escudier, R., Clementi, E., Cipollone, A., Pistoia, J., Drudi, M., Grandi, A., Lyubartsev, V., Lecci, R., Aydogdu, A., Delrosso, D., Omar, M., Masina, S., Coppini, G., Pinardi, N., 2021. A High Resolution Reanalysis for the Mediterranean Sea. Front. Earth Sci. 9.

García-Monteiro, S., Sobrino, J.A., Julien, Y., Sòria, G., Skokovic, D., 2022. Surface Temperature trends in the Mediterranean Sea from MODIS data during years 2003–2019. Reg. Stud. Mar. Sci. 49, 102086.

GRID-Arendal, 2013. Mediterranean Sea water masses: vertical distribution [WWW Document]. State Mediterr. Mar. Coast. Environ. URL https://www.grida.no/resources/5885 (accessed 3.1.23).

Lo Bue, N., Bosse, A., Velaoras, D., Amitai, Y., Ashkenazy, Y., Gildor, H., 1990. The Effect of the Source of Deep Water in the Eastern Mediterranean on Western Mediterranean Intermediate and Deep Water. Front. Mar. Sci. | www.frontiersin.org 1, 615975.

Pastor, F., Valiente, J.A., Palau, J.L., 2018. Sea Surface Temperature in the Mediterranean: Trends and Spatial Patterns (1982–2016). Pure Appl. Geophys. 175, 4017–4029.

Sakalli, A., 2017. Sea surface temperature change in the mediterranean sea under climate change: A linear model for simulation of the sea surface temperature up to 2100. Appl. Ecol. Environ. Res. 15, 707–716.

Samuel-Rhoads, Y., Zodiatis, G., Iona, S., Hayes, D., Georgiou, G., Konnaris, G., Nicolaides, M., 2011. Climate Change Impacts on Sea Surface Temperature and Salinity in the Eastern Mediterranean, Levantine Basin. Proc. 10th_Panhellenic Symp. Oceanogr. Fish. May 2012 9.

Soukissian, T.H., Denaxa, D., Karathanasi, F., Prospathopoulos, A., Sarantakos, K., Iona, A., Georgantas, K., Mavrakos, S., 2017. Marine renewable energy in the Mediterranean Sea: Status and perspectives. Energies 10, 1–56.

Zavatarielli, M., Mellor, G.L., 1995. A Numerical Study of the Mediterranean Sea Circulation. J. Phys. Oceanogr. 25, 1384–1414.

DMPCO 2023

e-Proceedings of the 2nd International Scientific Conference on Design and Management of Port Coastal and Offshore Works Thessaloniki, Greece, May 24-27 2023

Offshore wind farms – Design basis – Site conditions: How to reduce risks and optimize design during auction process

L. Barbetti[1], T. Koutrouveli[1*], M. Mathys[1]

[1]IMDC - Van Immerseelstraat 66, 2018 Antwerp, Belgium,
[*]Corresponding author: theofano.koutrouveli@imdc.be

Abstract

During the early years 2000 of the offshore wind development, project developers were granted by the national authorities of a concession site for a duration of 20-25 years. The collected data were (and are) key for the candidate bidders to prepare their optimal tender design which will include offshore wind farm layout and LCOE calculations, tender design for the WTG substructures, inter-array and export cables. In addition, the Site conditions of an offshore wind farm are subject to a specific certification process, where the reliability, the completeness and the quality of the collected and modelled data are verified according to the DNV standard (DNVGL-SE-0073). This paper aims to prove the importance of collecting specific site conditions and performing engineering studies during the preparation of auction plans for offshore wind concessions to help preparing an optimal design and installation methodology of the offshore wind farm assets.

Keywords: Offshore wind, subsea power cables, marine environment, wind resource assessment, offshore geotechnics.

1 INTRODUCTION

During the early years 2000 of the offshore wind development, project developers were granted by the national authorities of a concession site for a duration of 20-25 years. The main drivers for selecting a project developer were the supporting subsidies for electricity production, the financial stability of the companies and the willingness to invest in such new technology. Since then, a lot of experience has been built within the offshore wind industry leading to a more technical and financial competitive approach. Government institutions have drawn auction plans for granting new offshore wind concession sites. Tender selection criteria are becoming crucial for granting new offshore wind concessions, these criteria consider technical, financial, and sustainable aspects.

To allow candidate bidders to prepare an optimal technical and financial bid, national authorities (such as Netherlands Enterprise Agency (RVO) in the Netherlands and Federal Public Service in Belgium) are collecting in advance the site conditions of the next concession site, by coordinating offshore site investigations, desktop, and modelling studies. The Site Conditions for the Design Basis (DNVGL-SE-0073) and the Ecological Conditions to be collected regards mainly these categories:

- Environmental conditions
- Wind and metocean conditions
- Soil data
- Other site conditions

The collected data are key for the candidate bidders to prepare their optimal tender design which will include offshore wind farm layout and LCOE calculations, basic design for the WTG substructures, inter-array, and export cables. In addition, the Site conditions of an offshore wind farms are subject to a specific certification process, where the reliability, the completeness and the quality of the collected and modelled data are verified according to the DNV standard (DNV-SE-0073).

2 SITE AND ECOLOGICAL CONDITIONS

2.1 General

For the layout of an offshore windfarm, important information to be collected is the presence of seabed obstructions which will define a preliminary restriction zone (including a safety perimeter) for the layout of the OWF. These obstructions might be composed by third-party assets (i.e., cables, pipelines, platforms), presence of Unexploded Ordinance (UXO) or other natural (boulders…) or anthropogenic features (wrecks, chains, anchors…). During the mapping phase, a desktop study shall be performed for collecting information from public and private available databases. A data gap analysis and recommendations for the scope of works of field investigations shall be drafted as result of the desktop study.

As part of the study, an archaeological heritage and UXO desktop study should be performed. The aim of this study is to define risks and mitigating measures which could result in executing geophysical surveys, a combination of multibeam-echosounder (MBES), side-scan sonar (SSS) and magnetic (MAG) surveys, eventual underwater inspection and removal campaigns that will result in eventual As Low as Reasonably Practicable (ALARP) certificates for the execution of the works.

2.2 Environmental conditions

Environmental surveys are performed to determine the environmental baseline of the project area and the environmental impact of an offshore wind farm. These surveys are used as baseline for the Environmental Impact Study which results eventually in an environmental permit. Following environmental surveys and analyses are typically performed for an OWF project, depending on the specific relevance for the project site (The Crown Estate and ORE Catapult, 2019):

- Benthic environmental surveys are used to define areas of similar environmental conditions on the seabed and to inform habitat and species impact studies.
- Fish and shellfish surveys establish what species are present in the water column within the proposed wind farm site and surrounding areas.
- Ornithological environmental surveys establish the presence and behaviour of birds within the wind farm boundary and surrounding areas.
- Marine mammal environmental surveys establish the diversity, abundance, distribution, and behaviour of cetaceans (including porpoises, dolphins and whales) and seals within the wind farm boundary and surrounding areas.
- Onshore environmental surveys consider the potential ecological impact that cable-laying and onshore substations may have on the onshore environment.
- Human impact studies (fishing, recreational, marine traffic…) assess the impact that a proposed wind farm may have on the community living in and around the coastal area near the wind farm.

2.3 Wind and metocean conditions

To determine the energy yield of the offshore windfarm and its optimal layout, and to understand the forces acting on the substructures of the wind turbines generators (WTG), monitoring of metocean parameters is performed by deploying floating Lidar, met masts, metocean buoys and /or a combination of those. Hindcast data (15yrs) in vicinity and short-term monitoring (from few months to 1-2 yrs.) are typically collected from the project site to perform additional studies to define:

Table 1. Wind and metocean site conditons

Parameter	Description
Hydrodynamic conditions	Wind measurements
	Site specific wind data (normal and extreme conditions)
	Wind resource assessment
	Normal and extreme conditions for Waves, Currents

	Water levels and tides
	Cyclones and Typhoons
	Micro-siting study (positionings of WTG)
	Breaking waves
	Return periods (25, 50, 100yrs)
Wind / wave relation study	Joint probability of correlation of wave / wind cases
Workability	Workability tables based metocean and wind data series

The output of the modelling studies results in statistical parameters (normal and extreme conditions) which are used to define hydrodynamics forces acting on OWF assets (substructures, foundations, WTG, cable, offshore substation) but also to plan the offshore operations and construction schedule.

2.4 Soil and seabed conditions

The characterization of geology, geotechnical properties, seabed morphology and morphodynamics is necessary to optimize the offshore wind farm design such as WTG substructures/foundations, subsea cables burial and protection strategies, detection of seabed anomalies. Based on a desktop study and analysis of available (if any) site specific data, following offshore investigations are typically performed:

- Geophysical surveys such as bathymetries, side scan sonar (SSS), magnetometer and seismic (reflection and refraction),
- Geotechnical investigations such as vibrocores, CPT, boreholes, and lab testing.

These field investigations are accompanied by specific desktop and modelling studies aimed to define the seabed and geotechnical conditions:

Table 2. Soil and seabed conditions

Parameter	Description
Geology	Geological conditions
	Geological desktop study
	Geological Ground Model including interpretation of seismic reflection / refraction surveys and integration with geotechnical data
	Geological layers composition, lithology, and estimated thickness
Geotechnical	Geotechnical site conditions
	Geotechnical design parameters
Seabed	Morphological and Morphodynamics site conditions, seabed design levels
	Scour assessment and natural seabed erosion…
	Anomalies on seabed such as debris, UXO, wrecks…

2.5 Other site conditions

There are other site conditions which are typically collected and become part of the Design Basis. These are:

- Anthropogenic activities (marine traffic, fishing activities, third party assets, proximity and crossing agreements, UXO…)
- Noise
- Seismicity
- Tsunami
- Salinity
- Temperature, ice, and snow
- Marine growth

3 CASE STUDY

The presented case study aims to justify the importance of a solid Design Basis and engineering studies through the project lifetime for optimizing construction and O&M costs and reducing project risks.

The project, located in the Belgian Part of the North Sea, is the Thorntonbank C-Power OWF (C-Power, 2023) project (48x6MW and 6x5MW) that was fully commissioned and became operational in 2013. The OWF site is in sandy soil conditions with presence of mobile sand waves and in water depths between -10 and -35m. The OWF and its offshore high voltage substation are connected to the onshore grid via two export subsea power cables (2 x 150kV) for approx. 35km.

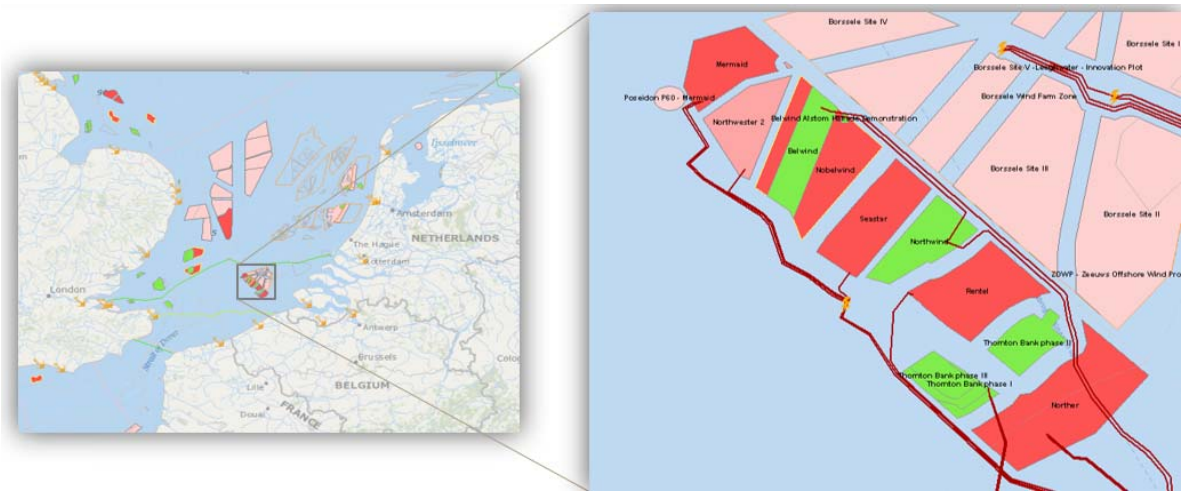

Figure 1. Thorntonbank C-Power OWF project (48x6MW and 6x5MW)

The two export cables (cable A and B) are crossing several sand banks areas with presence of mobile sand waves (up to 4-5m height and with mobility rates up to 4-5 m/year). These specific site conditions imply particular attention for defining the burial (and protection) strategy of subsea power cables which has also a big influence on construction methodologies and O&M plans. For this specific project two cable burial strategies were implemented:

- The export cable A (installed and commissioned in 2008) was buried for its entire length by ploughing and jetting. The as-built data showed sufficient burial depths (>1.5m) along the full cable length but after a couple of years, Cable A was found to be exposed and with burial depth <60cm in several sections along the cable route (2-3% of total length). To avoid risks of the cable getting exposed on the seabed and getting damaged by external marine traffic hazards or exposed to cable fatigue, the project owner decided to plan and execute expensive (and unexpected) remedial burial operations during the O&M phase.
- By using lessons learnt from Cable A engineering and installation works, a different strategy was used for the export cable A (installed and commissioned in 2011).
- During the engineering phase, the project owner supported by owner's engineering has performed a Cable Burial Risk Assessment (CBRA) study (Carbon Trust, 2016) with the objective to assess natural and anthropogenic hazards and their impact on subsea power cable burial / protection strategy, by provide mitigating design measures. A typical table of content with the different assessed hazards is given in figure below.
- In addition to marine traffic, the main hazard characterizing the specific site conditions is the seabed morphodynamics (sand waves). One of the main conclusions form this study led to implementing a different strategy for export B where pre-sweeping (pre-lay dredging) of areas where the cable B was crossing sand waves was planned. By implementing this strategy, the cable B was laid on the seabed in a pre-lay trench and still after 10yrs, there are no issues on cable burial depth.

To conclude, seabed morphodynamics (sand waves and natural seabed erosion) shall be considered during development and engineering phase of a subsea cable and OWF project for many reasons:

- To optimize the cable route and burial protection strategy
- To minimize costly remedial works during O&M
- To optimize installation and maintenance costs
- To reduce project risks during O&M

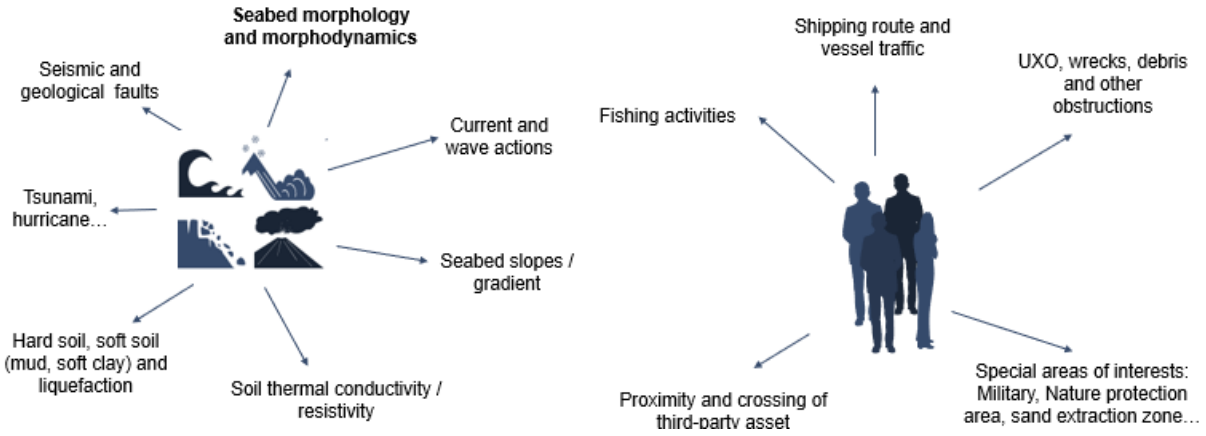

Figure 2. List of natural and anthropogenic hazards for Cable Burial Risk Assessment (CBRA) study

CONCLUSION

This paper illustrates the importance of collecting specific site conditions and performing engineering studies during the preparation of auction plans for offshore wind concessions to help preparing an optimal design and installation methodology of the offshore wind farm assets.

References

The Crown Estate - ORE Catapult (2019), Guide to an offshore wind farm, Published on behalf of The Crown Estate and the Offshore Renewable Energy Catapult

C-Power (2023), c-power.be website

Carbon Trust (2016), Cable Burial Risk Assessment methodology

DMPCO 2023

e-Proceedings of the 2nd International Scientific Conference on Design and Management of Port Coastal and Offshore Works Thessaloniki, Greece, May 24-27 2023

Multi-criteria cost-benefit analysis of offshore wind farms in the Aegean Sea

M. Gavalas[1], D. Kollias[1], C. Tsiara[1], L. Vasileiadis[1], V. Katsardi[1*]

[1]Department of Civil Engineering, University of Thessaly, Volos, Magnesia, 38334, Greece
[*]Corresponding author: vkatsardi@civ.uth.gr

Abstract

The present research proposes an integrated implementation plan for the assessment and classification of potential sites for offshore wind farm spatial planning practices. Considering a plethora of technical, economic and environmental criteria, this paper concludes in a decision-making tool, implemented on the Cyclades island complex. In more detail, the categorization of viable locations takes into consideration exclusion areas due to legal, scientific, or ethical concerns, while attributing a score value dependent on each site's performance regarding parameters such as wind potential, water depth, distance from shore etc. The scoring process also accounts for the overall cost of offshore wind farm projects, via the life-cycle cost breakdown structure in coherence with the levelized cost of energy method. For the case study of Cyclades, the results are simultaneously affected by the site-specific attribute of visibility from shore. Based on the national legislative framework and comparative literature, this methodological approach is performed through Geographical Information Systems (GIS) combined with multi-criteria analysis methods, namely the Analytical Hierarchy Process (AHP).

Keywords Offshore wind farm sitting, Cost breakdown analysis, Sustainable planning, Geographic Information Systems (GIS).

1 INTRODUCTION

Given the current global circumstances of climate change and energy crisis, the present paper is centered on a holistic and minimal environmental impact approach regarding the sustainable exploitation of renewable energy sources on a country level. Focusing on offshore wind power implications as a strategy towards energy security, this research deals with the topic of strategic planning concerning projects of offshore wind turbine platforms in the Aegean Sea, from an environmental as well as a techno-economical aspect. This work's aim is to develop an integrated methodology targeted towards the identification and evaluation of the suitable areas for siting offshore wind farms in the Aegean Sea both fixed and floating, using multi-Criteria Analysis in combination with Geographic Information Systems (GIS). Similar work has been presented by Spyridonidou et al. (2020) and in terms of localized sitting by Tsarknias et al. (2022).

2 METHODOLOGY

In general terms, the optimal sites for sitting offshore wind farms in the Aegean Sea, are concluded as a function of each site's location, depth, wind speed, sea soil properties, location-specific legislative restrictions, cost, environmental impact etc. The asset that differentiates the present study is the final product which comprises of a multi-layered map in ArcMap environment, that visualizes the plethora of parameters being considered, as well as site-specific values that correspond to the performance of each site to each criterion. The unification of the individual layers regarding each criterion, results in a fixed, gridded map of the Aegean Sea that directly correlates each site to a definitive score, based on every parameter taken into account.

2.1 Exclusion Areas

This category of locations concerns the areas that raise legal, scientific and/or ethical concerns and practically constitute the majority of the surface of the Aegean Sea. To avoid confusion, these particular regions are definitively excluded as opposed to others which simply received a lower overall score, due to being less appealing from an investment perspective. Namely, the latter areas mainly concern the

site's distance from shore, nearest port, and high voltage electricity grid. The exclusion areas are thoroughly presented in the following paragraphs.

2.1.1 Boundaries of Greek Territorial Waters

The most invasive restriction of the overall exclusion process is the regions outside the boundaries of Greek territorial waters since the remaining suitable area is a strictly legal-bound zone. The viable space option concerns the 6 Nmi zone from shore. In intricate locations where Greek and Turkish territorial waters technically overlap, the implication is resolved by a mid-distance boundary line (Gavalas 2023). However, given the profitability of an offshore wind farm project, both in economic and environmental terms, the present research does not eliminate the possibility of a transnational negotiation and potential agreement. In that spirit, the corresponding map layer depicts three scenarios: i) the current state – 6Nmi restriction; ii) 12 Nmi restriction; iii) no restriction considered.

2.1.2 Mean Wind Velocity

This exclusion criterion was derived from the international literature concerning areas characterized by mean wind velocity lower than 6 m/s at 10 m height above sea level (Vagiona and Kamilakis 2018), which constitutes the lower threshold value of mean wind velocity, below which the investment is deemed high risk. Corresponding to a typical wind turbine hub height, other researchers have utilized data regarding 80 meters height above the sea level and have set the minimum value to 6 m/s (Spyridonidou et al. 2020) or altered the wind potential variable entirely from velocity to annual wind power density with the lower threshold value set to 260 W/m^2 (Soukissian et al. 2020). The remaining viable location options were scored regarding their corresponding mean wind velocity value. If considering a specific case-study, another indicative parameter would be the high velocity winds' frequency of occurrence.

2.1.3 Water Depth

The bottom depth suitability differentiates according to the type of the offshore wind energy devices' support structure. The sea depth parameter constitutes a technical criterion which highly impacts the overall cost of such projects. Specifically, considering the amplified by depth anchoring, cabling and mooring costs, an increase in depth from 10-20 meters to 40-50 meters translates to almost a tripling of the total foundation cost (Argin et al. 2019). The depth restrictions derived from comparative literature and applied to the current research are characterized by bottom levels of i) $\leq$ 40 meters for monopile devices; ii) $\leq$ 100 meters for tripod/jacket installations; iii) $\leq$ 600 meters for floating foundations. The subsequent suitable locations were scored negatively as a function of the depth increase.

2.1.4 Path Restrictions

The term refers to the potential overlap of a suitable location for the establishment of an offshore wind farm with underwater cables, ship routes and/or corridors. In this framework, the first two cases are generally avoided, however the third is strictly excluded.

2.1.5 Environmental Restrictions

This subcategory of restrictions refers to legal concerns regarding biodiversity and consequently ethical spatial planning practices. The environmental concerns raised about wind energy exploitation in general are thoroughly analyzed in subsequent paragraphs. As recommended in the framework of the Special Framework for Spatial Planning and Sustainable Development for Renewable Energy Sources and in coherence with the prevalent values of the literature review, a mandatory safety radius is defined regarding regions that fall into the categories of NATURA 2000 and protected areas (1 km) and blue flag beaches (1.5 km). Wildlife refuges and migration corridors are excluded within a zone of 3 km.

2.2 Cost Assessment Methodology

The methodology used for cost assessment purposes derives from the breakdown of the life-cycle cost structure and is coherent with the levelized cost of energy method. The former comprises an integrated and environmentally centered approach in order to assess the impact of wind energy technology in quantitative terms. In more detail, life-cycle cost analysis (LCCA) is a systematic, holistic methodology, used to determine the total cost of an implementation measure from inception to disposal. The LCCA

comprises of three elements: the capital expenditure (CAPEX), the operation and maintenance costs (OPEX) and the decommissioning costs (DECOM) (e.g., Wang et al. 2019, Li et al., 2021).

Herein, the procedure used regarding the assessment of the life-cycle cost of an offshore wind farm was derived from the work of Castro-Santos et al. (2016); with a case-study located in Portugal. This methodology is also applicable to hybrid wind and wave projects and has been previously used in the case study of three offshore locations in the Aegean Sea (Tsipouras et al. 2021).

In this framework, the life-cycle cost of an offshore wind farm is broken down into categories, related to the different phases regarding the development of the project. Specifically, these are concept definition (C1), design and development (C2), manufacturing (C3), installation (C4), exploitation (C5) and dismantling (C6). In order to achieve more indicative results, the six separate costs are divided further into sub-costs so that they are also coherent with parameters such as each site's distance from shore, depth, wind speed etc.

For the time being the aim of this research is a macroscopic assessment of the optimal sites for offshore wind energy exploitation. However, this implementation plan could be applicable as a strategic spatial planning tool to a specific case-study, by calibrating it in order to include the individual needs and characteristics of the site (Table 1).

Table 1 Cost breakdown for the case-study of Limnos, Greece (Tsipouras et al. 2021)

C1	C2	C3	C4	C5	C6	Sum in €
4,080,000	240,000	318,936,000	269,168,890.9	130,864,588.9	15,865,353.4	739,154,833.2

2.3 Environmentally Sensitive Areas – Biodiversity

2.3.1 Levels of noise concerning mammals

Since the beginning of the planning and installation of offshore wind farms practices, the possible impacts on the marine environment, especially on marine mammals, have been discussed intensively within the public and the scientific community (Stöber and Thomsen 2021). The most important possible adverse effect of offshore wind farms relates to the underwater noise generated during the construction and operation of wind turbines (Thomsen et al. 2006). At the same time, this issue regards mostly the foundation works of monopiles, that are hardly suitable for the Aegean's large water depths.

2.3.2 Routes of migrating birds

Migratory birds are an integral part of the Aegean ecosystem, and the safeguarding of their safe routes cannot be absent from a complete environmentally friendly proposal. Migratory bird corridors are found in the study area at its western and eastern edge, these corridors were excluded as incompatible with the installation of offshore wind facilities. However, it should be mentioned that new practices based on innovative efforts to detect and repel birds flying near the rotating blades have effectively contributed to this achievement. Special sensors mounted on the wind turbine identify protected birds near wind farms, predict if their path poses a risk of hitting the blades and prevent by emitting special sounds and frequencies. One such system is the Bird Monitoring System which combines high-tech hardware and artificial intelligence software to protect wildlife in wind farm areas. Furthermore, the large oceans allow for optimized spacing between wind turbines, thus yielding more uniform energy production compared to land-based ones.

2.3.3 Regions of Posidonia

The areas in the Aegean area with a rich existence of Posidonia were excluded, consistently with the country's law since they are a particularly important part of the marine ecosystem (Panayiotis et al. 2022). A key target of the offshore wind farm construction project is to preserve or even enhance pristine ecosystems and provide protection for endangered populations and species. Once the operational phase begins, the effects of the turbines can be characterized as negligible. For effective conservation, positive effects should also spread to surrounding areas (Hammar et al. 2016). Therefore, in our work, Posidonia areas are considered both as an exclusion criterion and as one considered with care.

2.3.4 NATURA 2000 Regions

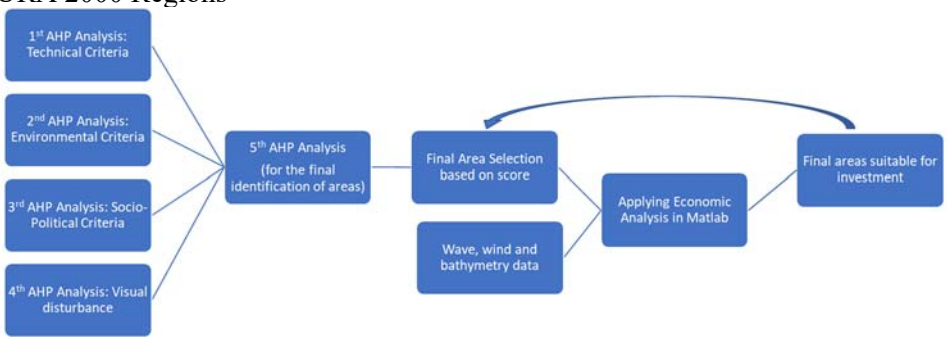

Figure 1: Flow chart of the summary operation of the OWTP spatial model

The areas in Greece that are under protection correspond to 1.5% of the sea area; mostly belonging to the European Ecological Network Natura 2000. In the study area there are eight Natura 2000 areas which are excluded as incompatible with the installation of offshore wind farms.

3 RESULTS & DISCUSSION

The methodology has been also applied to the island complex of Cyclades. This case study location constitutes an integral region of Greece from a historical, geographic, and economic perspective, given amongst else its high potential for wave and wind exploitation. Factoring in the plethora and complexity of the criteria considered, the Analytic Hierarchical Process (AHP) was implemented in 5 stages. This approach constitutes the optimal methodology for multi-criteria sitting of offshore wind farms (Diaz et al. 2022, Al-Shabeeb et al. 2016), given the need for spatial planning tools that factor in multiple viable locations and provide the user with calibration options. The criteria were divided initially into four individual categories. Namely, the implementation plan comprises of technical, environmental, socio-political, and visual disturbance related criteria (Figure 1). The AHP was applied for the purpose of classification via score attributing, to each location regarding its performance in each criterion. The fifth and final implementation of the method was used to receive the definitive, overall score of each location, prior to conducting cost-breakdown analysis. The necessity for visual disturbance related criteria is justified partially by residents' concerns regarding the sitting of wind farm projects (Karali 2010, Bili 2017), but on the other hand they are more positive in offshore sites. The ArcGIS Visibility tool was used, requiring the elevation raster file of the study area as well as the elevations of the potentially visible target point and observer. The key assumption made for compatibility purposes between the data and the Visibility tool restrictions, was the reduction of polygonal areas (e.g., NATURA 2000 areas) to a point, in this case their geometric center.

It should be noted that the visual nuisance acts as an inhibitor to the full achievement of the criteria, leading to suitable areas relevant to an excessive increase of the cost of construction/operation of the respective park. Thus, due to the complexity of the given space, as well as the multitude of criteria, a location solution will be sought based on a lower completeness score of the criteria offered by the solution method, accepting the visual nuisance or the careful location within some "prohibition zone". From the results of the 5th Hierarchical Analysis, the areas resulting with a score of over 95%, 85% and 75% will be studied, with the results of each criterion (Figure 2), after the economic benefit analysis. By observing the results, we identify two forms of positioning. Areas either large with numerous wind turbines or small with almost completeness of the criteria unprofitable basis with regards to the economic aspect. This must be considered during the initial design/programming, answering the questions of whether we want many and small or individual and large areas, balancing the environmental & social benefit with the financial one in the case of remote parks. Finally, which set-up will be more acceptable in the local communities? The proposed automated model can provide a solution for each user and region, with little parameterization in the initial data, with the results being extracted immediately and almost automatically. At the same time, the above knowledge of the areas by specialized scientific personnel, e.g., habitat of fauna or flora, can clarify exclusion zones, lead to greater precision during construction in order to avoid disturbance of the environment, deterioration of critical

infrastructure, obstacles to navigation and social rejection of investment. Indeed, local communities must help in making decisions about them. In addition, an ally to the above tool is the continuous integration of new technologies in the RES sector, such as sonar systems for birds, synthetic wings that do not block telecommunications and radars, more efficient rotors, and others, making the positioning and investment even safer.

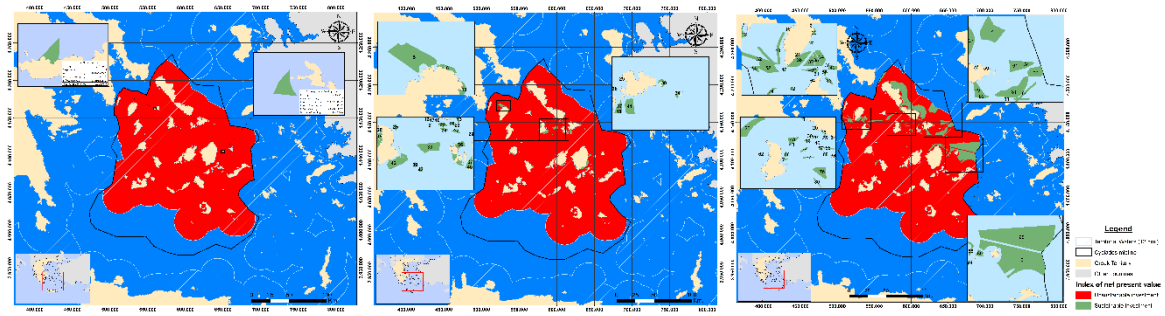

Figure 2: Final Results per scoring scenario (in order of 95%, 85% and 75%) in the Cyclades Island Complex

References

Al-Shabeeb, A, Al-Adamat, R, Mashagbah, A (2016) AHP with GIS for a Preliminary Site Selection of Wind Turbines in the North West of Jordan, International Journal of Geosciences, 7.10: 1208–1221.

Argin M, Yerci V, Erdogan N, Kucuksari S (2019) Exploring the offshore wind energy potential of Turkey based on multi-criteria site selection. Energy Strategy Reviews 23: 33-46.

Bili A. (2017) Selection of optimal areas of inland wind farms by the using multicriterian analysis and geographical information systems: The case of Andros, AUTH.

Castro-Santos L, Martins E, Soares C (2016) Cost assessment methodology for combined wind and wave floating offshore renewable energy systems. Renewable energy 97: 866-880.

Díaz H, Teixeira A, Soares C (2022) Application of Monte Carlo and Fuzzy Analytic Hierarchy Processes for ranking floating wind farm locations, Ocean Engineering, 245: 110453.

Gavalas M. (2023) Spatial planning of offshore wind farms in the island complex of Cyclades, UTH.

Hammar L, Perry D, Gullström M (2016) Offshore Wind Power for Marine Conservation. Open Journal of Marine Science, 6, 66-78.

Karali A. (2010) Administration of public reactions: The case of wind farms, NTUA

Li Q, Duan H, & 9 o. (2021) Life cycle assessment and life cycle cost analysis of a 40 MW wind farm with consideration of the infrastucture, Renewable and Sustainable Energy Reviews, 138, 110499.

Panayiotis P, Papathanasiou V, Gerakaris V et al. (2022) Seagrass meadows in the Greek Seas: presence, abundance and spatial distribution. Botanica Marina 65.4: 289-299.

Soukissian T, Karathanasi F, Belibassakis K, Kontoyiannis H (2020) Marine renewable energy in the Greek seas. In: The handbook of environmental chemistry, Springer, Berlin, Heidelberg, p 1-22.

Spyridonidou S, Vagiona D, Loukogeorgaki E (2020) Strategic planning of offshore wind farms in Greece. Sustainability 12.3: 905. doi:10.3390/su12030905

Stöber U, Thomsen F (2021) How could operational underwater sound from future offshore wind turbines impact marine life? The Journal of the Acoustical Society of America 149.3: 1791-1795.

Thomsen F, Lüdemann K, Kafemann R, Piper W (2006) Effects of offshore wind farm noise on marine mammals and fish. Biola, Hamburg, Germany on behalf of COWRIE Ltd, 62:1-62

Tsarknias N, Gkeka-Serpetsidaki P, Tsoutsos T (2022) Exploring the sustainable siting of floating wind farms in the Cretan coastline. Sustainable Energy Technologies and Assessments 54: 102841.

Tsipouras L, Spiliotopoulos G, Katsardi V (2021) Optimal sustainability solutions for the location of a floating wind energy farm in the Aegean Sea with the incorporation of wave energy hybrid systems, ESCC2021

Vagiona D, Kamilakis M (2018) Sustainable site selection for offshore wind farms in the South Aegean – Greece. Sustainability 10.3: 749.

Wang S, Wang S, Liu J (2019) Life-cycle green-house gas emissions of onshore and offshore wind turbines, Journal of cleaner production, 210, p. 804-810.

DMPCO 2023

e-Proceedings of the 2nd International Scientific Conference on Design and Management of Port Coastal and Offshore Works Thessaloniki, Greece, May 24-27 2023

A GIS-based MCDM approach for floating offshore wind farms site selection in Greece

V.I. Chalastani[1], E.Feloni[2] , A.Katradi[1], A. Papadimitriou[1] and V.K.Tsoukala[1]

[1] Laboratory of Harbour Works, Department of Water Resources and Environmental Engineering, School of Civil Engineering, National Technical University of Athens (NTUA), Zografou 15780, Greece.
[2] Laboratory of Hydrology and Water Resources Management, Department of Water Resources and Environmental Engineering, School of Civil Engineering, National Technical University of Athens (NTUA), Zografou 15780, Greece.
*Corresponding author: vanesachala@hotmail.com

Abstract

Wind power has gained attention as an important renewable source of energy generation, which reduces the greenhouse gas emissions, thus being an alternative to fossil fuels. Floating wind farms could be deployed in deep water, such as the ones of the Mediterranean Sea and contribute to the renewable energy portfolio of the Mediterranean countries. However, location selection for offshore wind farms is a major challenge for renewable energy policy, marine spatial planning, and environmental conservation. To address these issues, this research work considers the entire marine space of Greece to propose a methodology of Multi-Criteria Decision-making method, namely the Analytic Hierarchy Process, using Geographical Information Systems' techniques to define the most suitable areas for the installation of floating wind farms in Greece. Firstly, 19 criteria were set to demonstrate the eligible areas. In the context of ecosystem-based Marine Spatial Planning (MSP), the current as well as the projected national marine protected areas were taken into account. The eligible areas were evaluated according to 10 suitability criteria and two different scenarios: a technoeconomic and an environmental one. The results indicate that the areas of Cyclades, Northern Aegean Sea, as well as the areas between Crete and Karpathos islands and between Cephalonia Island and Astakos are the most promising ones. The methodology is solely based on publicly available data and could be reproduced to identify candidate areas for floating wind farms in other countries with similar characteristics.

Keywords Floating wind farms, Marine spatial planning, Sustainable siting, Multi-criteria decision making

1 INTRODUCTION

Switching to renewable energy currently seems the only way to tackle fossil fuel depletion, dependency on third countries for traditional energy sources and its associated geopolitical instability, as well as climate change. Offshore wind energy (OWE) has been identified as such source, capable to contribute to decarbonization and greenhouse gas emission reduction, while achieving the United Nations Sustainable Development Goal (SDG) 7; Affordable and Clean Energy. Europe constitutes the global leader in offshore wind energy, with some of the largest offshore wind farms in the world located in the European waters. In 2018, more than 80% of the global installed offshore wind capacity was located in Europe (IEA 2019). Furthermore, the European Offshore Renewable Energy Strategy was published as part of the European Green Deal and the Council agreed, in the context of "Fit-for-55" package, to set a binding target of 40% of energy from renewable sources in the overall energy mix, by 2030. The EU's current target is to reach 60 GW of installed offshore wind capacity by 2030, which would require significant investment and expansion of offshore wind infrastructure. Planning and optimal sitting of OWE are inherently embedded in the Marine Spatial Planning (MSP) process and explicitly mentioned in the the EU MSP Directive (2014/89). In Greece, despite the numerous scientific studies of OWE power plants site selection (e.g., Loukogeorgaki et al. 2018, Spyridonidou et al. 2020), currently no such plant has been deployed within the Greek territorial waters. Greece has significant potential for offshore wind energy due to its long coastline and windy conditions. Floating structures seem to be the most promising alternative for deep seawaters found not only in Greece, but in the Mediterranean Sea as a whole. Identifying the most suitable sites for OWE could be trivial, due to the number of parameters to be taken into account, including legislative, physical, technical and socio-economic restrictions. MSP

that considers the full spectrum of synergies and conflicts in the marine space could resolve the latter and provide robust results regarding site selection.

2 MATERIALS AND METHODS

Despite that most studies incorporate Geographic Information Systems (GIS) techniques and Multicriteria Decision Making (MCDM) approaches, they usually consider data anavailable online, as well as different exclusion and suitability criteria (EC and SC respectively). In this research work, to address the above issues, proper OWE locations are identified for the entire marine area of Greece by:

- Considering solely public open spatial data (Table 1);
- Incorporating all necessary EC according to the country's legislative framework, the relevant literature review and potential conflicts with other marine uses. For EC3 (Table 1), three (3) different options are considered: i) the current state of marine protected areas (NATURA 2000) in Greece, (ii) the increase of protected areas within 6 nm from the coast (Kartsakli 2022) and; (iii) the increase of protected areas within 12 nm from the coast (Kartsakli 2022).
- Investigating different scenarios regarding SC weighting; amongst all combinations, two indicative scenarios are presented: a technoeconomic and an environmental one.

The proposed methodology consists of four main steps:

1. The determination of the appropriate EC (Table 1), which are then set as constraints (i.e., Boolean Maps where "0" denotes the unsuitable and "1" the suitable areas).
2. The selection of the relevant SC (Table 2), which are considered for selecting OWE farms' optimal siting. For these criteria, values between 0 and 1 are assigned through a standardization process, i.e., through performing linear transformation in a predefined range (i.e., [0,1]).
3. The calculation of each SC's weight per scenario is conducted with the use of the Analytical Hierarchy Process (AHP; Saaty 1977). Two (2) scenarios are developed: (i) a technoeconomic scenario, where criteria relevant to technical aspects (Table 2) bear higher weights, and (ii) an environmental scenario, where the SC that are related to the environment (Table 2) are weighted with higher scores. In the context of ecosystem-based MSP and for illustration purposes, the case of increased protected areas within 6 nm is considered (Figure 2).
4. The evaluation of suitability areas (represented by 10^4 m^2 cells in GIS environment) is undertaken through the ranking of the final score (FS) of each cell. The latter is achieved via combining all SC per cell. For this purpose, the weighted linear combination (WLC) is implemented in GIS environment, according to Eq. 1:

$$FS = \sum w_i x_i \cdot \prod c_i \qquad (1)$$

where, FS is the final score of each cell; w_i and x_i stand for the weights and the corresponding SC, respectively, and c_i represents the EC. This formula results in values ranging from FS=0 in cases where at least one EC is identified, to FS≤1, denoting the cells which represent suitable locations.

Table 1. Exclusion criteria

	Criterion	Exclusion zone	Buffer zone	Source
EC1	Water depth	<50 m & >1000 m	-	https://emodnet.ec.europa.eu/en
EC2	Average wind velocity	<4 m/s	-	https://climate.copernicus.eu/
EC3	Environmentally protected areas (EPAs) - Natura 2000	All	1000 m	http://geodata.gov.gr, Kartsakli 2022
EC4	EPAs - areas of outstanding natural beauty (AONB)	All	1000 m	https://filotis.itia.ntua.gr
EC5	EPAs - important areas for birds	All	3000 m	https://old.ornithologiki.gr/
EC6	EPAs – seagrass meadows	All	1000 m	Topouzelis et al. 2018

EC7	Areas of cultural heritage (CHAs) - underwater antiquities	All	1000 m	https://thalchor-2.ypen.gov.gr
EC8	CHAs – monuments	All	3000 m	https://thalchor-2.ypen.gov.gr
EC9	CHAs - archaeological and historical sites	All	500 m	https://thalchor-2.ypen.gov.gr
EC10	CHAs – traditional settlements	All	1500 m	https://thalchor-2.ypen.gov.gr
EC11	Human settlements	All	1000 m	http://geodata.gov.gr
EC12	Bathing coasts	All	1500 m	http://geodata.gov.gr
EC13	Areas of military exercise	All	-	https://emodnet.ec.europa.eu/en
EC14	Marine routes	All	500 m	https://emodnet.ec.europa.eu/en
EC15	Fisheries areas	All	500 m	https://emodnet.ec.europa.eu/en
EC16	Areas of aquaculture	All	500 m	https://ypen.gov.gr
EC17	Airports	All	3000 m	http://geodata.gov.gr
EC18	Underwater cables (UC) – telecommunication	All	500 m	https://thalchor-2.ypen.gov.gr, https://www.submarinecablemap.com
EC19	UC - energy	All	500 m	https://www.admie.gr

Table 2. Suitability criteria

	Category	Criterion	Target
SC1	Technoeconomic criteria	Water depth	Min
SC2	Technoeconomic criteria	Average wind velocity	Max
SC3	Environmental criteria	Environmentally protected areas (EPAs) - Natura 2000	Max
SC4	Environmental criteria	EPAs - areas of outstanding natural beauty (AONB)	Max
SC5	Environmental criteria	EPAs - important areas for birds	Max
SC6	Environmental criteria	EPAs – seagrass meadows	Max
SC7	Safety criteria	Marine routes	Max
SC8	Safety criteria	Airports	Max
SC9	Technoeconomic criteria	Ports	Min
SC10	Technoeconomic criteria	UC - energy	Min

3 RESULTS

The criteria presented in Tables 1 and 2 were combined to firstly define the candidate areas of OWE siting in Greece (Figure 1). Eligible areas that have arisen as a result of the ECs implementation showcase the effect of marine protected areas in the total areas available for floating OWE siting. In particular, when only the current marine areas protected by the NATURA 2000 network are considered ($24.4*10^9$ m^2 in the marine area), then the eligible areas for OWE constitute a total area of 64160.53 km^2. The expansion of marine protected areas within 6 nm off the coast leads to an increase of protected areas by 10.2% (Kartsakli 2022) and a respective decrease of eligible areas by 10.03%, whereas the expansion of protected areas within 12 nm increases the protected areas by 10.6% (Kartsakli 2022) and restrain the eligible areas by 10.56%.

To assess the suitability of the eligible areas, two (2) different scenarios regarding SC's weighting where formed: (i) a technoeconomic (Figure 2a) one, where the SC characterized as technoeconomic (Table 2) bore higher weights compared to the others, and (ii) an environmental (Figure 2b) one, where the environmental SC were considered as equally important in each pairwise comparison. As shown in Figure 2, after performing the second scenario regarding hierarchy, the FS reduces significantly in most areas (Figure 3). In particular, the reduction score is around 15% for Cyclades complex and around 10% for the Northern Aegean Sea, whereas the reduction score is less for the Ionian regions and the area around Karpathos, denoting the areas where environmental requirements need attention.

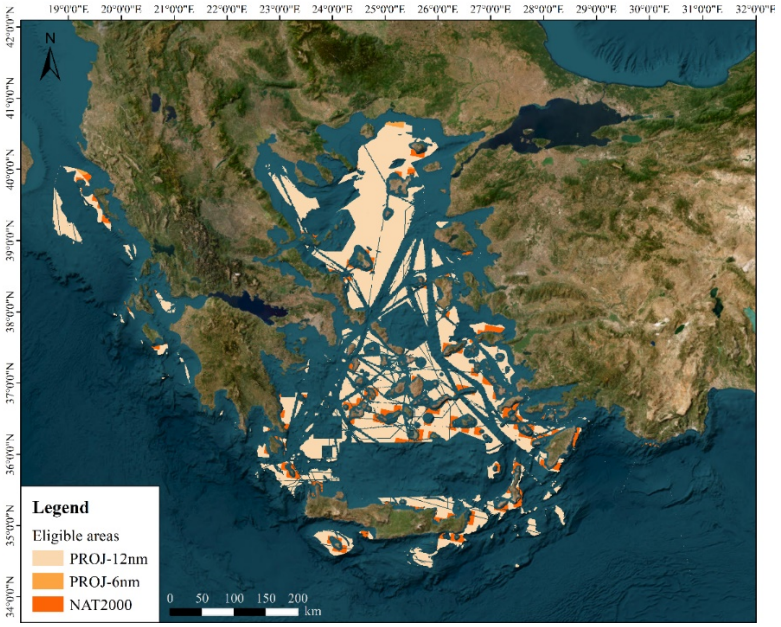

Figure 1. Eligible areas for OWE siting in Greece. The light pink colour depicts the eligible areas when marine protected areas within 12 nm from the coast (Kartsakli 2022) are considered. The light orange colour denotes the eligible areas when marine protected areas within 12 nm from the coast (Kartsakli 2022) are considered. The orange colour represents the eligible areas when only the current state of marine NATURA 2000 areas is considered.

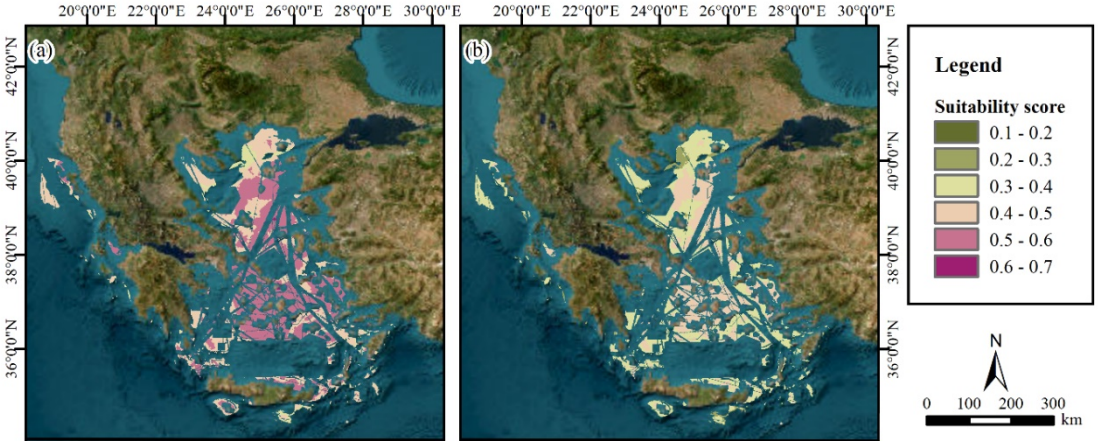

Figure 2. Suitability of eligible areas according to the **(a)** technoeconomic scenario and **(b)** environmental one. Green colour represents the least suitable areas whereas the dark purple colour depicts the most suitable ones.

4 CONCLUSIONS

Floating wind turbines can be an important asset for the Greek renewable energy portfolio, particularly because they can significantly raise the marine space available for OWE installation in areas with limited shallow waters, such as Mediterranean Sea, while reducing visual and noise disturbance in comparison with fixed-bottom wind turbines. Therefore, the entire marine area of Greece is considered to present a GIS-based decision support model for assessing the optimal siting of floating OWE farms in Greece. In total, 19 and 10 criteria were considered as "exclusion" and "suitability" criteria respectively. The results indicate that in both the technoeconomic and the environmental scenarios, the areas of Cyclades, Northern Aegean Sea and the area between Crete and Karpathos islands were identified as the most promising, since they had high scores in most of the SC. The latter is in accordance with the current national plans for the installation of wind turbines, though they mostly refer to fixed-bottom ones. However, usually the Ionian Sea is not considered by similar studies, probably due to the higher average wind velocities found in the Aegean Sea. In this paper, the marine space between Cephalonia Island and

Astakos was identified as eligible for OWE installation. The difference of FS between the two (2) scenarios (Figure 3) indicate that the areas of Cyclades and Northern Aegean Sea show the highest difference in suitability once the environmental factors are prioritized against the technoeconomic ones. GIS are a valuable tool in the process of site selection, especially when combined to MCDM techniques, such as AHP. However, in most cases the spatial data considered are unavailable online, which affects the reproducibility of the proposed methodologies. The current work contributes to the development of existing multi-criteria methods through GIS by using only publicly available data, to ensure transparency and further elaboration on the trivial issue of optimal siting of floating OWE systems.

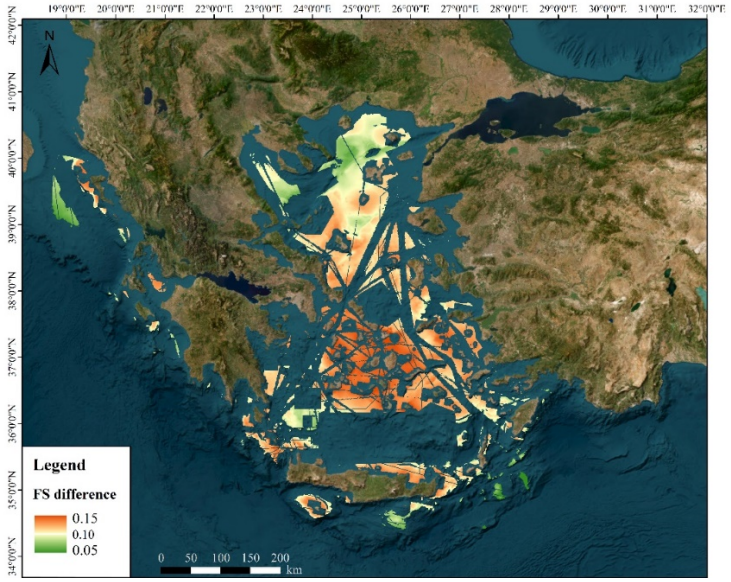

Figure 3. Difference in final score between the two scenarios. Orange colour represents the highest percentage difference and the green the least percentage difference between the scenarios.

Acknowledgments

The authors would like to thank Prof. M. Papadopoulou, NTUA and Mrs N. Kartsakli for sharing the shapefiles of the projected marine protected areas, both for 6 and 12 n.m., developed in the context of Mrs. Kartsakli's postgraduate thesis, supervised by Prof. Papadopoulou.

References

International Energy Agency (2019) Offshore Wind Outlook 2019. IEA Paris. Available at: https://www.iea.org/reports/offshore-wind-outlook-2019. Accessed 5 Apr 2023

Kartsakli N (2022) Planning of new marine protected areas in the Greek marine space. Postgraduate diploma thesis. Supervised by: Papadopoulou M. School of Rural, Surveying and Geoinformatics Engineering. National Technical University of Athens. Available at https://dspace.lib.ntua.gr/xmlui/handle/123456789/55998. Accessed 5 Apr 2023

Loukogeorgaki E, Vagiona DG, Vasileiou M (2018) Site selection of hybrid offshore wind and wave energy systems in Greece incorporating environmental impact assessment. Energies 11:2095. doi: 10.3390/en11082095

Saaty (1977) A scaling method for priorities in hierarchical structures. Journal of Mathematical Psychology 15:234-281. doi: 10.1016/0022-2496(77)90033-5

Spyridonidou S, Vagiona DG, Loukogeorgaki E (2020) Strategic planning of offshore wind farms in Greece. Sustainability 12:905. doi: 10.3390/su12030905

Topouzelis K, Makri D, Stoupas N, Papakonstantinou A, Katsanevakis S (2018) Seagrass mapping in Greek territorial waters using Landsat-8 satellite images. International Journal of Applied Earth Observation and Geoinformation 67:98-113. doi: 10.1016/j.jag.2017.12.013

Tsarknias N, Gkeka-Serpetsidaki P, Tsoutsos T (2022) Exploring the sustainable siting of floating wind farms in the Cretan coastline. Sustainable Energy Technologies and Assessments 54:102841. doi: 10.1016/j.seta.2022.102841

DMPCO 2023

e-Proceedings of the 2nd International Scientific Conference on Design and Management of Port Coastal and Offshore Works Thessaloniki, Greece, May 24-27 2023

Greek port infrastructures assessment towards floating offshore wind farms development

A. Tsakos[1*], E. Loukogeorgaki[1]

[1]Department of Civil Engineering, Aristotle University of Thessaloniki, Thessaloniki 54124, Greece
*Corresponding author: tsakosag@civil.auth.gr

Abstract

Ports have a prominent role for developing Floating Offshore Wind Farms (FOWFs) and, thus, exploiting offshore wind energy in deep waters. Those facilities can provide sufficient space and services during the various FOWFs lifecycle phases and, thus, they can support efficiently the relevant local supply chain and logistics, contributing to costs reduction. Greece offers significant potential for the development of FOWFs. Despite the recent initiatives of the Greek government to promote offshore wind developments in the country, there are still challenges that must be addressed, including among others the existence of adequate ports infrastructures. Along these lines, the present paper focuses on the assessment of six large key Greek ports (Piraeus, Thessaloniki, Alexandroupoli, Patras, Volos, and Heraklion ports) in terms of their suitability to support the development of FOWFs in the country. Various suitability criteria are taken into account related to the port's physical characteristics, connectivity and layout, while the assessment is implemented for different scenarios by modifying the manufacturing location of the floating platform. The results demonstrate the need to upgrade and expand existing ports infrastructures in Greece to support the new and ever-increasing demands.

Keywords Floating offshore wind farms, Port infrastructures, Suitability criteria, Greece.

1 INTRODUCTION

Floating offshore wind technology corresponds to an emerging field with a significant growth during the last decades aiming at the efficient exploitation of the vast offshore wind in deep waters. Accordingly, numerous concepts and designs of Floating Offshore Wind Turbines (FOWTs) have been tested by different developers through demonstration and pilot projects, with the HyWind and WindFloat technologies (Castro-Santos and Diaz-Casas, 2016) presenting nowadays the most mature ones. Those technologies have been deployed for the realization of pilot and/or commercial Floating Offshore Wind Farms (FOWFs) corresponding to the HyWind Scotland 30 MW pilot project, the HyWind Tampen FOWF (88 MW), the WindFloat Atlantic FOWF (25 MW) and the 50 MW Kincardine project (WindFloat technology) in Scotland, which is currently the larger commercial FOWF (Aegir Insights, 2022). Ports are key players in the supply chain of FOWFs. As the interface between land and sea, they can provide sufficient infrastructure and services during the various FOWFs lifecycle phases (from storage and pre-assembly to O&M) and they can support efficiently the relevant local supply chain and logistics, contributing to costs reduction (Wind Europe, 2020). However, the continuous evolvement of the offshore wind energy market towards the construction and operation of large-scale floating projects requires significant investments for ports to upgrade and expand their capacity, including diversification of their operations to support the specific and ever-increasing demands.

Greece, with its extensive coastline and strong winds, offers significant potential for the development of FOWFs. The recent relevant Greek legislation framework presents a very important step towards this direction. Nevertheless, there are still critical challenges that must be efficiently addressed, including among others the existence of adequate ports infrastructures (Offshore Wind Consultants, 2022).

Motivated by this, in the present paper we assess six large key ports in Greece (Piraeus, Thessaloniki, Alexandroupoli, Patras, Volos, and Heraklion ports) in terms of their suitability to support the development of FOWFs in the country. Specific suitability criteria, adopted from existing FOWF, are considered related to the port's physical characteristics (e.g., water depth), connectivity (e.g., proximity to steel production units) and layout (e.g., storage facilities). The results highlight the need for investments towards the upgrade and expansion of the Greek ports to accommodate the operational capacity for FOWFs.

2 METHODOLOGY

For assessing the examined Greek ports, specific suitability criteria, adopted from existing FOWFs, mainly in northern Europe, are considered. For each criterion, a minimum quantitative or qualitative requirement is assigned, and the suitability of the ports is assessed based on the number of criteria satisfied in terms of the aforementioned

requirements. Specific scientific articles and technical reports were studied to adequately define those requirements. The assessment is implemented for three different scenarios by modifying the manufacturing location of the floating platform. In the following sections, the aforementioned suitability criteria along with the examined scenarios are described in detail, while, finally, some key assumptions of the deployed methodology are cited.

2.1 Suitability criteria

The suitability criteria are grouped into three different categories corresponding to the physical characteristic, the connectivity, and the layout of the port (Akbari et al., 2017). Those criteria are cited in Table 1 and are considered for both the construction and the O&M phases of a FOWF.

Table 1. Port's suitability criteria for FOWFs development in Greece

Port's physical characteristics	Port's connectivity	Port's layout
Entrance's depth & width (C1.1)	Road and/or railway network connection (C2.1)	Storage space & workspace (C3.1)
Number of quays with adequate depth and length (C1.2)	Proximity to steel production units (C2.2)	Parts handling equipment (C3.2)
Quay loadbearing capacity (C1.3)		Construction area (shipyards) (C3.3)
Absence of aerial obstacles (C1.4)	Proximity to concrete production units (C2.3)	Office facilities (C3.4)
Available sheltered waters (C1.5)		

Regarding the minimum requirements of the criteria related to the port's physical characteristics, an entrance of at least 12 m depth and 135 m width (C1.1) is required for the safe movement of the specialized vessels. Furthermore, the port should have at least 2 quays of length > 200 m and depth > 15 m (C1.2). The loadbearing capacity of these quays (C1.3) should be at least 25 tn/m^2. The absence of any aerial obstacles (C1.4), such as bridges and cables, as well as the availability of sheltered waters with depth larger than 12 m (C1.5), required during the construction phase, are also considered as essential attributes for a suitable port (Elkinton et al., 2014).

As for the suitability criteria related to the port's connectivity, the existence of a good connection with a road and/or a railway network (C2.1) is taken as minimum requirement for supporting the transportation of the required components of the wind turbine. Additionally, the closer a port to steel and/or concrete productions units (C2.2-C2.3) is, the more suitable the port is considered, since in this way the cost of production is reduced and the local supply chain is strengthened (Matha et al., 2017).

With regard to the minimum requirements of the criteria related to the port's layout, a storage and workspace (C3.1) of at least 200 acres for components storage and wind turbine pre-assembly should be provided. The availability of special handling equipment (C3.2), such as clarks, cranes, Self-Propelled Modular Transporters (SPMTs) and 1000+ tn heavy lift cranes, enhances the suitability of a port. It is noted that although heavy lift cranes are necessary, the relevant requirement is a bit strict due to the scarcity of such an equipment. The existence of shipyard facilities at the port (C3.3) also enhance the port's suitability since those facilities could offer great convenience both in the construction and the maintenance phase of a FOWF project. Finally, the availability of office facilities (C3.4) is considered as a positive factor for the port's suitability.

2.2 Floating platform's manufacturing location scenarios

As mentioned above, the assessment of the examined Greek ports is implemented for three different scenarios (SC) by modifying the manufacturing location of the floating platform. In SC1, the platform is manufactured abroad, and it is transported to the port of interest, while in SC2, it is manufactured at the examined port's facilities. SC1 corresponds to the assessment of ports that fall under the category of a storage, assembly, and fit-out port. On the other hand, in SC2 we assess cluster ports, that enable the realization of storage, fabrication, assembly and fit-out activities. Finally, in SC3, the platform is manufactured at Greek shipyards, and it is, then, transported to the port. It should be noted that in the case of SC2 the minimum requirements of the suitability criteria C1.2 and C3.1 are modified compared

to those mentioned in the previous section. Specifically, for this scenario the port should have at least 3 quays of length > 200 m, while the available necessary area for work and storage increases from 200 to 400 acres (Porter and Phillips, 2016).

2.3 Key assumptions

In order to assess the Greek port infrastructures for the development of FOWFs, certain assumptions have been made. More specifically, it is assumed that the various components of the wind turbines, including the tower, the blades, the nacelle, and the transition piece, will be manufactured abroad and will be transported to the Greek port of interest for assembly and installation. This assumption is based on the current status of the offshore wind market, which is characterized by the concentration of components' manufacturing by companies with established expertise and specialized facilities (Figure 1) in certain countries that may not be available locally. Furthermore, all Greek port facilities examined in the present work consist mainly of cargo piers and quays with other commercial uses. This assumption reflects the current status of the Greek ports, where cargo handling is the major activity, and highlights the need for: (a) adequate infrastructure to accommodate the specific needs for the development of FOWFs or (b) diversification of the ports' operations. Finally, it is assumed that the ports will support the construction and O&M of commercial FOWFs with capacity larger than 30 MW. The deployment of wind turbines with a capacity of more than 8 MW is also taken into account, in line with the current practices of Northern European FOWFs.

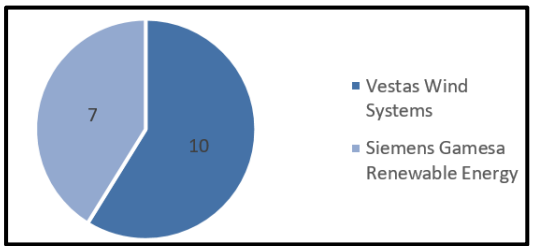

Figure 1. Key suppliers and number of wind turbines they supplied for FOWFs in Europe in 2021 (Wind Europe, 2022)

3 RESULTS AND DISCUSSION

In the present paper, six large key ports in Greece are assessed in terms of their suitability to support the development of FOWFs in the country. Those ports are the Port of Piraeus, the Port of Thessaloniki, the Port of Alexandroupoli, the Port of Patras, the Port of Volos and the Port of Heraklion. The locations of those infrastructures are shown in Figure 2. The required ports' data were collected through a combination of online mapping tools and research of publicly available datasheets from the relevant port organizations. Online mapping tools were used to obtain spatial information, such as the physical characteristic and layout of each port. This information was then cross-referenced with publicly available datasheets from the port organizations, where additional data on the port's infrastructures and operational capabilities were provided. Those data included the capacity and availability of quays, the maximum water depth, and the equipment available for cargo handling.

Following a similar approach, data were also collected for the Greek shipyards (SC3). The corresponding data were initially used to evaluate the suitability of the shipyards for the fabrication of the floating platforms. The corresponding results have illustrated that currently in Greece there are no shipyards that could accommodate the above activity or are actively operative with sufficient information regarding their infrastructure capabilities. Accordingly, the suitability of the six examined Greek ports is assessed only for SC1 and SC2. For both examined scenarios, all criteria of Table 1 are considered of equal importance, while by definition of SC1, C2.2 and C2.3 are not taken into account in the case of this scenario.

Figure 2. Location of examined ports

The assessment results for SC1 and SC2 are shown in Table 2 and 3 respectively. It can be easily concluded that that none of the examined ports meet the minimum requirements for all the suitability criteria. In the case of SC1, the ports of Patras, Volos and Heraklion satisfy only a few suitability criteria, while the ports of Piraeus, Thessaloniki and Alexandroupoli satisfy fully most of the examined criteria (8, 6 and 5 criteria respectively). The absence of sufficient water depth at the port's entrance (C1.1) or at the front of the quay (C1.2), the lack of available workspace and storage areas (C3.1) as well as of specialized equipment (C3.2) and drydock repair facilities (C3.3) were the most common drawbacks of the ports. Similar conclusions can be derived for SC2, which is more demanding compared to SC1. Specifically, only the ports of Piraeus and Thessaloniki satisfy most of the examined criteria (9 and 8 criteria respectively), while the ports of Alexandroupoli, Heraklion as well as the port of Patras fail also to satisfy C2.2 (i.e., proximity to steel production units).

Table 2. SC1 assessment results for all examined ports (P=Partially satisfied, NA=Not Available Data)

	C1.1	C1.2	C1.3	C1.4	C1.5	C2.1	C3.1	C3.2	C3.3	C3.4
Piraeus Port	√	√	NAD	√	√	√	√	X	√	√
Thessaloniki Port	√	P**	NAD	√	√	√	√	X	X	√
Alexandroupoli Port	√	P**	NAD	√	√	√	X	X	X	√
Patras Port	P*	X	NAD	√	X	X	√	X	X	√
Volos Port	P*	P**	NAD	√	X	√	X	X	X	√
Heraklion Port	√	P**	NAD	√	√	X	X	X	X	√

* Water depth < 12 m; ** Water depth < 15 m

For both examined scenarios, the Port of Patras failed to satisfy most of the suitability criteria among all the examined ports, including for example water depth both at the port's entrance and at the front of the quays (C1.1 and C1.2 respectively), adequate available storage and work space (C3.1), road and/or railway network connection (C2.1), as well as proximity to production units of the essential materials (C2.2). On the other hand, the Port of Piraeus seems to be the most suitable one among all six ports examined, since it satisfies most of the suitability criteria, and also it has the added advantage of available shipyard facilities in the case of SC2. The port of Alexandroupoli falls short in meeting the necessary suitability criteria for a FOWF development. Yet, it holds significant potential for future investments and upgrades, which is an important aspect taking into account that the adjacent sea area is considered currently favorable for the development of pilot FOWFs.

Table 3. SC2 assessment results for all examined ports (P=Partially satisfied, NA=Not Available Data)

	C1.1	C1.2	C1.3	C1.4	C1.5	C2.1	C2.2	C2.3	C3.1	C3.2	C3.3	C3.4
Piraeus Port	√	√	NAD	√	√	√	√	√	X	X	√	√
Thessaloniki Port	√	P**	NAD	√	√	√	√	√	√	X	X	√
Alexandroupoli Port	√	X	NAD	√	√	√	X	√	X	X	X	√
Patras Port	P*	X	NAD	√	X	X	X	√	X	X	X	√
Volos Port	P*	P**	NAD	√	X	√	√	√	X	X	X	√
Heraklion Port	√	P**	NAD	√	√	X	X	√	X	X	X	√

* Water depth < 12 m; ** Water depth < 15 m

4 CONCLUSIONS

The results of the present work demonstrate that none of the six examined Greek ports are capable of fully accommodating the necessary processes for the development of a FOWF in Greece. This highlights the need for significant investments and infrastructure upgrade projects, including dredging, expansion of current quays and increase of their loadbearing capacity, as well as improvement of railway connections. The supply of special handling equipment, such as heavy-lift and floating cranes, is also mandatory for the assembly of FOWTs. However, it should be noted that the acquisition and operation of such equipment could require significant investments. Furthermore, the construction of shipbuilding dry docks, as an upgrade measure, has a high cost and can change the commercial activities of a port. Choosing to build new suitable port facilities is another solution that requires a careful spatial study accounting for the interconnections with industrial centres in the mainland.

References

Aegir Insights (2022) Floating offshore wind – a global opportunity. Global Wind Energy Council.

Akbari N, Irawan CA, Jones DF, Menachof D (2017) A multi-criteria port suitability assessment for developments in the offshore wind industry. Renewable Energy 102 (Part A): 118–133. https://doi.org/10.1016/j.renene.2016.10.035

Castro-Santos L, Diaz-Casas V (2016) Floating offshore wind farms. Springer, Berlin/Heidelberg, Germany

Elkinton C, Blatiak A, Ameen H (2014) Assessment of ports for offshore wind development in the United States. Report No. 700694-USPO-R-03. Garrad Hassan America

Matha D, Brons-Illig C, Mitzlaff A, Scheffler R (2017) Fabrication and installation constraints for floating wind and implications on current infrastructure and design. Energy Procedia, 137: 299–306. https://doi.org/10.1016/j.egypro.2017.10.354

Offshore Wind Consultants (2022) Maritime's role on the road to Greece's 2 GW of offshore wind. Available at https://owcltd.com/maritimes-role-on-the-road-to-greeces-2gw-of-offshore-wind/. Accessed 26 April 2023.

Porter A, Phillips S (2016) Determining the infrastructure needs to support offshore floating wind and marine hydrokinetic facilities on the Pacific West Coast and Hawaii. Report. US Department of the Interior, Bureau of Ocean Energy Management, Pacific OCS Region, Camarillo, CA. OCS Study BOEM 2016-011

Wind Europe (2020) Ports a key enabler for the floating offshore wind sector. Technical Report. Wind Europe, Business Intelligence

Wind Europe (2022) European offshore wind farms map public, Interactive Data. Available at: https://windeurope.org/intelligence-platform/product/european-offshore-wind-farms-map-public/. Accessed 10 April 2023.

DMPCO 2023

e-Proceedings of the 2nd International Scientific Conference on Design and Management of Port Coastal and Offshore Works Thessaloniki, Greece, May 24-27 2023

Harvesting offshore wind energy for climate-neutral hydrogen production

V. Miserlis[1,*], E. Loukogeorgaki[1]

[1]Department of Civil Engineering, Aristotle University of Thessaloniki, Thessaloniki 54124, Greece
*Corresponding author: miserlisbasilis13@gmail.com

Abstract

The extensive intrusion of renewable energy sources in the total energy consumption is considered nowadays necessary for decongesting the planet from greenhouse gas emissions. For this reason, new technologies, such as climate-neutral hydrogen production, are promoted. The present paper focuses on the production of climate-neutral, green, hydrogen through water electrolysis by harvesting offshore wind energy. The proposed process deploys offshore wind turbines to produce the electricity required for the desalination of the seawater and for its subsequent electrolysis. A methodology is developed, where the produced amount of climate-neutral hydrogen and the weighted cost of its production are calculated for a given, available for this purpose, capacity of installed Offshore Wind Farms (OWFs). The proposed methodology is applied for the case of Greece by deploying floating OWFs at appropriate marine areas in the Aegean Sea. A total capacity of 2 GW is considered available for producing climate-neutral hydrogen and two portfolios of OWF projects are formed and assessed. The results illustrate that the cost for producing green hydrogen from offshore wind is high. However, the produced hydrogen could contribute to cover electricity demands in both the industrial and transport sectors in Greece.

Keywords: Climate-neutral hydrogen, Green hydrogen, Offshore wind energy, Greece

1 INTRODUCTION

In the present consumer era, where the world population and the request of social needs are on a persistent increment, there is an expanded requirement to discover vitality resources to utilize. For mitigating climate change impacts and reducing greenhouse gas emissions, it is indispensable to use environmentally friendly fuels, dodging the broad utilize of oil makers. Therefore, in the 21st century, significant efforts are made towards the development of technologies/processes that will exploit efficiently Renewable Energy Sources (RES) for energy production and at the same time will enable energy storage in periods of excess production for later use. Green hydrogen, produced from a RES by water electrolysis, could satisfy the above two targets, since as a clean energy carrier it can be used to: (a) produce energy with zero greenhouse gas emissions for various purposes and/or (b) store adequate amounts of energy. Generally speaking, hydrogen is a flexible product that can be used to achieve high temperatures through its combustion, even as a raw material in the primary sector (European Commission, 2020). Accordingly, it can be utilized in the chemical industry for producing ammonia and methanol, in the heavy industry sector for the production of steel, cement and glass, as well as for the refining of oil and the production of synthetic fuels (IRENA, 2022). For achieving the Net-Zero Emissions goal by 2050, a major upscale in green hydrogen needs is necessary, which in turn, leads to a huge increase of the required hydrogen electrolysis capacity (Ibrahim et al., 2022). Large-scale offshore wind projects could be deployed to meet these new requirements, considering that offshore wind energy will play a key role in the renewable energy sector within the forthcoming years.

Motivated by this, the present paper focuses on the production of climate-neutral, green, hydrogen through water electrolysis by harvesting the vast offshore wind energy. The proposed process involves the deployment of Offshore Wind Turbines (OWTs) to produce the electricity required for the desalination of the seawater and for its subsequent electrolysis, enabling the production of hydrogen with no greenhouse gas emissions. A three-phase methodology is developed, where the produced amount of climate-neutral hydrogen and the weighted cost of its production are calculated for a given, available for this purpose, capacity of installed Offshore Wind Farms (OWFs). The produced hydrogen is then distributed and used in the industrial and transport sectors directly as a fuel or for electricity production. The proposed methodology is applied for the case of Greece considering floating OWFs installed in the Aegean Sea.

2 METHODOLOGY

The developed in the present paper methodology consists of three phases and aims at calculating the produced amount of climate-neutral hydrogen (APH) along with the Total Levelized Cost (TLC) of its production (€/kWh) for a given capacity of OWFs. Each phase is related to a specific component of the whole hydrogen production process and includes the calculation of the corresponding levelized cost. Specifically, Phase 1 focuses on the production of electricity from OWFs, Phase 2 is related to the seawater desalination process and, finally, Phase 3 deals with the electrolysis process. Accordingly, TLC is quantified as follows:

$$TLC = LCoE + LCoDS + LCoH \quad (1)$$

In Eq. 1, $LCoE$ is the levelized cost of the energy (the electricity) produced by the OWFs, $LCoDS$ corresponds to the levelized cost of the seawater desalination process and $LCoH$ is the levelized cost of the electrolysis process for the hydrogen final production.

As for the calculation of APH (kg) the following equation is applied, where, AEP (kWh) is the annual energy produced by the OWFs and ECE (kWh/kg) is the energy per kilogram of hydrogen consumed by the electrolysis process:

$$APH = \frac{AEP}{ECE} \quad (2)$$

In the following sections, the three phases of the proposed methodology are described in detail.

2.1 Phase 1: OWFs Electricity Production and LCoE Calculation

As mentioned above, Phase 1 focuses on the production of electricity from OWFs, which will be utilized for the realization of the seawater desalination (Phase 2) and the electrolysis process (Phase 3), as well as on the calculation of the corresponding levelized cost ($LCoE$ in Eq. 1). The above are numerically realized by deploying the System Advisor Model (SAM) software (Freeman et al., 2014).

Initially, a capacity of OWFs available for climate-neutral hydrogen production is defined. Next, the marine locations of the OWFs are selected based on specific, depending upon the application area, siting criteria related to legal, technical, economic, environmental, societal, and political factors (e.g. Spyridonidou et al., 2020). Subsequently, all data required as input in the SAM software are collected and/or defined for each one of the examined locations. Those data correspond to the wind velocity, the OWFs' characteristics, i.e., number and layout of OWTs, WT capacity and support structure type, OWF's losses, CAPEX and OPEX values. The losses result from various sources and correspond to wake, availability, electrical, turbine performance, electrical, environment and curtailment/operational strategies losses (Clifton et al., 2016; Lee and Fields, 2021). Based on the above, SAM software calculates for each marine site the AEP, the capacity factor (%) and, finally, the $LCoE$, using Eq. 3:

$$LCoE = \frac{CAPEX + OPEX}{AEP} \quad (3)$$

2.2 Phase 2: Seawater Desalination and LCoDS Calculation

Phase 2 of the proposed methodology is related to the seawater desalination process and includes the calculation of the required for the electrolysis desalinated water as well as the corresponding levelized cost ($LCoDS$ in Eq. 1). To achieve zero climate footprint, part of the electricity produced from the OWFs is used for the desalination process, which is realized in the present work by deploying the Mechanical Vapor Compression (MVC) method (Gude et al., 2010). MVC is a thermal desalination technique, where saltwater is heated to the boiling point to induce evaporation by producing steam, and after the steam is condensed, salt-free water is created. This technology is considered more suitable at offshore areas, since it responds well to variations in wind power, while, furthermore, it requires low maintenance over its lifetime (Kalogirou, 2005). As for $LCoDS$, this quantity is defined as the ratio of the Total Desalination Cost (TDC) to the energy carried by the produced hydrogen (EPH), namely:

$$LCoDS = \frac{TDC}{EPH} \quad (4)$$

For finalizing the desalination process with the MVC method, 10 kWh/m^3 of water are approximately consumed. Considering that the corresponding TDC equals to 0.002 €/kg and that according to the water electrolysis reaction, the production of 1 kg of H_2 requires 10 kg of H_2O, Eq. 4 is modified as follows:

$$LCoDS = \frac{0.002*(10*APH)}{EPH} \quad (5)$$

2.3 Phase 3: Electrolysis Process and LCoH Calculation

Phase 3 deals with the electrolysis process, where the desalinated water enters the electrolysis cell and with the action of electricity is broken down into its basics elements, hydrogen and oxygen (Eq. 6):

$$2H_2O + Electricity \rightarrow 2H_2 + O_2 \quad (6)$$

In the preset work, the method of Proton Exchange Membrane ELectrolysis ($PEMEL$) (Li et al., 2021) has be chosen to implement the electrolysis process. $PEMEL$ responds to the intermittent form of the wind energy and also requires low maintenance during its operation, making it suitable for offshore usage. The electrolysis process begins with the intake of desalinated water into the electrolysis cell. Then, the water comes into contact with the anode and breaks down into oxygen, protons and electrons. The protons, after passing through the membrane, enter the side where the cathode is located, and join the electrons, transported by an external circuit, to produce the desired hydrogen.

Regarding the levelized cost of the electrolysis process, $LCoH$ is defined as the ratio of the Total Electrolysis Cost (TEC) to the energy carried by the produced hydrogen (EPH), namely:

$$LCoH = \frac{TEC}{EPH} \quad (7)$$

For implementing the electrolysis process with the $PEMEL$ method, 4.4 kWh/m^3 of H_2 are required, while the corresponding TEC is approximately equal to 4.77 €/kg. Taking into account that hydrogen as an energy carrier contains 33.333 kWh/kg (LBS, 2022), the application of Eq. 7 leads to an $LCoH$ value approximately equal to 0.1431 €/kWh. Finally, considering that the density of hydrogen is equal to 0.082 kg/m^3 the production of 1 kg of H_2 requires 53.328 kWh.

3 RESULTS AND DISUSSION

The methodology described above is applied for the case of Greece by deploying floating OWFs at appropriate marine areas in the Aegean Sea. Those areas (Figure 1) have been selected based on Spyridonidou et al. (2020) focusing on siting criteria related to the average water depth and the wind speed 50 m above the mean water level. Specifically, seven marine sites of total area ~390 km^2 are taken into account with average wind speed varying between 6 m/s and 8 m/s, average water depth of 250 m and average distance from shore varying from 20 km up to 40 km.

Each OWF consists of floating OWTs of 8 MW rated capacity with a semi-submersible floater. The CAPEX and OPEX for these types of OWTs have been calculated equal to 5104.85 €/kW and 112.572 €/kW respectively according to Stehly and Duffy (2020), after applying a correction factor (Ng and Ran, 2016) based on the water depth at the examined locations and the corresponding distance from shore. OWF projects of capacity 48 GW (OWF1 with 6 OWTs), 56 GW (OWF2 with 7 OWTs), 96 GW (OWF3 with 12 OWTS) and 104 GW (OWF4 with 13 OWTs) have been taken into account. By applying the SAM software, the average AEP per OWT has been calculated equal to 18.7 GWh (Areas 1 and 2), 29.9 GWh (Areas 3, 4 and 5), 21.8 GWh (Area 6) and 23.6 GWh (Area 7). The capacity factor and the $LCoE$ for each examined OWF project per location have been estimated as follows: 26.7% and 0.1639 €/kWh (Area 1), 26.7% and 0.1682 €/kWh (Area 2), 42.8% and 0.1004 €/kWh (Area 3), 42.8% and 0.1031 €/kWh (Area 4), 42.8% and 0.1010 €/kWh (Area 5) 31.1% and 0.1382 €/kWh (Area 6), 33.7% and 0.1300 €/kWh (Area 7).

For producing climate-neutral hydrogen a total capacity of 2 GW has been considered available. OWF projects of 2 GW are distributed to: (a) all the examined marine locations, with maximum coverage area of 40% per location (Portfolio A) and (b) specific marine areas in terms of reducing the $LCoE$, with maximum coverage area of 75% per location (Portfolio B). The characteristics of the examined portfolios are shown in Table 1.

Figure 1. Examined marine areas in Greece for floating OWFs installation

Table 1. Characteristics of the two examined portfolios (the numbers in parenthesis correspond to Portfolio B)

	Area 1	Area 2	Area 3	Area 4	Area 5	Area 6	Area 7
OWF1		1					
OWF2	3		(4)	(1)		1	2
OWF3			3 (3)	3 (3)			
OWF4	1		3 (6)	4 (4)	1 (1)	1	
Total Capacity (MW)	272	48	600 (1136)	704 (760)	104 (104)	160	112
AEP(GWh)	636.2	112.3	2249.9 (4259.9)	2639.9 (2849.9)	389.9 (389.9)	436.1	330.3

In Table 2, the final results for the two examined portfolios are cited, assuming that only half of the AEP will be used for hydrogen production. All quantities have been derived taking into account the losses in all three Phases' processes. The losses of Phases 1 and 2 are quite small, contrary to Phase 3, where the corresponding losses are ~62%. It is also noted that the conversion of hydrogen into electricity has been calculated considering an efficiency of approximately 65% (IEA, 2019).

Table 2. Main results for Portfolio A and B

Quantity	Portfolio A	Portfolio B
OWFs produced electricity (TWh)	3.4	3.8
Produced hydrogen, APH (tn)	63707.4	70317.3
Energy carried by hydrogen (TWh)	2.124	2.344
Available electricity from hydrogen conversion considering losses (TWh)	1.381	1.524
$LCoE$ (€/kWh)	0.112	0.101
$LCoDS$ (€/kWh)	0.001	0.001
$LCoH$ (€/kWh)	0.143	0.143
TLC (€/kWh)	0.256	0.245

Finally, taking into account the 2030 national targets set in the Greek Long-term strategy for 2050 (Greek Ministry of Environment and Energy, 2020), we highlight in Table 3 the electricity demands that can be covered in the Greek industrial and transport sectors by the hydrogen produced in both portfolio cases. The corresponding percentages have been derived assuming that the amount of hydrogen produced is shared equally between the two sectors.

Table 3. Electricity demand coverage by Portfolios A and B in the Greek industrial and transport sector

Quantity	Industry	Transport
Electricity demand (TWh)	13.258	1.395
Portfolio A (%)	5.21	49.5
Portfolio B (%)	5.75	54.62

4 CONCLUSIONS

The results of the present work indicate that there are quite large losses when converting electricity into hydrogen, and backwards, while the cost of producing green hydrogen from offshore wind is high. The electrolysis process affects the price of losses and the final cost of producing climate-neutral hydrogen, since a significant amount of energy is consumed to achieve this process. So, there are still challenges that have to be efficiently addressed to come up with cost-efficient hydrogen production solutions. The exploitation of the hydrogen's storage ability may be considered as a driver for "balancing" these challenges. By 2030, the electricity demand in the Greek transport sector could be covered by ~50% by both examined portfolios, while the corresponding percentage is a bit low in the case of the Greek industrial sector. However, significant efforts towards the electrification of both sectors is required.

References

Clifton A, Smith A, Fields M (2016) Wind plant preconstruction energy estimates: Current practice and opportunities. Technical Report, National Renewable Energy Laboratory, USA.

European Commission (2020) A hydrogen strategy for a climate-neutral Europe, COM/2020/301. EU, Brussels.

Freeman J, Jorgenson J, Gilman P, Ferguson T (2014) Reference manual for the System Advisor Model's wind power performance model. Technical Report, National Renewable Energy Laboratory, USA.

Greek Ministry of Environment and Energy (2020) Long-term strategy for 2050. Available via https://ec.europa.eu/clima/sites/lts/lts_gr_el.pdf. Accessed 22 April 2023.

Gude V, Nirmalakhandan N, Deng S (2010) Renewable and sustainable approaches for desalination. Renewable Sustainable Energy Rev 14(9): 2641–2654. https://doi.org/10.1016/j.rser.2010.06.008.

Ibrahim OS, Singlitico A, Proskovics R, McDonagh S, Desmond C, Murphy JD (2022) Dedicated large-scale floating offshore wind to hydrogen: Assessing design variables in proposed typologies. Renewable Sustainable Energy Rev 160: 112310. https://doi.org/10.1016/j.rser.2022.112310.

IEA (2019) The future of hydrogen for G20. Seizing today's opportunities. Report prepared by the International Energy Association for the G20, Japan.

IRENA (2022) Green hydrogen for industry: A guide to policy making. International Renewable Energy Agency, Abu Dhabi.

Kalogirou S (2005) Seawater desalination using renewable energy sources. Prog Energy Combust Sci 31(3): 242–281. https://doi.org/10.1016/j.pecs.2005.03.001.

Lee J, Fields JM (2021) An overview of wind-energy-production prediction bias, losses and uncertainties. Wind Energ Sci 6: 311–365. https://doi.org/10.5194/wes-6-311-2021.

Li J, Liu W, Qi W (2021) Hydrogen production technology by electrolysis of water and its application in renewable energy consumption. E3S Web of Conferences 236: 02001. https://doi.org/10.1051/e3sconf/202123602001.

Ludwig-Bölkow-Systemtechnik GmbH (LBS) (2022) The Hydrogen and Fuel Cell Information System: Hydrogen Data. Available at: http://www.h2data.de/. Accessed 22 April 2023.

Ng C, Ran L (2016). Offshore wind farms: Technologies, design and operation. Woodhead Publishing.

Spyridonidou S, Vagiona D, Loukogeorgaki E (2020) Strategic planning of offshore wind farms in Greece. Sustainability 12(3): 905. https://doi.org/10.3390/su12030905.

Stehly T, Duffy P (2020) 2020 cost of wind energy review. Technical Report, National Renewable Energy Laboratory, USA.

DMPCO 2023

e-Proceedings of the 2nd International Scientific Conference on Design and Management of Port Coastal and Offshore Works Thessaloniki, Greece, May 24-27 2023

Investigatıng the potential of new Marine Protected Areas (MPAs) in the Greek marine territory

N. Kartsakli[1*], M.P. Papadopoulou[2]

[1]Spatial Planning and Development Engineer, Thessaloniki, Greece
[2]Laboratory of Physical Geography & Environmental Impacts, School of Rural, Surveying and Geoinformatics Engineering, National Technical University of Athens, 15780 Athens, Greece
*Corresponding author: nikikartsakli95@gmail.com

Abstract

In 2021, the PM of Greece addressing the general assembly of IUCN in Marseille stated that Greece will not allow fishing in 10% of its seas, with the aim of better protecting and stimulating the ecosystems of the Mediterranean, which has been affected by overfishing. In this paper, an analysis based on this commitment is developed to identify new Marine Protected Areas (MPAs) within the Greek marine territory. The purpose of the analysis is mainly to designate new MPAs by developing alternative scenarios (conservative, realistic and optimistic) and to analyze how geopolitical conditions in the Easter Mediterranean basin may contribute to the determination of them. Essentially, an attempt was made to strengthen the willingness of Greece to establish the 12nm border line at the sea through certain geopolitical hypotheses related to the designation of new MPAs. To achieve this objective, an analysis of the fundamental issues - associated with Exclusive Economic Zones (EEZs), continental shelf, the current treaties concerning EEZs between Greece and foreign states involved and the current situation with the foreign states with which no final agreement has been reached - is performed, pointing out the importance of maritime spatial planning. Then, the current environmental legislation for the protection of the marine environment is analyzed and a prioritization of endangered species is carried out. Based on this preliminary analysis, twenty eight marine fauna species, which are classified as species under protection, were identified and three scenarios of MPA delineation were developed considering environmental and geopolitical criteria. The analysis showed that even with the most conservative scenario, the 30% goal of MPAs within the Greek territorial area could be achieved, whereas the goal is overachieved for the realistic (33.69%) and the optimistic (87.43%) scenarios. There are important maritime areas in all three scenarios which are of particular geopolitical importance, because they are considered to be grey zones from Turkey. By delimiting these areas as MPAs, Greece's sovereignty over its territorial waters is enriched and the existence of a continental shelf is recognized.

Keywords Marine Biodiversity, Marine Spatial Planning, Aegean and Ionian Seas, Geopolitics, Demarcation.

1 PLANNING ACTIVITIES IN MARINE AREAS – MARINE SPATIAL PLANNING (MSP)

In recent years, there has been considerable debate about the ongoing geopolitical and economic development in the Eastern Mediterranean. Efforts are being made by the Greek Administration to extend its marine territorial zone to 12 nautical miles (nm) and to designate country's EEZ with neighboring states. Also, discussions are taking place on how Greek Administration can exploit E.E.Z for the unitization of energy resources while protecting its unique marine environment. There are numerous criteria (social, economic, environmental, geopolitical, etc.) upon which a Member State (MS) within EU may decide whether to allow the establishment of economic activities in the marine space and at the same time to ensure the protection of the marine environment. The European Union (EU) defines marine spatial planning as *"the process whereby public authorities analyse and make spatial and temporal allocations of human activities in marine areas to achieve ecological, economic and social objectives"* (EC, 2010). The MSP defines the appropriate areas, taking into account all criteria, for the development of economic activities in the marine area and also acts as a tool for the delimitation of EEZ in the States where there is an MSP. According to Reuchlin-Hugenholtz and McKenzie, (2015) a Marine Protected Area (MPA) is defined as an area dedicated for the protection of marine habitats, fauna and flora species and their functions. These functions are critical, because they significantly contribute to the restoration and recovery of natural environment affecting not only environmental but also economic,

social and cultural aspects of people's life. In this context there is the direction of proper management and demarcation of MPAs within the marine territorial zone of a State aiming at the protection of marine habitats, marine biodiversity species and their functions that contribute to the restoration and replenishment of the marine environment. Greece, following the decision of the EU to increase the percentage of Greek MPAs up to 30% by 2030, wishes to define new MPAs, in order to reach 30% from 19.6% of the country's marine area.

2 METHODOLOGY FOR THE DESIGNATION OF NEW MARINE PROTECTED AREAS

The inclusion of new marine sites must be coherent and representative within the network of MPAs and characterised by ecosystem biodiversity. According to Article 3 of Directive 92/43/EEC, a preliminary assessment of the sites' importance for each habitat type and species listed in Annex I and II respectively is carried out at national level. The site assessment criteria for each fauna species are (EC, 1992):

1. The size and population density of the species found in the area in relation to the national population of the species concerned.
2. The degree of conservation of the natural habitat features for the species concerned and the capacity for restoration.
3. The degree of isolation of the population found in the area in question in relation to its overall natural distribution area.
4. The evaluation of the site based on the three previous criteria and other site elements that vary from species to species and include human activities in the areas that affect the conservation of the species.

The selection of sites considers the different phases of the life cycle of the protected species (breeding period, migration period, wintering period, etc.). Each MS then classifies the sites in a national list as sites of Community importance and assess them according to the following criteria (EC, 2007):

1. The relative value of each site at national level.
2. The geographical location of each site in relation to species migration routes and its potential to be part of an ecosystem on either side of an internal border.
3. The total area of the location.
4. The number of habitats and species identified.
5. The ecological value of the site for the geographical areas and/or the total terrain of which the site is characterized and their combination.

2.1 Assessment of marine species in Greece

According to the International Union for Conservation of Nature (IUNC), the Important Marine Mammal Area (IMMA) and the 4th national report on the implementation of Directive 92/43/EEC Art. 12 and 17 for the period 2013 - 2018, as submitted by Greece (Eionet, 2019), there are 28 species of marine fauna of Community interest for which field data are available. In Table 1, the categorization and ranking of marine fauna species is summarized.

2.2 Scenarios for the demarcation of new marine protected areas

The development of the proposed scenarios was based on the following assumptions:

- The implementation of the scenarios for the demarcation of new MPAs was based on a limit of 12nm of the Greek marine territorial zone, as defined by the international law of the sea and the Seville Charter.
- The proposed scenarios were based on the hierarchy of marine fauna species (Table 1).
- Only the criterion of biodiversity of marine fauna species was taken into account.

Scenario 1 - Conservative scenario

In the conservative scenario, the common geographic locations of species from the 1st to the 5th ranking category are depicted. In this scenario, species in 6th category were not considered, due to insufficient data available to characterize risk levels. The common geographic locations of species in the 1st, 2nd, 3rd and 5th ranking categories were first identified in pairs and trios. In the 4th ranking category, no common geographical locations were identified, because it is only the species Pseudorca crassidens that exists there. The next step was to find the common geographical crossings by four, five, six and seven species

of the 1st category respectively. Finally, in the conservative scenario, the proposed MPAs were identified as the transects of the spatial range of at least 3 species at a time (Figure 1).

Table 1: Proposed ranking of marine fauna species (Eionet, 2019)

	Code Natura 2000	Species name	IUNC classification	Directive 92/43/EEC - Barcelona Protocol (Annex II & III)	Ranking
Invertebrates					
1	1001	Corallium rubrum	Endangered	Annex III	2
2	1008	Centrostephanus longispinus	Data Deficient	Annex II	6
3	1027	Lithophaga lithophaga	Data Deficient	Annex II	6
4	1028	Pinna nobilis	Critically Endangered	Annex II	1
5	1090	Scyllarides latus	Data Deficient	Annex II	6
Reptiles					
6	1223	Dermochelys coriacea	Vulnerable	Annex II	3
7	1224	Caretta caretta	Least Concern	Annex II	5
8	1227	Chelonia mydas	Endangered	Annex II	2
Fish					
9	1095	Petromyzon marinus	Least Concern	Annex III	5
10	1100	Acipenser naccarii	Critically Endangered	Annex II	1
11	1101	Acipenser sturio	Critically Endangered	Annex II	1
12	1103	Alosa fallax	Least Concern	Annex III	5
13	1152	Aphanius fasciatus	Least Concern	Annex II	5
14	2488	Acipenser stellatus	Critically Endangered	Annex II	1
Mammals					
15	1345	Megaptera novaeangliae	Least Concern	Annex II	5
16	1349	Tursiops truncatus	Vulnerable	Annex II	3
17	1350	Delphinus delphis	Endangered	Annex II	2
18	1351	Phocoena phocoena	Endangered	Annex II	2
19	1366	Monachus monachus	Critically Endangered	Annex II	1
20	2028	Pseudorca crassidens	Near Threatened	Annex II	4
21	2030	Grampus griseus	Vulnerable	Annex II	3
22	2034	Stenella coeruleoalba	Vulnerable	Annex II	3
23	2035	Ziphius cavirostris	Least Concern	Annex II	5
24	2618	Balaenoptera acutorostrata	Least Concern	Annex II	5
25	2621	Balaenoptera physalus	Vulnerable	Annex II	3
26	5031	Physeter catodon	Endangered	Annex II	2
Birds					
27	A464	Puffinus yelkouan	Vulnerable	Annex II	3
28	A392	Phalacrocorax Aristotelis Desmarestii	Least Concern)	Annex II	5

Scenario 2 - Realistic scenario

In the realistic scenario, the localization areas of four (e.g. Pinna nobilis, Acipenser naccarii, Acipenser sturio and Acipenser stellatus) out of the five species (1st ranking category) were considered and no other species of the other ranking categories was taken into account, because the purpose of the scenario is to define areas where 'Critically Endangered' species are found and for which protection areas must be

strictly defined. Furthermore, Monachus monachus was not included in this scenario, since it is found in a much larger area compared to the other species, which exceeds 50% of the national waters (Figure 2).

Scenario 3 - Optimistic scenario

In the optimistic scenario the localization areas of the five species of the 1st ranking category were taken into account, while the species of the other categories were not. In the optimistic scenario (Figure 3) a large, unified buffer that covers the whole South Aegean Region is proposed. This buffer together with the existing protected areas creates a large protection and exclusion zone. The outcomes of the analysis showed that, even with the most conservative scenario, the 30% goal could be achieved. However, the goal is overachieved for the realistic (33.69%) and the optimistic (87.43%) scenarios (Figure 1). In addition, the optimistic scenario recommends a strict protection zone covering more than 50% of the 12nm of Greece's territorial zone (Table 2).

Figure 1: Conservative scenario of the proposed MPAs within 12nm

Figure 2: Realistic scenario of the proposed MPAs within 12 nm

Figure 3: Optimistic scenario of the proposed MPAs within 12nm

3 DISCUSSION - GEOPOLITICAL ASPECTS

The proposed scenarios were based on three main geopolitical assumptions Greece has signed: a) the Montego Bay Convention on the Law of the Sea in 1982, that has been harmonized within the national legal framework stating the right to extent its marine territorial zone up to 12nm, b) the Law of the Sea Convention that has been signed by 163 countries and it is taken as part of customary law stating that all islands are entitled to a coastline, contiguous zone, continental shelf and EEZ and therefore c) the Greek islands are also entitled to it. Initially, in the conservative scenario, marine space, where species from the 1st up to the 5th ranking category, are located, was mapped and their respective total area within 6nm marine territorial zone covers 11,255 km^2 and 9.82%. The total area of this scenario is exactly the same as that of the conservative scenario, where the territorial sea border line is in 12nm. From a geopolitical aspect, new MPAs are proposed in this scenario that include marine areas southeast of Rhodes, Symi, the entire eastern sea side of Kos and the northern sea part of Samos, where there is a dispute from Turkey about the national sovereignty of Greece (Figure 4a).

Table 2. MPAs coverage based on the examined scenarios

		Greek E.E.Z (km^2)	Greek Territorial Zone 12nm	Greek Territorial Zone 6nm
	Area (km^2)	*482.910*	*184.446*	*114.520*
Conservative	**11.255**	**2,33%**	**6,10%**	**9,82%**
Realistic	**22.924**	**4,75**	**12,43%**	**20,01%**
Optimistic	**122.052**	**25,27%**	**66,17%**	**82,31%**
Existing Natura 2000	39.214	8,12%	21,26%	19,6%

Subsequently, in the realistic scenario, the respective areas of 4 out of 5 species (1st ranking category) were considered and their areas were consolidated. The respective total area for the realistic scenario is 22,919 km^2 covering 20.01% of the 6nm marine territorial zone. It is important to note that in this scenario new MPAs are proposed in areas south-east of Lesvos, north and west of Chios, north and east of Samos, in the extension of the existing protected areas west of Leros, east, north, and south of Kos, Symi, Kastellorizo and the islet of Roe (Figure 4b). In this way, the extension of the 12 nm secured the Greek national sovereignty in these areas and the right to delimit the EEZ is validated based on the Seville Charter, the Convention on the Law of the Sea and European environmental legislation. Also, the Turkish-Libyan Memorandum, which did not consider the Greek national sovereignty within the aforementioned areas, is annulled. Finally, in the optimistic scenario, areas with respect to 1st ranking species were considered and also the respective total area within the 6nm zone is 94.260 km^2 covering 82.31% of the Aegean Sea has been taken into account. It is important to note that according to ~~in~~ this scenario (Figure 4c) the proposed protected area creates a large buffer zone peripheral to the islands and islets (the area of the Dodecanese cluster, southeast of Lesvos, all of Chios, Kastellorizo and the islet of Roe) that the Turkish side is lately challenging Greek sovereignty. All three scenarios contain maritime areas of geopolitical importance.

a) b) c)

Figure 4. Proposed MPAs within 6nm Greek Marine Territory - conservative (a), realistic (b) and optimistic (c) scenarios

4 CONCLUSIONS

In recent years, there has been a continuous discussion concerning the marine environment in the Eastern Mediterranean. This paper focuses on the effort to delineate new MPAs. Twenty eight marine fauna species were identified, which are classified as species under protection based on IUCN classification, and three scenarios of MPA delineation were developed. Based on the analysis, the conservative and realistic scenarios are close to the target set from the Greek administration to declare 30% of the marine territory as MPAs by 2030. Also, the optimistic scenario creates a strict protection zone covering more than 50% of the 12nm zone. There are important maritime areas in all three scenarios which are of particular geopolitical importance, because they are considered grey zones from Turkey. By delimiting these areas as MPAs, Greece's sovereignty over its territorial waters is enriched and the existence of a continental shelf is recognized. In conclusion, the strengthening of the extension of the 12 nm works as a tool of the proposed delimitation of new marine protected areas, following the current European environmental and legal framework, and vice versa, meaning that the proposed delimitation of the new MPAs is considered as a geopolitical tool to strengthen the extension of the 12 nautical miles.

References

Eionet (2019) Birds Directive Article 12 2019 GR – Redelivery report 2013-2018, Eionet. Available at: https://cdr.eionet.europa.eu/gr/eu/art12/envxz8njg/ (Access date: 20 March 2022).

EC (1992) Directive 92/43/EEC on the Conservation of Natural Habitats and of Wild Fauna and Flora, Official Journal of the European Union. Available at: https://eur-lex.europa.eu/legal-content/EN/TXT/PDF/?uri=CELEX:31992L0043

EC (2007) Guidelines for the establishment of the Natura 2000 network in the marine environment. Implementation of the Habitats and Wild Birds Directives. Available at: https://ec.europa.eu/environment/nature/natura2000/marine/docs/marine_guidelines.pdf

EC (2010) Communication from the Commission to the European Parliament, -Maritime Spatial Planning in the EU - Achievements and Future Developments. Available at: https://eur-lex.europa.eu/legal-content/EL/TXT/PDF/?uri=CELEX:52010DC0771&from=EN

Reuchlin-Hugenholtz, E., McKenzie, E. 2015. Marine protected areas: Smart investments in ocean health. WWF, Gland, Switzerland. Available at: https://files.worldwildlife.org/wwfcmsprod/files/Publication/file/8u8uxvczvw_Smart_Investments_in_Ocean_Health.pdf

DMPCO 2023

e-Proceedings of the 2nd International Scientific Conference on Design and Management of Port Coastal and Offshore Works Thessaloniki, Greece, May 24-27 2023

Assessing coastal and port vulnerability through a single composite index to support MSP

V.I. Chalastani[1], M.Koulouri[1], E.Feloni[2] and V.K. Tsoukala[1]

[1] Laboratory of Harbour Works, Department of Water Resources and Environmental Engineering, School of Civil Engineering, National Technical University of Athens (NTUA), Zografou 15780, Greece.
[2] Laboratory of Hydrology and Water Resources Management, Department of Water Resources and Environmental Engineering, School of Civil Engineering, National Technical University of Athens (NTUA), Zografou 15780, Greece.
*Corresponding author: vanesachala@hotmail.com

Abstract

Coastal zone constitutes a narrow, yet vital part of the world since it hosts numerous human activities, settlements, and critical infrastructure such as seaports. Coastal areas are themselves vulnerable areas due to their nature and location and are further threatened by climate change impacts. Indicator-based vulnerability assessment methods, mainly through the development of indices, have been widely used to estimate both coastal vulnerability (CVI) and seaport vulnerability (PVI) in a sectorial manner. However, assessing vulnerability of a system requires holistic approaches that take into account inherent interactions. For this reason, a 6-step framework is proposed, which considers the multiple activities and infrastructure of coastal areas, along with their interdependencies and climate change. For this reason, a composite vulnerability index (VIcomp) is developed by incorporating both coastal and seaport vulnerability indicators divided into four sub-indices: the physical, the environmental, the technical and the socioeconomic ones. The indicators are quantified and scored according to a predefined scale to assess the current and the future vulnerability by taking into account climate projections and future strategic planning. The proposed framework and index are particularly useful to stakeholders who need to prioritise interventions to reduce coastal areas' vulnerability, while serving as a valuable input for climate-smart marine spatial plans that incorporate land-sea interactions.

Keywords Coastal vulnerability, Port vulnerability, Marine spatial planning, Climate change.

1 INTRODUCTION

Coastal areas lie at the land-sea interface where heterogeneous social settlements can be found, from coastal megalopolises to low-density areas with scattered communities. These areas host not only more than one-third of the total human population, but also a variety of human activities and crucial infrastructure, including ports. The growing human activities in the sea have generated competing demands for ocean marine space, which challenge established institutional governance arrangements. As a result, marine spatial planning (MSP) emerged as a policy framework to optimize marine space allocation, avoid negative interactions, improve synergies, and advance toward a sustainable ocean economy, as reflected in explicit mandates for MSP, such as the EU MSP Directive (2014/89) (Chalastani et al. 2020). Despite the fact that MSP usually focuses on large marine areas (from coastal to open-ocean regions), whereas Integrated Coastal Zone Management (ICZM) tends to be more focused on the coastal zone (Kerr et al. 2014), there is an increased interest in the incorporation of land-sea interactions into the MSP process. The reason could be twofold: i) marine spatial plans are mandatory for the European countries with marine space within their boundaries and ii) coastal zone is a narrow, yet vital part of the ocean, where numerous human activities are undertaken and affect the entire marine space. However, both coastal areas themselves, coastal communities and critical port infrastructure are threatened by climate change and its associated impacts. Coastal zone has been identified as a vulnerable area, affected by sea level rise, storm surges and coastal flooding related to climate change. Therefore, assessing vulnerability of the coastal zone in a holistic, rather than sectorial manner, seems to be the first input for MSP initiatives seeking to minimize climate impacts and improve coastal resilience.

2 ASSESSING VULNERABILITY OF THE COASTAL ZONE: DEFINING THE GAPS

Vulnerability definitions are numerous and mainly express the risks to different elements of natural and man-made environment by various sources, among them climate change (Kontogianni et al. 2019). When comparing vulnerability of multiple disparate systems, indicator-based vulnerability assessment methods can yield standardized metrics, allowing for both the proper identification of areas or systems of concern (McIntosh and Becker 2019) and the development of targeted adaptation interventions.

Traditionally, the vulnerability of the coastal zone is assessed through the Coastal Vulnerability Index (CVI), calculated via Equation (1) (Gornitz et al. 1991) and is mainly focused on physical, geomorphological, and geometrical parameters of the area.

$$CVI = \sqrt{\frac{(a*b*c*d*e*f)}{6}} \qquad (1)$$

where a represents geomorphology, b is the coastal slope, c refers to sea level change, d represents the shoreline displacement, e is the significant wave height and f shows the tidal range. Equation (1) has been used in various forms to assess coastal vulnerability and efforts have been made to incorporate additional elements of the coastal zone besides its physical and geomorphological characteristics. In particular, there are studies that have considered technical (e.g., Kantamaneni et al., 2019) and socio-economic factors (e.g., Ružić et al., 2019), or climate change effects (e.g., Vandarakis et al. 2021). Over the years, peer-reviewed publications related to CVI have been increased in the Scopus database (Figure 1a). Particularly for the years 2011-2015, only 45 out of 281 publications undertake a CVI application, indicating that there is a strong need for developing a robust methodological framework for such assessments before applying it to case studies.

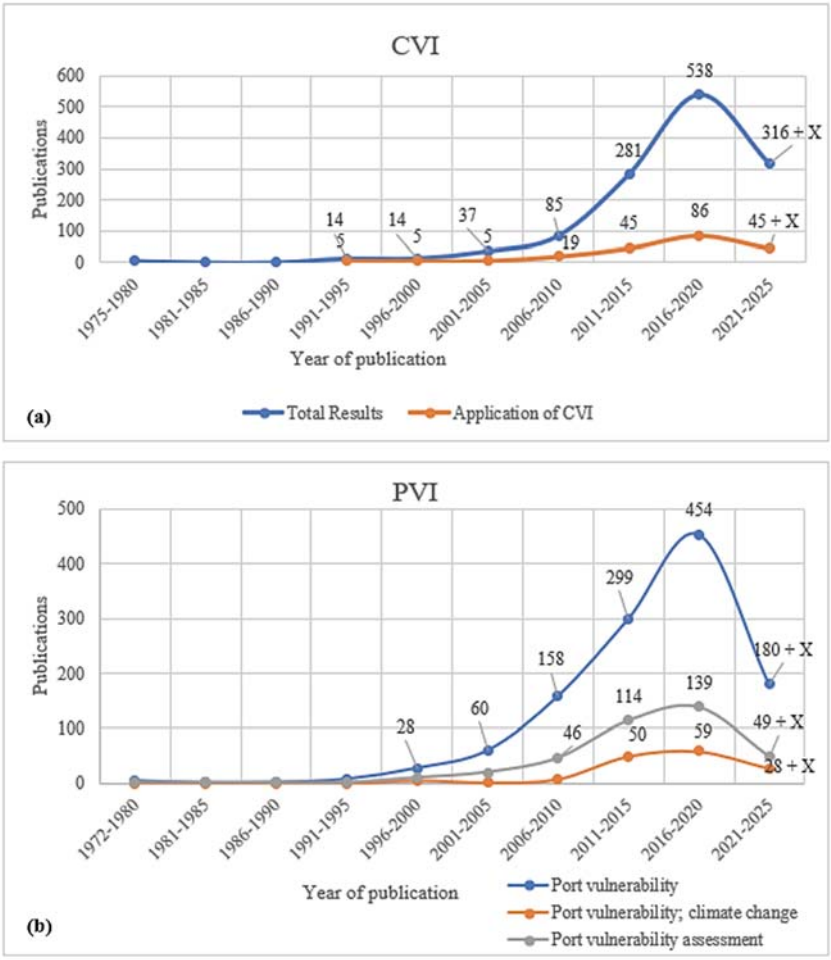

Figure 1. Growth rate of publications based on Scopus results (cut-off date 08/2022) for: **(a)** CVI, **(b)** PVI

On the other hand, port infrastructure and its functions are studied as a separate system through Port Vulnerability Index (PVI). These indices range from assessing vulnerability of large seaports (e.g., McIntosh and Becker 2019) to small fishing shelters (e.g., Kontogianni et al. 2019). They are mostly focused on climatic, technical and operational indicators (e.g., air pollution days, harbour size, containership capacity; McIntosh and Becker 2019), while trying to capture the three (3) dimensions of vulnerability within their contents: exposure, sensitivity and adaptive capacity, since vulnerability is *"a function of the character, magnitude and rate of climate change and variation to which a system is exposed, its sensitivity and its adaptive capacity"* (IPCC 2001). Most of the indicators and indices used so far incorporate hindcast data to assess current vulnerability. Explicit climate projections are rarely used and mostly to inform risk assessments, rather than vulnerability ones (e.g., Izaguirre at al. 2021). Publications related to port vulnerability keep increasing over the years (Figure 1b). However, for the years 2016-2020 only 1/3 of the publications actually assess port vulnerability, while only half of these incorporate climate change (Figure 1b).

For both coastal and port vulnerability assessments, indices that include various indicators are used. However, few assessments analyse the interactions between the coastal system and critical port infrastructure, let alone the communities and the other human activities of the coastal zone, such as fisheries and aquaculture (e.g., Koromilas et al., 2019; Tsaimou et al., 2022). Furthermore, the parameters considered to develop these indices are considered as equally important despite that, in reality, different vulnerability settings should be studied as a compiled record of differently weighted factors. Integrated vulnerability approaches and composite indices based on multi-criteria decision approaches and weightening methods could be used to inform MSP scenarios and visioning processes.

4 COASTAL AND PORT VULNERABILITY ASSESSMENT FRAMEWORK FOR MSP

To address the sectorial approach of vulnerability assessment in the coastal zone, we propose a 6-step framework (Figure 2) that considers the multiple activities and infrastructure of coastal areas, along with their interdependencies and climate change, to inform MSP. The proposed steps are set as follows:

1. Selecting the area of interest; definition of geographical boundaries.
2. Mapping of existing conditions; identification of physical conditions, existing port infrastructure, human population dynamics, human activities, and interdependencies.
3. Developing a comprehensive and composite vulnerability index (VIcomp); selection of appropriate indicators that describe potential vulnerability of natural assets, ports and other critical infrastructure, humans, and human activities in the coastal zone.
4. Evaluating indicators to determine current vulnerability; data collection that allows for indicators' quantification and assignment of values to each indicator selected.
5. Considering climate change and its impacts; re-evaluation of indicators based on climate change projections, when available, or on perception of the climate change impacts on assets.
6. Using vulnerability assessment to support MSP; comparison of current and future vulnerability index and identification of the most vulnerable assets/areas to inform a dynamic, climate-related MSP process.

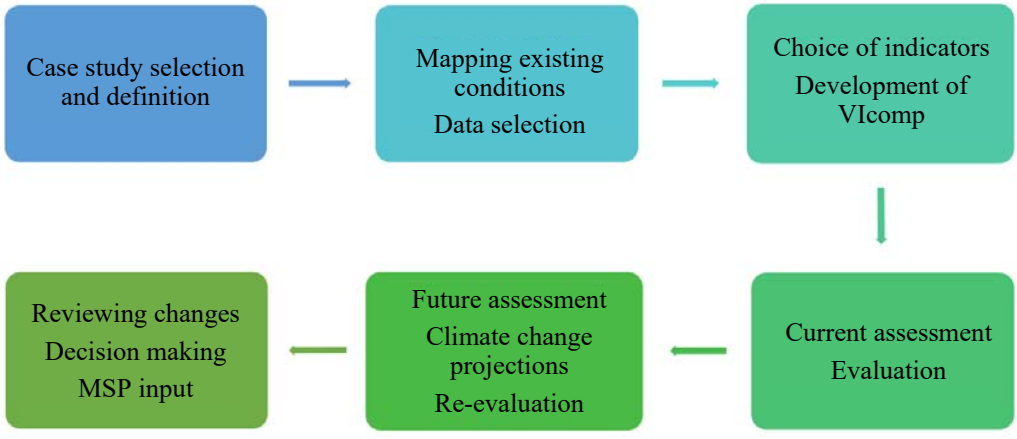

Figure 2. 6-step framework to assess vulnerability of the coastal zone in a holistic manner.

5 VIcomp INDEX

The composite vulnerability index developed in the context of this research work encompasses indicative indicators divided in four (4) different sub-indices, namely the physical, the environmental, the technical and the socioeconomic index (Figure 3). The purpose is to easily categorise indicators, but also to identify the most vulnerable parameters and allow for targeted interventions that reduce vulnerability. The indicators are quantified, based on measurements or robust expert judgement, in a scale one (1) to five (5) to showcase current and future vulnerability. To assess future vulnerability, climate change projections are needed for a series of indicators (e.g., temperature, significant wave height), while strategic planning and socioeconomic projections are important for indicators such as land uses, traffic, working patterns etc. (Figure 3). The results are particularly important for MSP efforts, since they create valuable input for climate-smart marine spatial plans that take into account land-sea interactions by considering the full spectrum of activities and infrastructure in the coastal zone.

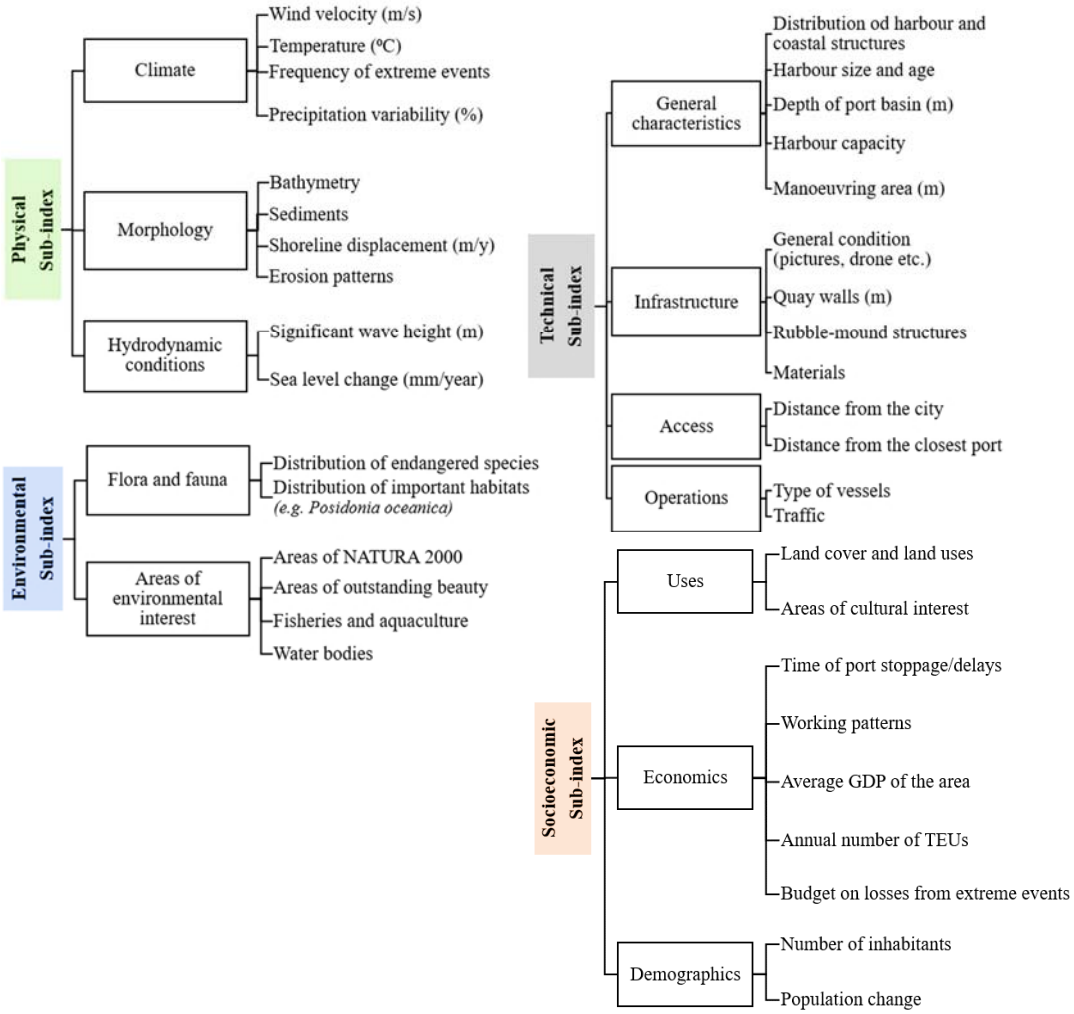

Figure 3. Sub-indices and indicative indicators of VIcomp.

6 CONCLUSIONS

The results of this research work demonstrate that the inherent vulnerability of a system is increased by climate change and that the use of indicators and coherent indices could be useful to assess vulnerability, monitor changes and plan targeted interventions. The framework and the index proposed could be adopted in cases where assessing coastal vulnerability in a holistic way is desired. The results of such an analysis could be particularly relevant for local and regional stakeholders who need to prioritise interventions and allocate funding according to the most vulnerable components of their coastal zone. Furthermore, MSP efforts could take advantage of such indices to inform climate-smart plans that consider not only the marine space, but also land-sea interactions.

Coastal vulnerability and port vulnerability should no longer be assessed separately since coastal areas contain ports and other coastal infrastructure within their boundaries, while seaports do not only refer to their technical and operational features, but also to the adjacent terrestrial and marine areas and their interaction. VIcomp seeks to combine CVI and PVI into one single index. The indicators used are indicative and could be further informed or weighted according to the particular conditions of the area examined. However, public data may not be available for all indicators which shows the need for data sharing and transparency.

The general framework proposed to assess vulnerability of the coastal zone is based on simple, sequential steps that could be used despite the geographical location of the area assessed. Particularly, the need to assess both current and future vulnerability is the key to the proposed framework which seeks to become a tool for stakeholders who want to improve their areas' resilience against climate change impacts while strategically planning their coastal area's sustainable future.

References

Chalastani VI, Manetos P, Al-Suwailem AM, Hale JA, Vijayan AP, Pagano J, Williamson I, Henshaw SD, Albaseet R, Butt F, Brainard RE, Coccossis H, Tsoukala VK, Duarte CM (2020) Reconciling Tourism Development and Conservation Outcomes Through Marine Spatial Planning for a Saudi Giga-Project in the Red Sea (The Red Sea Project, Vision 2030). Frontiers in Marine Science 7. doi: 10.3389/fmars.2020.00168

Gornitz V (1991) Global coastal hazards from future sea level rise. Palaeogeography, Palaeoclimatology, Palaeoecology 89:379-398. doi: 10.1016/0031-0182(91)90173-O

IPCC (2001) Impacts, Adaptation, and Vulnerability: Contribution of Working Group II to the Third Assessment Report of the Intergovernmental Panel on Climate Change. Intergovernmental Panel on Climate Change (2001)

Izaguirre C, Losada IJ, Camus P, Vigh JL, Stenek V (2021) Climate change risk to global port operations. Nature Climate Change 11:14-20. doi:10.1038/s41558-020-00937

Kantamaneni K, Gallagher A, Du X (2019) Assessing and mapping regional coastal vulnerability for port environments and coastal cities. Journal of Coastal Conservation 23:59–70. doi: 10.1007/s11852-018-0636-7

Kerr S, Johnson K, Side JC (2014) Planning at the edge: integrating across the land sea divide. Marine Policy 47:118–125. doi: 10.1016/j.marpol.2014.01.023

Kontogianni A, Damigos D, Kyrtzoglou T, Tourkolias C, Skourtos M (2019) Development of a composite climate change vulnerability index for small craft harbours. Environmental Hazards 18: 173-190. doi: 10.1080/17477891.2018.1512469

Koromilas A, Kotidou G, Athanasopoulou A, Tsoukala V (2019) Development of a combined physical and anthropogenic activities vulnerability index for coastal infrastructures: a GIS-based approach for Central Greece. Paper presented at the 1st International Conference of DMPCO, Book of Abstracts, Athens, Greece.

McIntosh RD, Becker A (2019) Expert evaluation of open-data indicators of seaport vulnerability to climate and extreme weather impacts for U.S. North Atlantic ports. Ocean & Coastal Management 180:104911. doi: 10.1016/j.ocecoaman.2019.104911

Ružić I, Jovancevic SD, Benac C, Krvavica N (2019) Assessment of the Coastal Vulnerability Index in an area of complex geological conditions on the Krk Island, Northeast Adriatic Sea. Geosciences, 9: 219. doi: 10.3390/geosciences9050219

Tsaimou C, Kagkelis G, Papadimitriou A, Chalastani V, Sartampakos P, Chondros M, Tsoukala V (2022) Advanced Multi-Area Approach for Coastal Vulnerability Assessment. Paper presented at the 7th IAHR Europe Congress, Athens, Greece.

Vandarakis D, Panagiotopoulos IP, Loukaidi V, Hatiris GA, Drakopoulou P, Kikaki A, Gad FK, Petrakis S, Malliouri DI, Chatzinaki M, Morfis I, Kanellopoulos TD, Kapsimalis V (2021) Assessment of the Coastal Vulnerability to the Ongoing Sea Level Rise for the Exquisite Rhodes Island (SE Aegean Sea, Greece). Water 13:2169. doi: 10.3390/w13162169

Spatial delimitation of the coastal zone in the context of evaluating environmental impacts of artificial constructions

A. Karditsa[1,2*], I.E. Margaritou[2,3], G. Alexandrakis[2], E. Stanota[4], Th. Paramana[3], V. Kotinas[3] & S. Poulos[2,3]

[1]Department of Ports Management and Shipping, National and Kapodistrian University of Athens, Evripos Campus, Greece
[2]Institute of Applied and Computational Mathematics, Foundation for Research and Technology-Hellas, Heraklion, Greece
[3]Department of Geology and Environment, National and Kapodistrian University of Athens, Greece
[4] Ilida Consulting Engineers S.R.O. 63 Arch.Elis & Ag.Triados, TK 27059, Havari, Ilia
kkarditsa@pms.uoa.gr

Abstract

Spatial delimitation of coastal zone is one of the most crucial factors in the management of coastal environment. However, the there are several complementary definitions of what constitutes a 'coastal zone' based on a series of natural, legislative and management criteria and various corresponding factors. The aim of this study is to analyze the institutional, social and physio-geographic characteristics instrumenting the coastal environment in order to define the crucial factors for operational coastal zone delimitation. It is shown that although the definition of crucial zone is mainly based on the narrow dynamic and changing zone, socioeconomic activities taking place in the broader coastal environment have to be thoroughly considered in the strategic management of coastal zone.

Keywords: ICZM, natural factors, socio-economic activities, administrative framework

1 INTRODUCTION

The coastal zone is the area where most human activities (tourism, fishing, aquaculture, maritime transport, ports, agriculture, and industry) take place, exhibiting significant economic development. It is estimated that over 200 million of the European population (680 million in total) are concentrated within 50 km of the coastline. In the meantime, coastal zones are highly dynamic and changing systems, both in space and time, vulnerable to physical to factors such as hydrodynamic and sedimentological activity and prone to erosion and flooding (e.g., Vousdoukas et al., 2020; Phillips 2018; Di Paola et al., 2014). However, although the term 'coastal zone' is generally comprehensible, there is no common definition of what exactly constitutes a 'coastal zone', but rather several complementary definitions, each serving a different purpose, occasionally using arbitrary criteria. For instance, many studies refer specially to the administrative delimitation of the area, whilst others focus on the zone's determination based on the physiographic and geomorphic characteristics of the coastal area (e.g., Brenner et al., 2006; Barragan et al., 2004; Sarda et al., 2005). In any case, it is substantial that, in the framework of ICZM, coastal zone geographic boundaries should consider both causes and impacts (Boesch et al., 2001). The aim of this study is to analyze the institutional, social, and physio-geographic characteristics instrumenting the coastal environment in order to define the crucial factors for operational coastal zone delimitation.

2 METHODOLOGICAL APPROACH

The definition of the coastal zone calls for a comparative analysis of the specific coastal management laws, national legislation, and thorough understanding of the natural environment. Methodologically, an integrated approach to the coastal area should consider the following aspects:

- analysis of the institutional framework,
- evaluation of the applicable regulatory instruments,
- criteria used to determine the geographical area,
- operative (e.g., land use, socio-economic) criteria.

3 RESULTS & DISCUSSION

The coastal zone is a complex and vulnerable area where balance is prone to disturbance by a series of factors. Table 1 summarizes the boundaries of the coastal zone considering all involved factors, as defined in the diverse institutional, legislative, management and physio-geographic contexts that, in the framework of integrated coastal zone management, planners, engineers and stakeholders have to encounter when proceeding with any engineering activities along the coastline. In brief all factors are aggregated in the following criteria:

- The European legislative framework relevant to the coastal zone, such as the Habitat Directive (92/43/EC), Water Framework Directive (2000/60/EC), Marine Strategy Framework Directive (2008/56/EC), Maritime Spatial Planning Directive (2014/89/EU).
- The institutional context, as introduced by the United Nations Convention on the Law of the Sea (UNCLOS, 1982).
- The physiogeographic context, as defined by the prevailing morphological, hydrodynamic and morphodynamic regime.
- The national legislative regime and specificities, such as law L.2971/2001 in the case of Greece.
- The management context, as introduced by the Integrated Coastal Zone Management Protocol of the Barcelona Convention (Art.8, §7).

Accordingly, Figure 1 presents graphically the corresponding spatial delimitation.

Table 1. Delimination of coastal zone based on the various criteria and factors

CRITERIA	FACTORS	LIMITS	
		Onshore	**Offshore**
NATURAL	Morphodynamic	Natural or artificial characteristics of the backshore zone	Closure depth
	Hydrodynamic	Maximum (winter) wave run-up waterline	Intermediate waters
	Geological	Watershed line	Shelf boundary
LEGISLATIVE	Inland water (river) Management (WFD)	Watershed line	1 nm
	Floods (Floods Directive)	Setback zone	Coastline
	Ecosystems and Biodiversity (MSFD)	Coastline	Exclusive Economic Zone
	Uses and Activities (MSPD)	Coastline	Exclusive Economic Zone
	Concervation of Habitats (Habitat Directive)	Setback zone	Continental Shelf
	L.2971/2001	25 m setback zone landwards (from swash maxima)	
INSTITUTIONAL	UNCLOS		Territorial Sea
MANAGEMENT	ICZM (art.8-2)	At least 100 m setback zone landwards (from swash maxima)	Territorial Sea

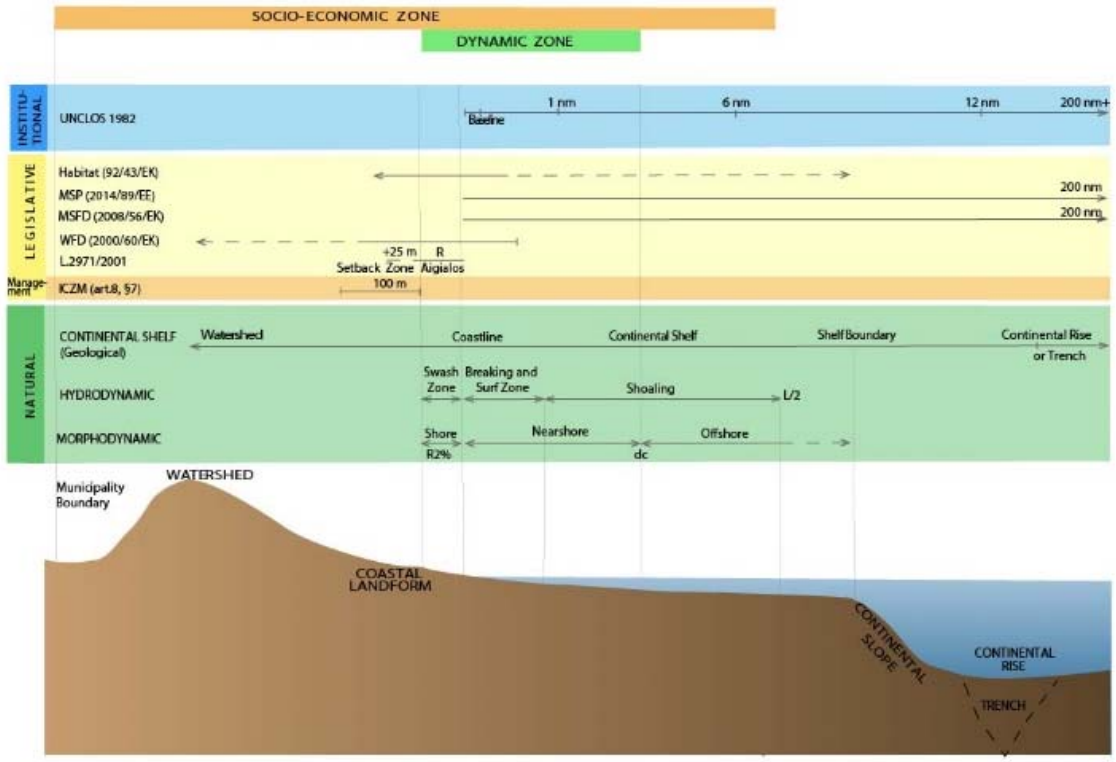

Figure 1. Definition of the Coastal Zone in diverse contexts.

Coastal behavior is largely site-specific, which means that many different factors need to be carefully considered. Besides the inherent difficulty, establishing criteria for the definition of the coastal zone area can be viewed as a challenge as it entails flexibility in its application depending on the raised definition requirements.

In physical geographic terms, the coastal front defines the dynamically changing zone shaped by the specific geomorphological characteristics of the area (e.g. geology, bathymetry, petrology, sedimentology and coastal hydrodynamics). In addition, coastal depositional geomorphs (e.g. deltaic coasts, lagoons, beaches, cliffs) are considered to be particularly vulnerable to both changes in natural processes and various human interventions.

The Integrated Coastal Zone Management Protocol of Barcelona Convention calls for the consideration of environmental degradation caused by human activities and protection from the effects of human intervention (e.g., erosion), including those related to climate change. Within this scope, amongst other measures Article 8(2) of the ICZM protocol suggests the definition of a setback buffer zone of at least 100 m landwards up to maximum (winter) wave run-up waterline, where no further constructions or development is allowed. Seawards, the boundary of the coastal zone is referred to be territorial sea or is set at approximately 50m depth, where the majority of activities and uses are concentrated.

Marine Spatial Planning Directive (MSPD) extends the area of application offshore, in order to ensure spatial development and integrated management of human activities. Across coastal zone MSPD acts as a complementary tool of ICZM the joint implementation of which safeguards effective management and sustainable planning. In this area, Marine Strategy Framework Directive (MSFD) was activated to protect the marine ecosystem and biodiversity upon which marine-related economic and social activities depend, by reviewing the existing knowledge and proposing a roadmap for the science-policy interface.

Moreover, within an even more ecosystemic approach, the Habitats Directive aims to ensure that a series of species and habitat types are maintained, or restored, to a favorable conservation status.

In addition, the Water Framework Directive (WFD), although refers to the terrestrial part of coastal zone, introduces the term of coastal waters defined as water, that has not been designated as transitional

water, extending one nautical mile from a baseline defined by the land points where territorial waters are measured. WFD combines qualitative, ecological and quantitative goals for the protection of aquatic ecosystems and the maintenance of good environmental status of all water resources and sets as a central idea their integrated management at the geographical scale of River Basins.

Alongside, Floods Directive Art. 2 places special emphasis on river and coastal flooding, as a particular challenge in low-lying areas as deltas and coastal plains and subsidence caused by sediment deficits or groundwater extraction can further exacerbate the problem.

Taking into account all environmental and administrative factors the strategic management area over which planning has to be applied in the context of evaluating environmental impacts of artificial constructions includes (i) the beach zone itself and associated sand dunes considering natural processes and (ii) a broader backshore area depending on human activities and associated pressures.

4. CONCLUSIONS

The delimitation of coastal zone in terms of natural environment and human presence interrelationship has to take into consideration:

- Physical (including climatic forces) and artificial installations
- Existing and future socio-economic activities
- Ecosystem and relative ecosystem services
- Existing administrative regulations

However, it is essential that management efforts focus on the prevention of coastal risks related to human interventions and strengthen of resilience against climate change. This can be achieved through in-depth understanding the natural contributors of this spatially narrow, dynamic zone, though, also respecting the socio-economic character of the broader coastal zone.

Acknowledgments

The authors acknowledge research Project ILIDA-KIT funded by GSRT (T2EDK-02795).

References

Barragan JM. (2004) Las areas litorales en Espana. Del analisis geografico a la gestion integrada. Ed. Ariel; 215.

Boesch DF. (2001) Science and integrated drainage basin coastal management. Chesapeake Bay and Mississippi Delta. In: von Bodungen B, Turner RK, editors. Science and integrated coastal management. Berlin: Dahlem University Press; 37–50.

Brenner J, Jimenez JA, Sarda R. (2006) Definition of homogeneous environmental management units for the Catalan coast. Environmental Management 38: 993–1005.

Di Paola, A., Caporaso, L., Di Paola, F., Bombelli, A., Vasenev, I., ... & Valentini, R. (2018) The expansion of wheat thermal suitability of Russia in response to climate change. Land Use Policy 78: 70-77.

Phillips, J. D. (2018). Environmental gradients and complexity in coastal landscape response to sea level rise. Catena 169: 107-118.

Sarda R, Avila C, Mora J. A. (2005) methodological approach to be used in integrated coastal zone management processes: the case of the Catalan coast (Catalonia, Spain). Estuarine, Coastal and Shelf Science 62: 427–39.

Vousdoukas, M. I., Ranasinghe, R., Mentaschi, L., Plomaritis, T. A., Athanasiou, P., Luijendijk, A., & Feyen, L. (2020). Sandy coastlines under threat of erosion. Nature climate change 10(3): 260-263

Design of coastal aquaculture structures and allocated zones for aquaculture development in Cyprus

I. Kyriakides[1,2*], F. Gavrıel[1,3], P. Lemonarıs[3] S. Charalambous[4], M. Menicou[5,6], M. Charalambides[5,6], R. Abu Alhaija[7], D. Hayes[7], O. Nisiforou[8], G. Nikolaidis[9], E. Hadjisolomou[1,10], G. Triantafyllou[11] and G. Triantaphyllidis [1, 11]

[1] University of Nicosia Research Foundation, 46 Makedonitissas Avenue, CY-2417 P.O. Box 24005, CY-1700 Nicosia, Cyprus
[2] Cyprus Marine & Maritime Institute, CMMI House, Vasileos Pavlou Square, P.O.Box 40930, 6023 Larnaca, Cyprus
[3] FP Marine Ltd, 20, Queen Frederica Street, Office 403, 1066 Nicosia, Cyprus
[4] T.C. Geomatic Technologies Ltd., 1095 Nicosia, Cyprus
[5] Frederick Research Center, 7 Y. Frederickou Str., CY-1036, P.O. Box 24729, CY-1303, Nicosia, Cyprus
[6] Frederick University, 7 Y. Frederickou Str., CY-1036, P.O. Box 24729, CY-1303, Nicosia, Cyprus
[7] Cyprus Subsea and Services Ltd, 34A Paragogikotitas St, Lakatamia 2023, Cyprus
[8] Cyprus University of Technology - Department of Chemical Engineering, Corner of Athinon and Anexartisias 57, Lemesos 3603, Cyprus
[9] Oceanography Center, University of Cyprus, Nicosia, Cyprus
[10] Department of Electrical Engineering, Computer Engineering and Informatics, Cyprus University of Technology, 3036 Limassol, Cyprus
[11] Hellenic Centre for Marine Research, Institute of Oceanography, 46.7 km Athens-Sounio Avenue, PO Box 712, GR 19013 Anavyssos, Attica, Greece

*Corresponding author: Ioannis.Kyriakides@CMMI.BLUE

Abstract

Aquaculture is an activity that requires the use of extensive marine space as well as coastal infrastructure and competes for space with other marine activities such as tourism, fisheries, marine navigation, energy, sea recreational activities, and coastal activities. A Marine Spatial Study specific to Open Sea (OS) aquaculture was executed in three phases, first by identifying the available areas suitable for OS Aquaculture by adopting exclusion criteria related to conflict with other activities and high impact on the natural environment, considering the weather (wind/waves), water depth, and proximity to harbour facilities. Selection of optimal candidate areas was made after consultations with Governmental Departments and Services and the involved stakeholders and led to the selection of four candidate areas: Xylofagou West, Larnaka, Governor's Beach, and Aphrodite Hills. A steel semi-submersible rigid fish cage system with multiple draughts adequate to withstand a maximum significant wave height of 8 meters was conceptualized. Two to four rectangular or circular cages of breadth 10 or 20 meters may be installed in each of the two compartments. The two pontoons maintain ballasting and de-ballasting provisions to adjust the structure's draught. Each pontoon hull is divided into three watertight compartments for enhanced survivability. On the top platform, a deckhouse is installed consisting of a diesel generator compartment, including a separate fuel tank and feed storage compartment, which may also include feeding equipment, machinery, office, and cabin space. Every individual structure can be anchored with either an eight-point mooring system or single-point mooring.

Keywords Aquaculture, Cage, Cyprus, Semi-submersible fish cage, Mooring system, marine spatial planning

1 INTRODUCTION

Aquaculture requires extensive marine space and coastal infrastructure, competing for space with activities such as tourism, fisheries, marine navigation, energy, recreational and other coastal activities. Although open sea aquaculture alleviates space constraints, its wide use is hindered by the availability of robust fish cage and mooring systems able to withstand open sea conditions. The Open Sea Aquaculture in the Eastern Mediterranean (OS Aqua) Project will enable the strategic development of

an open sea aquaculture industry in Cyprus. The project takes a multidisciplinary approach to minimize environmental impact and resolve socioeconomic constrains. Herein the results of the maritime zone definition and open sea cage system design are presented. The project among other activities produced a Marine Spatial Planning study (MSP) specific to open sea (OS) aquaculture development in the Republic of Cyprus and a cage system with its associated mooring system.

2 MARINE SPATIAL PLANNING (MSP) IN CYPRUS

To determine suitable areas for the establishment of the Allocated Zones for Aquaculture (AZAs), an MSP methodology implemented in three phases:

1. Application of exclusion criteria to define the available maritime space (see Table 1). The geographical data used included data from sources such as the Department of Land and Surveys (DLS), Ministry of Interior, the cartographical database of T.C. Geomatic Ltd, Geomatic Maps™ (Geomatic), and Department of Environment, Ministry of Agriculture, Rural Development and Environment (DoE).
2. Application of proximity and weather conditions criteria to define a series of more specific candidate OS AZAs. Once the results of Phase 1 were generated, nine locations were selected to be investigated in terms of weather conditions, and specifically wind and waves. Wave and wind datasets were calculated by the Oceanography Center of the University of Cyprus and data were retrieved by the UCY WAM that runs at the University of Cyprus. Data used was the 24-hourly forecast between 2010 and 2017 averaged over time. For temperature, currents, and salinity parameters, Copernicus reanalysis was used between 2010 and 2015 (max availability at time). For the currents, the values extracted were the maximum values over depth averaged over time. From the data analysis, it was clear that all the areas west of Lemesos have been assigned as of lower priority as they are more exposed to the weather (waves). Nevertheless, it was decided for research purposes to include an area (Southeast from Paphos) in the subsequent assessment of the areas.
3. Selection of the optimal candidate areas for further investigation by considering the opinions of relevant stakeholders and partners. The outcome was the selection of four (4) candidate areas: Xylofagou West, Larnaca, Governor's Beach, and Aphrodite Hills (Figure 1).

Table 1. The criteria for the spatial analysis of the AS Aqua Project

STEPS	AREAS / INFRASTRUCTURES	CRITERIA	STEPS	AREAS / INFRASTRUCTURES	CRITERIA
1	Areas not controlled by the Republic of Cyprus	Excluded	**10**	*Posidonia oceanica* meadows	500m dist.
2	Areas over 200m deep	Excluded	**11**	Shipwrecks	500m dist.
3	Swimming Areas (Polygon)	1 km dist.	**12**	Desalination Stations	2 km dist.
4	Natura 2000 Network	1 km dist.	**13**	Artificial Reefs	1 km dist.
5	Port Infrastructure Areas	1 km dist.	**14**	Existing fish farming areas	1 km dist.
6	Anchorages (Polygon)	1 km dist.	**15**	Military Material Depot Areas	2 km dist.
7	Ship Routes	1 km dist.	**16**	Sewage disposal points	2 km dist.
8	Disposal Pipes	1 km dist.	**17**	Protected Areas from Fishing	Excluded
9	Sea Shooting Ranges	1 km dist.	**18**	Airports	3.7 km dist.

3 DEVELOPMENT OF A RIGID-TYPE FISH CAGE SYSTEM

Market research was conducted to evaluate the advantages and disadvantages of various existing and proposed aquaculture structures to identify the most suited structure for Cyprus. The designs considered included SUBflex system[1], Havfarm ("Ocean Farm")[2], Evolution Pen[3], SeaStation®[4], Aquapod[4], AquaSol, KZO Sea Farms Mari-culture Parks, Ocean Farm 1 of the Norwegian SalMar, NSENGI

[1] See: https://www.giliocean.com/
[2] See: https://www.youtube.com/watch?v=y8UGeFRUUPc
[3] See https://www.innovasea.com/open-ocean-aquaculture/submersible-aquaculture-systems/
[4] See http://www.innovasea.com/

(Nippon Steel & Sumikin Engineering Co., Ltd), Smart Fish Farm[5], OCEANIS (Badinotti), the Tension Leg Cage concept, Aquaculture Technology Innovation by Aquatec[6], Neptun developed by Aquafarm Equipment[7], Marine Harvest's to farmsalmon in a container ship, Aquatraz fish cages[8], Shenlan 1 and 2 of Wanzefeng Fishing Co., Ltd, Egget ® of Hauge Aqua[9], Fusion Marine Triton[10], Pisbarca, , Marine donut – Close containment concept design of Marine harvest, the Eco-Ark, De Maas' Spar Fish Farm, Australian floating platforms[11] and PLOCAN platform. Planning a strategy to operate in the open sea is a complex process that may require multiple steps and approaches. For example, there could be a combination of using the existing near-shore farms to raise the fry to 40 or 100 grams (in Cyprus, the most common fish species reared are European seabass *Dicentrarchus labrax* and gilthead seabream *Sparus aurata*) and then to transfer it further offshore to the open sea. Alternatively, the OS AQUA cages could be stocked with fry of 10 gr instead of 2 gr fish as with the near-shore units. To reduce negative impacts on growth, fish quality, and production, fish grading typically occurs at 25-40 g, approximately at 100 gr and at 180-200 gr. In general, it is preferable to have enough cages to allow continuous management.

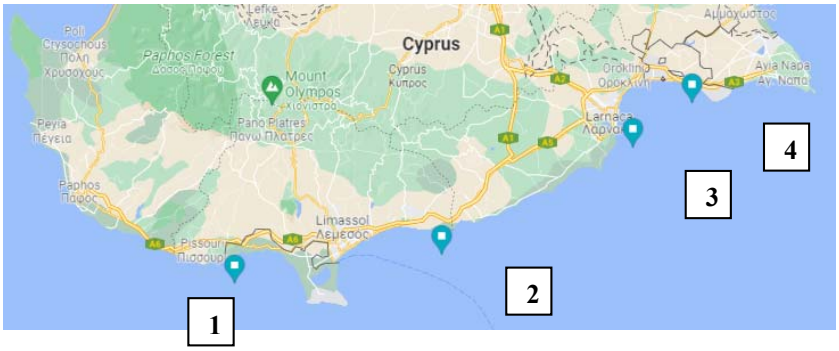

Figure 1. The selected four candidate areas for open sea aquaculture development in the Republic of Cyprus: 1) Aphrodite Hills, 2) Governor's Beach, 3) Larnaca, and 4) Xylofagou West.

Based on this research and requirements, a cage system with its associated mooring system was designed for specific locations in Cyprus territorial open sea waters (unprotected waters). The design parameters are listed below:

• One structure of submersible fish cage system, with a minimum of two (2) and maximum of four (4) individual cages, is envisaged.

• The structure's length should be 50-60 meters and the breadth around 20-24 meters (the length and the breadth are limited to the available dry-docks in Cyprus for carrying out the relevant structure maintenance).

• There are four (4) possible points for anchoring with the following particulars (considered as open sea condition): prevailing weather (max wind speed - approximately 20 knots, max significant wave height - 5.0 to 6.50 meters), depth of anchoring - 120 to 165 meters, estimated distance from support base - 5.5 km.

• Approximate depth of nets (below surface of water) that would be acceptable for normal operation up to 12 meters

• There must be a storage area for fish food, fish feeding hoppers arrangements, short term accommodation for two persons, and one crane capable of serving all cages of the structure and the area around the structure.

• Capability of the structure to ballast and de-ballast, in order to achieve different drafts during the winter and summer seasons (depending on the sea stage) and to be easily towed. Towing in the empty (no fish) condition can be carried out with the structure floating on the pontoons.

[5] See https://www.salmar.no/en/offshore-fish-farming-a-new-era
[6] See https://www.aquatec.co.id/
[7] See https://aquafarm.no/
[8] See https://aquatraz.com/en/
[9] See https://haugeaqua.com/
[10] See https://www.youtube.com/watch?v=TfhgIrub6rM
[11] See https://www.dnv.com/to2030/technology/multipurpose-offshore-platforms.htm

• The structure should be cost-effective and be able to be constructed in Cyprus, considering the existing facilities.
• Provisions for autonomous survivability of the structure to be provided (i.e., solar panels, automated feeding equipment etc.).
After an initial proposal was discussed with the ichthyologists, a naval architecture design loop was carried out to achieve the final design main particulars of the proposed submersible fish cage system. The design loop included the stability and strength calculations of the structure in transit and various operational situations. The specifications are depicted in Table 2. The structure is a steel semi-submersible type rigid fish cage system for open sea conditions with multiple draughts, adequate to withstand maximum significant wave height of 8 meters. Rectangular or circular cages may be installed in a combination of two (2) to four (4) individual cages of breadth 10 or 20 meters, depth 12 - 15 meters and adjustable length up to 20 meters.

Table 2. The Open Sea semi-submersible fish cage structure specifications

Specifications		**Specifications**	
Material of construction	Shipbuilding Steel	Depth (total)	20.15 meters (to top of platform)
Length (OA) Length (BP)	50.00 meters	Draughts	2.75 meters (Transit - Tow condition) 15.00 meters (Operation mode 1 - Winter season) 18.50 meters (Operation mode 2 - Summer season)
Breadth (extreme)	24.50 meters	Displacements	approx. 1250 tonnes (Transit) approx. 2250 tonnes (Operation mode 1 - Winter season) approx. 2400 tonnes (Operation mode 2 - Summer season)
Breadth of Demi-hull	4.50 meters	Depth of Demi-hull	3.60 meters

Access ladder is provided amidships on one side leading to the top platform. The two pontoons maintain provisions for ballasting and de-ballasting (with appropriate valves and submersible electric pumps) to adjust the structure's draught. Each pontoon hull is divided into three watertight compartments for enhanced survivability, trim, and heel adjustment. The top platform provides access to the structure's perimeter and provides personnel protection with handrails. Mooring points for supporting vessels are provided perimetrically on the top platform. Towing points are fitted on the pontoons. A hydraulic crane with a radius of 27 meters is provided on the port side, serving the structures over the side and able to reach any combination of cages. On the top platform, in the way of the mid-passageway, a deckhouse is installed consisting of the following spaces separated by bulkheads:

- **Diesel generator compartment**, including a separate fuel tank. The diesel generator will supply electrical power for the submerged ballast pumps and remote valves, feeding equipment, electro-hydraulic crane, lighting and communications, accommodation etc. It is envisaged that the generator will not be utilized on a continuous basis. Instead, it will be used only when required, and thus the capacity of the fuel tank does not have to be very large. When the generator is off, electrical power can be supplied by solar panels and an accumulator system. This compartment will also include the electrical control and monitoring panel for all operations.

- **Feed storage compartment**, which may also include feeding equipment machinery. The support craft shall supply the feed and can be loaded in the feed compartment via a sliding roof hatch using electro-hydraulic crane. It can then be fed to the fish either with feeding machinery if fitted or using the crane and small hopper.

- **Office and cabin space**. It includes a small toilet / shower, two (2) bunks and a desk with communication equipment. It is designed for brief stays only; however, it could be further expanded if required for longer personnel stays onboard.

Additional equipment may be installed on the walkways / platform if required. Emergency access to the pontoons for inspection and for checking the submersible ballast pumps and the associated valves is provided via the large cylindrical tubes of 2.5 meters diameter, with watertight hatches accessed from the level of the walkway. The structure can have various operational draughts so that it can withstand large waves in heavy weather. The large operational freeboard (up to 5 meters in heavy weather and 1.5 meters in fair weather) ensures that extreme motions are considerably reduced, and the top platform and equipment is adequately protected. Towing to and from the location can be effected with the structure supported only on the pontoons (transit draught is 2.75 meters) and carried out at a reasonable towing speed and with a relatively smaller tug boat(s). Every individual structure can be anchored with either an 8 point mooring system or single point mooring, depending on the chosen area (available surface) and the number of structures that will be required for a complete fish cage system. The animated proposed design is illustrated in Figure 2. The structure's estimated structural weight, excluding platform structure, machinery, equipment, and other arrangements, is 574 tonnes. The structure's Vertical Center of Gravity is 7.486 m from Baseline.

Figure 2. Animated design of the Open Sea semi-submersible fish cage structure for Cyprus

3.1 Mooring system

The single point mooring approach has the benefit that the structure is allowed to rotate around a single fixed point (to "weathervane"), thus reducing the environmental loads exerted to the mooring system. The disadvantage is that the mooring system utilizes a "turret" which includes rotating parts and thus makes the system complicated, maintenance intensive and expensive to produce. In the eight point mooring arrangement, each cage is anchored in a fixed position by 8 mooring lines (two (2) at each corner of the structure), each attached to an anchor on the seabed. The more conventional method utilizes anchor chains and standard anchors lying on the seabed. This requires large and heavy chain lengths for each mooring line, as a large portion of the total chain length must lie on the seabed to ensure safe cage mooring. Alternatively, the use of taut mooring lines attached to vertically loaded anchors (VLA) may be utilized. The distances between cages in this case will be much shorter as the need to avoid overlapping of chains lying on the seabed is avoided. Furthermore, this system will be easier and faster to install and more cost-effective. The orientation of the cages will have to consider the prevailing weather conditions (direction of wind, current and waves), as the cages will not be able to weathervane.

4 CONCLUSIONS

The proposed open sea semi-submersible fish cage structure can offer a platform for further advancing and testing technologies and systems that will allow the development of sustainable aquaculture, improved feeding and monitoring systems, advanced water quality management, and renewable energy systems for powering the cage reducing the risk of environmental pollution from the release of culture effluents in sensitive nearshore habitats.

Acknowledgements

The Open Sea Aquaculture in the Eastern Mediterranean Project (OS Aqua), co-financed by the European Regional Development Fund and the Republic of Cyprus through the Research and Innovation Foundation (Grant No. INTEGRATED/0918/0046).

DMPCO 2023

e-Proceedings of the 2nd International Scientific Conference on Design and Management of Port Coastal and Offshore Works Thessaloniki, Greece, May 24-27 2023

A shipping commitment against plastic pollution in the Mediterranean: action plan for harbours

X.L. Loizidou[1*], M.I. Loizides[1], D. Petsa[1], D. Orthodoxou[1]

[1] ISOTECH LTD Environmental Research and Consultancy, P.O. Box 14161, 2154, Nicosia, Cyprus
[*]Corresponding author: xenia@isotech.com.cy

Abstract

Approximately 20%-30% of marine litter in the Mediterranean comes from sea-based sources, including cruise and commercial shipping. Most of the waste produced by the shipping industry is plastic waste, putting plastics at the forefront of the shipping industry's waste management efforts. In an increasingly connected global economy, the development of fit-for-purpose port reception facilities that encourage and incentivise waste minimisation and waste management optimisation is a mandatory prerequisite to the minimisation of marine litter and the achievement of a circular economy within the shipping industry. Cyprus can take a leadership role towards this direction. This article presents the results of the implementation of the DeCyDe-4-Shipping decision-support participatory method in Cyprus, through which key shipping industry stakeholders identified the problems they face in relation to waste management, recorded the waste management optimization practices implemented by the industry, and provided suggestions and solutions for improvement. The process resulted in the development of the solution-oriented 2022-2023 Action Plan for Shipping Waste Minimisation and Waste Management Optimization in Cyprus, which includes specific provisions to create fit-for-purpose port infrastructure and port reception facilities.

Keywords Waste management, Participatory decision-making, Shipping, Port reception facilities.

1 INTRODUCTION

Marine litter is one of the world's most pressing environmental problems, particularly in the Mediterranean, which has been identified as the most polluted sea in the world (Gerigny *et al*., 2019; Fossi *et al.*, 2018). Twenty to thirty percent of marine litter comes from sea-based sources, including cruise and commercial shipping. The most common type of waste in shipping is plastic (Moheea *et al*., 2012), putting plastic waste at the forefront of the shipping industry's waste management and marine litter reduction efforts.

Marine litter, and especially plastic marine litter, poses a serious threat to marine ecosystems and to human health, and serious economic damage to the tourism and shipping industry (Boucher & Bilard, 2020). Thus, several policies are in place and expert work is implemented to address the issue. The European Union has in place the Marine Strategy Framework Directive, the Packaging and Packaging Waste Directive, the Single Use Plastics Directive and the Port Reception Facilities Directive. The International Maritime Organisation (IMO) has in place Annex V of the MARPOL Convention, which mandates the proper separation and disposal of waste. In 2018, the Marine Environment Protection Committee (MEPC) of the IMO published its Action Plan to Address Marine Litter by 2025, which includes practices that relate to the shipping industry.

Shipping is a global industry, making waste management optimisation particularly challenging. The legislative framework and implemented practices vary significantly between home ports and ports of call across the world. In an ever increasingly connected global economy, the development of fit-for-purpose port reception facilities that encourage and incentivise waste minimization and waste management optimization is a mandatory prerequisite to the achievement of a circular economy within the shipping industry. The Cyprus shipping sector, the 3rd largest in Europe and the 11th largest in the world, can play a leading role towards this direction.

This article presents work implemented with shipping industry stakeholders in Cyprus, including policymakers and port reception facilities. Through a specially designed decision support participatory

process, the shipping stakeholders of Cyprus identified the problems they face in relation to waste management, recorded the waste management optimization practices that are implemented by the industry, and provided suggestions and solutions for improving the situation. The process resulted in the development of a solution-oriented Action Plan with specific time frames for implementation. This article focuses on the part of the process that refers to further and continuous improvement towards creating fit-for-purpose port infrastructure and port reception facilities.

2 METHOD

For this study, the DeCyDe-4 method and tools were implemented to engage stakeholders in the decision-making process concerning waste minimization and waste management optimization in the Cypriot shipping industry. DeCyDe-4 was developed by ISOTECH Ltd.'s experts in participatory decision-making and stakeholder involvement facilitation. It is an adaptable, site- and case-specific decision-support method that leads to informed, science-based and justifiable decisions on issues relating to sustainability and resilience. The method has been extensively described by Loizidou *et al.* (2016; 2017; 2021) and Schumacher *et al.* (2018). The initials 'DeCyDe' are a play on the word 'decide' where the 'ci' has been replaced by 'Cy', which stands for Cyprus, the country where ISOTECH is based. The suffix '-4' stands for the word 'for' and is included to denote the fact that the main "DeCyDe" method is adapted to meet the specificities of each decision-making problem at hand, forming dedicated "DeCyDe-4" tools. In this specific study, DeCyDe-4 was adapted to develop the DeCyDe-4-Shipping version and associated tools.

This article presents the results from the second year that DeCyDe-4-Shipping was implemented in Cyprus. The first year the participatory process served as a baseline study, a first scan for the identification of the problems of the industry related to waste management. In cooperation with the Cypriot Deputy Ministry of Shipping, all key actors across the Cypriot shipping industry value chain, including policymakers, port reception facilities, ship owners and managers, consultants, research/academia and NGOs, were invited to participate at the DeCyDe-4-Shipping decision-making workshop. The results of the process were elaborated to develop the 2021-2022 Cypriot Action Plan for Waste Minimization and Waste Management Optimization in Shipping, the first of its kind.

In this second year of implementation, the participatory process was structured in three phases. ***Phase A*** concerned the identification of stakeholders, upgrading the list of 2021. ***Phase B*** concerned the implementation of the workshop. The facilitators presented the 2021-2022 Action Plan, which included actions for the plastic waste minimization and waste management optimization in the Cypriot shipping industry, split across four pillars: Pillar A. Creating fit-for-purpose Port Reception Facilities; Pillar B. Policy Implementation and Enforcement; Pillar C. Research and Innovation; and Pillar D. Environmental Behaviour and Awareness Raising.

This article focuses on the Actions in Pillar A, which were:

- Action 1: Define waste categories and identify suitable and authorized waste handlers. This action was considered the first step in the optimization of waste management at Port Reception Facilities. It concerns the definition of the categories/streams in which waste usually arrives at the various ports/terminals, as well as the volumes of each waste stream at each port/terminal, as well as the identification of authorized waste handlers for each of these waste streams.
- Action 2: Develop necessary infrastructure and waste segregation schemes. This concerns the deployment of the necessary infrastructure at each port/terminal, including receptacles for accepting separated waste, and relevant weighing stations to allow for effective monitoring of shipping waste.
- Action 3: Revise fees to incentivize waste minimization. The concerns the implementation of a combination of indirect fees and a Pay As You Throw (PAYT) scheme to incentive waste minimisation onboard. The Indirect Fee could cover certain minimum amounts of waste, whereas the PAYT scheme would ensure that only those that keep producing large amounts of avoidable waste must pay extra for their disposal.

- Action 4: Transform Cypriot ports into pioneering circular ports. This concerns the creation of Circular Ports in Cyprus, to set them apart from their competition and encourage their use. For this to be achievable, a holistic and out-of-the box thinking of Port Reception Facilities is required.

Once these actions were presented, the stakeholders were asked to identify and record practices that they already implement to progress the 2021-2022 Action Plan. Each stakeholder was given 10 minutes to identify their organization's practices and then these were presented in plenary.

Phase C of the DeCyDe-4-Shipping method engaged the stakeholders in the identification of additional actions that the Cypriot shipping industry should take, in the next year, to further optimize waste management, and create fit-for-purpose port reception facilities on the island. This resulted in the new 2022-2023 Action Plan for Waste Minimisation and Waste Management Optimization in the Cypriot Shipping Industry.

3 RESULTS AND DISCUSSION

The workshop was implemented on October 5th, 2022, in Nicosia, Cyprus, as a side event to the 9th Environment for Europe Ministerial Conference. Fifteen Cypriot shipping industry stakeholders participated, representing the Shipping Deputy Ministry, the Cyprus Shipping Chamber, ship management companies, shipping service providers, research centres, environmental NGOs, and consultants working with the shipping industry.

3.1 Shipping industry initiatives to optimize waste management

Eight practices towards achieving the aims of the 2021-2022 Action Plan for waste management optimization at port reception facilities were reported by the stakeholders participating at the workshop (Table 1). Some of these practices are implemented in Cyprus and concern exclusively activities at Cypriot port reception facilities, whereas others, reported mainly by shipping management companies and logistics/supply provisions companies, concern practices that are implement on-board or at ports of call. The wider geographic coverage of the practices demonstrates the positive impact that waste management minimization and optimization practices implemented by the Cypriot shipping industry can have globally.

Table 6 Actions implemented by the Cypriot shipping industry to improve waste management optimization at port reception facilities

Action Category	Implemented Actions
A1. Define waste categories and identify suitable and authorised waste handlers	- Identification of licensed companies, implementation of waste separation [Cyprus Port Authority]. ***Implemented in Cyprus.*** - Defining waste stream categories, storage methods, and licensed handlers [Privately management port authority] ***Implemented in Cyprus.***
A2. Develop necessary infrastructure and waste segregation schemes	- More equipment (skips) is made available at ports, and compactors have been purchased [Cyprus Port Authority] ***Implemented in Cyprus.*** - Waste categorization and segregation and correct storage [Ship management company] ***Implemented abroad.*** - Promote and help suppliers around the world to collect packaging materials from vessels [Logistics/supply provision company] ***Implemented abroad.***
A3. Revise fees to incentivise waste minimisation	- Law includes provision for reduced fees to vessels that implement waste minimization measures. Implementation of the provisions of the Law pending [Cyprus Port Authority] ***Implemented in Cyprus.*** - Made agreements with collaborating suppliers in Singapore so that when they complete their deliveries to ships they also collect all recyclables within MARPOL categories A (plastics) and C (other dry recyclables) without any additional costs to the ships. These dry recyclables are then delivered by the supplier to recycling plants [Logistics/supply provision company] ***Implemented abroad.***

A4. Transform Cyprus ports into pioneering Circular Ports	- Identify entities that can reuse "waste" such as euro pallets, wire ropes, tyres etc [Privately operated port authority] ***Implemented in Cyprus.***

3.2 Definition of the 2022-2023 Action Plan

The recording of already implemented practices provided the background against which the shipping industry could set its annual Action Plan for the next steps that should be implemented to develop fit-for-purpose port reception facilities in Cyprus (Table 2). While the Cyprus Port Authority, and privately managed port terminals already have lists of waste management companies that are licensed to collect and transport waste that comes to Cypriot ports, the industry believed that it is important to review this list and add stricter criteria in the selection of these contractors, so that emphasis is placed on identifying contractors that are able to utilize the waste that they collect in accordance to the principles of the circular economy. It was widely acknowledged by the participants that, currently, this is not the case. The participants were also concerned about the way that waste is collected at port reception facilities and how this might hinder practices for waste reduction and waste management optimization. Specifically, it was noted that while ships are obliged to separate their onboard waste according to MARPOL requirements, once at Cypriot ports, the waste is collected all together in a skip. This is a practice that is implemented by the Cyprus Port Authority (CPA), which later transports the waste to a specific on-site area where it is manually segregated. While the CPA noted that this was done to ensure proper waste segregation, this could lead to waste contamination and thus devalued waste, not fit for collection and reprocessing within a circular economy. Thus, developing the necessary infrastructure that will allow waste to be properly segregated and thus valorised was identified by the industry as an important action (A2).

The stakeholders noted that the relevant legislative framework on the operation of ports includes an article that allows the Cyprus Port Authority to impose reduced fees to vessels that call at Cypriot ports if they can prove that they have implemented practices for the reduction of their waste. However, neither the law nor the CPA specify what type of proof would be acceptable, resulting in uncertainty among vessels, which in turn leads to the non-application of this particular article. The stakeholders considered that it is a matter of priority for the CPA to issue guidelines clarifying the documentation that vessels need to procure to benefit from the reduced fees. This would act as an excellent incentive for further waste minimization.

Finally, it became clear to the industry stakeholders that significant work must be implemented to transform Cypriot ports into circular ports, and while this is not something that can be achieved in a year, the stakeholders maintained that this should remain a part of the Action Plan as steps must begin to be taken in this direction.

Table 7 The 2022-2023 Action Plan for Pillar A: Creating fit-for-purpose Port Reception Facilities

Pillar Category	Action	Organizations Involved
A1. Define waste categories and identify suitable and authorized waste handlers	Emphasis should be placed on identifying licensed contractors that utilize the waste they collect according to the principles of the circular economy	Cyprus Shipping Deputy Ministry, Cyprus Port Authority, privately managed port terminals, individual shipping companies
A2. Develop necessary infrastructure	Following on from measure A1, additional infrastructure must be developed to ensure that the waste is properly segregated in a way that facilitates its collection and valorisation	Cyprus Shipping Deputy Ministry, Cyprus Port Authority, privately managed port terminals, individual shipping companies
A3. Revise fees to incentivize waste minimisation	Clarify the provisions of Cypriot law that allows reduced fees to vessels that implement waste minimization measures. This will ensure that vessels are aware of what proof is required by the Cyprus Port Authority.	Cyprus Shipping Deputy Ministry, Cyprus Port Authority
A4. Transform Cyprus ports into pioneering circular ports	The Circular Economy must become part of the strategy and operations of ports, setting Cypriot ports ahead of the competition.	Cyprus Shipping Deputy Ministry, Cyprus Port Authority, privately

	managed port terminals, Expert consultants

4 CONCLUSIONS

In this article we presented the actions to be taken to make Cypriot commercial ports more sustainable through the optimization of waste management infrastructure. The DeCyDe-4-Shipping participatory method resulted in the identification of actions that are relevant, effective, implementable, and stem from stakeholder consensus, indicating a commitment for action by the industry. The Cyprus Shipping Deputy Ministry and the Cyprus Port Authority have very important roles to play with regards to moving the Action Plan forward, as all the identified actions would require not simply their input but their leadership. Individual shipping companies must be involved in the decision-making process for the waste categorisation and the development of the necessary infrastructure, and expert consultants working with the industry and public authorities will be instrumental in identifying ways in which Cypriot ports can move towards circularity. The Cyprus Shipping Strategy, issued by the Cyprus Shipping Deputy Ministry, aims for "Cyprus to be a significant and influential actor leading positive change in global shipping and an attractive maritime centre striving for sustainable growth and excellence" (https://cyshippingstrategy.com). The implementation of annual participatory policy-making processes, such as the one presented here, is an optimal vehicle towards this direction.

Acknowledgements

This study has been co-funded by BeMed (www.beyondplasticmed.org) through the initiative "A Shipping Commitment against Plastic Pollution in the Mediterranean". The views and opinions expressed in this manuscript are the sole responsibility of the authors.

References

Boucher, J., Bilard, G., (2020). The Mediterranean: Mare plasticum. Gland, Switzerland: IUCN. x+62 pp.

Fossi, M.C., Pedà, C., Compa, M., Tsangaris, C., Alomar, C., Claro, F., Ioakeimidis, C., Galgani, F., Hema, T., Deudero, S., Romeo, T., 2018. Bioindicators for monitoring marine litter ingestion and its impacts on Mediterranean biodiversity. Environmental Pollution, 237, pp.1023-1040.

Gerigny, O., Brun, M., Fabri, M.C., Tomasino, C., Le Moigne, M., Jadaud, A. and Galgani, F., 2019. Seafloor litter from the continental shelf and canyons in French Mediterranean water: distribution, typologies and trends. Marine pollution bulletin, 146, pp.653-666.

Loizidou X.I., Loizides, M.I., Orthodoxou, D.L., (2016). Marine strategy framework directive: Defining joint monitoring opportunities for the Eastern Mediterranean and the Black Sea, through dedicated decision making workshops and innovative policy tools. *Marine Policy*, 6: 76–82.

Loizidou X.I., Loizides, M.I., Orthodoxou, D.L., (2017). Marine Strategy Framework Directive: Innovative and participatory decision-making method for the identification of common measures in the Mediterranean. *Marine Policy*, 84: 82–89.

Loizidou, X.I., Orthodoxou, D.L., Loizides, M.I., Krestenitis, Y.N., (2021). A community-based approach for site-specific policies and solutions on marine litter: the example of Paphos, Cyprus. *Environment Systems and Decisions*, 41: 33-44.

Moheea, R., Surroopb, D., Mudhoob, A., Rughooputhc, B. (2012). Inventory of waste streams in an industrial port and planning for a port waste management system as per ISO14001. Ocean and Coastal Management, 61(6), 10 – 19.

Schumacher, J., Schernewski, G., Bielecka, M., Loizides, M.I., Loizidou, X.I., (2018). Methodologies to support coastal management – A stakeholder preference and planning tool and its application. *Marine Policy,* 94: 150-157.

Circular economy re-use of building materials at an island's port project

S.M. Gouloumis[1*], S.N. Michas[2]

[1]Civil engineer, N.T.U.A., member of HYDROEX S.A, Evoias 3, T.K. 15125 Marousi, Greece
[2]Civil engineer PhD, Director of HYDROEX S.A, Evoias 3, T.K. 15125 Marousi, Greece
[*]Corresponding author: spirosgls@gmail.com

Abstract

During the transition from linear economy to "circular economy", referring to a production and consumption model that aims to increase the efficiency of raw materials through the use of materials for a longer period of time, it is necessary to try re-use building materials whenever possible, especially when it comes to the limited natural resources of the Greek islands that have to be preserved. Thus, during an older construction contract of a fishing shelter at Xilokeratidi, Amorgos Island, many artificial blocks and the embankment material were "temporarily" gathered on a nearby beach, until the project was halted. About 20 years later, during the newer design and construction of the fishing shelter, all previously gathered materials were used, reducing the environmental footprint through the minimization of waste and the reuse of the limited natural materials, reshaping the beach of Katapola as well.

Keywords Circular economy, Re-use, Building, Materials.

1 EXCAVATION, CONSTRUCTION & DEMOLITION WASTE (AEKK)

Excavation, construction and demolition wastes, belong to the heaviest and most voluminous wastes produced in the European Union. They represent approximately 25% – 30% of all waste generated in the European Union and consist of materials such as concrete, iron, bricks, plaster, wood, glass, metals, plastics, asbestos and soil, materials that can be recycled, produced from activities concerning the construction of buildings and public infrastructure, total or partial demolition of buildings and infrastructure, renovations of buildings or apartments and the construction and maintenance of roads. It has been found that a circular economy development path could reduce carbon dioxide emissions up to 50% by 2030, compared to 2018 levels, before the coronavirus pandemic.
Community directives on waste, packaging and waste management have been in force for decades (e.g., EG/2008/98, 94/62/EG and 1999/31/EG). Cities like Amsterdam or London do show the way through programs like "London's Circular Economy Route Map" or "Towards a Circular Economy in Amsterdam", "Schiphol Airport, Amsterdam NL, circular lighting and displays".

Greek performance in the alternative management of AEKK is presented in the following data validated with the decision no. 170.5 of the Board of Directors of the Hellenic Recycling Agency (EOAN). Referring to the "the country's performance in the alternative management of Excavation, Construction and Demolition Waste (AEKK) concerning years 2016, 2017 and 2018", quantities are listed below:

Table 1. Management of Excavation, Construction and Demolition Waste (AEKK)

Year	Ingoing AEKK (tn)	Outgoing AEKK (tn)
2016	529,084	263,923
2017	990,455	734,809
2018	2,854,191	2,164,467

It can be noted that the portion of reused waste quantities is still very poor in Greece, still growing from year to year.

2 GREEK LEGAL FRAMEWORK

The Joint Ministerial Decision No. 36259/1757/E103/2010 Official Gazette 1312/B/24-8-2010, describes "Measures, conditions and programming for the alternative management of waste from excavations, constructions and demolitions (AEKK)". The accounting costs of a construction project include also the A.E.K.K. reception fee (asphalt, stones, soils, gravel, lightly reinforced concrete, etc.) where decision 4834/25-01-2013 is clarifying the requirements.

Law 4030/2011 FEK 249/A/25-11-2011, article 40 refers to “Issues related to waste from excavation, construction and demolition (AEKK)”

Law 4042/2012 (ΦΕΚ 24/A/13-02-2012), article 27 refers to "Reuse and recycling”

But that does not account for the environmental cost…, especially when it refers to the limited area Greek islands, where every consequence is magnified, being difficult to reverse.

3 INITIAL DESIGN OF THE FISHING SHELTER

In 2002, EOT’s technical services (Greek Tourism Organization) design a tourist boats’ shelter, at Xylokeratidi, northeast of Katapola Bay, Amorgos Island. During the construction phase, embankment materials had been gathered and several solid and cellular artificial blocks were constructed.

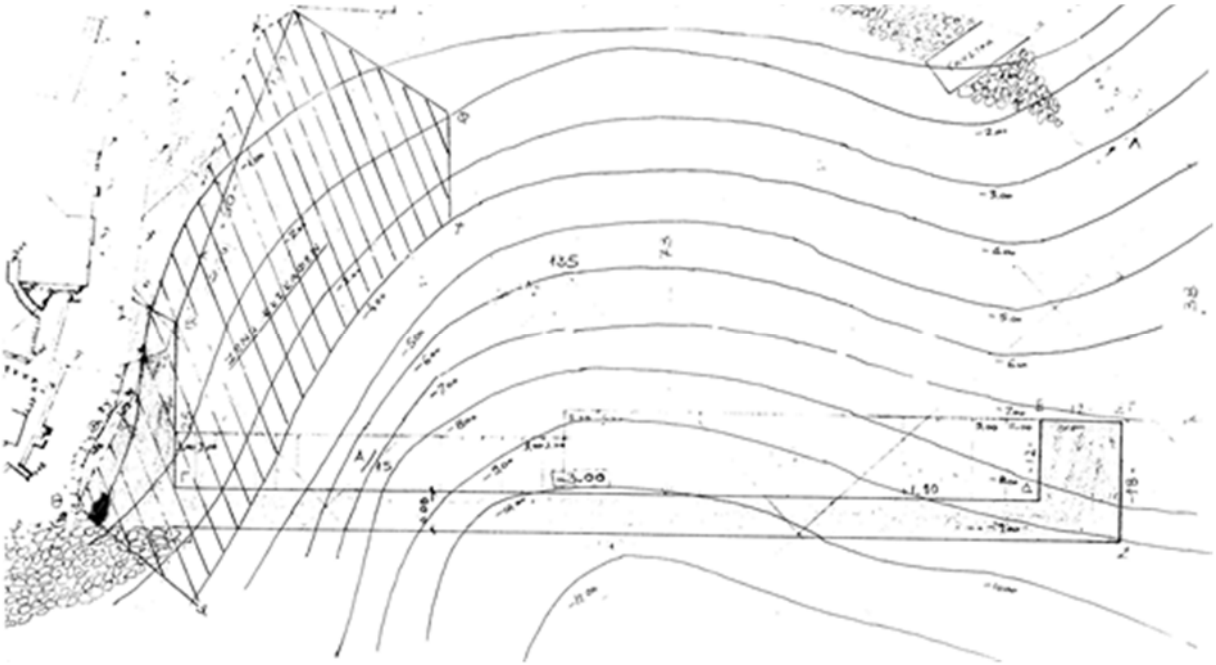

Plan 1. Initial planning of the fishing shelter. The breakwater formed with vertical docks, crosses the bathymetric contours up to -10.50 m

The project was initiated and the constructor had already gathered materials to start the construction but many opposed the project and it was finally canceled due to legal decisions (S.T.E.).

The embankment materials and many artificial blocks had to be "temporarily" deposited on Katapola beach, forming a whole new pier on the coast, splitting the beach in two parts, causing visual and environmental damage, resulting to strong reactions from swimmers, locals and visitors affected.

Photo 1. Katapola beach (2015) shortened by the pier, consisted of embankment material and 17 concrete blocks

In total, the quantities that had been deposited forming the new 1,780 m^2 area pier on the beach of Katapola bay, were : about 3,000 m^3 of embankment materials, 12 solid blocks (2.0m x 3.0m x 1.5m = 12 x 9.0 m^3 =108.0 m^3) and 5 big cellular blocks (4.0m x 7.0m x 1.3m = 5 x 36.4 m^3 =182.0 m^3).

2 

3 

Photo 2. Embankment materials and artificial blocks deposited from the previous contract.
Residents' reactions aiming to their removal were continuous, as can be seen on the protest banner (left).
Photo 3. The large-sized cellular artificial blocks were difficult to manage, causing great dissatisfaction

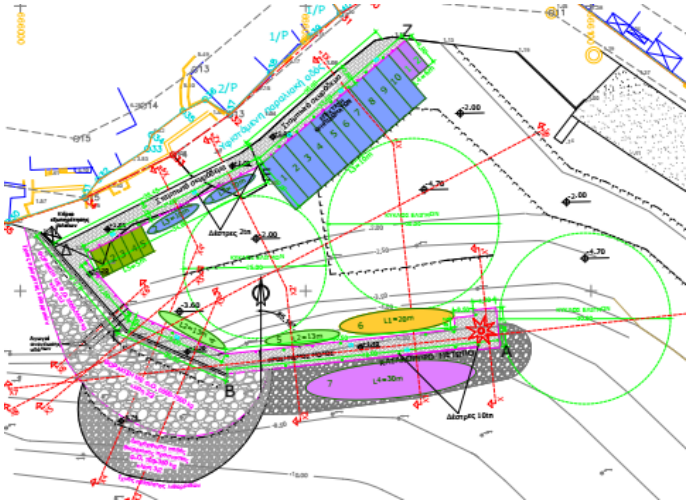

Drawing 1. New fishing shelter's design, following sea bottom's contours

During the new study (Drawing 1), the port basin was protected by a breakwater designed to mostly follow the relief of the sea bottom, aiming to save construction materials. Further on, the new design was adapted to incorporate all embankment material and artificial blocks deposited on the beach from the previous contract. Thus, during the construction of the new fishing shelter, the 5 cellular blocks weighing 68.22 tons each, were used to form the head of the breakwater (Photo 4), while the solid blocks, weighing 21.60 tons each, were incorporated into the construction of the shelter's docks.

Photo 4. The fishing shelter's breakwater head, was built using the existed cellular artificial blocks

5 

6 

Photos 5 & 6. Satellite and drone photos of Katapola bay, before (5) and after (6) the construction of the fishing shelter (formed on the left side of Katapola bay's photo). The artificial pier's materials have been incorporated into shelter's breakwater and the beach has been already returned to its initial condition.

Photo 7. Old contract materials were forming a pier perpendicular to Katapola beach (2015)

Photo 8. After the construction of the shelter, Katapola beach has been freed and rebounded (2022)

4 CONCLUSIONS

Circular economy should be a key objective for the islands and island regions development, contributing to the achievement of a balanced development that will make the islands sustainable for all days of the year, despite their particularities. Thus, it is considered necessary during the construction of major works to attempt reducing the environmental footprint through the minimization of waste and the reuse of the limited natural materials.

References

ΚΑΙΝΟΤΟΜΙΑ ΕΡΕΥΝΑ & ΤΕΧΝΟΛΟΓΙΑ, 115, (2019) A new economic model for sustainable development, Enterprise Europe Network-Hellas

Tratsa M. (2022): Circular economy as a "tool" for saving the climate, OT FORUM.

Zempilis D, Dipl.-Ing. TU München, Construction expert, Member of DGNB, BDSF, TEE. Available via https://ecopress.gr/kykliki-oikonomia-ston-kataskevasti/

DMPCO 2023

2nd International Conference

DESIGN AND MANAGEMENT OF PORT, COASTAL AND OFFSHORE WORKS

MAY 24-27, 2023

Aristotle University's Research Dissemination Center

Thessaloniki, Greece

Sponsors:

RESEARCH COMMITTEE
ARISTOTLE UNIVERSITY OF THESSALONIKI

OWC
An ABL Group Company

HELLENIC PORTS ASSOCIATION

GREEN FUND

Έργο: Υποστήριξη διοργάνωσης 2ου Διεθνούς Επιστημονικού Συνεδρίου με θέμα «Σχεδιασμός και διαχείριση λιμενικών παράκτιων και υπεράκτιων έργων»
Πρόγραμμα - Μέτρο: «Εξωστρεφείς Δράσεις, Φυσικό Περιβάλλον και Καινοτόμες Δράσεις 2023»
Προϋπολογισμός έργου: 15000 €
Χρηματοδότηση: Πράσινο Ταμείο
Όνομα δικαιούχου: ΕΛΚΕ ΑΠΘ, ΠΟΛΥΤΕΧΝΙΚΗ ΣΧΟΛΗ – ΤΜΗΜΑ ΠΟΛΙΤΙΚΩΝ ΜΗΧΑΝΙΚΩΝ

Under the auspices:

HELLENIC REPUBLIC
MINISTRY OF TOURISM

ΣΕΓΜ
Μελετητικές Συμβουλευτικές Επιχειρήσεις για τις Υποδομές και την Ανάπτυξη

MINISTRY OF MARITIME AFFAIRS AND INSULAR POLICY

Civil Enginnering Department AUTh

TEE | TKM

ThPA S.A.
PORT OF THESSALONIKI

DMPCO 2023

LABORATORY OF MARITIME ENGINEERING AND MARITIME WORKS

Civil Engineering Department
Aristotle University of Thessaloniki

University Campus: Thessaloniki, 54124 Greece

ISSN: 2945-1299
ISBN: 978-960-99922-6-8 (set e-book)
ISBN: 978-960-99922-7-5 (Vol. I e-book)